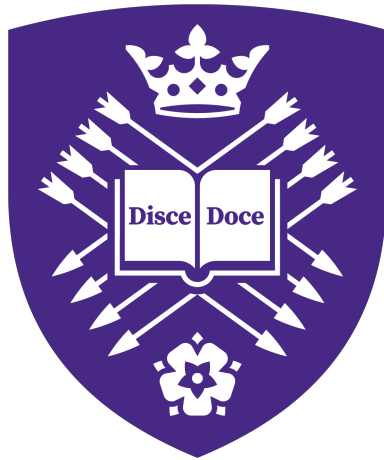


University of Sheffield

Investigating Damage within Zirconium Systems using X-Ray Diffraction Techniques



K. Sharma

A thesis submitted in partial fulfilment of the requirements for the degree of
Doctor of Philosophy

in the

Department of Materials Science and Engineering

2024

Investigating Damage within Zirconium Systems using X-Ray Diffraction Techniques

Kavi Sharma

A thesis submitted in partial fulfilment of the requirements for the degree of
Doctor of Philosophy

in the

Department of Materials Science and Engineering

January 2025

Non-Disclosure Agreement

The following work is under a non-disclosure agreement. It should only be shown to necessary internal staff at the University of Sheffield. Any sharing of the document outside of pre-arranged assessors should be discussed four weeks in advance to allow correspondence with the relevant departments.

Acknowledgements

The voyage of a PhD is never a simple one, facing numerous and difficult challenges at every corner. What has made it easier and substantially more pleasant are the people who have supported me throughout this journey, and I could not be more grateful.

First and foremost, I would like to give thanks to my academic supervisory team who, without their guidance, I would be stumbling through this world of research slightly aimlessly. Prof. Amy Gandy, who brought me on to this project, showing constant guidance, whether it was academically and personally, as well as the endless supply of optimism and encouragement throughout the hardships. Prof. Tamás Ungár, for all his patience and wisdom, taking his time to teach me a new and complex analytical technique and always putting up with my countless questions. A special thanks to my primary supervisor Dr. Lewis Owen, who, even though he got thrown into the deep end of my project, never seemed to run out of ideas and positivity. Without his wisdom in XRD, support and willingness to answer all my obvious and silly questions, my PhD and its research would not be at level it is today.

In addition to my academic supervisory team I would like to thank my industrial sponsors, National Nuclear Laboratory, and the corresponding industrial supervisory team. I would like to thank Dr Susan Morgan, whose oversight and wealth of knowledge gave me confidence in the research I was undertaking and broadened my understanding of the bigger picture. Dr Megan Jones, for her constant feedback and perspective, elevating my academic communication skills. Dr Helen Swan, without her expertise in XRD and TOPAS and her willing to always have meeting to advise, the analysis process would have been a lot more gruesome.

It would be remiss of me not to thank all the technical staff/post docs that, who without their support, time and hard work, none of my experimental work would be possible. Neil Hind for his heat treatment guidance, Tes Monaghan for her met-prep expertise, and a special thanks to Dr Robert Moorehead, who has played a vital part in preparing and conducting all of my Sheffield based XRD experiments, always willing to lend a guiding hand or ponder over strange diffraction data. I would like to thank Dr Gyula Zilahi, a MRF technician, for his help conducting Co XRD experiments and advice on XRD setups. To Dr Ross Nolan for advising and leading the cold rolling experiments. Last but not least, a notable thanks to Dr Rhys Thomas, a post-doc at University of Manchester, who not only worked tirelessly to help make CMWP work but was always willing to offer his expertise and free time to conduct experiments or discuss results.

This journey started with my cohort from the Advanced Metallic Systems CDT, and not only did they make my PhD but my life way more interesting. There are numerous fantastic people that stood beside me these last couple of years but there are a few that deserve a noteworthy mention. Thanks to Dr Ömer Koç for his kindness, TEM guidance and help in accessing equipment. Dr Sam Lister for his constant friendship throughout the years and discussions of food. Ashley Scarlett, who is always willing to play games or go on adventures, as well as allowing me to join his bubble during COVID, means more than I have ever said. A big thank you has to go to my two biggest supporters, Dr Frances Livera and Dr Lucy Farquhar, who have been emotional and mental pillars. Frances for the boundless generosity, always helping even when busy and being the best desk buddy a friend could ask for. Lucy for being my constant sounding board, Sheffield food tour buddy and a supply of endless entertainment. I do believe this journey without these two would have been nigh impossible.

Looking at the wider PhD community and friends, I am lucky to be in no short supply of wonderful people. I would first like to thank the people of H6 and H8, who have made my PhD experience drastically more entertaining. Thank you to a great group of friends, Funky Monkys, who made life more enjoyable and chaotic. Thank you to Jediah Capindale and Guo Jung Lian, my GTA buddies, who are always game for some friend chicken and soju. To Kieran Ralston, for being my card game and climbing partner. To Dr Tom Wilkinson, for being a voice of sanity and Matt Whittaker for being a voice of reason. To Dr Rachel Crawford, for being unapologetically caring and an emotional support. Lastly, to Matt Turton, for being the Night Fury to my Light Fury.

The support from my family has been paramount to me succeeding in this PhD - I believe words won't give it full justice. I would like to thank my wider family for always supporting me in the background, even if I do not say it out loud, I am appreciative of the words of encouragement and kindness. Thank you to my brother, whose calmness and wisdom has kept me grounded and afloat. To my baa and dada, who praised me, encouraged me, believed in me, I hope I have made you both proud. Finally to mum and dad, who have believed in me from day one, who think I can reach the stars if I try, I want to thank you.

I would like to thank the EPSRC and the National Nuclear Laboratory for funding this project. This work was supported by Science Foundation Ireland 18/EPSRC-CDT/3584 and the Engineering and Physical Sciences Research Council EP/S022635/1. This work was also supported by the Henry Royce Institute for Advanced Materials, funded through EPSRC grants EP/R00661X/1 and EP/P021727/1.

Abstract

The understanding of irradiation damage within nuclear materials, especially cladding material, is paramount to prolonging the lifespan of these materials or even preventing the potential failure mechanism they undergo. Therefore, a reliable, accessible and cost effective method of determining damage is key to stepping in the right direction.

In this work Convolutional Multiple Whole Profile (CMWP), an XRD analytical technique, is investigated to determine its validity and viability, by using a zirconium sample of varying deformation (as-received, heat treated, 30% cold worked, 48% cold worked and 60% cold worked) as well as different XRD radiation sources. As expected from an increase in deformation, the dislocation density increased and the crystallite size decreased. This was the same for both the Cu and Co source diffraction, with some slight quantitative differences. The discrepancy between between the Cu and Co data was determined to be due to the difference in resolution and penetration depth. The Co lab XRD was still deemed a viable option to use in conjunction with CMWP.

Current research into predicting deformation and failure mechanisms in nuclear materials primarily come from analogue, non-actively damaged samples (i.e proton or heavy ion implanted). The damage depth profile for these samples are much shallower than neutron irradiation. The grazing incident geometry was used with a NIST standard, Si, as there is known crystallite size and strain profile, to explore CMWP's capabilities at determining these physical parameters at these shallower damage depth profiles. The strain profile/dislocation density for both grazing incident (GI) and gonio geometry were refined to zero, matching with the NIST standard documentation. The crystallite size for GI's CMWP and TOPAS analysis and gonio's TOPAS analysis were fairly similar at approximately 240 nm, which was roughly two thirds of the NIST standard documentation (400 nm). The discrepancy was believed to be mainly due to the post-processing of the data to reduce noise, which inherently affected peak shape and height.

It is important to look into the thermal stability of dislocations which can be investigated through a thermal gradient - this provides a way to examine the accuracy of CMWP for a range of temperatures. A previous study, using high temperature synchrotron XRD (HT-SXRD), has investigated the effects of temperature on dislocation density as well as the effects of hydrogen and temperature on zirconium lattice parameters. The benefits of using a laboratory high temperature XRD (HT-XRD), would provide a cost effective and easily accessible method of investigating active materials in a hot cell. HT-SXRD provided an accurate representation of the increase in a lattice parameter but a less accurate determination of the relation between c lattice parameter and hydrogen dissolution. Where as HT-XRD had the inverse relation; the c lattice parameter had a continual increase and the a lattice parameter had no correlation with hydrogen dissolution. This was determined to be due to the texture of the sample relative to the geometry of the experimental setup (i.e. transmission or reflection) and the scattering vector.

Contents

1	Introduction	1
2	Background and Literature Review	4
2.1	Defects Formation and Effects	4
2.1.1	Point Defects	4
2.1.2	Line Defects	5
2.1.3	Planar Defects	6
2.1.4	Volumetric Defects	6
2.1.4.1	Cavities/Voids	7
2.1.4.2	Precipitates	7
2.2	Overview of Zirconium Metallurgy	8
2.2.1	Texture in Zirconium	9
2.2.2	Recovery and Recrystallisation	10
2.2.3	Crystallite Size	11
2.2.4	Dislocations	11
2.2.5	Comparison between Cold Worked and Irradiated Dislocations	14
2.2.6	Effects of Hydrides	15
2.2.7	Terminal Solid Solubility for Dissolution (TSSD) of Hydrogen	17
2.2.8	Ion Implantation Studies	19
2.3	Line Broadening	20
2.3.1	Overview of Line Broadening	20
2.3.2	Strain Broadening	21
2.3.3	Size Broadening	22
2.4	Current Methods of Determining Dislocation Density	23
2.4.1	TEM Methods	23
2.4.2	XRD Methods	24
2.5	Convolutional Multiple Whole Profile (CMWP)	27
2.5.1	Theory	27
2.5.2	Applications	31
2.5.3	Research Opportunity	33
3	Material Characterisation Techniques	34
3.1	X-Ray Diffraction (XRD)	34
3.1.1	Overview	34
3.1.2	XRD Geometries	35
3.1.3	Monochromators	37
3.1.4	Types of Detector	38
3.2	Scanning Electron Microscope (SEM)	39

3.3	Transmission Electron Microscope (TEM)	41
3.4	X-ray Fluorescence (XRF) Spectroscopy	43
4	Experimental Procedure	44
4.1	Heat Treatment of Zirconium	44
4.2	Cold Rolling/Working of Zirconium	45
4.3	Sample Preparation	46
4.3.1	Scanning Electron Microscopy (SEM)/X-ray Diffraction (XRD) Samples .	46
4.3.2	Electron Backscatter Diffraction (EBSD) Samples	47
4.3.3	Transmission Electron Microscopy (TEM) Samples	48
4.4	X-ray Diffraction Scan	51
4.4.1	Instrumental Standard - Lanthanum Hexaboride/Silicon	51
4.4.2	Zirconium Samples	51
4.4.3	High Temperature Zr-4 Scans	53
4.5	Data Processing for CMWP	55
4.5.1	Peak Index File	55
4.5.2	Instrumental Profile	56
4.5.3	Sample, Refining and Physical Parameters	57
4.5.4	Background Spline	58
4.6	Data Processing for TOPAS	58
4.6.1	Instrumental Effects	58
4.6.2	Sample Refinement	60
5	Accuracy and Sensitivity of CMWP	61
5.1	Introduction	61
5.2	Methodology	61
5.3	Results and Discussion	65
5.3.1	Sample Confirmation/Verification	65
5.3.2	Qualitative Comparison of Different XRD Radiation Sources	77
5.3.2.1	Cu Source	77
5.3.2.2	Co Source	79
5.3.2.3	Ag Source	80
5.3.3	Crystallite Size and Dislocation Density Analysis	82
5.3.3.1	Crystallite Size	82
5.3.3.2	Dislocation Density	87
5.4	Conclusion	91
6	Grazing Incident X-Ray Diffraction for CMWP	93
6.1	Introduction	93
6.2	Methodology	94
6.3	Results and Discussion	97
6.3.1	Minimum Grazing Incident Angle	97
6.3.2	Post-Processing of Data	98
6.3.2.1	Smoothing Function	98
6.3.2.2	Region of Diffuse Scattering	99
6.3.2.3	Absorption Edges	102
6.3.3	Crystallite Size Analysis	103
6.3.4	Viability of Heavy Ion Implantation Study	106

6.4	Conclusion	108
7	The Application of Lab HT-XRD on Hydrogen Charged Zr-4	110
7.1	Introduction	110
7.2	Overview of Previous Work	111
7.3	Methodology	112
7.4	Results	115
7.4.1	Qualitative Diffraction Pattern Analysis	115
7.4.2	Hydrogen Content	119
7.4.3	Lattice Parameter Expansion	120
7.4.4	CMWP - Line Dislocation Density	129
7.5	Conclusion	132
8	Conclusions	135
9	Future Work	137
	Bibliography	139
	Appendices	160

Nomenclature

β	FWHM
λ	Wavelength
μ	Attenuation Coefficient
ω	Grazing Incident Angle
ρ, d	Dislocation Density
σ, c	Crystallite Size Distribution
g	Diffraction Vector
m, b	Average Crystallite Size
ε_a	Total a Lattice Parameter Expansion
ε_c	Total c Lattice Parameter Expansion
a_1	HCP Contrast Factor 1
a_2	HCP Contrast Factor 2
R_e	Outer Cut-off Radius
a	a Lattice Parameter
c	c Lattice Parameter
x	Penetration Depth
b	Burgers Vector
C_{h00}	Average Contrast Factor
D	Crystallite Diameter
E_k	Kinetic Energy
K	Scherrer Constant
k	Reciprocal Space
l	Total Length of the Line

m_x	Mass of Species
M, e	Dislocation Arrangement
t	Number of Intersection with Dislocations
v_x	Velocity of Species

List of Figures

2.1	A visual representation of the three categories of point defects: vacancies, SIA and impurities (substitutional and interstitial impurity atom). Image recreated from Tanzi <i>et al.</i> [9].	4
2.2	Brightfield TEM images showing a) dislocation loops in annealed zirconium that have been neutron irradiated with a fluence of 1.5×10^{26} n.m ⁻² [14] and b) line dislocations in Zirc- 4 that has undergone conventional tensile testing [15]. The diffraction vector in each image was $g = 11\bar{2}0$ and $g = 0002$ respectively.	5
2.3	A schematic of the formation of a Frank loop dislocation, where the stress imparted onto the system is in the direction of the blue and red arrows. Recreated from Monavari <i>et al.</i> [19].	6
2.4	A micrograph of etched interstitial-free steel to show a clear example of grain boundaries [21].	6
2.5	Example of a diffraction pattern containing α -Zr and zirconium hydride taken on a beta-filtered Cu source lab diffractometer (Bruker D2 Phaser) [26].	7
2.6	An example of an EBSD map showing a reconstructed α -zirconium microstructure [47].	9
2.7	A Zr-H phase diagram [48].	9
2.8	EBSD maps showing grain elongation, deformation and texture of cold worked pure zirconium sheets of three different levels of deformation: a) 10%, b) 20% and c) 30%. The maps were taken in the RD-ND direction of the sample with a step size of 1 μ m [53].	10
2.9	A TEM micrograph showing $\langle a \rangle$ dislocations loops in annealed Zr at 700 K, a) fluence of 1.1×10^{25} n.m ⁻² , b) 1.5×10^{25} n.m ⁻² . The image was taken with a diffraction vector = $10\bar{1}1$ indicated by the black arrow [73].	12
2.10	A TEM micrograph showing $\langle c \rangle$ dislocations loops in annealed zircaloy at 550-580 K, a) non-irradiated zircaloy, b) 4×10^{25} n.m ⁻² . The image was taken with a diffraction vector = 0002 indicated by the black arrow [74].	12
2.11	A TEM micrograph showing $\langle a \rangle$ and $\langle c \rangle$ type dislocations formed in annealed zircaloy pressure tubing, by deformation, a) $\langle a \rangle$ dislocation, b) $\langle c \rangle$ dislocation. The image was taken with a diffraction vector = 0002 indicated by the black arrow [75].	13
2.12	An example of zirconium hydrides in both circumferential and radial directions. Examples of each are highlighted in red and blue respectively [100].	16
2.13	A graph showing the TSSD of Zr-2 and Zr-4 alloys, obtained by multiple measurement techniques, that are below 550°C [101].	18
2.14	A graph showing the TSSD and TSSP of Zr-2 and Zr-4 alloys, obtained by DSC and other multiple measurement techniques [23].	18

2.15	Two diffractions patterns of LaB ₆ showing the effects of line broadening: a) ideal environment with no line broadening and b) line broadening caused by sample and instrumental effects.	20
2.16	The effects of uniform and non-uniform microstrain on the lattice structure and the interplanar spacing (<i>d</i>) with the correlating effects on the diffraction pattern: a) A non strained material, b) a uniformly strained material and c) a non-uniformly strained material.	21
2.17	An example of the dislocation density intercept method on a GH2036 alloy. The number of intersections between the dislocations and drawn lines (yellow lines) is counted and divided by the total length of the line and thickness of the sample [142].	23
2.18	An example of a Williamson-Hall plot, showing a strained system, from a 60% cold worked ferritic steel [154].	24
2.19	The graphical representation of the linear relationship between $\frac{Y}{L^2}$ and lnL and how to get the dislocation density from the modified Warren-Averbach method [160].	26
2.20	An overview of the CMWP process demonstrated as a flowchart.	28
2.21	The effects of a) the change in the mean crystallite size (σ) and b) the change in variance (<i>m</i>), on XRD peaks. The increase in <i>m</i> shows an increase mainly in tail breadth, whereas an increase in σ shows an increase mainly in FWHM [3].	28
2.22	The effects of the dislocation arrangement parameter on XRD peaks: a) ordered dislocations with $M \ll 1$ and b) disordered dislocations with $M \gg 1$ [3].	29
2.23	A graphical representation of the convolution operation on two functions [170].	30
2.24	The CMWP software user interface.	30
2.25	A comparison of line dislocation density values, from TEM and sXRD, from zircaloy-2 at different proton fluences [169].	32
2.26	A figure comparing the dislocation density determined from CMWP analysis of sXRD and XRD data from two different temperature and dpa points: a) 450 °C and 2 dpa and b) 350 °C and 4 dpa [174].	32
3.1	A schematic diagram of a laboratory sealed tube [177].	34
3.2	Two graphs showing a) The range of X-rays produced in a sealed tube, indicating the continuous and characteristic wavelength regions [181] and b) A representation of how a beta filter removes the beta characteristic wavelengths.	35
3.3	A schematic diagram of the XRD geometries: a) Gonio geometry and b) Grazing incidence geometry [183].	36
3.4	A schematic diagram of transmission XRD, applying to both lab XRD and sXRD [185].	36
3.5	A schematic diagram comparing sXRD/tXRD and lab XRD with regards to their sensitivity towards surface contamination/defects.	37
3.6	The principle of a 0D detector via a schematic drawing.	38
3.7	The principle of a 1D detector via a schematic drawing.	39
3.8	The principle of a 2D detector via a schematic drawing.	39
3.9	A schematic diagram of the key features of an SEM [181].	40
3.10	Radiation produced from an electron beam's interaction with a sample [194].	41
3.11	A schematic diagram of a conventional TEM in imaging mode [200].	42

3.12	The principle of characteristic X-ray emissions showing the energy levels of a material and the corresponding characteristic emission lines. An interpretation from Margui et al. [208].	43
4.1	A schematic drawing showing the sectioned Zr foil.	44
4.2	Heat treatment temperature profile in the furnace.	45
4.3	Edge cracking on zirconium foil due to cold rolling. The initial edge cracking is highlighted in blue and the final extent after 60% is shown in red.	45
4.4	The donut rig used to manually grind and polish a sample.	47
4.5	The Struers bulk electropolisher setup.	48
4.6	The grinding machine to remove surface impurities and residues from TEM samples before electropolishing.	49
4.7	A vessel used for methanol and electropolishing solution to clean the machine and electropolish TEM sample respectively.	50
4.8	The electropolisher TEM sample holder.	50
4.9	The sample holder used for powders such as the LaB ₆ and Si standards.	51
4.10	Powder XRD standard samples, LaB ₆ and Si: a) LaB ₆ standard used to determine instrumental broadening and b) Si standard used as a reference because of its known crystallite size and strain.	51
4.11	Bulk sample holder used in the Panalytical Powder X'Pert and Malvern Panalytical Empyrean.	52
4.12	The absorption edge produced by a nickel beta-filter on an eight hour long XRD scan.	52
4.13	The crucible and XYZ stage used in HT-XRD: a) alumina (Al ₂ O ₃) crucible and b) XYZ stage.	53
4.14	The high temperature XRD (HTXRD) setup for the X'Pert.	54
4.15	The recorded temperature profile furnace against the theoretical temperature profile.	55
4.16	The method of identifying peaks and their intensities as well as the formatting for the peak index file.	56
4.17	An example of peak separation and background intensity removal and centring of K α_1 for the instrumental data.	56
4.18	An example of how the background spline can be adjusted whilst observing those effects of the calculate diffraction pattern.	58
4.19	TOPAS interface showing the LaB ₆ microstructural parameters.	59
5.1	The grid placed on TEM images of Zr-HT (from three different locations) to obtain the number of interception points to calculate line dislocation density. The images were taken on a JOEL JEM F200 with a 200 keV electron beam.	65
5.2	The identification of the peak positions of α -zirconium phase and unknown phases.	66
5.3	A BSE image and the resultant EDX results for Zr-HT show the even distribution of all elements that were determined by the instrumentation.	67
5.4	An overlay of Zr-HT-M and diffraction patterns of possible secondary phases.	69
5.5	An overlay of Zr-HT-M and diffraction patterns of possible secondary phases.	69
5.6	An SE image of a Zr-HT sample, after electropolishing, which revealed needle-like structures.	70
5.7	A comparison of diffraction patterns between Zr-AR-M and Zr80CW-RT, a sample with known hydrogen content, to gauge the significance of the hydrogen content within Zr-AR-M.	71

5.8	A Le Bail TOPAS fit of Zr-HT-Cu (Manchester), using α -Zr and ZrH ₂ , showing qualitatively the goodness of fit.	72
5.9	A high magnification EBSD map of Zr-48 showing the difficulties with indexing due to the high deformation and strain within the material. EBSD map taken in the ND-TD direction. The upper and lower misorientation angle thresholds were set to 10° and 3° respectively.	73
5.10	EBSD Map of Zr-HT to show alpha zirconium and grain orientation. EBSD map taken in the ND-TD direction. The upper and lower misorientation angle thresholds were set to 10° and 3° respectively.	74
5.11	EBSD Map of Zr-30 to show grain misorientation and preferential grain orientation. EBSD map taken in the ND-TD direction. The upper and lower misorientation angle thresholds were set to 10° and 3° respectively.	75
5.12	The misorientation in the material represented by KAM maps for: a) Zr-HT and b) Zr-30. The misorientation angle threshold was set to 2.5°.	76
5.13	A diffraction pattern of Zr-AR taken from the Manchester Cu source XRD machine, with its peak indexing of α -zirconium phase and delta zirconium hydride.	77
5.14	A comparison of monochromated Cu source (Manchester) XRD results for Zr samples.	78
5.15	A magnification of peaks at approximately 45° and 64° to show the peak broadening effect caused by the increase in mechanical deformation from heat treated to 60% cold worked samples.	79
5.16	A comparison of monochromated Co source XRD results for Zr samples.	80
5.17	A comparison of Ag source XRD results for Zr samples.	81
5.18	The initial modified Zr-HT Ag source diffraction pattern used to overcome the step change present around 15 - 16° and around 21 - 22°.	81
5.19	The final modified Zr-HT Ag source diffraction pattern used to overcome the step change present around 15 - 16°.	82
5.20	The crystallite size distributions calculated from EBSD maps from a) Zr-HT and b) Zr-30.	83
5.21	A graph showing the comparison of crystallite size trend, determined by CMWP, for the Cu and Co X-ray source experiments.	85
5.22	An example of the quality of fit for CMWP Zr-HT-Cu. The measured pattern was taken on a Cu source XRD machine with an approximate 24 hour scan time. The blue line is the measured pattern, the red line is the calculated pattern and the black dotted line is the difference.	86
5.23	An example of the quality of fit for CMWP Zr-HT-Co. The measured pattern was taken on a Co source XRD machine with an approximate 6.5 hour scan time. The blue line is the measured pattern, the red line is the calculated pattern and the black dotted line is the difference.	86
5.24	A graph showing the increase in strain, calculated from TOPAS using a Gaussian function, with an increase in deformation (Zr-AR to Zr-60) for both Cu and Co diffraction data. The blue line represents Cu data obtained from UoM and the red line represents Co data from MRF.	90
5.25	A graph showing the correlation between FWHM and deformation from four distinct Zr peaks: 002, 102, 004 and 104. The blue, red and yellow lines represent the FWHM from Cu, Co and Ag diffraction data respectively.	91

6.1	The interface of the SRIM software that was used to predict the damage depth profile of a self-interstitial zirconium ion, with an energy of 86.5 keV, within the target zirconium layer.	96
6.2	Two visual representations of the damage depth profile of an 86.5 keV Zr ion implanted into a target Zr interface at a perpendicular angle. a) The damage cascade produced and b) The frequency of ions at various target depths.	96
6.3	A comparison of diffraction patterns for the different grazing incident angle (ω angle) used on Si to determine viability of CMWP on lab XRD. The ω angles tested are: 0.32° , 1.00° , 1.30° , 1.50° , 1.75° and 2.00°	97
6.4	A comparison of a 5, 10 and 15 point moving average processing on the instrumental data, Si, to demonstrate the optimal number for the smoothing function.	99
6.5	A magnified image of a peak at approximately 88°, showing the comparison of the range of point moving averages.	99
6.6	The Le Bail TOPAS refinement of the original GIXRD LaB ₆ , showing the effects of the region of diffuse scattering on the fitting.	100
6.7	The Le Bail TOPAS refinement of the modified GIXRD LaB ₆ , showing the improvement of the fitting.	101
6.8	The removal of the diffuse scattering for TOPAS analysis. The blue line is the original diffraction data and the orange line is the modified diffraction data.	101
6.9	The background spline in CMWP that minimises the effects of the region of diffuse scattering.	102
6.10	The removal of the absorption edge on the Gonio Si diffraction data. The blue line is the original diffraction data and the orange line is the modified diffraction data.	102
6.11	The Le Bail TOPAS refinement of the modified GIXRD Si.	104
6.12	The Le Bail TOPAS refinement of the Gonio Si.	104
6.13	The CMWP fitting of the GIXRD Si diffraction data.	105
6.14	The CMWP fitting of the Gonio Si diffraction data.	106
7.1	A heating profile, during HT-XRD, for Zr80CWH.	113
7.2	An example of a peak indexed sample, with the unknown tertiary phase.	115
7.3	Phase identification of the tertiary phase in the HTXRD experiments, resulting in the identification of Al ₂ O ₃	116
7.4	A comparison of the diffraction patterns, from room temperature to 600°C (blue to red colour gradient), for Zr80CWA. The temperature at which the hydride peaks disappear is indicated by the black line - which is at 200 °C.	117
7.5	The formation of a shoulder at the left of (002), (102) and (103) peaks, above 460 °C. These hkl peaks are indicated by green, blue and yellow circles respectively.	118
7.6	A comparison of the diffraction patterns, from room temperature to 600°C (blue to red colour gradient), for Zr80CWH. The temperature at which the hydride peaks disappear is indicated by the black line - which is at 260 °C.	118
7.7	A comparison of the diffraction patterns, from room temperature to 600 °C (blue to red colour gradient), for Zr80CWB. The temperature at which the hydride peaks disappear is indicated by the black line - which is at 280 °C.	119
7.8	A graph showing the comparison of ‘expected’ hydrogen content values, determined through HVE measurements or nominal state, and the ‘actual’ hydrogen content values, determined through interpolations of TSSD curves found in literature.	120

7.9	An example of the trend of both a and c lattice parameter expansion, from HT-XRD, for Zr80CWA from room temperature to 600 °C.	121
7.10	A comparison of the goodness of fit (GOF) values, from the TOPAS analysis, for Zr80CWA, Zr80CWB and Zr80CWH.	122
7.11	An example of a Le Bail TOPAS fitting of Zr80CWA, at 340 °C, to show the contribution of the hydride phase once the hydride peaks have disappeared. . . .	122
7.12	A schematic diagram of a) lab and b) synchrotron XRD with the alignment of grains, due to cold rolling, to demonstrate the effects on the diffraction pattern. .	123
7.13	A diffraction pattern of Zr80CWA via sXRD, showing the faint signal from the basal plane (0002) [233].	124
7.14	A comparison of the a lattice parameters, from HT-sXRD, for Zr80CWA and Zr80CWH from room temperature to 800 °C [233]	124
7.15	A comparison of the a lattice parameters, from HT-XRD Le Bail TOPAS analysis, for Zr80CWA, Zr80CWB and Zr80CWH from room temperature to 600 °C. The vertical lines indicate the temperature at which the hydride peaks disappear for their respective samples.	125
7.16	A comparison of the two diffraction patterns of Zr80CWH, from HT-sXRD, at 60 °C (left) and 670 °C (right), to show the difference in intensities [233].	125
7.17	A comparison of the c lattice parameters, from HT-sXRD, for Zr80CWA and Zr80CWH from room temperature to 800 °C [233].	126
7.18	A comparison of the c lattice parameters, from HT-XRD Le Bail TOPAS analysis, for Zr80CWA, Zr80CWB and Zr80CWH from room temperature to 600 °C. The vertical lines indicate the temperature at which the hydride peaks disappear for their respective samples.	127
7.19	The trend determined for the total lattice parameter expansion of both a and c lattice parameter from HT-XRD data. The analysis was conducted on Zr80CWA, from room temperature to 600 °C, specifically on two separate peaks - 004 peak for c lattice parameter and 104 Zr peak for a lattice parameter.	128
7.20	A graphical representation of the difference in total lattice parameter expansion to determine the effects of hydrogen dissolution on said expansion. The difference between Zr80CWA-Zr80CWH (Δ 23.7 wt.ppm) and Zr80CWA-Zr80CWB (Δ 41 wt.ppm) for both a and c total lattice parameter expansion is shown in red/green and blue/yellow respectively.	129
7.21	A graph showing the dislocation density, determined from CMWP, on the HT-sXRD data. Graph taken from Swan <i>et al.</i> paper [233].	129
7.22	A graph showing the dislocation density, determined from CMWP, on the HT-XRD data.	130
7.23	A close-up of the CMWP fitting, of Zr80CW-400C, on a Al ₂ O ₃ double peak found around 43°.	131
7.24	A graph showing the TOPAS calculated Gaussian strain, using Le Bail analysis, on Zr80CWA, Zr80CWH and Zr80CWB. The black line represents the temperature at which the artefacts began appearing on the peak.	132
7.25	A graph showing the TOPAS calculated Lorentzian crystallite size, using Le Bail analysis, on Zr80CWA, Zr80CWH and Zr80CWB. The black line represents the temperature at which the artefacts began appearing on the peak.	132
A1	An example of file formatting for instrumental peak profile.	161

A2	The TOPAS interface in which the relevant instrumental parameters can be fixed or refined.	161
A3	An image demonstrating the refinement of the Peak Type - PVII parameter. . .	161
A4	An example of the sample parameters that refined/fixed when performing Le Bail analysis.	162
B1	The qualitative fit for the CMWP analysis of Zr-AR-M.	163
B2	The qualitative fit for the CMWP analysis of Zr-30-M.	163
B3	The qualitative fit for the CMWP analysis of Zr-48-M.	164
B4	The qualitative fit for the CMWP analysis of Zr-60-M.	164
B5	The qualitative fit for the CMWP analysis of Zr-AR-Co.	165
B6	The qualitative fit for the CMWP analysis of Zr-30-Co	165
B7	The qualitative fit for the CMWP analysis of Zr-48-Co	166
B8	The qualitative fit for the CMWP analysis of Zr-60-Co	166
B9	A graph showing the decrease in crystallite size, calculated from TOPAS using a Lorentzian function, with an increase in deformation (Zr-AR to Zr-60) for both Cu and Co diffraction data. The blue line represents Cu data obtained from UoM and the red line represents Co data from MRF.	168
C1	A comparison of the diffraction patterns for the ω angles 0.11° and 1.30°	169
C2	The goodness of fit of the CMWP fitting of Si when ω 1.30° and a smoothing function of 10 MPA.	170
C3	The goodness of fit of the CMWP fitting of Si when ω 1.30° and a smoothing function of 15 MPA.	170
C1	An example CMWP fitting on Zr80CW at 400°C	172

List of Tables

2.1	A table surmising the dislocation density, from relevant Zr systems, found in literature.	14
2.2	A table showing the identified slip planes and directions in an α -zirconium system [53].	14
2.3	A table showing the irradiation parameters (i.e. implantation energy and fluences), for desired damage depth and displacement per atom (dpa), to simulate neutron irradiation damage within zircalloys.	19
4.1	The rolling procedure runs on the zirconium strips. Highlighted regions are where the samples were taken out for their chosen deformation profile.	46
4.2	The final proposed grinding and polishing method of zirconium for XRD and SEM.	47
4.3	The final proposed grinding and polishing method of zirconium for EBSD.	47
4.4	Scanning parameters for the high temperature X'Pert mode.	54
4.5	Initial parameter values for CMWP that are not refined.	57
4.6	Initial physical parameters values.	58
4.7	A table of relevant instrumental parameters that were set when undergoing Le Bail refinement.	59
4.8	A table of the sample parameters that were either refined or fixed during the sample Le Bail analysis.	60
5.1	The scanning parameters of the XRD machines used.	62
5.2	A table showing the Smith-Guttman line intercept values obtained from analysing the TEM micrographs of Zr-HT and literature.	65
5.3	XRF results from Goodfellows.	67
5.4	XRF results from University of Manchester.	67
5.5	ICP-OES and HVE composition results via the Sheffield Assay Office.	68
5.6	The peak index for both alpha zirconium and delta zirconium hydride for a Cu radiation source.	77
5.7	Crystallite size results from different radiation sources using multiple analysis techniques.	83
5.8	The normalised weighted sum of square residual (WSSR) between the measure and CMWP fitted patterns for Cu and Co source XRD data.	87
5.9	A table showing the line dislocation densities, and the average, calculated by employing the Smith-Guttman line interception method on TEM micrographs. Images A, B and C refer to three different sites on one sample of Zr-HT.	87
5.10	CMWP dislocations density results from different radiation sources.	89
5.11	The comparison of the main physical parameters, for Zr-30-Cu, Zr-48-Cu and Zr-60-Cu, that are believed to be the main contributors to the outlier data of Zr-48-Cu.	89

6.1	Scanning parameters for the Panalytical X'Pert Powder in grazing incident geometry.	94
6.2	The mass, initial energy and final energy of a projectile (i.e. neutron) and target (i.e. Zr ion) in ballistic/elastic collision for the calculation of the transfer energy to a Zr ion if momentum and kinetic energy are conserved.	95
6.3	The comparison of crystallite size from NIST standard documentation, GIXRD CMWP analysis, Gonio CMWP analysis and TOPAS for Si.	103
6.4	A table showing the grazing incident angles (omega angles) required to investigate ion irradiated zircaloy found in the literature.	107
7.1	The sXRD scanning and temperature parameters used in the diffraction experiments.	111
B1	The weighted sum of square residual (WSSR) between the measure and CMWP fitted patterns for Cu and Co source XRD data.	167
B2	The crystallite size distribution parameter from CMWP fitted patterns for Cu, Co and Ag source XRD data.	167
B3	The Goodness of Fit (GoF) between the measure and CMWP fitted patterns for Cu, Co and Ag source XRD data.	167
B4	The dislocation arrangement parameter from CMWP fitted patterns for Cu, Co and Ag source XRD data.	168
C1	Physical parameters for the fitting of Si at 1.30° with a smoothing function of 0 (unsmoothed), 10 MPA and 15 MPA.	171

Chapter 1

Introduction

A major concern in the nuclear industry is the failure of active components, especially the cladding material that encapsulates nuclear fuel, during the post-discharge and storage process of spent nuclear fuel [1]. The cladding material used predominantly in UK nuclear reactors is zirconium alloys, Zircaloy-4 (Zr-4) and Zircaloy-2 (Zr-2), due to their low neutron cross-sectional area and relatively high corrosion resistance at high temperatures [1, 2]. Due to the harsh conditions experienced during operational nuclear reactors, such as high temperatures and neutron fluence, significant irradiation damage is introduced into these materials. Considerable research has focused on characterising, quantifying and understanding the effects of neutron irradiation damage, especially dislocations and zirconium hydride effects, on cladding material. Dislocation density is of primary interest due to the adverse effects of dislocations on the material properties; irradiation induced dislocations can cause effects such as radiation induced hardening (RIH), irradiation induced growth (IIG) and radiation induced embrittlement, which is likely to lead to mechanical failure and severe fallout. Investigating dislocation density could better help understand the mechanism by which they form and distribute, potentially providing a better and earlier indication of when parts could fail, and reducing the margin of error.

Owing to the limited access to research labs - such characterisation on active samples is difficult. Further issues arise from the time and operational costs associated with preparing and analysing samples using current conventional analytical techniques such as Transmission Electron Microscopy (TEM) and Synchrotron XRD (sXRD). The key advantages of using sXRD are the high resolution and short experimental time, whereas for lab XRD, the key advantages are their ability to investigate bulk material (i.e. more representative of the material) and the short sample preparation and experimental setup. The research community have overcome the active sample hurdle by using analogues for neutron irradiation damage: proton irradiation, heavy ion implantation and cold working. All of these methods have the ability to simulate neutron irradiated damage to varying degrees, with different damage depth profiles, without activating the material to the same degree. Although proton irradiation and heavy ion implantation have the closest approximation to neutron irradiation damage due to similar interaction and stopping mechanisms present, the accessibility to the technique is low and operational costs are high for such experiments. Therefore, cold working has been deemed a viable solution to replicate the magnitude of damage produced; the main difference in the damage between cold working and neutron irradiation is the type of dislocation loops present, where cold working presents predominantly $\langle a \rangle$ line dislocations, whereas irradiation damage at lower dpa/fluences starts with $\langle a \rangle$ loops and with the increasing dpa/fluences evolves into $\langle c \rangle$ loops.

Past research characterising and quantifying radiation and analogous damage from diffraction

data are very indirect. The line broadening analysis methods rely on the examination of individual peaks followed by the deconvolution of the profiles that contribute to the line broadening (i.e. instrumental, crystallite size and strain profiles). However, an up-and-coming diffraction pattern analysis technique, Convolutional Multiple Whole Profile (CMWP), has been developed to analyse phases as a whole using a more in-depth understanding of the line broadening parameters (i.e physical parameters that constitute the instrumental, crystallite size and strain profiles) [3]. Current investigations using CMWP research have been conducted primarily on sXRD and neutron diffraction data [4, 5]. The materials used for these experiments were Zr-4, Zr-2, aluminium-magnesium (Al-Mg) alloys, and a few stainless steel (SS) alloys, with damage primarily caused by proton irradiation. Studies using lab sources XRD machines and CMWP are uncommon.

To enable the expansion of CMWP, further validation and technique development of CMWP on multiple lab XRD geometries and radiation sources was deemed necessary. To increase the viability and reach of the technique, an understanding of whether the analytical technique is valid on different radiation sources, such as copper (Cu), cobalt (Co) or silver (Ag), is paramount. Furthermore, a concern with lab diffraction experiments, due to the standard gonio geometry, is the penetration depth of the X-rays, and as a result the volume of investigation. With proton irradiation or heavy ion implantation, the penetration depth of the damage profile is fairly shallow, especially in comparison to prolonged neutron irradiation or cold working. Therefore, the strain profile/dislocation density analysis of proton/heavy ion implantation would be less representative. The exploration into using grazing incident XRD (GIXRD) geometry in conjunction with CMWP is then key to investigate deformation closer to the surface of the sample. Additionally, the investigation of high temperature proton irradiated or heavy ion implanted samples has typically been conducted with high temperature sXRD (HT-sXRD). The direct comparison of high temperature XRD (HT-XRD) and HT-sXRD will provide useful insight into whether a more physically and financially accessible experimental setup is feasible in achieving viable diffraction in a pseudo-active material state. The pseudo-active material state is defined as re-reaching operational temperatures in an active material once they have been discharged and cooled to simulate an *in-situ* experiment.

The research presented in this following thesis will be sectioned into three experimental chapters:

- Chapter 5 - Accuracy and Sensitivity of CMWP
- Chapter 6 - Grazing Incident X-Ray Diffraction for CMWP
- Chapter 7 - The Application of Lab HT-XRD on Hydrogen Charged Zr-4

The aims of Chapter 5 is to validate CMWP by investigating the dislocation density and crystallite size of zirconium in five different deformed states: as-received from supplier, heat treated, 30% cold worked, 48% cold worked and 60% cold worked (where the % indicates sample thickness reduction). These results from CMWP are then compared to other analytical techniques such as Electron BackScatter Diffraction (EBSD) and TOtal Pattern Analysis Solution (TOPAS) as well as results obtained from different radiation sources (i.e. Co and Ag source diffractometers).

Chapter 6 will explore the validity of the GIXRD geometry for CMWP. The investigation of an XRD standard powder specimen, silicon (Si), due to its known crystallite size profile and strain profile, will determine the accuracy of GIXRD in conjunction with CMWP. The GI CMWP results are then compared to National Institute of Standards and Technology (NIST) documentation (i.e. NIST 640f standard), CMWP analysis in Gonio mode as well as TOPAS analysis in both GI and Gonio geometry.

The final experimental chapter, Chapter 7, aims are split into two: 1) investigating the validity of using HT-XRD for analogous pseudo active samples by comparing to HT-sXRD and 2) further technique development of HT-XRD CMWP by testing the accuracy against results obtained by HT-sXRD. Additionally, to further validate the accuracy of the CMWP, the trend in a heavily deformed (80% cold worked) material undergoing a temperature change (room temperature to either 600 °C or 800 °C for HT-XRD and HT-sXRD respectively) was determined.

Chapter 2

Background and Literature Review

2.1 Defects Formation and Effects

Neutron irradiation causes defects within metals such as dislocations, point defects (self-interstitial atoms (SIA) and vacancies), precipitates, He bubbles and voids that affect the materials' mechanical properties [6]. The lattice defects can be categorised into four groups: point defects, line defects, planar defects and volume defects [7].

2.1.1 Point Defects

Point defects can be divided into three further groups: SIAs, vacancies and impurities, and they are all comparable in size to a lattice atom, as shown in Figure 2.1. A SIA is classified as an atom, of the same species as to one of the constituents of the bulk material, located outside of a lattice site. A vacancy is defined as a space within a lattice site, where an atom should be. Incident radiation on a material causes the displacement of a primary knock-on atom (PKA) which in turn leads to the further displacement of atoms from their lattice site, due to its energy being above the displacement threshold, producing an SIA and vacancy, which is known as a Frenkel pair. This process is called a collision cascade [8]. An impurity defect can either be interstitial or substitutional (replaces a lattice atom) and is defined as an atom foreign to the composition of the material. A combination of two or more point defects can be formed, known as complex point defects, such as point defect clusters or compound clusters.

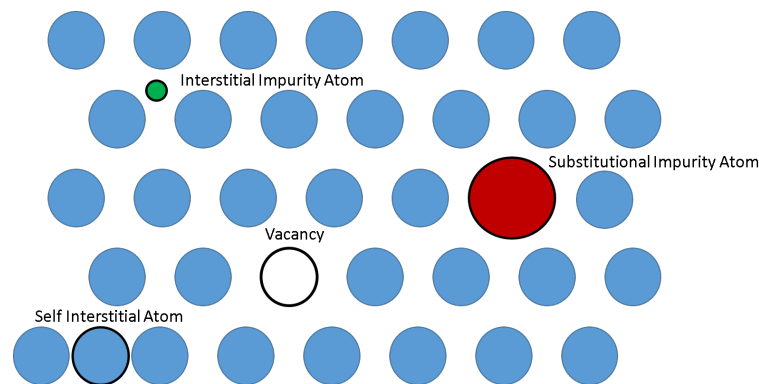


Figure 2.1: A visual representation of the three categories of point defects: vacancies, SIA and impurities (substitutional and interstitial impurity atom). Image recreated from Tanzi et al. [9].

2.1.2 Line Defects

With regards to the remaining three categories of lattice defects, their dimensions/sizes are much larger than the crystal atoms [7]. Line defects are produced when atoms are added or removed, introducing localised strain in the lattice surrounding the defects. Line defects form when it is energetically favourable for the point defects to cluster or the vacancy cluster to collapse, forming an extra half-plane or missing half-plane respectively, in the crystal lattice [10]. These defects are also referred to as dislocations. In a crystal, a dislocation can not end abruptly, it must end on either a free surface, grain boundary, another dislocation (forming a node) or itself (dislocation loop) [11]. An example of line dislocations and dislocation loops is shown in Figure 2.2, where the dislocations are marked with red and green arrows. The diffraction vector for the TEM micrographs containing loops and lines was $g = 11\bar{2}0$ and $g = 0002$ respectively.

For a HCP crystal structure (i.e. zirconium system), dislocation loops can be further categorised into three groups: $\langle a \rangle$ dislocation loops, $\langle c \rangle$ dislocation loops and $\langle c + a \rangle$ dislocation loops [12]. These categories refer to which plane these dislocation loops reside on. When discussing irradiated materials, at low neutron fluences dislocations are dominated by $\langle a \rangle$ dislocation loops, however, at the higher neutron fluences $\langle c \rangle$ and $\langle c + a \rangle$ dislocation loops start to become more predominant [13].

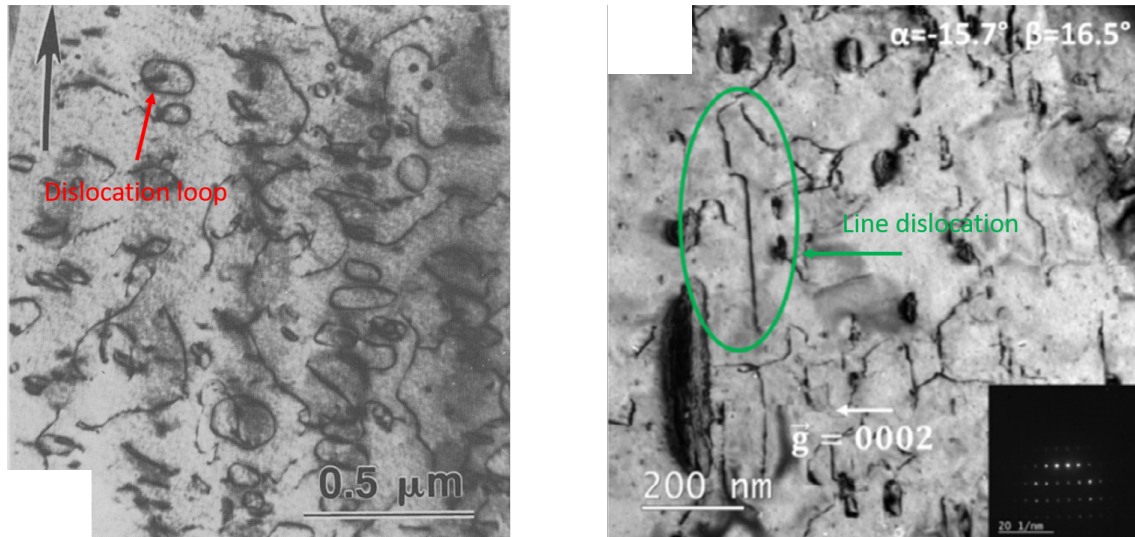


Figure 2.2: Brightfield TEM images showing a) dislocation loops in annealed zirconium that have been neutron irradiated with a fluence of $1.5 \times 10^{26} \text{ n.m}^{-2}$ [14] and b) line dislocations in Zirc-4 that has undergone conventional tensile testing [15]. The diffraction vector in each image was $g = 11\bar{2}0$ and $g = 0002$ respectively.

A step further than a dislocation loop is, when it is energetically favourable, for a group of dislocation loop to collapse and form a dislocation network or for line dislocations to cluster together [16, 17]. A dislocation can also form a Frank loop, which is where a dislocation is pinned by point defects and shear stress deforms the dislocation, where once it passes the critical point a Frank loop dislocation is formed [18]. Figure 2.3 shows the formation of the Frank loop, where the dislocation starts as the thick black line, and with increasing stress inputted in the direction of the blue arrow, the dislocation is deformed outwards following steps 1 - 3. At step 3, a nearly formed Frankel loop is created (blue line) and a new dislocation begins forming (red line). With the continued stress inputted, step 4 is where a complete Frankel loop and a new

dislocation line is formed.

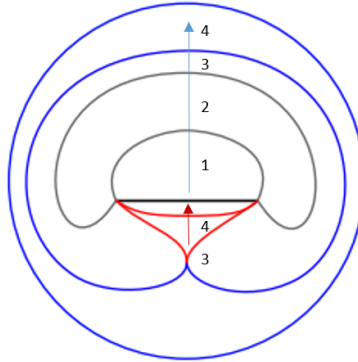


Figure 2.3: A schematic of the formation of a Frank loop dislocation, where the stress imparted onto the system is in the direction of the blue and red arrows. Recreated from Monavari et al. [19].

2.1.3 Planar Defects

Planar defects are discontinuities within a plane such as grain boundaries, twin boundaries and stacking faults [7]. Grain boundaries are planar defects, present in all crystals, which are boundaries between two misaligned grains (crystalline grains of different orientations), as shown in Figure 2.4 [20]. The other two planar defects, twin boundaries and stacking faults, are introduced into the system through crystal growth and plastic deformation.

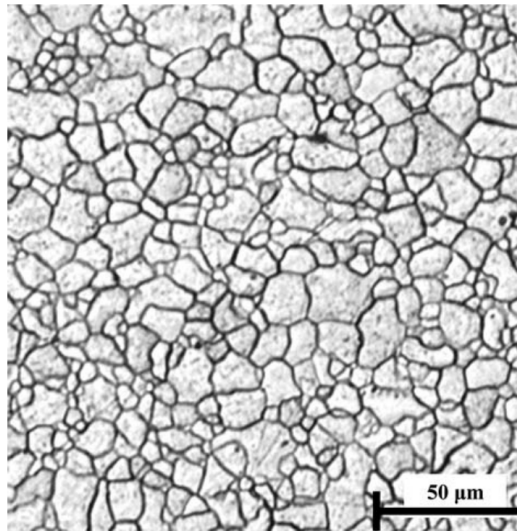


Figure 2.4: A micrograph of etched interstitial-free steel to show a clear example of grain boundaries [21].

2.1.4 Volumetric Defects

Volumetric defects are three-dimensional defects and can be split into two categories: cavities/voids and precipitates [7].

2.1.4.1 Cavities/Voids

Cavities are the clustering of vacancies via diffusion due to either residual stress gradients or because it is more energetically favourable than numerous smaller vacancy clusters [22]. A cavity/void, as it is more energetically favourable, can contain gas and form bubbles such as helium (He) bubbles.

2.1.4.2 Precipitates

Precipitates are the final defects that need to be discussed and can be described as secondary phases within the bulk material. A typical precipitation that occurs during zirconium alloy irradiation is the formation of zirconium hydrides [23]. This occurs via two methods: 1) when the system cools down during post-discharge and storage, therefore the hydrogen produced from the reaction stated in Equation 2.1, becomes less mobile and reacts with the zirconium [24] and 2) when zirconium reaches its terminal hydrogen solubility limit - the maximum concentration hydrogen can be in the matrix before it is readily reacting with zirconium, producing zirconium hydride precipitates [23, 25]. An example of the zirconium hydride phase in a zirconium-zirconium hydride diffraction pattern is shown in Figure 2.5 [26].

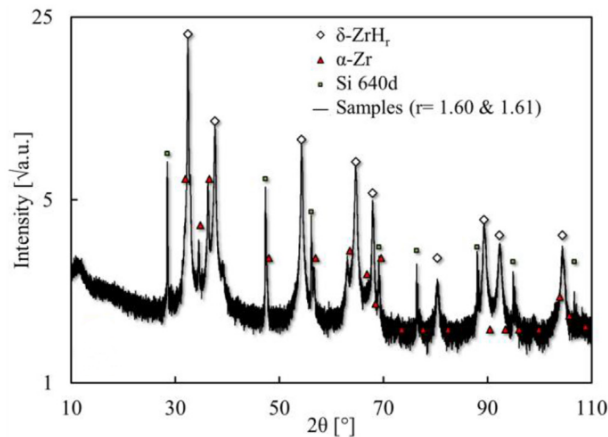


Figure 2.5: Example of a diffraction pattern containing α -Zr and zirconium hydride taken on a beta-filtered Cu source lab diffractometer (Bruker D2 Phaser) [26].

Hydrogen is a common by-product of neutron irradiation via an oxidation reaction or the radiolysis of water and though it diffuses rapidly into the environment, it may still have adverse effects on damage at low concentration due to it being highly chemically active [27]. The half equations for the oxidation reaction are shown in Equation 2.1 [28]. Radiolysis is the phenomenon that occurs when a molecule, in this case, water, is destabilised by ionising irradiation particles such as phonons, electrons or heavy ions.



Another important precipitate mechanism is the formation of secondary phase precipitates (SPPs) from alloying elements in order to control the mechanical and chemical performance of the material (i.e. increase the service life of fuel components). The size of the SPPs varies and is determined by thermo-mechanical processing parameters.

In zirconium and its alloys, the addition of elements such as silicon (Si), between 0.01 - 0.1 wt%, can improve corrosion resistance and ultimate tensile strength as well as decrease hydrogen uptake within the component [29]. The more common alloying elements are tin (Sn), iron (Fe), chromium (Cr), nickel (Ni) and niobium (Nb), which when precipitate out and are greatly and evenly distributed, highly affect the corrosion kinetics and hydrogen pick-up [30]. The alloying of Sn (low concentration of 0.01 - 0.93 wt%) mainly remains in solid solution with Zr, however, SPPs can form in the oxide layer, improving its stability and therefore improving corrosion resistance [31–33]. Fe, Cr and Ni precipitates in zirconium alloys (as two structures - $Zr_2(Fe,Ni)$ and $Zr(Fe,Cr)_2$) which improve creep resistance and strengthening under irradiation as well as suppressing hydrogen uptake by replacing Zr ion sites in the oxide layer, consequently decreasing the potential gradient and reducing hydrogen diffusion [34–36]. The addition of Nb and its precipitation significantly improves the corrosion and creep resistance of Zr by producing a denser oxide layer and a segregation layer (β -Zr-Nb layer that concentrates at α -Zr grain boundaries) between the oxide layer and bulk material. The denser oxide layer acts as a protective layer and reduces hydrogen pick-up, whereas the segregation layer improves the grain boundary cohesion between the oxide layer and the bulk material [37–39].

2.2 Overview of Zirconium Metallurgy

This section will cover a brief overview of zirconium metallurgy and the defects produced during irradiation and cold-rolling.

Zirconium is an allotropic element that consists of two main phases: α hexagonal closed-packed (HCP) crystal structure and β body-centred cubic (BCC) structure [40]. When looking at zirconium and its alloys, under ~ 852 °C, the material is predominantly in the alpha phase, an example of α -zirconium microstructure is shown in Figure 2.6. Above ~ 852 °C, zirconium and its alloys reside predominantly in the beta phase, as shown in Figure 2.7 [41, 42]. β -Zr is more susceptible to hydride formation as hydrogen is a β -Zr stabiliser, as can be seen from Figure 2.7 where the β -Zr transformation temperature decreases with an increase in hydrogen percentage, therefore is more susceptible to hydrogen cracking [43]. In the UK, the operating temperature of nuclear reactors ranges between 280 - 350 °C (553 K - 623 K), therefore, zirconium during reactor operation is mainly α -Zr [44–46].

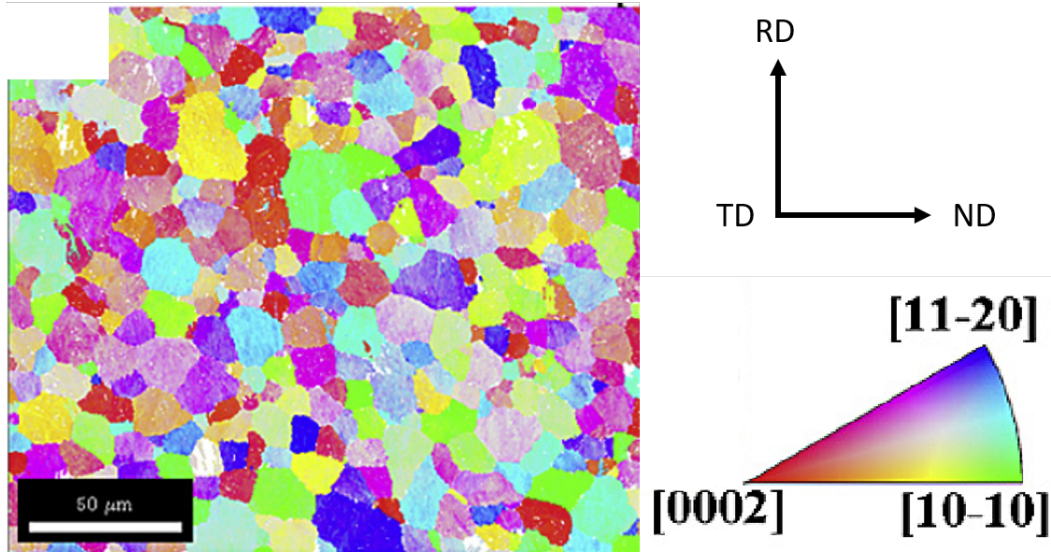


Figure 2.6: An example of an EBSD map showing a reconstructed α -zirconium microstructure [47].

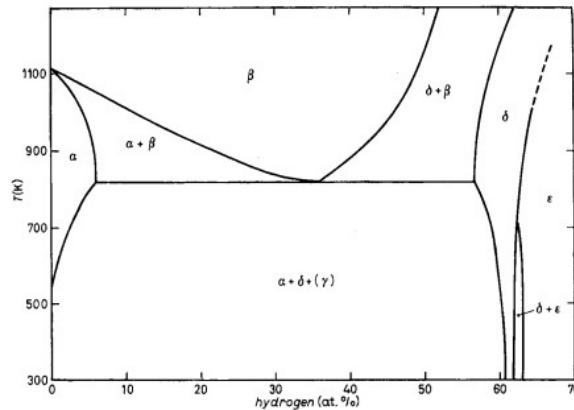


Figure 2.7: A Zr-H phase diagram [48].

2.2.1 Texture in Zirconium

Texture can be defined as the orientation distribution of crystallites within a polycrystalline material and due to Zr crystallites having a c/a ratio of 1.593, it is easy for it to develop a crystallographic texture [49]. The texture of zirconium and its alloy, in an as-received state, is bimodal - the crystallites facing from $\langle 10\bar{1}0 \rangle$ to $\langle 11\bar{2}0 \rangle$ [50]. The development of crystallographic texture from there is dependent on post thermo-mechanical processes such as cold rolling or annealing and varies depending on the composition of the alloy [51].

For industrial pure zirconium (i.e. containing no more than 0.01% Hf), when undergoing hot rolling, there is a diffuse texture that deviates approximately $20 - 90^\circ$ from the basal plane along the transverse direction (TD). However, cold rolling develops a less diverse range of deviation, with the crystallites orientated approximately 20° from the basal plane. Liu *et al.* determines by cold working industrial pure zirconium to 30% deformation [52, 53]. An example of texture in 10%, 20% and 30% cold worked Zr, represented via EBSD maps, is shown in Figure 2.8.

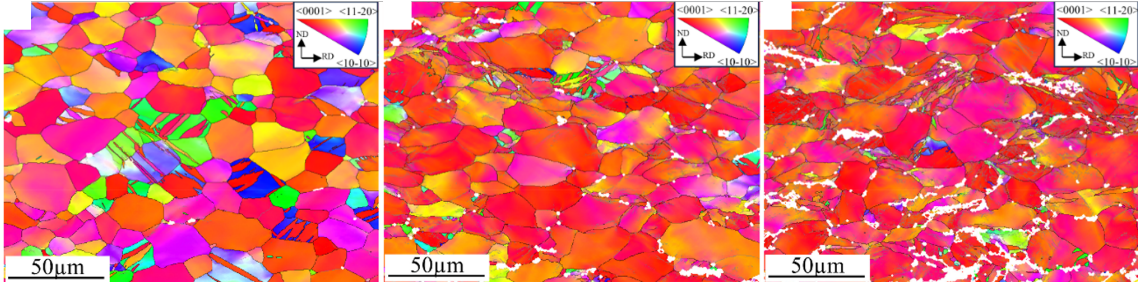


Figure 2.8: EBSD maps showing grain elongation, deformation and texture of cold worked pure zirconium sheets of three different levels of deformation: a) 10%, b) 20% and c) 30%. The maps were taken in the RD-ND direction of the sample with a step size of 1 μm [53].

When Zircaloy-4 (Zr-4) undergoes cold rolling the c axis orientates so that it is relatively in line with the normal direction (ND), this is due to the pyramidal and prismatic $\langle a \rangle$ slip systems allowing for compression of the c axis when under said compression [54]. A study by Grange *et al.* confirmed this by investigating a hydrogen charged Zr-4 plate that was cold worked to 450 μm , where the study states that the basal planes are orientated approximately 20° away from ND (c axes close to parallel to ND). This was corroborated by Guo *et al.* studying texture development in Zr-4 plates that had been cold rolled to 33% and 66%, which states that the c axis becomes predominantly approximately parallel to ND [55, 56].

Whereas for Zircaloy-2 (Zr-2) and Zr-2.5Nb, the basal planes (0001) orientate themselves so that they are parallel to the rolling plane and the direction is parallel to TD or rolling direction (RD) depending on the extent of cold rolling. This is reported by Qiao *et al.* investigating the texture in moderately cold worked Zr-2 and corroborated by Reid *et al.* [57–59].

2.2.2 Recovery and Recrystallisation

Recovery and recrystallisation are thermal processes that affect and/or rearrange the microstructure to different extents during annealing. Recovery is the process in which the energy of the system is reduced by the annihilation of point defects and the rearrangement of dislocations into lower energy configurations [60]. It is a low temperature process that removes the residual stress within the material without reducing its strength [61]. Recrystallisation is the heat treatment process in which deformed grains are replaced with new and relatively undeformed grains in order to remove the effects of strain hardening [62]. It is where the nucleation of relatively undeformed grains forms within the deformed grain and the growth of said new grain occurs via the formation and movement of high-angle grain boundaries [63].

Typically, in cubic structures, it is found that recrystallisation has a significant effect on texture where it can remove preferential grain orientation from the cold rolling and induce a randomise grain orientation [64, 65]. However, for zirconium, the literature states that primary recrystallisation does not have a major impact on its texture, depending on the extent of the previous deformation [50]. Gerspach *et al.* suggests that primary recrystallisation produces a texture change in Zr702 that is cold rolled to 40% as there is no orientation-dependent nucleation, whereas deformation from 50 - 80%, the texture remains stable. The exception is when Zr702 has been cold rolled in the TD compared to the previous hot rolling direction and primary recrystallisation changes texture at all deformation states [66]. This is supported by Zimmermann *et al.*, which states that in pure Zr and in Zr-4 plates that have been cold worked to 55%, after primary recrystallisation at temperatures between 550 - 575 $^\circ\text{C}$, the texture remains stable for

both materials [67]. To remove preferential grain orientation and induce a texture change (i.e. complete recrystallisation), the annealing process may require higher temperatures and longer hold times [68].

2.2.3 Crystallite Size

Zirconium and its alloys, like many other materials, have a microstructure that is formed by an agglomerate of individual crystallites, whose size varies depending on the thermo-mechanical process the material has been through as well as limitations of the characterisation techniques.

IAEA suggests that undeformed zirconium alloys have approximately an average crystallite size of 1 - 20 μm . The materials that were tested had undergone extensive heat treatment to ensure full recrystallisation and some grain growth and the grain sizes were determined using ASTM standard 10 and ASTM standard 15 [69]. However, one consideration to take into account for these grain size values is the heat treatment process, where the material was treated for between 1 - 10 hours at 600 - 750 $^{\circ}\text{C}$ - this process is likely to instigate grain growth (at the higher temperatures and hold times) and produce large grain sizes. Another consideration is the measurement technique, which was done by an intercept method on an etched optical image, thus restricting the grain size to the limit of resolution of the optical instrument, hence possibly producing an overestimate of the average grain size.

Jedrychowski *et al.* suggests that alpha zirconium, which was a) initial state (i.e. recrystallised and b) previously cold rolled to 16% and then partially recrystallised with a heat treatment of 650 $^{\circ}\text{C}$ for 15 minutes, have a crystallite size of approximately 16.0 and 12.7 μm respectively [70]. The crystallite size analysis was conducted from EBSD characterisation, which was conducted with a step size of 1.2 μm , therefore limiting the minimum crystallite size to the resolution of the equipment. In addition, it was a partial recrystallisation process, which means there are complete nucleation of new grains and removal dislocations. Both of these considerations could lead to an overestimation of the crystallite size.

2.2.4 Dislocations

Zirconium and its alloys are widely used in the nuclear industry, such as cladding and structural materials, as they have excellent corrosion and radiation resistant properties (i.e. have a low neutron cross-section and a high resistance to heat and chemical corrosion) [71]. However, even with high resistant properties, with the large amount of neutron bombardment that occurs, irradiation-induced defects and dislocations are still produced [6, 72]. Choi *et al.* showed that there are three types of dislocation loops formed in zirconium and its alloys, $\langle a \rangle$, $\langle c \rangle$ and $\langle c+a \rangle$ dislocation loops, with their growth correlating to temperature and neutron fluence. Dislocation loop density decreases with an increase in temperature but the loop size increases. However with fluence, dislocation loop density increases with an increase in fluence, as shown in Figure 2.9 [73].

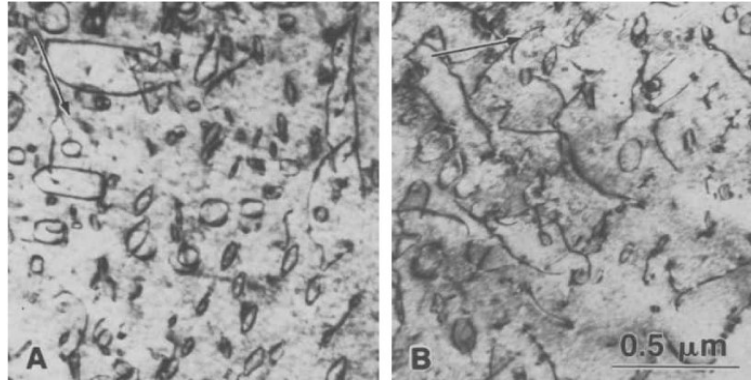


Figure 2.9: A TEM micrograph showing $\langle a \rangle$ dislocations loops in annealed Zr at 700 K, a) fluence of $1.1 \times 10^{25} \text{ n.m}^{-2}$, b) $1.5 \times 10^{25} \text{ n.m}^{-2}$. The image was taken with a diffraction vector = $10\bar{1}1$ indicated by the black arrow [73].

Furthermore, Adamson *et al.* presents a study where a non-irradiated zircaloy with dislocations is neutron irradiated at a fluence of $4 \times 10^{25} \text{ n.m}^{-2}$ and rapid growth of $\langle c \rangle$ type dislocation loops is observed, as shown in Figure 2.10 [74].

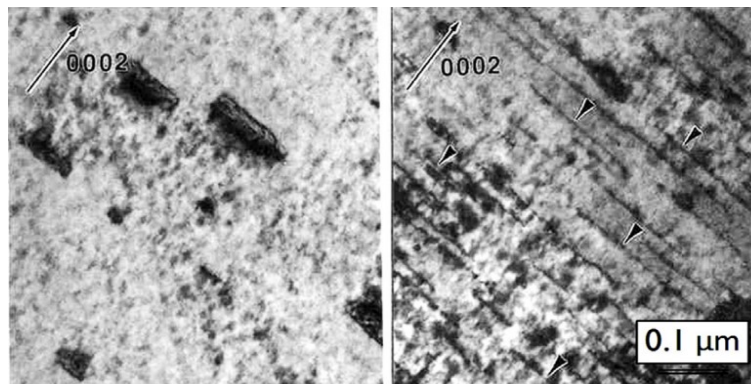


Figure 2.10: A TEM micrograph showing $\langle c \rangle$ dislocations loops in annealed zircaloy at 550-580 K, a) non-irradiated zircaloy, b) $4 \times 10^{25} \text{ n.m}^{-2}$. The image was taken with a diffraction vector = 0002 indicated by the black arrow [74].

The damage above is representative of irradiation-induced dislocations, whereas the current work is based around cold-worked induced dislocation, which was used as proxy radiation damage within the material. Holt *et al.* discusses in a paper the formation of $\langle a \rangle$ and $\langle c \rangle$ type dislocations in zirconium pressure tubing due to deformation, as shown in Figure 2.11. The paper suggests that with a 27% reduction in area, from a cold-drawing process, the total dislocation density was approximately $3 - 4 \times 10^{14} \text{ m}^{-2}$ with 10 - 20% of that being from $\langle c \rangle$ type dislocations - this was determined by deconvoluting XRD data [75]. Defining deconvolution as post-processing analysis; back-calculating the constituents of the strain profile, using assumptions or graphical interpretation/extrapolation, to determine the physical parameters (in this case dislocation density).

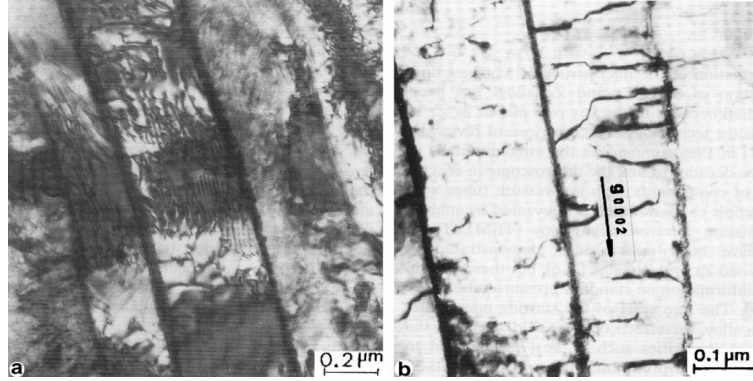


Figure 2.11: A TEM micrograph showing $\langle a \rangle$ and $\langle c \rangle$ type dislocations formed in annealed zircaloy pressure tubing, by deformation, a) $\langle a \rangle$ dislocation, b) $\langle c \rangle$ dislocation. The image was taken with a diffraction vector = 0002 indicated by the black arrow [75].

Previous studies by Long *et al.* have investigated hot rolled Zr-2.5Nb, in both the rolling direction (RD) and the normal to rolling direction (ND). In the undeformed Zr-2.5Nb it was found that, using line profile analysis (eCMWP - an old online version of CMWP) on neutron diffraction data, both in the ND and RD samples, the dislocation densities were fairly similar, with it being $1.76 \times 10^{14} \text{ m}^{-2}$ and $1.02 \times 10^{14} \text{ m}^{-2}$ respectively [76]. However, a paper by Balogh *et al.* suggests that the unirradiated and undeformed Zr-2.5Nb sample has a dislocation density of $6.4 \times 10^{14} \text{ m}^{-2}$ [77]. It is worth noting that both of these results were determined using eCMWP (online version of CMWP) from neutron diffraction measurements.

Two samples, Zircaloy-2 and Zr-2.5Nb alloys, were also investigated by Mukherjee *et al.*. Both samples were subjected to a 30% cold rolling deformation process and was found that, by a Cu sourced X-ray diffraction line profile analysis (modified Williamson-Hall procedure), that the dislocation density was determined to be $3.73 \times 10^{15} \text{ m}^{-2}$ and $3.82 \times 10^{15} \text{ m}^{-2}$ respectively [78]. However, a different study by Moran *et al.* determined that the dislocation density of a 30% cold rolled Zr-2.5Nb alloy is $20 \times 10^{14} \text{ m}^{-2}$, using the modified Warren-Averbach analysis [79]. Although, a consideration to take into account is that Mukherjee *et al.* used a simplified line profile analysis technique which likely overestimated the dislocation density as the dislocation arrangement factor was not included, which helps explain the discrepancies in the results. The summary of the dislocation densities found in the literature can be seen in Table 2.1.

Table 2.1: A table surmising the dislocation density, from relevant Zr systems, found in literature.

Sample	Dislocation Density (x 10 ¹⁴ m ⁻²)	Sample	Dislocation Density (x 10 ¹⁴ m ⁻²)
Undeformed (RD) - Zr2.5Nb [76]	1.76	Cold Worked 30% - Zr-2 [78]	37.3
Undeformed (ND) - Zr2.5Nb [76]	1.02	Cold Worked 30% - Zr2.5Nb [78]	38.2
Undeformed/ Unirradiated - Zr2.5Nb [77]	6.4	Cold Worked 30% - Zr2.5Nb [79]	20
Cold Worked 27% - Zr2.5Nb [75]	3 - 4		

2.2.5 Comparison between Cold Worked and Irradiated Dislocations

From the literature discussed above, it was found that at low neutron fluences, the predominant type of dislocation is the $\langle a \rangle$ dislocation loops. However, as the fluences increase, there is a decrease in $\langle a \rangle$ dislocation loops and an increase in $\langle c \rangle$ dislocation loops and $\langle c + a \rangle$ dislocation loops [80, 81]. The full mechanism in which $\langle a \rangle$ dislocation loops develops into a $\langle c \rangle$ dislocation loops is not currently fully understood.

For cold worked zirconium and its alloys, the predominant type of dislocation at all severity of deformation was found to be $\langle a \rangle$ dislocation lines, with the $\langle a \rangle$ dislocation lines percentage not decreasing below 60% [76–78].

Comparing the dislocation from low neutron fluence irradiation and cold-working, at this current stage of research, shows that the dislocation loops and lines are similar and grow in the same direction. However, further research needs to be conducted to determine whether cold-working zirconium is a good non-active replacement for introducing dislocations into materials, rather than irradiation-induced damage.

Table 2.2: A table showing the identified slip planes and directions in an α -zirconium system [53].

System	Plane	Direction
Prismatic	{10-10}	$\langle 11-20 \rangle$
Basal	{0001}	$\langle 11-20 \rangle$
Pyramidal $\langle a \rangle$	{10-11}	$\langle 11-20 \rangle$
Pyramidal $\langle c+a \rangle_1$	{10-11}	$\langle 11-2-3 \rangle$
Pyramidal $\langle c+a \rangle_2$	{11-22}	$\langle 11-2-3 \rangle$

In the case of irradiation damage and cold work damage, though they produce different types of dislocations and defects, they both affect material properties. In the case of cold working, the dislocation produced from the process hinders the movement of dislocations when undergoing further deformation, therefore, more force is required to move the dislocation to achieve the required strain and level of cold working. This process is called work hardening - increasing the material's strength and hardness whilst reducing its ductility. Work-hardened material, if

continually cold worked, has a build-up of internal stresses due to the dislocations and the force applied, which could lead to cracking and mechanical failure [82–84].

Radiation-induced defects, such as point defects, dislocations, hydrides and He bubbles, have many detrimental effects on the mechanical properties of Zr cladding and therefore, effects on its performance and lifespan (i.e. mechanical failure). Dislocations and point defects can induce a phenomenon called radiation-induced hardening (RIH), which is where the defects produced from irradiation block/hinder the movement of dislocations, causing a decrease in ductility and an increase in hardening - similar to work hardening in mechanically damaged materials [85, 86]. Irradiation can also cause a dislocation bias producing irradiation-induced growth (IIG); one form being dislocations during irradiation absorb more interstitials than vacancies, possibly leading to vacancy clustering and the phenomenon called irradiation-induced swelling. An example of this is where He accumulates at these vacancy clusters, as it is energetically more favourable, causing the He bubble swelling. These irradiation-induced swelling defects can consequently cause embrittlement of the cladding material and increase the susceptibility of cracking at grain boundaries (which is where He bubbles are likely to form) [87, 88]. Hydrogen and hydrides affect Zr by decreasing ductility and increasing susceptibility to cracking. The effects of hydrogen and hydrides are discussed in more detail later. Another form of irradiation-induced growth is the anisotropic growth of zirconium, where vacancies and interstitials preferentially migrate causing the positive strain in a direction and negative strain in c direction [73, 89]. Due to the significance of the impact of these irradiation-induced defects as well their non-active proxy, cold worked induced dislocations, it is important to gain a better understanding of the mechanisms that lead to the formation of the defects and the consequent failure of the part.

2.2.6 Effects of Hydrides

The production of hydrogen and the evolution of hydrides have been discussed previously in Section 2.1.4.2. The following will explore the effects of hydrogen and the hydrides on zirconium and its alloys. The importance of understanding the effects of hydrides on zirconium and its alloys will possibly allow the reduction of the margin of error required on cladding material and therefore potentially increase the lifespan within the nuclear reactor. This will minimise the cost and risk of replacing fuel rods, as well as provide a better indicator of failure during post-discharge which allows a safe and more informed storage treatment. The effects of hydrogen and hydrides on zirconium can be further understood by investigating the impact on the microstructure, such as lattice parameter expansion due to hydride dissolution (i.e. hydrogen going into the zirconium matrix), which will be discussed later in the thesis in Section 7.

The absorption of hydrogen is a major contributor to the degradation of zirconium cladding and the reduction of its lifespan. The formation of hydrides, which is a brittle phase, during operation and post-discharge, leads to the embrittlement of the cladding (i.e. reducing its fracture toughness). The decrease in the ductility of zirconium and its alloys is caused by the hydrides pinning/hindering dislocation movement, thereby reducing the mobility of dislocation [90, 91]. This particular phenomenon is called hydrogen-induced embrittlement (HIE). This reduction in fracture toughness can then increase the susceptibility of cracking from the build of stress within a material caused by things such as irradiation-induced growth, dislocation formation, swelling for He bubbles and from the hydrides themselves [28, 92]. This process is called hydrogen-induced delayed hydride cracking (DHC) or hydrogen-induced cracking (HIC). There are three factors that contribute to these hydrogen induced mechanical failures: 1) a large fraction of the hydrogen precipitates into hydride platelets, 2) the fraction of those platelets in the radial

orientation and 3) the extent of the continuous hydride network through the cladding thickness [93, 94]. Hydride formation can either occur in the circumferential or radial direction; usually, they preferentially form in the circumferential direction. This is because of the crystallographic relationship between α -Zr and hydrides; due to the $(0001)_{\alpha\text{-Zr}}-(111)_{\text{ZrH}_x}$ relationship and the strong basal texture of cladding material, it is more energetically favourable if the hydride is in the circumferential direction [95, 96]. However, under a thermo-mechanical load, hydrides are likely to re-precipitate in the radial direction and this is attributed to the contention between tensile stress-assisted hydride nucleation and strain-induced resistance to nucleation [94, 95].

The extent of the reduction in ductility and increase in the likelihood of mechanical failure is dependent on the hydride distribution. When the radial orientated hydrides are uniformly distributed throughout the cladding material, there is a decrease in ductility. When the hydrides are configured into a linear network, the fracture resistance and ductility are drastically reduced, leading to the possibility of DHC or HIC [97–99]. An example of zirconium hydrides in both of their orientations is shown in Figure 2.12.

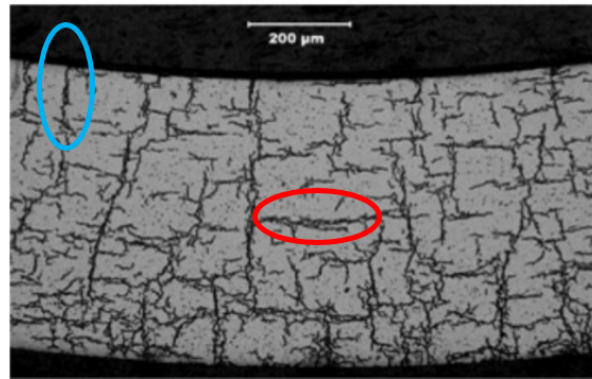


Figure 2.12: An example of zirconium hydrides in both circumferential and radial directions. Examples of each are highlighted in red and blue respectively [100].

It has been determined that approximately 120 wt ppm of hydrogen can be ‘picked up’ by a zirconium alloy during operation/elevated temperatures and once it reaches its solubility limit and/or when the temperature reduces, a large fraction of hydrogen is likely to precipitate [101]. However, a critical detail that needs to be considered is the conditions in which the orientation of said hydrides is likely to shift into a radial position. Reorientation of the hydride platelets is believed to occur during the cooling period, while a tensile hoop stress is applied [102]. One instance in which the hoop stress is applied is when the spent nuclear fuel (SNF) is dried, after being placed in a spent fuel pond, to dry out the sample. The cyclic heating and cooling applied to the SNF increases the internal pressure from fission gases, produced during operation, thus inducing a tensile hoop and axial stresses to the material [103].

The formation of these hydride platelets, especially in the radial direction, causes a phenomenon called hydrogen-induced embrittlement (HIE). This is where the hydrides cause a decrease in the ductility of zirconium and its alloys by pinning/hindering dislocations, thereby reducing the mobility of dislocation [90, 91]. With the reduction in ductility, there comes the increased likelihood of mechanical failure, with the extent of reduction in ductility and increase in mechanical failure dependent on the hydride distribution. When the radial orientated hydrides are uniformly distributed throughout the cladding material, there is a decrease in ductility. When the hydrides are configured into a linear network, the fracture resistance and ductility are drastically reduced,

leading to the possibility of DHC or hydrogen-induced cracking (HIC) [97–99]. An example of zirconium hydrides is shown in Figure 2.12.

2.2.7 Terminal Solid Solubility for Dissolution (TSSD) of Hydrogen

The terminal solid solubility for dissolution (TSSD) of hydrogen within zirconium is the temperature at which all the hydrides within a sample, at a given hydrogen concentration, dissolve into the matrix during heating [25, 104]. This parameter is important to understanding the effects of hydrogen on zirconium and its alloys (e.g. lattice parameter expansion), and therefore, has been subjected to many investigations, using various techniques to measure this value (e.g. dilatometry and calorimetry).

A study by Kearns investigates the TSSD of hydrogen within zirconium and its alloys, below 550 °C, using measurement techniques such as diffusion gradient, P.C.T, diffusion gradient calorimetry, X-ray diffraction and diffusion equilibrium. The TSSD for this study was calculated using a form of the Arrhenius equation, shown in Equation 2.2, where A and B are constants, C is the terminal solid solubility, R is the ideal gas constant and T is the temperature in K. The TSSD was then plotted against the inverse of the respective temperature as shown in Figure 2.13 [101].

$$\ln C = A - B/(RT) \quad (2.2)$$

A study by Une *et al.* followed this by investigating the TSSD and terminal solid solubility precipitation (TSSP) of hydrogen, specifically in Zr-2 and high Fe Zr alloys, with a hydrogen content range of 40 - 542 ppm. The results were obtained by differential scanning calorimetry (DSC) as well as from literature. The DSC experiment was conducted in a purified Ar environment, with a flow rate of 50 cm³min⁻¹, and the samples were heated up from 50 °C to 600 °C and then cooled down to 150 °C with temperature rate of 10 °Cmin⁻¹. There was a 5 minute hold at 600 °C. Une *et al.* used Equation 2.2 to calculate TSSD and TSSP results from DSC and plotted them against the reciprocal temperature as shown in Figures 2.14a. The TSSD data, obtained from other bodies of work and experimental techniques, was collated in this study as a comparison and is shown in Figure 2.14b [23].

In the two studies, and the literature presented in both, the TSSD was determined using similar alloyed zirconium, with hydrogen content of a similar range (from approximately 40 to 600 ppm). Though TSSDs were determined using a range of measuring techniques, the temperatures were in relatively good agreement with each other. The conclusions determined from both these studies indicate that minor differences in alloying elements will have little effect on TSSD, whereas the effects of strain (e.g. cold rolling) and supersaturation of hydrogen is more significant, though the extent of this is unknown. Supersaturation of hydrogen is defined as hydrogen concentration above the value determined for a given temperature at equilibrium [105]. The solubility curves presented in this section will be used to determine the TSSD temperatures and hydrogen content of Zr-4 samples that are investigated in Section 7.

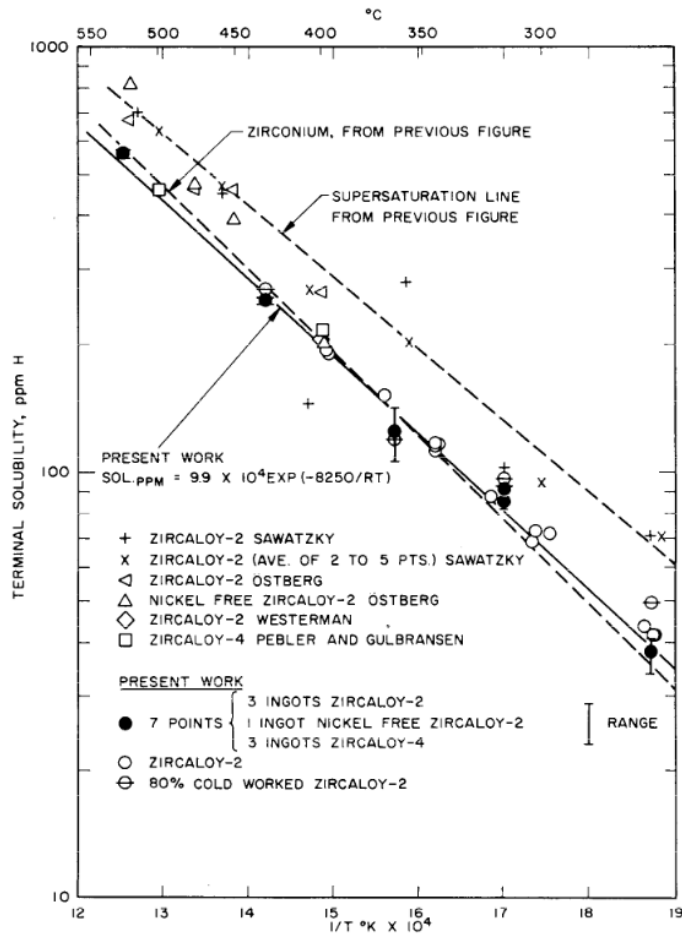


Figure 2.13: A graph showing the TSSD of Zr-2 and Zr-4 alloys, obtained by multiple measurement techniques, that are below 550°C [101].

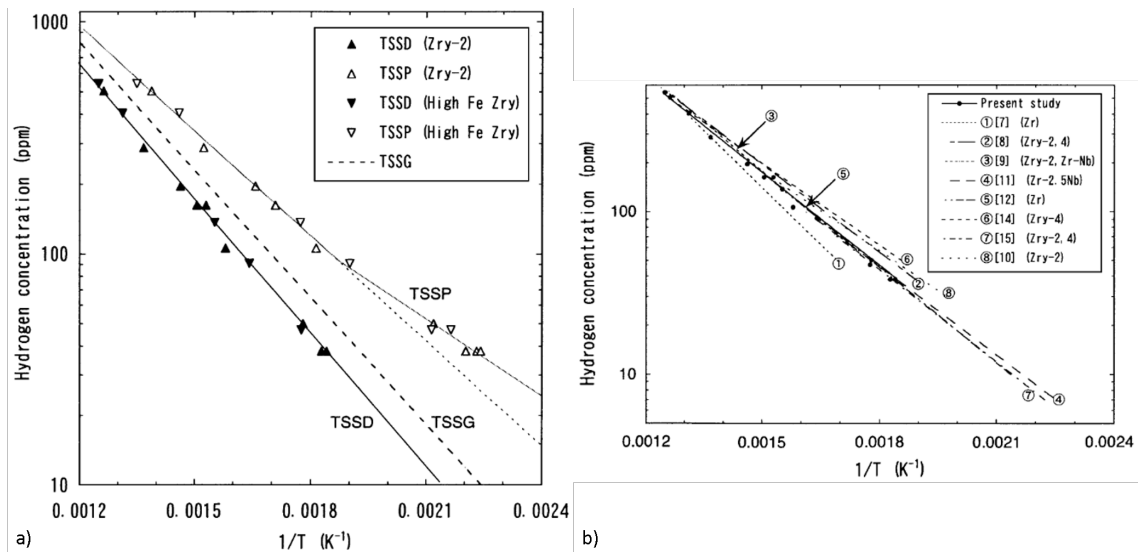


Figure 2.14: A graph showing the TSSD and TSSP of Zr-2 and Zr-4 alloys, obtained by DSC and other multiple measurement techniques [23].

2.2.8 Ion Implantation Studies

Ion implantation is a common method used to produce comparable microstructural damage to neutron irradiation, in zirconium and its alloys, without activating the material to the same extent. The damage profile produced from ion implantation is non-uniform, however, the period in which the damage can be produced can be significantly shorter by adjusting fluences, making it a viable process. Many studies have discussed this process, and this section will contain an overview of the elements used and the respective irradiation parameters to produce a known damage [106, 107]. The consolidation of some of these studies and their irradiation parameters on zirconium alloys are shown in Table 2.3.

Table 2.3: A table showing the irradiation parameters (i.e. implantation energy and fluences), for desired damage depth and displacement per atom (dpa), to simulate neutron irradiation damage within zircalloys.

Species	Energy/ MeV	Fluence/ 10^{15} cm^{-2}	Peak DPA	Target Material	Damage Depth/ nm
C⁺ [108]	1.4	10	1.7	Zr/Nb NMMs	1000
Si⁺ [108]	1.8	4	2.5		
Cu⁺ [108]	2.225	1.5	2.41		
Kr⁺ [109]	0.1	10	22.7	Zr-4	45
Kr²⁺ [110]	1	-	1	Zr	800
Zr⁺ [111]	0.6	0.48	2.9	Zr-4	400
Zr⁴⁺ [112]	40	3	21	Zircaloy M5	5500

*NMMs = Nanoscale Metallic Multilayers

Dagbouj *et al.* studied the response of Zr/Nb nanoscale metallic multilayer (NMMs) materials under carbon (C⁺), silicon (Si⁺) and copper (Cu⁺) ion irradiation, which were fine-tuned to mimic dpa produced from neutron irradiation. The energy of the ions was adjusted so that the maximum penetration depth for the damage profile was approximately 1000 nm for each species - this was calculated by conducting iterative Stopping Range of Ions in Matter (SRIM) simulations to achieve the desired depth. The fluence for each species was then adjusted to achieve three levels of displacements per atom (dpa): low damage ~ 0.2 dpa, medium damage ~ 2 dpa and high damage ~ 6 dpa. Table 2.3 refers to medium damage values as these were recorded for all three species. The main consideration for this study was the material investigated, which was a layered Zr/Nb structure, whose response to irradiation damage and therefore damage depth profile, will differ from standard zircalloys used in the nuclear industry (i.e. Zr-4, Zr-2 and Zr-2.5Nb alloys). Another consideration is the strain and microstructural evolution analysis, conducted via a lab XRD, was believed to be done in a Gonio geometry, which would dilute the values of strain with the incorporation of non-deformed Zr/Nb NMM layers [108].

A common microstructural defect formed during irradiation and transmutation, as stated previously, is the formation of bubbles which are insoluble and detrimental to the mechanical properties of zircalloys. Pagano *et al.* explored the general behaviour of bubbles in Kr⁺ irradiated Zr-4 and Zr-2 alloys via post-implantation TEM analysis. As stated in Table 2.3, the experiment was conducted using a 100 keV Kr⁺ beam; 100 keV was chosen to ensure the Kr⁺ remained within the sample but the dpa of 22.7 was tuned by adjusting the fluence to $1 \times 10^{16} \text{ cm}^{-2}$. Pagano *et al.* later furthered these studies by investigating nucleation and growth behaviour of Kr bubbles within Zr-4/Zr-2 systems, using the same energy and fluence Kr beam, via in-situ implantation TEM analysis [109, 113]. Idrees *et al.* also conducted Kr ion (Kr²⁺) irradiation experimentation to investigate defect accumulation and evolution, specifically <a> type dislocations, within pure

zirconium systems at a range of temperatures. An array of fluences was used to investigate behaviours of defects at a range of dpas, in this circumstance, the highest dpa was used as a reference [110]. The irradiation, in all three of these studies, was conducted on both thin foil and bulk samples, before being examined via TEM, therefore, the limiting factor of the energy of the ion beam was the sample thickness.

Furthermore, a few studies have considered the evolution of dislocation loops through the view of self-interstitial ion irradiation, in zircalloys, being an acceptable analogue for neutron irradiation damage [107]. Tournadre *et al.* determined the ion implantation energy by performing conservation of momentum and energy between a 2 MeV neutron and a Zr^+ , which predicted an energy of 600 keV [111]. Whereas Hengstler-eger *et al.*'s approach was to use a very high energy Zr^{4+} ion on bulk material to achieve sufficient damage depth to then produce a magnitude of thin foil samples for TEM and EBSD analysis (i.e. no bulk analysis was conducted) [112]. Other studies have been conducted on self-interstitial and heavy ion irradiation on zircalloys, with high energy beams to produce significant damage depth profiles, but they were mainly investigated via TEM.

2.3 Line Broadening

2.3.1 Overview of Line Broadening

In principle, in a perfect environment, diffraction peaks from an infinitely large crystal with no external effects would be diffraction lines, at specific angles, with no line broadening (Figure 2.15a) [114]. However, in reality, the instrument and the sample both contribute to line broadening, therefore the observed profile of a material is the convolution of the true sample profile and the instrumental profile (Figure 2.15b). This in simple mathematical terms, is shown in Equation 2.3 [115, 116].

$$I(2\theta) = I_{\text{instrument}}(2\theta) * I_{\text{sample}}(2\theta) \quad (2.3)$$

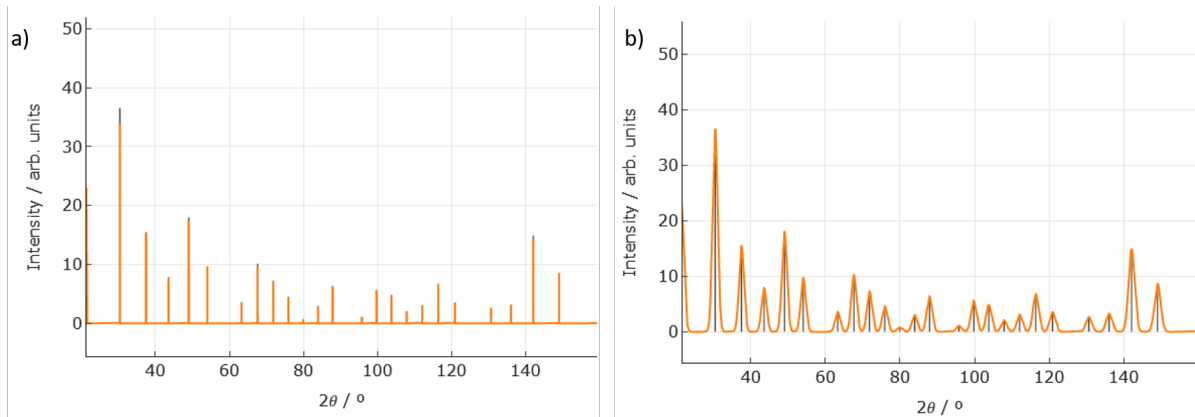


Figure 2.15: Two diffractions patterns of LaB_6 showing the effects of line broadening: a) ideal environment with no line broadening and b) line broadening caused by sample and instrumental effects.

The instrumental broadening is the intrinsic properties of the diffractometer that produces line broadening and possibly asymmetry within the peak; the factors that define this profile are [117]:

1. Dispersion of X-rays

2. Lorentz-Polarization factor
3. Sample setup
4. Machine setup and alignments

The current method of calculating the instrumental profile is to use a Standard Reference Material (SRM), which has known lattice parameters and is prepared to have minimal line broadening. A common SRM used is Lanthanum Hexaboride (LaB_6), which has a cubic structure (space group = $\text{Pm}\bar{3}\text{m}$) and a large number of non-overlapping peaks, with fairly high intensities [118, 119]. The non-overlapping peaks provide the best environment for peak broadening analysis as separating peaks is difficult and can create errors. High intensity peaks provide a high signal-to-noise ratio and, therefore when processed, provides minimal errors. The LaB_6 powders are annealed at 1700 °C for an hour under high purity argon to remove crystallographic defects and grow crystallites to minimise size broadening effects [120].

Peak broadening due to sample effects consists of two factors: crystallite size profile and the strain profile, expanding Equation 2.3 to Equation 2.4 [121, 122].

$$I(2\theta) = I_{\text{instrument}} * I_{\text{crystallite size}} * I_{\text{strain}} \quad (2.4)$$

2.3.2 Strain Broadening

When a polycrystalline metal undergoes a form of deformation (i.e. cold rolling), the grains within the system change shape - the resultant change in shape being affected by the deformation process and by the constraints of the neighbouring grains [123]. Depending on the strain in the material, the effects on the lattice structure, and hence the diffraction pattern will vary, this is demonstrated in Figure 2.16 [124]. In a cold rolled material, the main source of strain is dislocations, suggesting a non-uniform distribution of strain, this is denoted in Figure 2.16c [125]. This is known as microstrain broadening; in this body of work, microstrain will also be referred to as strain.

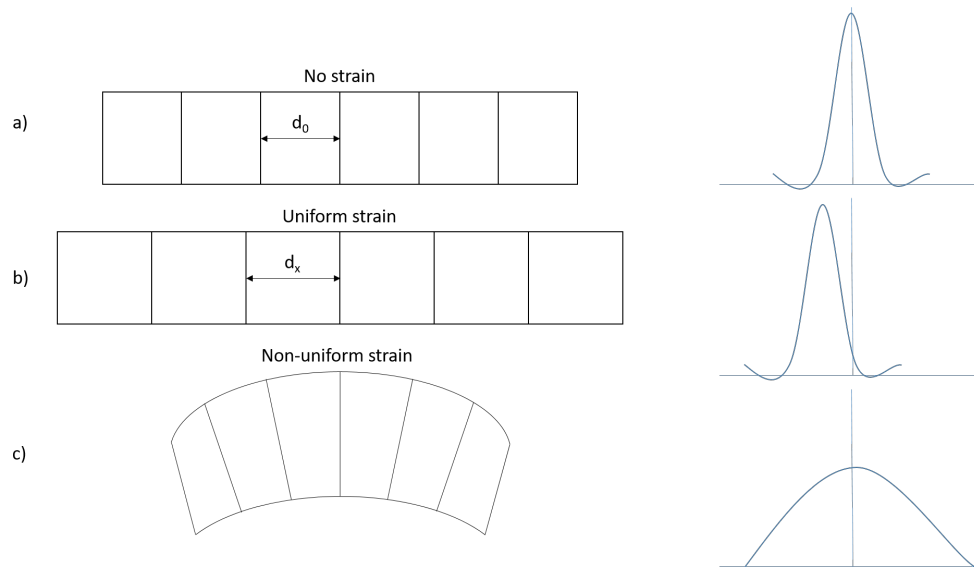


Figure 2.16: *The effects of uniform and non-uniform microstrain on the lattice structure and the interplanar spacing (d) with the correlating effects on the diffraction pattern: a) A non strained material, b) a uniformly strained material and c) a non-uniformly strained material.*

The most simple strain model is the $\tan\theta$ dependence of the peak broadening due to inhomogeneous (non-uniform) strain. The relationship between the strain and the peak broadening is approximated by relating the strain to the differential of Bragg's Law (in terms of $\delta d/d$ - differentiating in terms of d -spacing). The model for this relationship is shown in Equation 2.5. Where β_ε is the strain broadening and \mathbf{C} is the constant dependant on the assumptions made on the strain (usually either 4 or 5) [126, 127].

$$\beta_\varepsilon = \mathbf{C}_\varepsilon \tan\theta \quad (2.5)$$

Further, more in-depth models of strain are discussed later in Section 2.4.2.

2.3.3 Size Broadening

With a decrease in crystallite size, there is a decrease in destructive interference due to the restricted number of reflection planes, which leads to peak broadening [128, 129]. This inversely proportional relation between crystallite size and peak breadth is also reflected in the Scherrer equation (Equation 2.6). Where D is crystallite diameter, λ is wavelength, θ is the Bragg angle, β is FWHM and K is the Scherrer shape factor constant [130]. A common assumption made when calculating the size profile is the shape of the crystallite, where it is assumed to be a sphere, however, to correct for this assumption to determine the true crystallite size, the Scherrer constant is used [131]. Another assumption used when using the Scherrer equation is that the material system contains no microstrain, which would change overall peak broadening [132].

$$D = \frac{K\lambda}{\beta \cos \theta} \quad (2.6)$$

When there are many crystallites with varying sizes, as with a polycrystalline material, the size profile is more indicative of a size distribution function, which includes average crystallite size and crystallite size variance. There are numerous distribution functions that could be used, including a log-normal size distribution function, which has been proven to be a reliable distribution function for the use of crystallite size analysis [133]. The assumption made for the log-normal distribution is that the shape of the crystallites is spherical [134].

The size profile, with the bases of log-normal size distribution, can be described using Equation 2.7, where m is the median crystallite size and σ is the variance in the distribution of crystallite size. As stated previously, the median crystallite size is inversely correlated to the peak breadth and that is also the case with the crystallite size distribution (i.e. crystallite size variance), where a larger crystallite size range produces broader peaks.

$$f(x) = \frac{1}{\sqrt{2\pi}\sigma} \frac{1}{x} \exp\left[-\frac{(\log(\frac{x}{m}))^2}{2\sigma^2}\right] \quad (2.7)$$

Another common size distribution function is the Gamma distribution function [3]. The Gamma distribution function, shown in Equation 2.8, depends on a single variable and its averaged value. Where a/b are parameters of the distribution and $\Gamma(x)$ is the Gamma function [135, 136]. The function is similar to the log-normal distribution function where it is dependant on a singular parameter ($\Gamma(x)$ for Gamma function and σ for log-normal), however, through previous experimental and computational observations it was found the log-normal was a more flexible and reliable crystallite size distribution function [3, 135].

$$f(x) = \frac{1}{a\Gamma(b)} \left(\frac{x}{a}\right)^{b-1} e^{-x/a} dx \quad (2.8)$$

2.4 Current Methods of Determining Dislocation Density

There are two main methods of calculating the dislocation density from experimental data: quantitative analysis of Transmission Electron Microscopy (TEM) images or the mathematical deconvolution of XRD diffraction patterns.

2.4.1 TEM Methods

The quantification of dislocation density via TEM can be determined through direct observation and is usually believed to be a highly accurate technique [137]. The Smith-Guttman line intercept method is an example of a direct observation method, where multiple lines are drawn, randomly distributed or in a grid arrangement, on the TEM image, with a total length l [138, 139]. The number of intersections (n) between the dislocations and the lines are counted and the line dislocation density is calculated using Equation 2.9 [140, 141]. Where t is the thickness of the sample. An example of the line intercept method is shown in Figure 2.17.

$$\rho = \frac{2n}{lt} \quad (2.9)$$

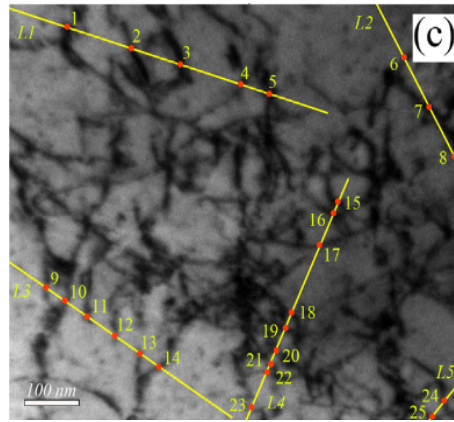


Figure 2.17: An example of the dislocation density intercept method on a GH2036 alloy. The number of intersections between the dislocations and drawn lines (yellow lines) is counted and divided by the total length of the line and thickness of the sample [142].

However, to accurately quantify the dislocation density, multiple TEM images must be taken under different Bragg conditions as not all dislocations are visible under the same conditions. This condition is called the invisibility criterion, where if the product of the diffraction vector (\vec{g}) and Burgers vector (\vec{b}) does not equal zero then the dislocation are visible and visa versa (Equation 2.10). This phenomenon is true only for pure edge and screw dislocations [143, 144]. To be able to achieve the invisibility criterion, the TEM must be under two-beam conditions (i.e. tilting of a sample so that only one diffraction beam is excited), which allows the tilting of the sample in order to change the diffraction vector and hence the focus of the electron beam on a different diffraction spot.

$$\vec{g} \cdot \vec{b} \neq 0 \quad (2.10)$$

There are a few disadvantages to this method of quantification, one being the time and labour required to systematically image the sample at all available positions in order to accurately

determine the dislocation density - 88 possible imaging positions for HCP and 61 possible imaging positions for BCC. The reliance on the user's imaging ability and their ability to distinguish dislocations within the image [145, 146]. Another limitation of this technique is the amount of deformation within the material. At higher deformed samples, due to the number of dislocations, it can be very difficult to distinguish between dislocations and hence difficult to count the number of intersections [147]. Another concern is the sample size under investigation and whether it will be representative of the damage within the bulk material in question, as depending on the damage depth profile, the number of dislocations may not be uniform throughout the material.

2.4.2 XRD Methods

The estimation of strain and dislocation density by the means of XRD is a much more indirect method in comparison to TEM, where the peak broadening of a diffraction pattern is analysed and the results are then deconvoluted in order to obtain the dislocation density [148].

Williamson-Hall Procedure

Simplified

A method for determining the strain profile is the simplified Williamson-Hall procedure [149]. This method determines the strain profile by investigating the peak breadth (Δk), which is also known as the full width at half maximum (FWHM), with respect to the reciprocal space (k) at that given angle [150, 151]. The Williamson-Hall procedure determines the extent of the strain within the system by using the gradient of the plot; if there is a straight horizontal line, there is no strain within the material, whereas a slope would indicate strain [152, 153]. The limitation of this analysis technique is the assumption that a uniform deformation model is present, which is not always the case. An example of a Williamson-Hall plot is shown in Figure 2.18, where the analysis took place on a 60% cold worked ferritic steel [154].

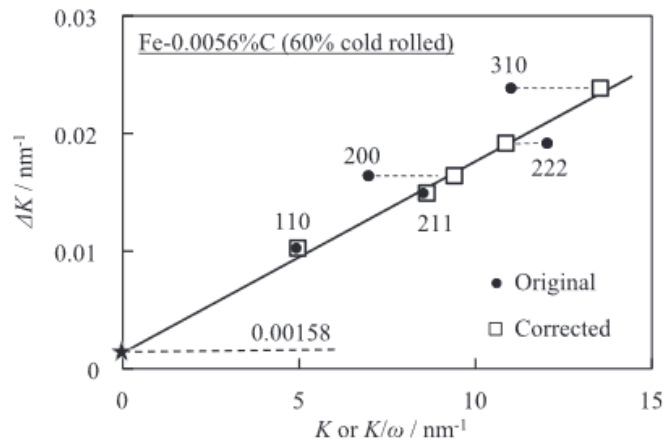


Figure 2.18: An example of a Williamson-Hall plot, showing a strained system, from a 60% cold worked ferritic steel [154].

Modified

Another method is the modified Williamson-Hall plot which is an expanded version of the Williamson-Hall procedure. The modified Williamson-Hall procedure includes the contrast factor

in its procedure, therefore, Equation 2.11 is expanded to Equation 2.12. Where Δk is FWHM, α is a crystallite size factor, k is the reciprocal space, C is the average contrast factor (the effect of dislocations on a family of planes), A is the dislocation distribution, b is the Burgers vector and ρ is dislocation density [155].

$$\Delta k = \alpha + \varepsilon k \quad (2.11)$$

$$\Delta k = \alpha + \varphi k \sqrt{C}$$

$$\text{where } \varphi = \left(\frac{\pi}{2}\right)^{0.5} A b \sqrt{\rho} \quad (2.12)$$

The plotting of Δk against $kC^{\frac{1}{2}}$ or Δk^2 against k^2C will produce a linear relationship. The gradient of the line determines the φ parameter, which includes the dislocation density parameter [156]. As there are no methods to solely calculate A , a dislocation distribution needs to be assumed ($M \simeq 10$ can be used), which is dependant on the dislocations and the respective outer cut-off radius [157].

The main limitations of using the modified Williamson-Hall and modified Warren-Averbach methods is the indirect/deconvolution mathematical procedure required to determine the dislocation density; both techniques require the calculation of the gradient and an assumption to be made before ρ can be determined. The method also assumes that the peak broadening is solely from dislocation, not taking into account instrumental effects which is likely to produce an overestimation of dislocation density [157].

Warren-Averbach Analysis

Simplified

Another peak broadening analysis method is the Warren-Averbach analysis, which separates the effects of strain and crystallite size [158]. The Warren-Averbach is a more rigorous technique than the Williamson-Hall procedure as it is based on the peak broadening of the reflections of a family of planes instead of investigating each peak individually. The Warren-Averbach analysis involves a convolution of the Fourier transforms of both the size and strain profile, which is shown in Equation 2.13. Where $A(L)$ is the overall broadening effects, $A^S_{\text{hkl}}(L)$ is the Fourier transform of the size profile and $A^D_{\text{hkl}}(L)$ is the Fourier transform of the strain profile [159].

$$A(L) = A^S_{\text{hkl}}(L) * A^D_{\text{hkl}}(L) \quad (2.13)$$

Modified

One method of calculating the dislocation density is using the modified Warren-Averbach procedure (Equation 2.14), which is the expanded version of the Warren-Averbach strain profile. It was found that there was a relationship between $\ln A(L)$ and $K^2\bar{C}$, where the text in **red** is y, the **blue** section is the gradient and **green** is the y-intercept [160, 161]. Equation 2.15 shows that the gradient can be arranged as an equation in terms of L. Equation 2.15 is expanded and rearranged to Equation 2.16. Figure 2.19 shows this equation was discovered to have a linear relationship between $\frac{X(L)}{L^2}$ and $\ln(L)$, where the gradient of this regression line was used to determine the dislocation density in form of $\frac{\rho\pi b^2}{2}$. In the case of Figure 2.19, $\frac{Y}{L^2} = \frac{X(L)}{L^2}$.

$$\ln A(L) = \ln A^S(L) - \frac{\rho \pi b^2}{2} L^2 \ln\left(\frac{R_e}{L}\right) (K^2 \bar{C}) + Q(K^4 \bar{C}^2) \quad (2.14)$$

$$X(L) = \frac{\rho \pi b^2}{2} L^2 \ln\left(\frac{R_e}{L}\right) \quad (2.15)$$

$$\frac{X(L)}{L^2} = \frac{\rho \pi b^2}{2} \ln R_e - \frac{\rho \pi b^2}{2} \ln L \quad (2.16)$$

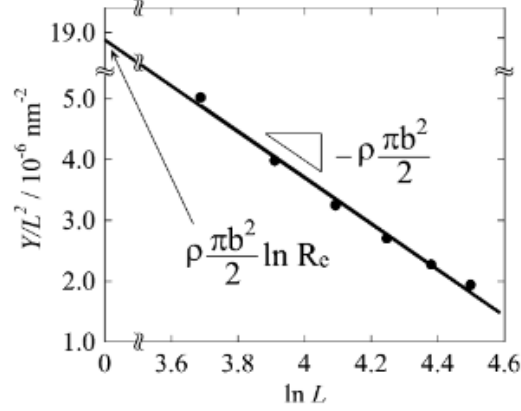


Figure 2.19: The graphical representation of the linear relationship between $\frac{Y}{L^2}$ and $\ln L$ and how to get the dislocation density from the modified Warren-Averbach method [160].

Modified Krivoglaz-Wilkens Method

An important theory of strain broadening is the modified Krivoglaz-Wilkens method, which suggests that strain broadening only occurs from one dimensional linear defects (i.e. dislocations) and this can be quantified using Equation 2.17. Where $\langle \varepsilon_{g,l}^2 \rangle$ is the mean squared strain profile (contributing to peak broadening) and ρ , C , b , L and R_e are dislocation density, contrast factor, burgers vector, distance between dislocation and outer cut-off radius of dislocations respectively [162, 163]. To be able to determine R_e , which is dependant on the dislocation density, another strain parameter was formulated, shown in Equation 2.18 [164]. This new dimensionless parameter, dislocation arrangement (M), characterises the strain field surrounding dislocations and therefore the outer cut-off radius of dislocations, where if M is small then the dislocations are very ordered and the strain field is small and visa versa [3].

$$\langle \varepsilon_{g,l}^2 \rangle = \frac{\rho C b^2}{4\pi} \cdot f\left(\frac{L}{R_e}\right) \quad (2.17)$$

$$M = R_e \sqrt{\rho} \quad (2.18)$$

With both the Williamson-Hall and Warren-Averbach procedures, it is possible to determine the dislocation density by using modified versions of each method and then deconvoluting the results, however, this is a much more difficult process and requires assumptions to be made. On the other hand, with the modified Krivoglaz-Wilkens method, as constituents of the strain profile (i.e. the dislocation parameters) are a part of the analysis, a convolution of all relevant physical parameters, it is therefore believed to be a more accurate procedure [165, 166].

2.5 Convolutional Multiple Whole Profile (CMWP)

Convolutional Multiple Whole Profile (CMWP) is an XRD analysis technique that uses peak broadening, from diffraction data, to determine physical parameters that contribute to said broadening (i.e. contrast factor, crystallite size, crystallite size distribution, dislocation density and dislocation arrangement). The motivation behind this analytical technique was to develop a better understanding of microstructural evolution during irradiation, especially irradiation-induced growth (IIG), as it can quantify dislocation density and use it as a complimentary technique to TEM to better understand the evolution of $\langle a \rangle$ and $\langle c \rangle$ loops. CMWP is a technique that analyses the diffraction pattern as a whole instead of individual peaks such as in the modified Williamson-Hall procedure. It is also a convolution of the physical parameters stated above, instead of the less direct/deconvolutional method used in the modified Warren-Averbach procedure.

2.5.1 Theory

Convolutional Multiple Whole Profile (CMWP), a type of diffraction fitting software, uses peak broadening from XRD data to identify types of defects and the dislocation density within the material [3, 4]. The method is mainly used on cubic, hexagonal or orthorhombic crystal lattices, however, it can still be used on other lattices [167]. The approach of CMWP is that it uses well-established principles based on the physical properties of specific lattice defects. When determining dislocation density, CMWP takes into account the size profile, strain profile and instrumental profile, which are the contributors to peak broadening [168].

To determine the calculated pattern, in the case of HCP (such as Zr), there are six physical parameters used: two contrast factors (a_1 and a_2), two crystallite size factors (mean crystallite size, m and crystallite size variance, σ) and two dislocation factors (dislocation density, ρ and dislocation arrangement, M). Furthermore, if planar defects, twin boundaries and intergranular strain become substantial then three more physical parameters may be used to optimise the CMWP procedure: planar defect density parameter, stacking fault from twin boundaries parameter (α or β) and elastic intergranular strain parameter (ε^{IGS}). To match the measured and calculated diffraction pattern, the peak positions and intensity are also fitted [3, 167, 168]. A schematic overview of the CMWP method is shown below in Figure 2.20.

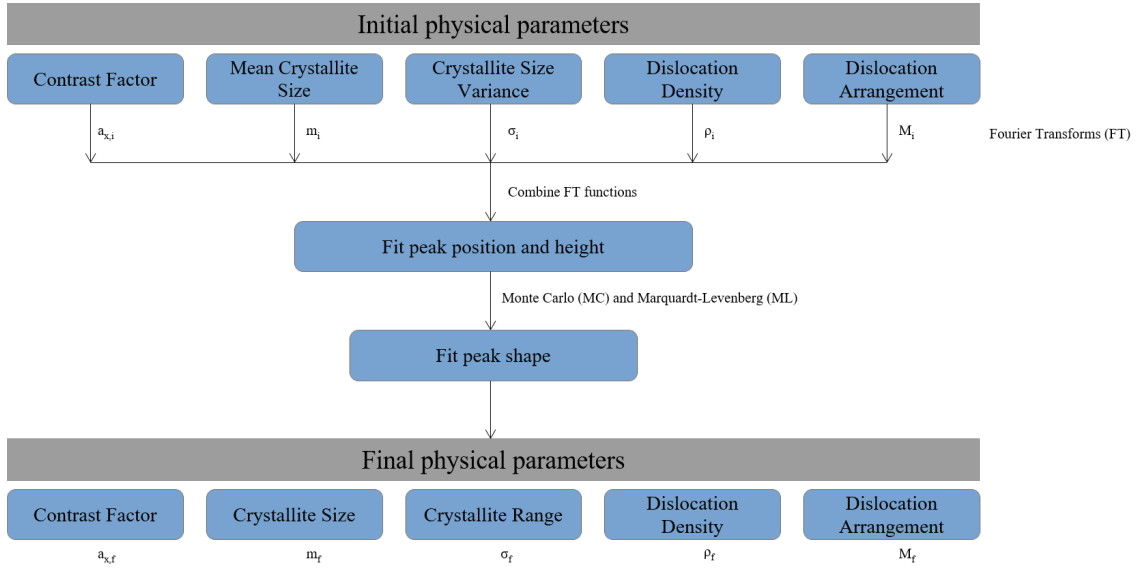


Figure 2.20: An overview of the CMWP process demonstrated as a flowchart.

The contrast factor is the effect of a displacement field, created by a dislocation, on a family of planes and is dependent on the orientation between Burgers and line vectors (b and l respectively), the particular diffraction vector (g) and the elastic constants (c_{ijkl}). Hence the contrast factor ($C = C(\mathbf{b}, \mathbf{l}, \mathbf{g}, c_{ijkl})$) is dependant on the symmetry of the lattice structure. A simple cubic system has one physical parameter to calculate as $a = b = c$, therefore the elastic constants are the same. Whereas in a HCP, there are two physical parameters due to two sets of axes ($a = a_1 = a_2 = a_3$ and c) [167, 169].

With the crystallite size factors the mean crystallite size (m) generally affects the tails of a peak, whereas the crystallite size variance (σ) mainly affects the broadening of the peak, therefore, affecting the full-width half maximum; the effect of these parameters are shown in Figure 2.21. Figure 2.21a shows the effects from the change in mean crystallite size and Figure 2.21b shows the effects from the change in variance. The variance is based on a log-normal distribution of crystallite size. If the crystallite size is larger than $2 \mu\text{m}$, the upper limitation of powder diffraction crystallite size determination, the software assumes a single crystal. In this case, it is assumed that the peak broadening is negligible from the crystallite size and is a result of strain and instrumental broadening only.

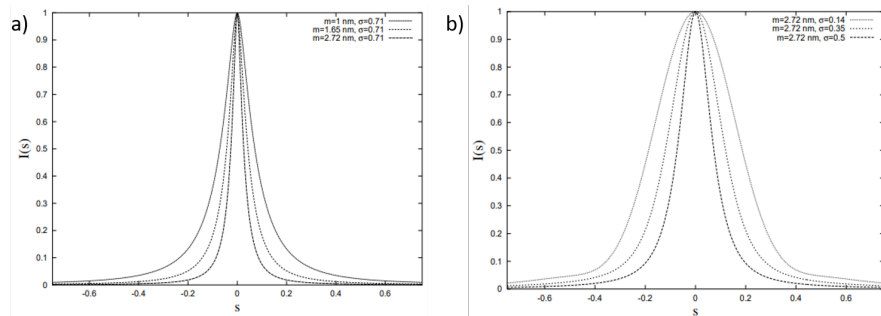


Figure 2.21: The effects of a) the change in the mean crystallite size (σ) and b) the change in variance (m), on XRD peaks. The increase in m shows an increase mainly in tail breadth, whereas an increase in σ shows an increase mainly in FWHM [3].

The strain profile is comprised of the contrast factors and the dislocation parameters. The dislocation parameters, ρ and M , were calculated via modified Krivoglaz-Wilkens' theory of microstrain. The effects of the dislocation arrangement parameters are shown in Figure 2.22. When the dislocations are ordered, $M \ll 1$ as the opposing dislocations minimise the effective outer cut-off radius (R_e) of either dislocation, producing a sharper diffraction peak and a longer tail. When the dislocations are randomly arranged (Figure 2.22b), the R_e is large as the interaction between each dislocation is weak, therefore $M \gg 1$ and the diffraction peaks are broader with shorter tails.

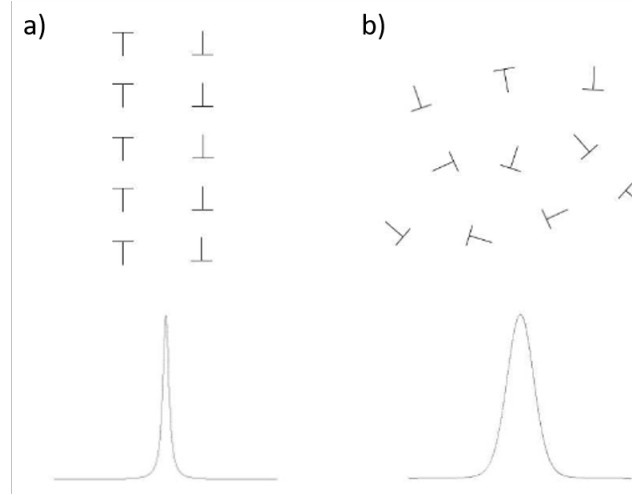


Figure 2.22: The effects of the dislocation arrangement parameter on XRD peaks: a) ordered dislocations with $M \ll 1$ and b) disordered dislocations with $M \gg 1$ [3].

The measured diffraction pattern is evaluated using Equation 2.19. It is the convolution of four functions relating to physical effects plus the background. Convolution means the resultant peak produced with all four functions working concurrently, with the four functions being crystallite size parameters (I_{Size}), dislocation and contrast parameters (I_{Strain}), Planar defect parameters if any ($I_{\text{Planar Faults}}$) and finally instrumental background parameters ($I_{\text{Instrumental}}$). Because these four functions in relation to physical effects do not have any background intensity, the background intensity is added after the convolution. Convolution of functions is the mathematical operation of how multiple functions overlap, it is the resultant function which is defined as the integral of the product of the functions in question. A graphical representation of the convolution operation on two functions is shown below in Figure 2.23.

$$I_{\text{measured}} = I_{\text{Size}} * I_{\text{Strain}} * I_{\text{Planar Faults}} * I_{\text{Instrumental}} + \text{Background} \quad (2.19)$$

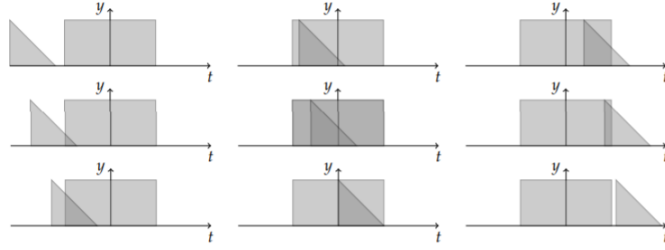


Figure 2.23: A graphical representation of the convolution operation on two functions [170].

The CMWP software, a frontend programme written in shell script language and the graphical functions written in JAVA, must be downloaded on Linux based computer. The most recent version of the software can be found on the CMWP website [3]. The user interface for the software is shown in Figure 2.24.

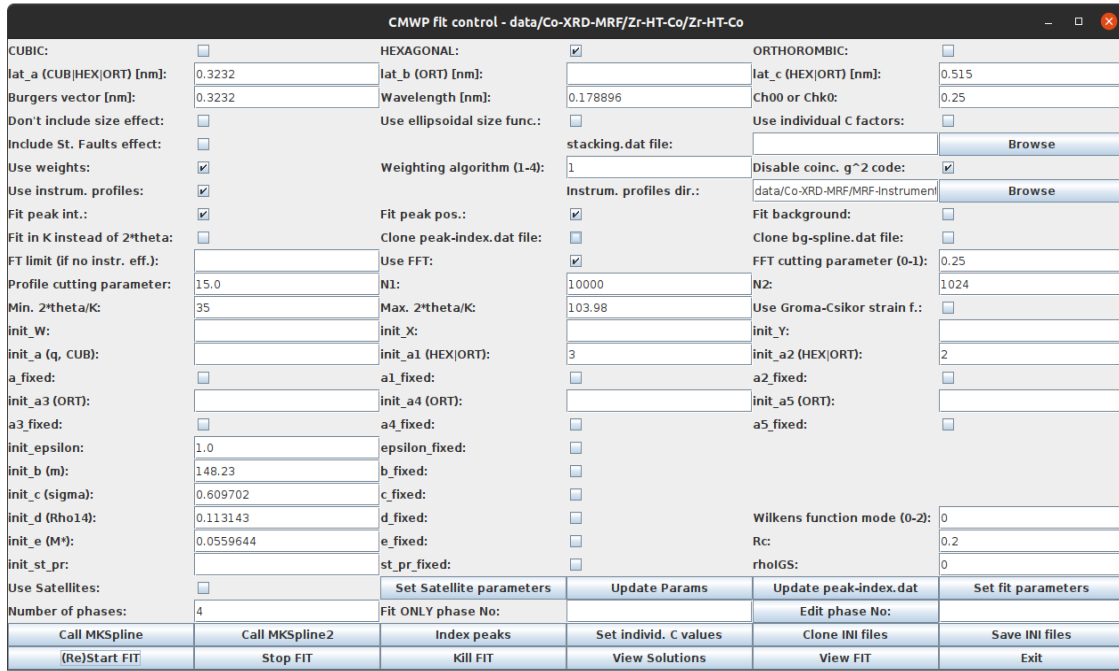


Figure 2.24: The CMWP software user interface.

Excluding all the parameters that have to be inputted, the rest of the steps are done automatically by the programme. After refinement, the resultant parameters, median and variance of the size distribution as well as the density and arrangement of dislocations, can be considered [171]. Further details of the CMWP fitting method will be discussed later in Section 4.

There are a few limitations/disadvantages to this technique, the first being that it can not analyse point defects or alloying elements (i.e. strain produced from substitutional atoms) very well. This is due to their small size, therefore, difficult to distinguish from the lattice atoms and the strain produced would be minimal. It is also suggested by Krivoglaz that strain broadening specifically is only produced by linear dislocations [168]. This links in well with the limitations for the distance between dislocations. Currently, there is no upper limit for the distance between dislocations, however, there is a lower limit of around 50 nm. This is due to the angular resolution

of the XRD machine being approximately 50 nm. At 50 nm or lower, peak broadening will not be present in the diffraction pattern and as the CMWP technique is based around the peak broadening, it will not be able to contribute any effects from the distance between dislocations.

To acquire accurate results from the CMWP method, high quality diffraction data is required. This entails having several clear diffraction peaks, good resolution and little to no instrumental broadening. One of the advantages of using XRD for material characterisation is the short collection data time, however, if the data does not have clear peaks with high enough intensity, it is suggested that longer scans between 5-10 hours may be required (usually the case with older laboratory XRD machines).

Another disadvantage of this technique is the sample preparation method. With conventional XRD (i.e. bulk gonio mode XRD), the sample preparation method is quite simple as it only requires the sample to be flat with at least a P800 grinding finish. However, with CMWP, a specific sample surface preparation technique is required to reduce deformation and optimise the intensities and resolution of the diffraction pattern.

2.5.2 Applications

Even though CMWP is a relatively new XRD analysis technique there have been several applications of it over the years. G. Ribarik *et al.* used the method to analyse aluminium-magnesium (Al-Mg) alloys for mechanical alloying. This is where Al powder, of 99.9% purity, is ball-milled together with 0, 3 and 6 wt.% high-purity Mg at room temperature. The CMWP procedure was used to determine crystallite size distribution and dislocation parameters and compare them against Multiple Whole Profile (MWP) techniques (i.e. MWP Fourier and MWP Intensity) [4]. CMWP has also been used on nanocrystalline copper (Cu), in order to evaluate stacking/twin fault effects on the microstructure and these results were then compared against Full Width at Half Maximum (FWHM) analysis results (i.e. Williams-Hall Plot procedure) [172]. Both experiments were conducted using a double-bounce monochromated Cu source diffractometer.

Now focusing on the applications to nuclear materials, another major application for CMWP has been the use on Zr-2 and Zr-4 alloys for the nuclear industry to determine the dislocation density produced by radiation. Ribárik *et al.* discusses the use of CMWP on hydrided Zr-4 alloy, from a palette section from a CANDU pressure tube, to determine the dislocation density, the subgrain size, the dislocation arrangement parameter, and the stacking fault density produced by neutron irradiation in the CANDU reactor. However, these results were not compared to another form of analysis to corroborate the results. Additionally, the diffraction experiments were conducted on a photon source synchrotron diffraction experimental setup [167, 173].

The use of CMWP on a Zr-2 alloy, a material used for channel-box and cladding material, was discussed by Ungár *et al.*, where the intention was to investigate the neutron/proton irradiation-induced dislocation loops within the nuclear material via synchrotron XRD (sXRD) CMWP analysis and compared it to electron microscopy methods, as shown in Figure 2.25. The discussion shows that there is a disparity between the CMWP and Transmission Electron Microscope (TEM) results; for a set of given fluences, the difference in line dislocation density between CMWP and TEM ranges from a factor 5 to 20 as shown in Figure 2.25. Therefore, both techniques should be used in conjugation with each other to provide a better understanding of the dislocations within the system [169].

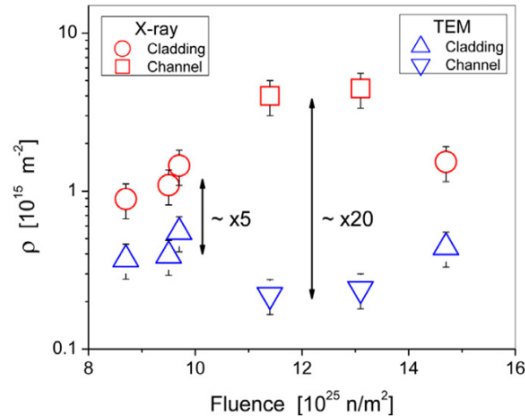


Figure 2.25: A comparison of line dislocation density values, from TEM and sXRD, from zircaloy-2 at different proton fluences [169].

Hattie's thesis conducted characterisation on proton irradiated pure zirconium and zircaloys to mainly investigate a common irradiation-induced phenomenon called irradiation-induced growth (IIG). The materials were proton irradiated to 2 and 4 dpa at 450 °C and 350 °C respectively and then characterised using Synchrotron XRD (sXRD), lab XRD, TEM and EBSD. A main discussion point was the comparison of CMWP between sXRD and lab XRD, where one of the challenges identified was the noise produced in a lab XRD and the consequent removal of background intensity. The difficulty in estimating the background contributed to the uncertainty in any subsequent fittings (especially fittings that rely heavily on tail shapes of Bragg peaks). This led to a slight disagreement in dislocation density, between sXRD and XRD CMWP analysis, by a factor of two. Figure 2.26a shows the difference in dislocation density in CMWP analysis between sXRD and XRD for Zr/Zr-4 at 450 °C with 2 dpa, where Figure 2.26b shows the comparison for Zr/Zr-4 at 350 °C with 4 dpa.

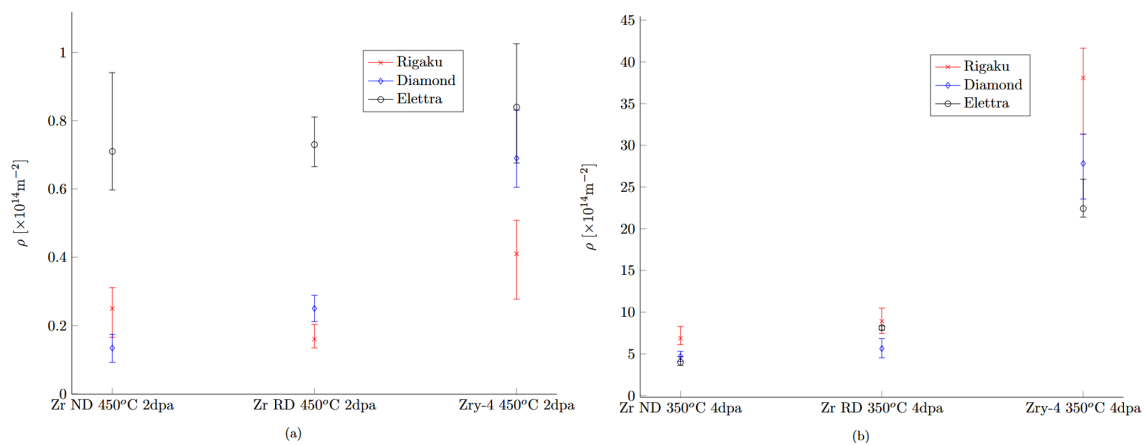


Figure 2.26: A figure comparing the dislocation density determined from CMWP analysis of sXRD and XRD data from two different temperature and dpa points: a) 450 °C and 2 dpa and b) 350 °C and 4 dpa [174].

A solution suggested was to use diffractometers that have a larger source, producing higher resolution and higher peak-to-noise ratio. Another issue identified was the effect of a stationary textured material on Gonio geometry lab XRD, where the prominent family of planes in the textured material will dominate the diffraction profile, creating significantly smaller intensity

peaks in other families of planes, and thus affecting further line profile analysis. A work around for this was to oscillate the sample in order to encapsulate more orientations of the sample, however, the limiting factor of this is the machine's oscillation capabilities, the beam footprint and the sample size. Finally, another major consideration was the effects of satellite peaks/artefacts on analysis, where it was concluded global fitting (i.e. whole diffraction pattern fitting) was difficult and focussing on single peaks or single grains would be the best way to understand the contributions of said satellite peaks/artefacts [174].

2.5.3 Research Opportunity

The main, published applications of CMWP have been briefly discussed in Section 2.5.2 and it can be seen that there is a gap in the research. Though Zr-4 and Zr-2 alloys, which are materials used in the nuclear industry for cladding material and other structural applications, have been investigated, the base material zirconium has not been fully investigated, which will be the main focus of the report. Also, with regards to the investigations of the zircalloys, the XRD data generated in those experiments were mainly produced by a synchrotron, which provides very high intensity and high-resolution data. Therefore, to test the capabilities of the CMWP procedure, using a lab XRD machine was considered - this is because, in comparison to a synchrotron, lab XRD produces much lower intensity and lower resolution data. Specifically, a lab XRD with different geometries (i.e. Gonio and grazing incidence mode) and different X-ray radiation sources (i.e. silver, copper and cobalt) will be considered to investigate the limitations of CMWP. There has not been extensive research on the comparison of the data from CMWP (especially from lab XRD data) and TEM. Ungár *et al.* discusses sXRD and TEM comparison with regards to proton irradiated Zr-2 and Hattie's investigation discusses the comparison of lab XRD, sXRD and TEM on proton irradiated Zr-4 and Zr. Hence, future work is intended to focus on lab XRD CMWP, in both Gonio and grazing incidence geometry, and TEM comparisons. By exploring the limitations and capabilities of CMWP on lab XRD, it will allow a more efficient and cost effective way of investigating irradiated materials in order to understand the evolution of material properties and failure mechanisms.

Chapter 3

Material Characterisation Techniques

3.1 X-Ray Diffraction (XRD)

3.1.1 Overview

XRD is one of the most common analytical techniques used for material characterisation, such as to identify phases, grain size, texture, crystal imperfections, composition, crystal structures and grain orientation[175]. X-rays are high energy electromagnetic waves, wavelengths between 10^{-3} - 10^1 nm, that can be produced either by laboratory equipment (sealed tube or rotating anode) or a Synchrotron [176]. The laboratory method generates X-rays by producing electrons from a heated tungsten filament in a vacuum, which are accelerated at a target sample, usually Cu as shown in Figure 3.1.

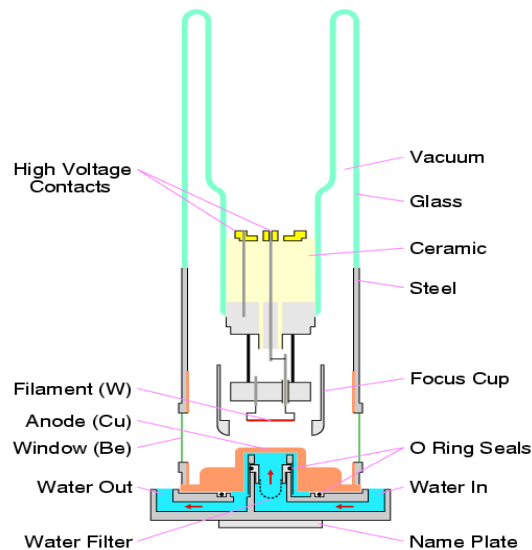


Figure 3.1: A schematic diagram of a laboratory sealed tube [177].

This produces two types of X-rays: characteristic and continuous. Continuous X-rays, also known as Bremsstrahlung X-rays, are produced due to the deceleration of electrons [178, 179]. Characteristic X-rays are generated via the ionisation of the target atom where an electron from

the inner shell is excited and ejected from the atom. To de-excite the atom, an electron from an outer shell has to fall energy levels to the lower shell to fill the gap, releasing an X-ray photon with an energy equal to the difference between the two energy levels [180].

XRD methods usually use characteristic X-rays of the highest intensity which, as can be seen from Figure 3.2, indicates that the highest intensity X-rays produced from a sealed tube is $K\alpha$. To effectively utilise the X-ray, it should be monochromatic, therefore, the X-rays produced must go through a filter to remove $K\beta$ and the white radiation. A method of filtering the radiation is to use a thin film, made from an element preceding the target material, which absorbs the most white radiation, and more importantly $K\beta$, due to these elements showing characteristic absorption edges [181]. However, as the filtering method is not perfect, $K\alpha_1$ and $K\alpha_2$, which are relatively close in wavelength (Figure 3.2a), are used and the wavelength is averaged.

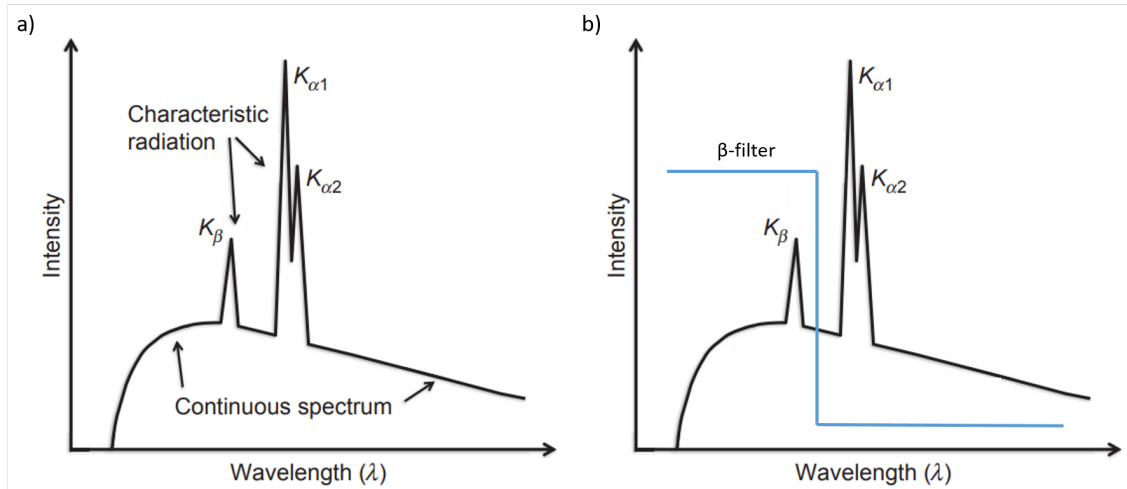


Figure 3.2: Two graphs showing a) The range of X-rays produced in a sealed tube, indicating the continuous and characteristic wavelength regions [181] and b) A representation of how a beta filter removes the beta characteristic wavelengths.

X-rays, when targeted at a material, undergo various interactions. The one of interest is elastic (coherent) scattering. The X-rays interact with the electron cloud surrounding the nuclei and the wavelength (hence energy) of the scattered X-ray does not change. The diffracted wave is the scattering of X-rays from planes, meaning the sample's lattice geometry determines the location of the peaks on the diffractogram [178]. The constructive interference of said diffracted waves will only occur when the incident angle and the diffracted angle obey Bragg's law (Equation 3.1), where n is order number, λ is X-ray wavelength, d is inter-planar spacing and θ is incident/diffraction angle [182].

$$n \cdot \lambda = 2d \cdot \sin(\theta) \quad (3.1)$$

The intensities of the peaks depend on the types of atoms and their arrangement within the lattice, and other factors such as absorption, Lorentz factor and the number of equivalent planes for a given scattering angle (2θ).

3.1.2 XRD Geometries

Multiple types of geometries are used in diffraction experiments to investigate different sample types. Two common types of geometries used during lab diffraction experiments are Gonio (i.e.

Bragg-Brentano and Parallel Beam) and grazing incidence. Gonio is where the incident and diffraction optics move in an arc (i.e. goniometer circle) which is centred around the sample. The incident (ω) angle, between the X-ray source and sample, is always half of the detector angle - both optics move at the same angular rate. The Gonio geometry is shown in Figure 3.3a. Grazing incidence is where the incident angle is fixed at near the critical sample angle (i.e. very low angles) and the X-ray is diffracted at the 2θ angle. Due to the low incident angle, the penetration depth of the X-rays, compared to the Gonio geometry, is substantially lower which is useful for investigating thin films or shallow damage depth from irradiation/implantation damage. The grazing incidence geometry is shown in Figure 3.3b [183, 184].

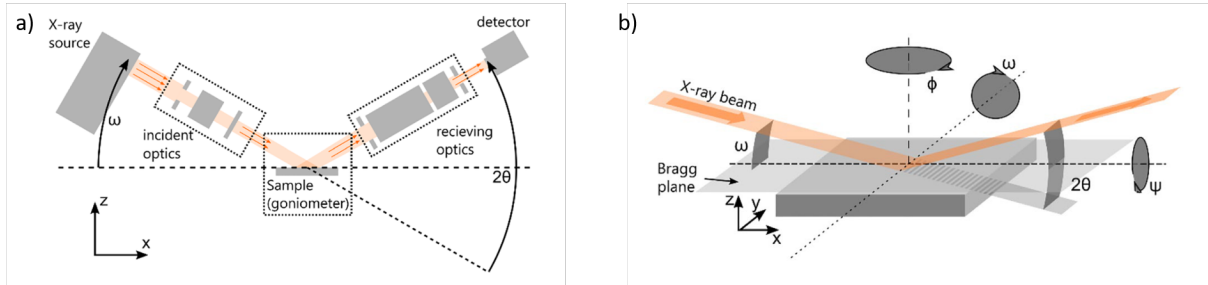


Figure 3.3: A schematic diagram of the XRD geometries: a) Gonio geometry and b) Grazing incidence geometry [183].

Another type of diffraction geometry is transmission, which is where the X-rays are diffracted through the sample and detected on the other side to obtain microstructural information. A schematic example of transmission XRD is shown in Figure 3.4. The transmission geometry is commonly used in lab diffraction experiments using a molybdenum (Mo) X-ray source and is used on much larger scales at facilities called Synchrotrons. The Synchrotron X-ray Diffraction (sXRD) follows the same principle as the transmission diffraction shown in Figure 3.4 but uses a much higher flux of X-rays, providing even higher intensities and resolution of data.

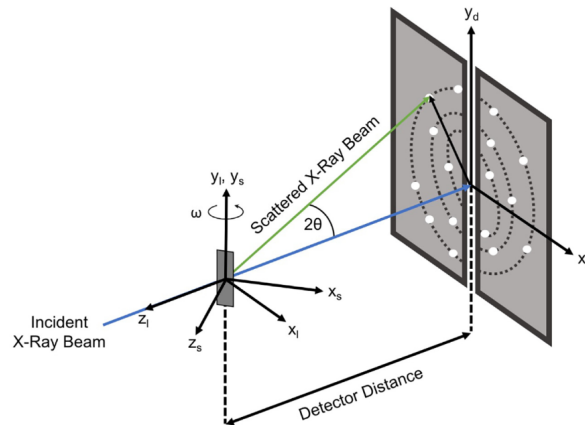


Figure 3.4: A schematic diagram of transmission XRD, applying to both lab XRD and sXRD [185].

A reason to use transmission XRD (tXRD) is that it can produce very high intensity and resolution data due to the high flux, and it is more optimised to investigate hkl s reflections at low angles in comparison to reflective XRD [186, 187]. However, a vital consideration to take into

account is that transmission XRD can only be used on small and thin samples, which may be less representative of the bulk sample. In addition, sXRD/tXRD are likely to be less sensitive to surface impurities/defects. This is demonstrated in Figure 3.5 which gives a simplified example of the possible information available, in a bulk Zr sample, during sXRD/tXRD and lab XRD. With a given sample thickness of x and the assumption that any surface contamination/defect does not permeate more than a quarter of x , it can be seen that the surface contamination:bulk sample information ratio would be more prominent in lab XRD than in sXRD/tXRD. Also, if the sample thickness is at least twice as large as the attenuation length of the lab XRD, with the given above assumption, sXRD/tXRD would be less sensitive to surface contaminations/defects

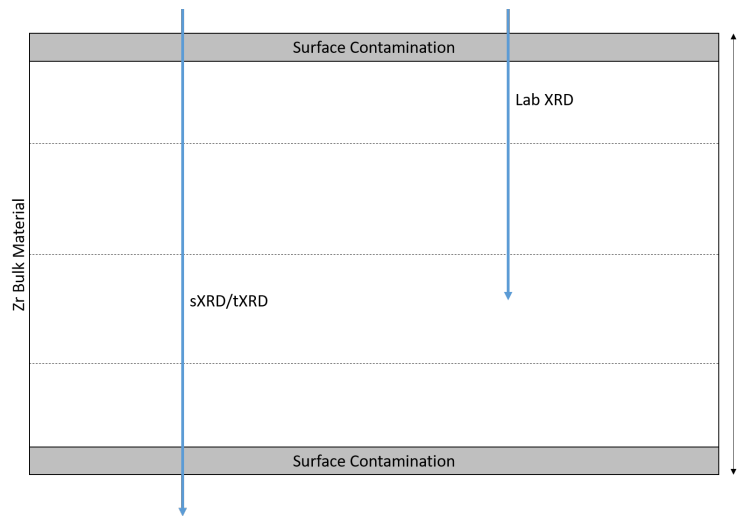


Figure 3.5: A schematic diagram comparing sXRD/tXRD and lab XRD with regards to their sensitivity towards surface contamination/defects.

The main advantages of using Synchrotron XRD over lab XRD are: 1) due to the higher flux, samples can be measured rapidly, 2) the X-ray wavelength at Synchrotron facilities is tuneable meaning that it can be changed to different lengths, 3) due to the high intensities there is an increase in sensitivity, and 4) they have high spectral resolution [188].

3.1.3 Monochromators

There are multiple ways of filtering X-rays: a beta filter, a single bounce monochromator and a double bounce monochromator.

A beta filter is an energetic filter, that uses a thin film of an element of a lower atomic number than the source (e.g. a nickel beta filter for a Cu source or a rhodium beta filter for an Ag source), which reduces the intensity of the $K\beta$ wavelength. The beta filter utilises the absorption edge of the filter element, which absorbs wavelengths smaller than the given absorption edge, to remove unwanted wavelengths.

Single bounce and double bounce monochromators are classified as physical filters, which remove unwanted wavelengths by preferential diffracting a chosen wavelength (or range of wavelengths). $K\beta$, $K\alpha_1$ and $K\alpha_2$ have different wavelengths, therefore according to Bragg's law, will diffract at different angles from the sample. As the wavelengths are known, the angle at which each are diffracted at can be calculated and therefore can be selected.

In the monochromators, mirrors are used to reflect the diffracted beams in order to have further separation of the pathways of $K\beta$, $K\alpha_1$ and $K\alpha_2$. The $K\alpha$ and $K\beta$ wavelengths are distinctly different, therefore a single bounce is sufficient to separate $K\alpha$ and $K\beta$ and to block the $K\beta$ pathway. Hence the name single bounce monochromator.

With $K\alpha_1$ and $K\alpha_2$, as the wavelengths are fairly similar, a double bounce of the diffracted beam is required to have adequate separation of the two $K\alpha$ wavelengths. In a double bounce monochromator, both $K\beta$ and $K\alpha_2$ can be removed.

3.1.4 Types of Detector

There are three types of detectors used when collecting X-ray diffraction data, and they are 0D, 1D and 2D. Data collection and analysis have usually been based on 0D and 1D detection, such as point or line detectors respectively. [189]. A 0D detector is where the diffracted X-rays are measured when they hit anywhere within the detector area (Figure 3.6). In 0D mode, the detector surface has no range of positional information, therefore the receiving angle, to comply with Bragg's law, is determined by the detector arm. To increase angular resolution, a receiving slit or parallel plate is used to narrow down the beam [190].

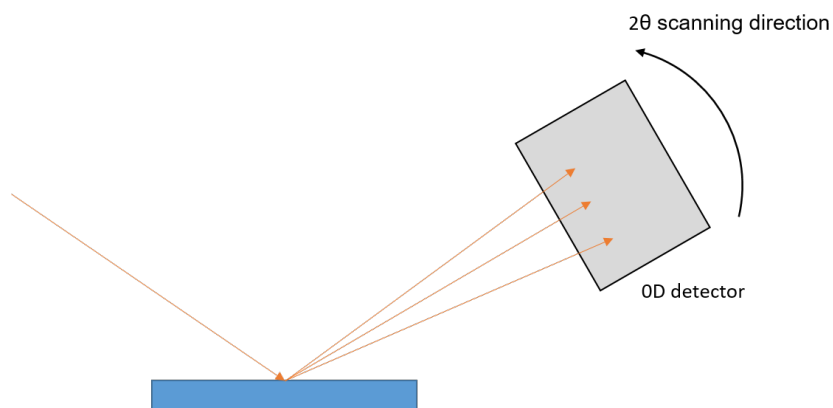


Figure 3.6: *The principle of a 0D detector via a schematic drawing.*

A 1D detector is where the detection area, having positional information, is split into line elements, which are perpendicular to the angular movement, as shown in Figure 3.7. The detector will have an angular range, where each line element will be a step size, therefore, if the angle range was $20 - 30^\circ$ and there were 11 line elements, each line element would be 0.1° .

When the detector moves by a step size, 0.1° in this case, there will be overlapping angles as the angle range would be $20.1 - 30.1^\circ$. This is repeated throughout the desired 2θ range; the overlapping angle intensities are summed together, producing a larger intensity than 0D detectors as well as a greater peak-to-background ratio.

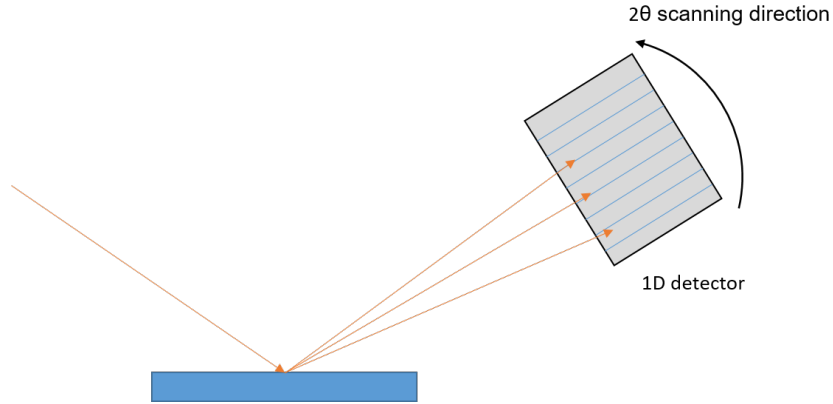


Figure 3.7: *The principle of a 1D detector via a schematic drawing.*

A 2D detector also has an angular range, however, instead of having line elements, the detector is made up of pixels. The array of pixels is able to more accurately detect the shape of Debye-Scherrer rings, as shown in Figure 3.8, which are produced from the X-rays [191]. This results in a higher resolution result than a 1D detector. Each ring element, similar to a 1D detector, will be a step size between the angular range of the detector and when the detector moves, the overlapping angle data will be integrated together.

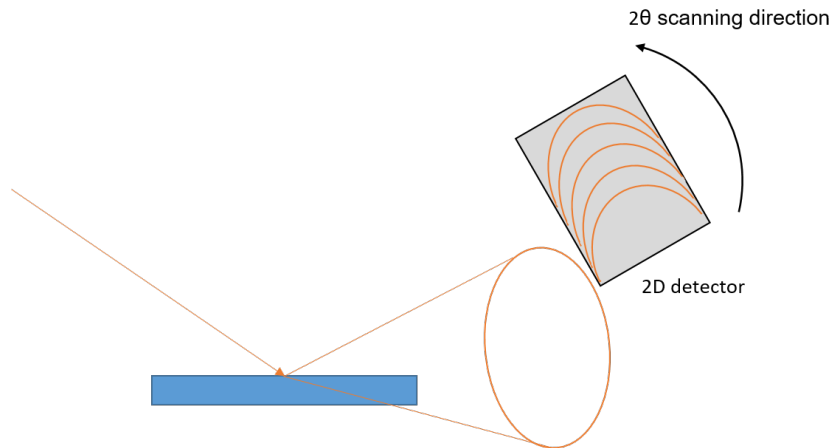


Figure 3.8: *The principle of a 2D detector via a schematic drawing.*

One of the limitations of XRD is that the characterisation technique is more accurate when measuring large sample quantities. Small sample volumes do not produce enough diffraction data to provide accurate results without assumptions, therefore, when trace amounts (i.e. small amounts of secondary phases) are considered, they may go undetected [192]. To obtain accurate crystallographic and physical data from XRD, a reference sample is required, therefore, if a reference is not available the results produced may contain errors as the instrument may not be properly calibrated.

3.2 Scanning Electron Microscope (SEM)

Scanning Electron Microscopy is one of the most common analytical techniques used to examine materials morphology and chemical composition. The analytical technique uses a focused electron

beam to scan over the surface of the sample systematically, producing an array of signals, which are detected and converted into images [193]. The key features of an SEM are the electron gun, the anode, the condenser and objective lens, the secondary electron (SE) detector and the backscattered electron (BSE) detector, as shown in Figure 3.9.

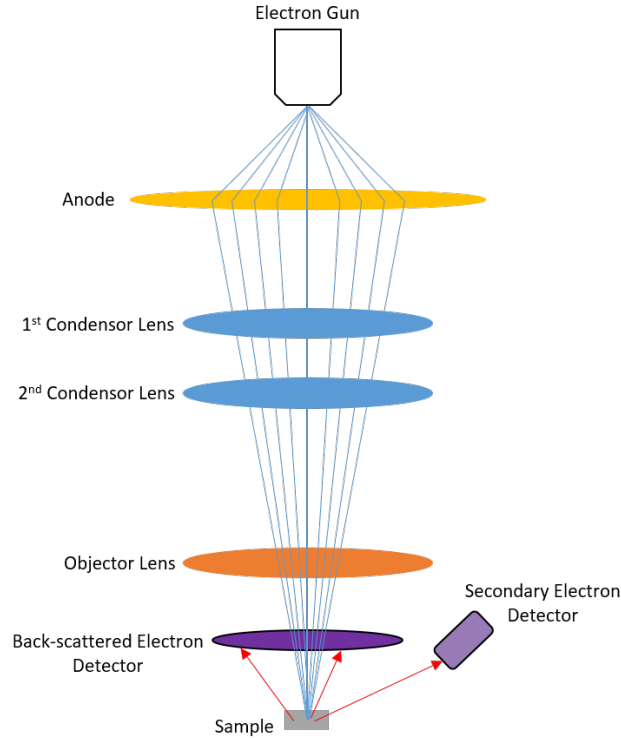


Figure 3.9: A schematic diagram of the key features of an SEM [181].

In the SEM, an electron beam produced by an electron source is accelerated using an anode, at a high current, in a low vacuum (usually $0.1-10^{-4}$ Pa) at the condenser lenses. The condenser lenses converge the electron beam, into a relative parallel beam, through the condenser aperture to exclude stray electrons. Usually, two condenser lenses are used to help control the focused beam. Due to the condenser aperture, the electron beam will start to diverge, therefore, the objective lens is there to refocus the stream onto a single point on the sample. Once the electron beam hits the sample, various interactions occur. The main interactions can be seen in Figure 3.10. The main focal point being the two different types of electrons: secondary electrons (SE) and backscattered electrons (BSE) [193].

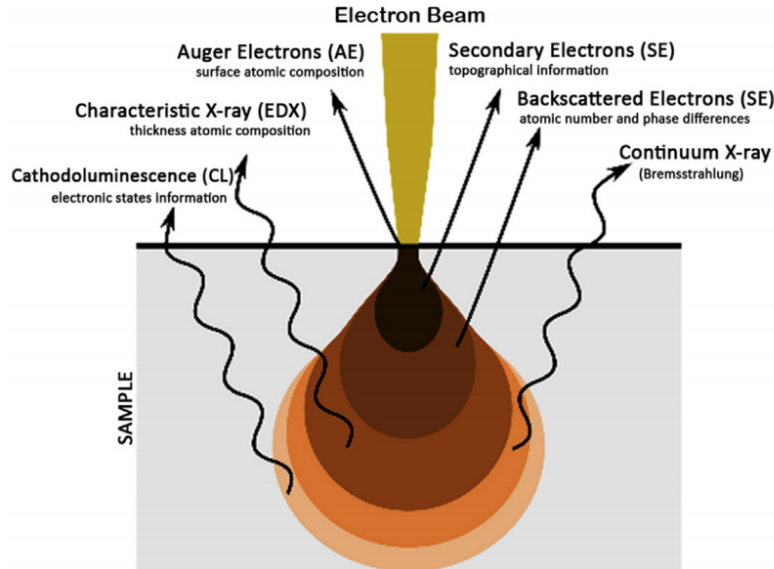


Figure 3.10: Radiation produced from an electron beam's interaction with a sample [194].

Secondary electrons are produced when the electron beam ionises atoms on the surface of the sample and outer electrons are emitted, as shown in Figure 3.10. Due to SE having low energies (< 50 eV), they can only escape from within a couple of nanometres of the sample surface [195]. Therefore, these electrons are commonly used for topographical analysis at high resolution. Emissions from a horizontal specimen are isotropic normal from the sample surface and the maximum intensity is reached at surface normal. Due to the asymmetric positioning of the detector, only half of the secondary electrons are detected, therefore, on average, less than 40 % of the produced signal is being received [196].

Back scattered electrons are primary electrons that have undergone significant scattering (primarily elastic scattering), enough so that their directions have completely reversed and they have been emitted through the sample surface [179]. As can be seen from Figure 3.10, BSEs reach further into the material, therefore provide more information such as specimen composition as different atomic numbers produce a different contrast of images [197]. The repulsive power generated by a nucleus is directly proportional to its atomic number, therefore, heavier elements produced more back-scattered electrons than lighter elements, causing the different contrast in an image [198].

A known disadvantage of SEM is that when using a material that is a strong insulator, it must be coated in gold or carbon before being analysed, in order to increase conductivity. However, this may lead to an artefact which is where the microstructure of the sample can slightly change and/or give rise to image distortion during analysis.

3.3 Transmission Electron Microscope (TEM)

TEM, like SEM, uses a high energy electron beam to probe the structure of a material. However, unlike the SEM, the electron passes through the sample, which is very thin, in order to produce an image which is magnified. The TEM is comprised of five major parts: the electron gun, the illumination stage, the objective lens, the magnification and projection systems, and the detector [199]. A schematic illustration of the setup of a conventional TEM is shown in Figure 3.11.

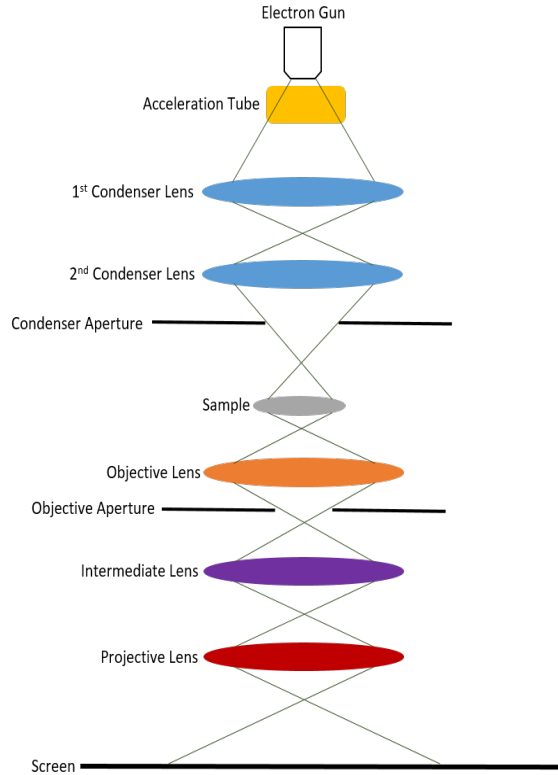


Figure 3.11: A schematic diagram of a conventional TEM in imaging mode [200].

The first condenser lens refines the beam into a higher intensity electron beam, whilst the second lens focuses the beam onto the area of interest on the specimen. Once the electron beam has gone through the sample, the ‘captured image’ goes through another three electromagnetic lenses: objective lens, diffraction/first intermediate lens and projector/second intermediate lens and onto a fluorescent screen or detector [200, 201]. The objective lens is used to focus and magnify the image of the specimen, the primary intermediate lens is used to magnify the image coming from the objective lens and the projector lens is to further magnify the image and project it onto a fluorescent/phosphorescence screen.

There are two image modes when discussing conventional TEM: bright field and dark field. Bright field mode is the most common method of TEM imaging and uses the transmitted electrons from the specimen to form the image and the scattered electrons are blocked. Therefore, the areas of higher atomic mass will appear darker [202]. With dark field, as the transmitted electrons are blocked and the scattered electrons are used to produce the image, areas with no scattering will appear dark and areas with material will be bright [203, 204]. With regards to dislocations, the lattice distortion created by the dislocation causes Bragg diffraction of the incident electron beam. This directs intensity away from the straight electron beam hence dislocations appear as dark lines/loops in bright field TEM [205].

A common disadvantage with electron microscopes, especially TEMs, is the cost of the equipment, installing it and maintaining it as they are highly specialised pieces of equipment. As TEMs are large, sensitive pieces of equipment, where magnetic fields and vibrations from other equipment/laboratories can interfere, a large laboratory space with extra safeguards is required in order to maintain the microscope’s accuracy. Also, due to the specialised nature of the microscope, years of training may be required in order to use it properly. A disadvantage, not with the

TEM itself, but the sample preparation method is that it introduces defects into the material, making it difficult to differentiate between induced damage and accidental sample preparation damage [206]. As this work contains an in-depth analysis of induced damage, TEM may not be suitable, hence XRD may be a viable option as it may provide a more representative damage profile.

3.4 X-ray Fluorescence (XRF) Spectroscopy

X-ray Fluorescence (XRF) Spectroscopy is a technique that determines, quantitatively and qualitatively, the major and trace elements within a material. High-energy X-ray radiation is fired at the target sample, exciting the atom by firing off an electron from the innermost orbital shell. In the de-excitation of the atom, an electron from an outer orbital replaces the released innermost electron, fluorescence radiation, characteristic of the element, is released with an energy equivalent to the difference between the electron shells [207–209]. This is represented in Figure 3.12.

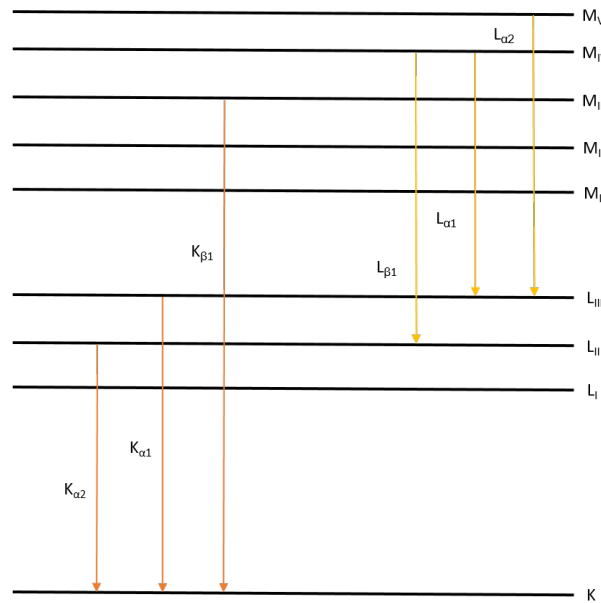


Figure 3.12: The principle of characteristic X-ray emissions showing the energy levels of a material and the corresponding characteristic emission lines. An interpretation from Margui et al. [208].

As there are multiple orbitals in which an electron can de-excite and replace an inner electron, there are multiple characteristic fluorescence radiation for each element, hence, it is possible to have very close characteristic fluorescence energy from different elements (e.g. Potassium $K\alpha = 3.314$ keV and Calcium $K\alpha = 3.692$ keV [210]). Therefore, a way to calibrate data produced from the XRF is to use the real density of the sample as well as elemental standards, to gauge realistic elements.

Chapter 4

Experimental Procedure

This section will cover a detailed methodology of the experiments covered throughout the thesis. Where methods differ between experimental chapters, particularly analysis, this covered in the specific relevant chapters.

4.1 Heat Treatment of Zirconium

The Zr foil bought from Goodfellows Cambridge Ltd was sectioned into four approximately equal strips, with dimensions of 38 mm x 150 mm x 7 mm (W x H x T). One of the strips was cut in half to produce two strips, with dimensions of 38 x 60 x 7 mm and 38 x 90 x 7 mm, that are referred to as zirconium as-received (Zr-AR) and zirconium plus a heat treatment to recrystallise the material (Zr-HT) respectively (as shown in Figure 4.1). The three long strips and one of the short strips underwent heat treatment to remove the defects produced in the processing of the material before being purchased. Due to zirconium being very susceptible to hydride formation, the heat treatment was completed under argon (high purity and low moisture) to suppress the hydride formation. The other three long strips from the original bulk material, referred to as cold worked material, are discussed in Section 4.2.

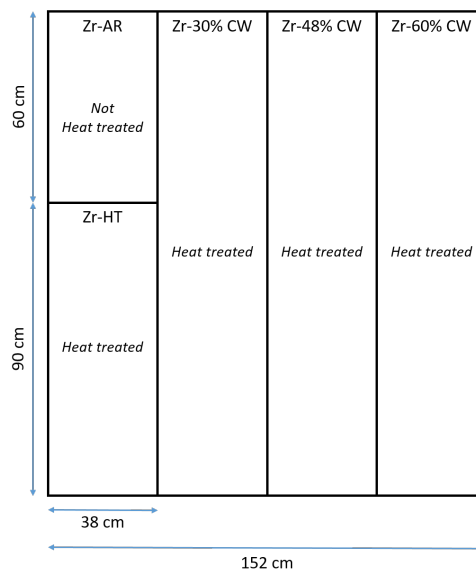


Figure 4.1: A schematic drawing showing the sectioned Zr foil.

The heat treatment of zirconium started at room temperature, which was assumed to be 25 °C as shown in Figure 4.2, the temperature was then increased, at 5 °C per minute, to 730 °C, taking 2 hours and 1 minute. The sample was held at 730 °C for 30 minutes before being furnace cooled under inert conditions. This took approximately 6 hours, equivalent to a cooling rate of 2 °C per minute. The parameters of this heat treatment were set to ensure that α -Zr was formed instead of β -Zr as well as minimise hydrogen pick-up (due to the susceptibility of hydride formation in β -Zr - explained in Section 2.2). The heat treatments were conducted by senior engineering technician Neil Hind at The University of Sheffield.

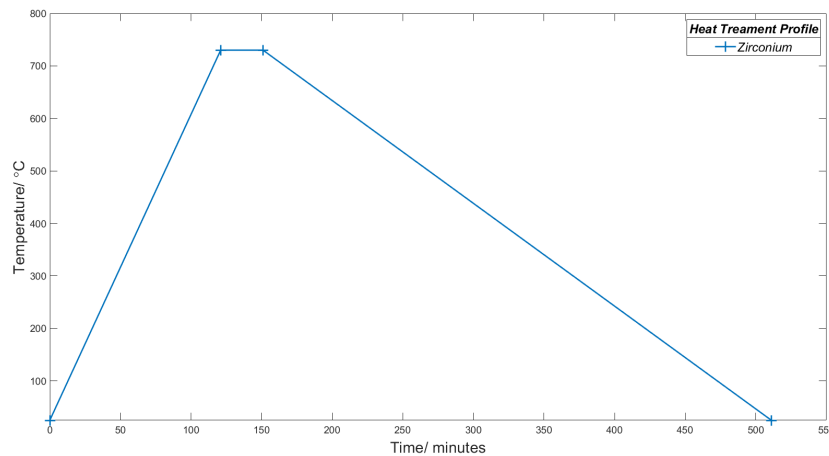


Figure 4.2: Heat treatment temperature profile in the furnace.

4.2 Cold Rolling/Working of Zirconium

The three long strips of material, shown in Figure 4.3, underwent various degrees of cold rolling to introduce mechanical deformation as an analogue for radiation damage. The intent was to have zirconium strips cold rolled to 30%, 60% and 80% thickness reductions; however due to cracking at the edge of the material, as shown in Figure 4.3, the strips were cold rolled to 30%, 48% and 60%. The cold rolling experiments were handled by Dr Ross Nolan at The University of Manchester.



Figure 4.3: Edge cracking on zirconium foil due to cold rolling. The initial edge cracking is highlighted in blue and the final extent after 60% is shown in red.

Table 4.1 shows the number of passes and the material thickness at each stage, where the highlighted values are the final roll gap and material thickness for each reduction. The cracking at the edge of the material began at pass no. 9, which achieved a 48% reduction in thickness. The cracking propagated when the rolling was continued to reach pass no. 12, obtaining a 60% reduction. The 30%, 48% and 60% reduction samples will be referred to throughout the thesis as Zr-30, Zr-48 and Zr-60 respectively.

Cold rolling induces dislocations within the material, however, at the edge of the material, there is an increased build up of stress. Due to grain boundaries, the edge boundary (i.e. surface) and room temperature cold rolling, there is reduced dislocation diffusion from the result of dislocation pinning and reduced dislocation mobility. Hence, as the cold rolling increases to higher reductions, the increase in stress within the material, specifically at the edge, leads to edge cracking instead of plastic deformation.

Table 4.1: *The rolling procedure runs on the zirconium strips. Highlighted regions are where the samples were taken out for their chosen deformation profile.*

Pass No.	Roll Gap/ mm	Material Thickness/ mm		
		30%	48%	60%
1	7.15	7.15	7.15	7.15
2	6.44	6.90	6.93	6.91
3	5.79	6.52	6.52	6.52
4	5.21	5.95	5.95	5.96
5	4.69	5.45	5.47	5.45
6	4.22	5.01	5.03	5.03
7	3.80		4.77	4.77
8	3.42		4.25	4.25
9	3.08		3.73	3.73
10	2.67			3.37
11	2.49			3.10
12	2.24			2.86

4.3 Sample Preparation

4.3.1 Scanning Electron Microscopy (SEM)/X-ray Diffraction (XRD) Samples

Each set of samples were sectioned into approximately 10 mm x 10 mm (W x H) blocks using a 10 inch silicon carbide blade (for hard non-ferrous materials) on the Struers Secotom-50. This sample size was to maximise the diffraction intensities, by providing a larger scan area, to provide sufficient data for Convolutional Multiple Whole Profile (CMWP).

A mirror-like finish was required for XRD to maximise the intensity and accuracy of the results. Multiple methods were attempted in order to achieve a mirror-like finish such as: using a donut rig (Figure 4.4) for hand grinding and polishing. The advantage of this technique was that the cold mounting of the sample on an aluminium cylinder would help eliminate the risk of annealing out dislocations or the creation of secondary phases. However, this method either caused bevelling or damage to the polishing pad as well as not providing a clean surface finish when using Oxide Polishing Solutions (OPS).



Figure 4.4: *The donut rig used to manually grind and polish a sample.*

The final method was to grind and polish the sample in a soft resin, Purifast, and then break them out for XRD and EBSD. The grinding and polishing procedure is described in Table 4.2. The platen speed for the grinding and polishing steps were 301 rpm and 121 rpm respectively and the head speed for all steps was 60 rpm. The colloidal silica was diluted in distilled water in a 4:1 ratio. Though the surface seemed to be mirror-like, under dark-field optical or SEM, micro scratches could be found, which hindered the ability to find clear and distinct Kikuchi bands thus making it unsuitable for Electron Backscatter Diffraction (EBSD). However, as the scratches were so small, they did not affect the procurement of reliable XRD and SEM data, thus deeming the sample preparation method appropriate for SEM and XRD.

Table 4.2: *The final proposed grinding and polishing method of zirconium for XRD and SEM.*

Step	Time/ mins:secs	Force/ N	Rotation
P400	01:00	15	Contra
P800	01:00	10	
P1200	00:15	10	
9 micron	10:00	15	
3 micron	00:30	15	
Diluted Colloidal Silica	30:00	25	
Water	10:00	25	

4.3.2 Electron Backscatter Diffraction (EBSD) Samples

The initial sample preparation method for EBSD samples is the same as in Section 4.3.1 but with a longer colloidal silica and water step. The initial EBSD sample preparation steps are presented in Table 4.3. Once the samples had been manually ground and polished, they were bulk electropolished - an electrochemical finishing process, that removes thin layers from the desired surface to provide an ideal surface finish, especially for EBSD.

Table 4.3: *The final proposed grinding and polishing method of zirconium for EBSD.*

Step	Time/ mins:secs	Force/ N	Rotation
P400	01:00	15	Contra
P800	01:00	10	
P1200	00:15	10	
9 micron	10:00	15	
3 micron	00:30	15	
Diluted Colloidal Silica	60:00	25	
Water	20:00	25	

In setting up the Tenupol electropolisher, the 70% perchloric acid that was diluted in a 1:10 solution with methanol, to make a total volume of 500 ml, was placed within the electrochemical container and chilled to $-30\text{ }^{\circ}\text{C}$ (taking approximately one hour). Whilst the solution was being chilled to the desired temperature, a plastic mask was placed over the cathode, which was used to direct the solution onto the sample and make sure the sample was not directly on the nozzle. Electrical tape was placed on the mask to ensure each sample was placed in the same position on the plastic mask and similar surface area was polished. The sample was then placed on the marked position and the anode was placed on top, ensuring contact with the sample to complete the circuit otherwise the electropolisher would not work. Once $-30\text{ }^{\circ}\text{C}$ had been reached, the voltage and flow rate of the pump were set. The flow rate of the pump was set so that the solution was just about flowing over the mask and not vigorously bubbling over. The voltage was chosen by first running a scan profile, which runs through a range of voltages and selects a value that produces a constant current over the scan time. The bulk electropolishing setup is shown in Figure 4.5.

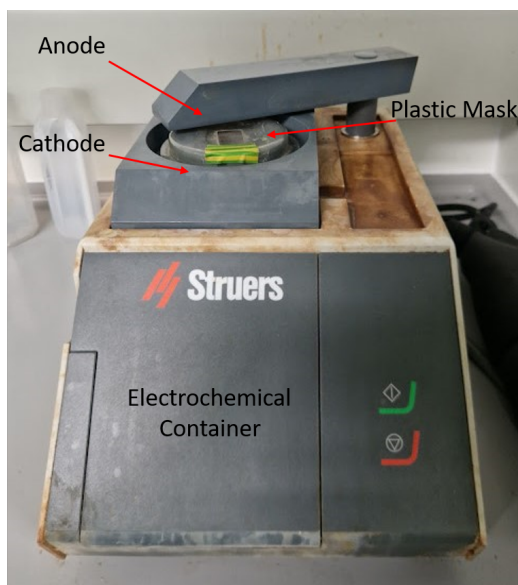


Figure 4.5: *The Struers bulk electropolisher setup.*

When electropolishing, the optimum finish is a stage between two undesirable surface finishes; if the scan is too short the sample surface will be etched and if the scan time is too long pitting will occur. Scoping tests were performed in order to determine the appropriate scan parameters; the optimum bulk electropolishing time was 40 seconds.

4.3.3 Transmission Electron Microscopy (TEM) Samples

TEM samples were produced by electropolishing, in a two step process: manually grinding to produce the correct sample thickness and subsequent electropolishing. In order for the sample to be cut into 3 mm discs for electropolishing, the sample must have a thickness of approximately 80 - 100 microns.

Samples were sectioned, using the Secotom-50, to approximately 500 - 1500 microns. They were then mounted on aluminium stubs, as described in Section 4.3.1, to be manually ground down to an acceptable thickness range. If the sample was $\geq 500\text{ }\mu\text{m}$, a coarse grit paper of P240 was

used to reduce the sample thickness to approximately 250 microns. The sample thickness was checked every grit paper change over, via a micrometer. Once it reached $\sim 250 \mu\text{m}$ and grit paper of P400 was used to grind the sample down to $\sim 150 \mu\text{m}$. If the sample was $\leq 500 \mu\text{m}$, then the finer grit paper of P400 was used until $\sim 150 \mu\text{m}$ was reached. A platen speed of 50 rpm was used.

Around $150 \mu\text{m}$, the samples will start peeling off the aluminium stub, therefore, they must ground down using a finger on a stationary platen. A P400 grit paper was then used to grind the sample down to the target sample thickness. The samples are ground down on both sides, to ensure a flat surface and to remove any of the wax substance used to adhere the sample to the stub. Once the desired thickness was acquired both sides of the sample were gently ground to remove any surface impurities and residue (using equipment in Figure 4.6) before being placed in the electropolishing sample holder.



Figure 4.6: *The grinding machine to remove surface impurities and residues from TEM samples before electropolishing.*

A 1 L mixture of 70% perchloric acid, methanol and 2-butoxyethanol was produced with a volumetric ratio of 3:600:397 respectively. Before starting the electropolishing procedure, a litre of methanol was used (up to the fill line as shown in Figure 4.7) in the cleaning process, which is repeated five times, to clean the interior of the Tenupol-5 equipment. The cleaning process was key to removing any residue/impurities from previous uses which may affect the electropolishing step.

The used methanol solution was then disposed of in an appropriate waste container (first wash, second wash or disposed) depending on how many times it has been used. Following this, the electropolishing vessel was rinsed out using a methanol spray bottle. The electropolishing solution was placed within the vessel and the equipment setup before turning on the bath and the coolant system with a set temperature of $-35 \text{ }^\circ\text{C}$.



Figure 4.7: A vessel used for methanol and electropolishing solution to clean the machine and electropolish TEM sample respectively.

The prepared TEM samples were then placed within the sample holder, ensuring that there were no gaps around the sample, and locked in with the front-end piece (Figure 4.8). Once the temperature of the bath was reached, the sample holder was inserted into the Tenupol-5, ensuring that the metal strip was facing the internal contact point, and the machine was turned on. According to literature and experts at the University of Manchester, a current of 40 - 60 mA needed to be achieved to obtain an adequate whole and minimal etching or pitting. This was done by choosing an appropriate voltage which was dependant on the electropolishing solution and the thickness of the sample. A voltage was found, via trial and error, to be approximately 40 - 45 V.



Figure 4.8: The electropolisher TEM sample holder.

Once the electropolishing was completed, the samples had to be immediately cleaned in methanol, in three separate solutions, in order to prevent over etching and pitting. Samples were then taken out of the sample holder and rinsed again, in the final cleaning process, with methanol, to remove any electropolishing solution that may have been within the holder. Samples were checked under an optical microscope to inspect the holes, and the voltage parameters were adjusted to improve hole size or to reduce over-etching/pitting. The edges of the holes are the electron transparent regions which are imaged during TEM. The electropolishing process was done in a fume cupboard.

4.4 X-ray Diffraction Scan

This section will describe the setup and scan parameters of the X-ray diffraction scans that occurred.

4.4.1 Instrumental Standard - Lanthanum Hexaboride/Silicon

This section will discuss the methods used to prepare a Lanthanum Hexaboride (LaB_6) XRD standard specimen (660c NIST standard) to help calibrate instrumental broadening.



Figure 4.9: *The sample holder used for powders such as the LaB_6 and Si standards.*

A standard method was used to prepare the powdered specimen. The powder sample holder, shown in Figure 4.9 and the glass slide were cleaned with isopropanol (IPA) to remove any residue/contaminants. The LaB_6 powder was then placed into the sample holder and flattened using the glass slide to ensure the surface is smooth and flush with the edges. The back of the sample holder was then attached, the sample flipped and the base removed, producing a smooth powder sample surface (Figure 4.10). The same method was used for the Si XRD standard (640e NIST standard).

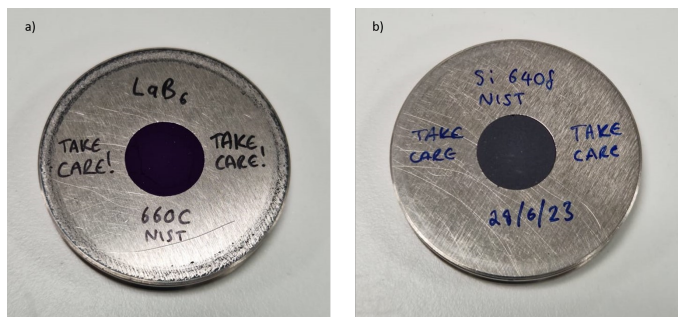


Figure 4.10: *Powder XRD standard samples, LaB_6 and Si: a) LaB_6 standard used to determine instrumental broadening and b) Si standard used as a reference because of its known crystallite size and strain.*

4.4.2 Zirconium Samples

Two setups were used when procuring bulk XRD data: a 1D detector and a 2D detector. The scans done at the University of Sheffield (UoS) on the Panalytical X'Pert Powder (X'Pert) and Malvern Panalytical Empyrean (Empyrean), with the Cu source and Ag source respectively, used the 1D detector setup. However, the scans done at the University of Manchester (UoM) and

Material Research Facility (MRF) in Culham, which used a Cu source and Co source respectively, used a 2D detector setup. The operation of the equipment was completed by Dr Rhys Thomas and Dr Gyula Zilahi at UoM and MRF respectively.

For the 1D detector setup, samples were placed on a bulk sample holder (Figure 4.11) and were made flush with the rim of the sample holder using a glass slide. Before the long scans were taken, a quick scan was done in order to obtain the correct sample orientation, to maximise peak intensity and numbers, because of preferential grain orientation for the cold rolled sample. All five zirconium samples (Zr-AR, Zr-HT, Zr-30, Zr-48 and Zr-60) plus the LaB₆ were all placed on the automated sample changer stand so that all the scans could be taken sequentially.



Figure 4.11: Bulk sample holder used in the Panalytical Powder X'Pert and Malvern Panalytical Empyrean.

Initially, the scans were done using a nickel filter, to remove the K- β , a 0.5 inch and a 0.25 inch diverging slit and anti-scatter slit respectively. As the scanning time was eight hours to provide high intensity, the nickel beta-filter produced an absorption edge as can be seen in Figure 4.12. This interfered with the tails of the peaks, interfering with the CMWP analysis, which produced inaccurate values. The description of the production of the absorption edge is referenced in Section 3.1. The removal of the absorption edge modified the tails of the peak, changing the broadening of the peaks, therefore, accurate results from CMWP were not obtainable.

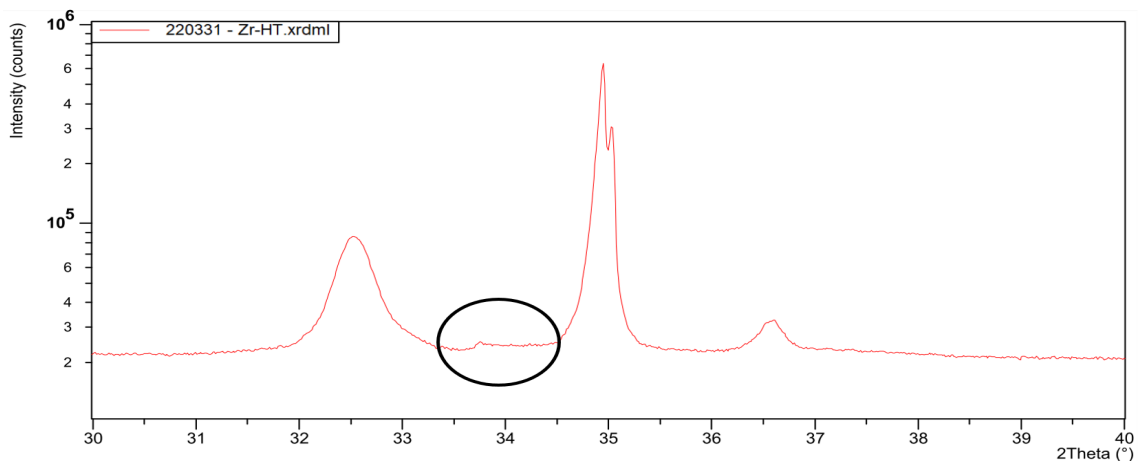


Figure 4.12: The absorption edge produced by a nickel beta-filter on an eight hour long XRD scan.

It was therefore decided to use a single bounce monochromator as it removes $K\beta$ without the use of a nickel beta-filter, which removed the issue of producing absorption edge interference. However, as it is a single bounce monochromator it only removes $K\beta$ and not $K\alpha_2$. There were slight optic differences between each radiation source, which meant that there were different areas of coverage. As the samples were cold rolled, the damage imparted onto the samples was assumed to be uniform, therefore, the difference in scan area should not affect the results. For the smaller scan areas, the scan time per step was increased to produce sufficient intensities. The samples that were scanned at UoM (Cu source) and MRF (Co source), due to the machine capabilities, also had a slight oscillation in the phi (ϕ) direction. The oscillation was to help minimise the effects of grain alignment from cold rolling as well as increase the investigation area which improved intensity and resolution. Each set of experiments for each different radiation source also had a LaB_6 , a sample to obtain instrumental effects, scanned under the same conditions and scanning parameters as the zirconium samples. The naming convention for each sample was set as follows: Zr-X-Y, where X represents the deformation status of the samples (as stated previously) and Y represents the radiation source from which the data set comes from. A detailed description of the scan parameters and optics used for the experiments will be presented in the methodology section of Chapter 4.12.

4.4.3 High Temperature Zr-4 Scans

The samples for high temperature, using the X'Pert with a Cu X-ray source, were placed on an alumina crucible (Figure 4.13a) on an XYZ stage (Figure 4.13b), with a required sample height of between 2.4 - 5 mm. The height of the sample was limited by the edge height of the crucible and the z -distance range by the XYZ stage. As described in Section 4.4.2, a pre-scan was done to determine the correct sample orientation for maximum peaks, the vacuum was not active for these scans.

Initially, a single bounce monochromator was used to remove $K\beta$, however, the intensities were too low and an increased scan time was not viable. Therefore, the nickel-beta filter was used, which ran the risk of producing the absorption edge.

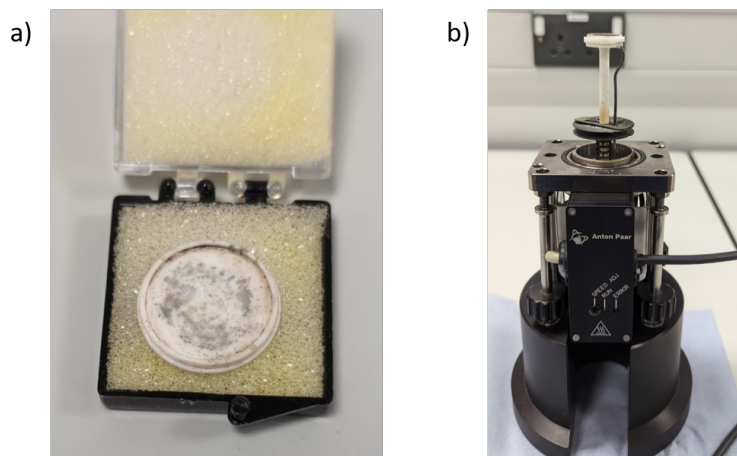


Figure 4.13: *The crucible and XYZ stage used in HT-XRD: a) alumina (Al_2O_3) crucible and b) XYZ stage.*

Once the correct orientation was found, the XYZ stage was placed within the furnace and screwed in place (Figure 4.14). Due to the samples having different heights and being on an XYZ stage,

they had to be aligned using the direct beam half cut method. The beam and the detector were set to a zeroed position, so they are inline with each other. The nickel-beta filter was removed and replaced with a Cu filter to protect the detector, and the same procedure as stated in the previous section was run. The difference in the direct beam half cut method between the facilities was the use of the Cu filter at the Sheffield facility to protect the detector. Once the alignment was completed all relevant optics were put back in.

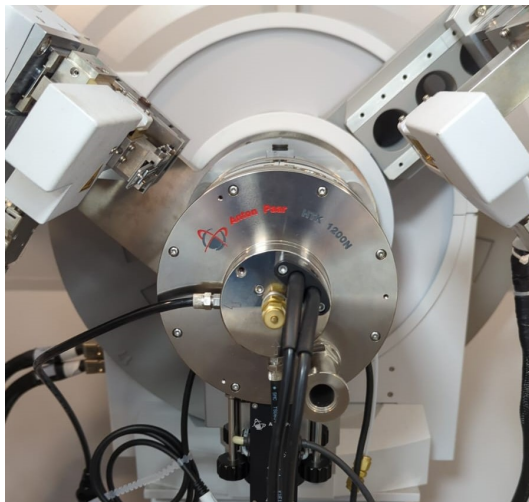


Figure 4.14: *The high temperature XRD (HTXRD) setup for the X'Pert.*

As zirconium readily forms zirconium oxide, especially at elevated temperatures, the high temperature experiments were run under vacuum. Following the SOP, once the correct orientation and height alignment was found, the vacuum pump was set. Whilst the vacuum reached the appropriate pressure (1.5×10^{-5} Pa) the room temperature scan was run, with the following parameters (Table 4.4):

Table 4.4: *Scanning parameters for the high temperature X'Pert mode.*

Parameter	Value
Angle Range/ °	30 - 102
Anti-scatter Slit/ inch	0.50
Divergence Slit/ inch	0.25
Filter	Nickel beta-filter
Primary Mask/ mm	10
Soller Slits/ Rads	0.04
Step Size/ °	0.0131
Time per step/ secs	157.8

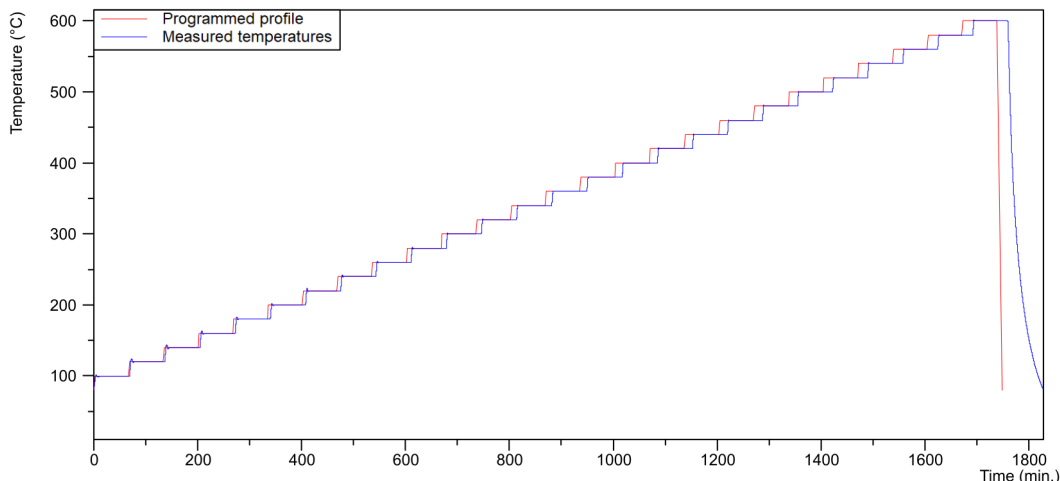


Figure 4.15: *The recorded temperature profile furnace against the theoretical temperature profile.*

A non-ambient batch programme was created to automate all the scans at elevated temperatures. Once the desired furnace temperature was reached the sample was held at this point for 5 minutes to ensure that the sample reached thermal equilibrium. The scan were then conducted, which were programmed for one hour. Due to the accuracy of the furnace, where temperatures are not well controlled below 100 °C, the first scan of the batch programme was at 100 °C for approximately an hour. Every subsequent scan was set to be done every 20 °C with a temperature gradient increase of 10 °C per minute. However, in reality there was approximately a 3 - 6 minute delay between each scan, as shown in Figure 4.15.

4.5 Data Processing for CMWP

Following the acquisition, the data was processed for subsequent fitting with CMWP.

4.5.1 Peak Index File

CMWP requires a ‘peak index file’ (Figure 4.16) as an input - containing the peak position, peak intensity, the ‘*hkl*’ and the phase number assigned to it. The file needed to be saved as ‘DataName.peak-index.dat’ (e.g. Zr-HT-Co.peak-index.dat) in order to be read by CMWP. The Panalytical software, Data Viewer, was used to manually identify peak positions and intensities, whilst the ‘*hkls*’ were found using the Powder Diffraction Files (PDFs) of the respective elements/compounds within the material. In Figure 4.16, the fourth column which represent the phase assigned, shows four numbers: 0, 1, 2 and 3, where 0 signifies the alpha zirconium phase and 1 represents the zirconium hydride phase. The 2 and 3 represent the α -Zr and δ -hydride phases, which have overlapping peaks such that they can not be fully distinguished from each other during the analysis and have some slight asymmetry, therefore, had to be fitted using a ‘dummy’ phase.

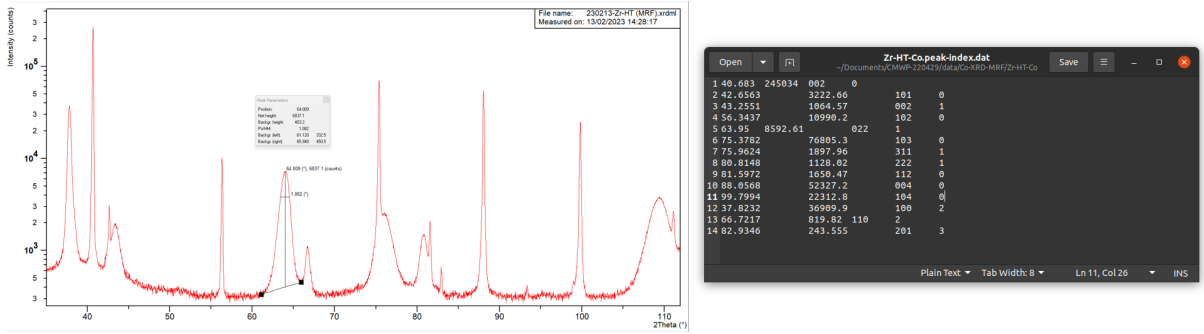


Figure 4.16: The method of identifying peaks and their intensities as well as the formatting for the peak index file.

4.5.2 Instrumental Profile

The LaB₆ instrumental data had to be converted into ‘*k*’, the reciprocal of the interplanar spacing, as shown in the rearranged Bragg’s Law equation (Equation 4.1). This is because it is easier and more practical to compare measured diffraction to theory when using ‘*k*’ [3].

$$k = \frac{1}{d} = \frac{2\sin\theta}{\lambda} \quad (4.1)$$

Where *k* is the reciprocal space, *d* is interplanar spacing, θ is the Bragg angle and λ is the radiation source wavelength.

The peaks within the instrumental profile were then split into its individual ‘*hkl*’ peaks, the background intensity removed, and the apex of $K\alpha_1$ centred on zero. The peak were identified, as previously with sample data, using Data Viewer and were separated and converted in ‘*k*’ in Excel, as shown in Figure 4.17. The removal of the background intensity was done using a background removal function in the ‘Fityk’ software. The software also allows the modification of the data via transformation functions, in this case, a translation. The $K\alpha_1$ peak position was identified and the data translated so that the $K\alpha_1$ peak was centred on zero, a representation of this is in Figure 4.17.

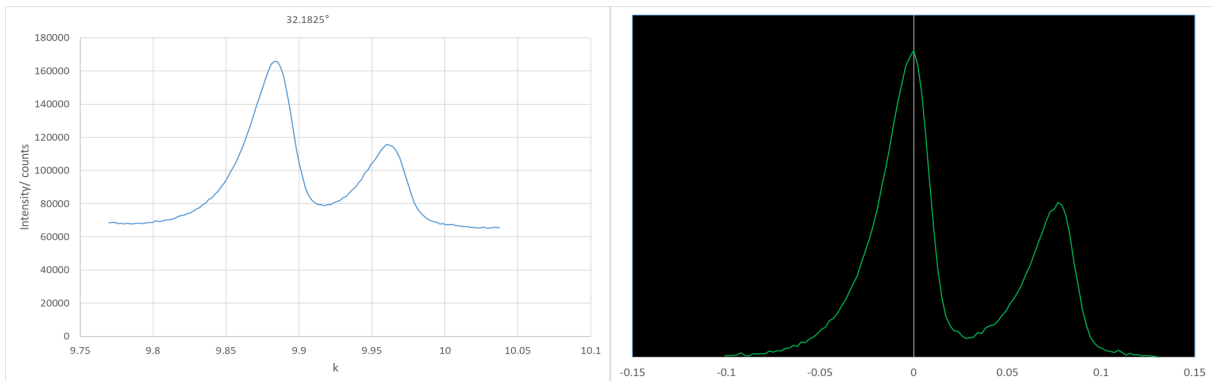


Figure 4.17: An example of peak separation and background intensity removal and centring of $K\alpha_1$ for the instrumental data.

Some of the noisier instrumental peaks, as an additional step, were fitted using ‘Fityk’. If there was some asymmetry a Split PseudoVoigt/Pearson7 profile was used to fit the peak but if there were two peaks, caused by $K\alpha_1$ and $K\alpha_2$, then two PseudoVoigt/Pearson7 profiles were used

instead. This fitting step would help smooth out the instrumental data, without adjusting the peak profile too much, in order to obtain a more reliable and accurate CMWP fitting.

The peak files were saved into an instrumental folder as a .DAT file type, however, the filename could not include the file extension type, otherwise, the software will not be able to read the data. An example of this is shown in Figure A1 in Appendix A.

4.5.3 Sample, Refining and Physical Parameters

Following the formatting of the data and instrumental profile, the subsequent steps stated below were used to run an initial CMWP fitting:

1. Select the crystal lattice type.
2. Set values for sample input parameters
 - Lattice parameters
 - Burgers vector
 - Average contrast factor C_{h00}
 - Wavelength of XRD machine radiation source
3. Specification of instrumental profiles location.
4. Determine background base points.
5. Peak searching intervals.
6. Specify fitting and plotting intervals.
7. Select size function.
8. Specification of sampling of the theoretical Fourier transforms.
9. Specification of the sampling of the simulated powder pattern data.
10. Specify the initial values of the parameters.
11. Peak parameters refinement and weighting.
12. Fit control by the number of iterations or changes between steps has reached specified limit.
13. Fitting.

The non-refining parameters, shown in Table 4.5, were set using known material and X-ray diffraction specifications. The initial physical parameter values, shown in Table 4.6, were set using experimental data from literature [3, 211, 212]. Where a_1 & a_2 are the contrast factors, b is the average crystallite size, c is the crystallite size distribution, d is the dislocation density and e is the dislocation arrangement parameter.

Table 4.5: *Initial parameter values for CMWP that are not refined.*

Parameter	Initial Value
a Lattice Parameter/ nm	0.3232
c Lattice Parameter/ nm	0.515
Burgers Vector/ nm	0.3232
C_{h00}	0.25
Wavelength/ nm	Dependant on X-ray source
Cutting Parameter	15
Sampling N1	10000
Sampling N2	1024

Table 4.6: *Initial physical parameters values.*

Physical Parameter	Initial Value
a_1	1.5
a_2	0.5
b (m)/ micron	50
c (σ)/ micron	0.7
d (ρ)/ $\times 10^{-14} \text{ m}^{-2}$	3
e (M^*)	2

4.5.4 Background Spline

Depending on the fitting, the background spline, implemented in step 4 above, was adjusted in order to have a better fit and a more reasonable background profile. With CMWP, the adjustment of the background spline can be done so that the effects on the fitted pattern can be seen as changes are being made, this is shown in Figure 4.18. The green line is the measured pattern, the blue line is the calculated pattern and the red line is the background spline being manipulated.

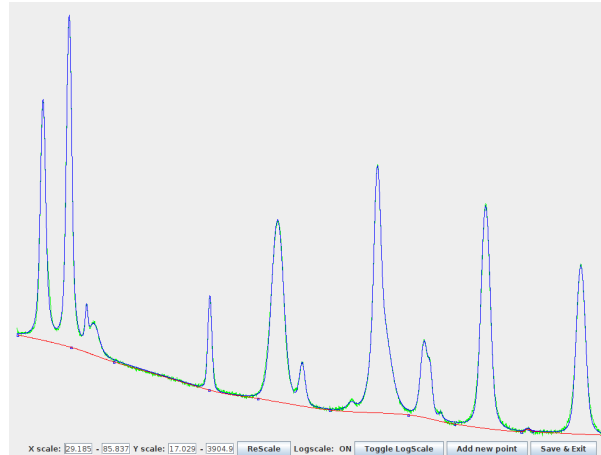


Figure 4.18: *An example of how the background spline can be adjusted whilst observing those effects of the calculate diffraction pattern.*

4.6 Data Processing for TOPAS

The data was subsequently processed via TOPAS to compare crystallite size to CMWP.

4.6.1 Instrumental Effects

To yield instrumental parameters, refinement of a standard sample was carried out, in this case, a 660c LaB_6 National Institute of Standards and Technology (NIST) standard was refined. Using the documentation provided by NIST, the lattice parameters, crystallite size and microstrain were input and fixed during refinement. The values were: 4.156826 \AA , 800 nm and approximately zero respectively. As phase fraction was not needed, a simpler refinement process was used: Le Bail analysis. With the Le Bail analysis, the spacegroup and the lattice parameter must be predetermined in order to run the analysis. A LaB_6 Crystallographic Information Framework (CIF) file was obtained from the Inorganic Crystal Structure Database (ICSD) database. This

created a ‘structure phase’ menu where sample parameters can be inputted, however, to use Le Bail, a ‘hkl phase’ menu was created from the ‘structure’ menu, which was then relabelled ‘LaB₆’. The TOPAS interface to be able to implement a Le Bail refinement and the sample parameters are shown in Figure 4.19.

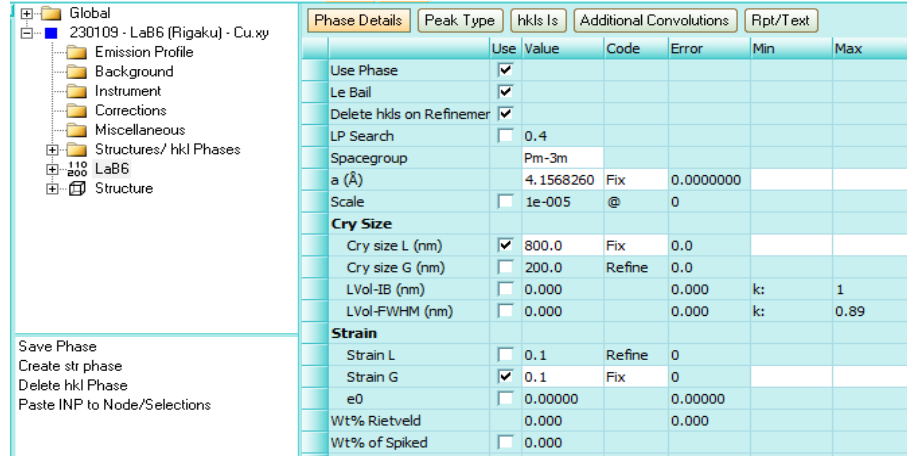


Figure 4.19: TOPAS interface showing the LaB₆ microstructural parameters.

For each specific XRD instrument, the experimental setup parameters were inputted. These parameters were: background function (Chebychev and Order), LP factor, appropriate wavelengths, radius of the X-ray source and detector (primary and secondary radius). To counter any sample misalignment, the zero error and sample displacement parameters were refined. These parameters are shown in Table 4.7, with an example screenshot shown in Figure A2.

Table 4.7: A table of relevant instrumental parameters that were set when undergoing Le Bail refinement.

Parameters	Setting
Chebychev (Background)	Refine
Order (Background)	1
Goniometer Radii (primary and secondary)	Experiment Specific
Zero error (Peak Shift)	Refine
Sample Displacement (Peak Shift)	Refine
LP correction factor	Fix
Wavelength	Experiment Specific

To obtain the instrumental effects, once the sample and experimental setup parameters were set, the ‘Peak Type’ parameter was set to refine the ‘PVII’ type peak shape (an example screenshot is shown in Figure A3). The ‘PVII’ peak shape was chosen because 1) it was similar to the refinement process used in the NIST standard documentation and 2) the six refinement parameters within this peak shape include effects on the overall diffraction patterns as well effects separately on the higher and lower 2θ angle range (includes the Cos and Tan functions). The six parameters are:

- Ha
- Hb / Cos(θ)
- Hc Tan(θ)
- mc + 0.6
- mb / Cos(θ)
- mc / Tan(θ)

4.6.2 Sample Refinement

Refining the sample data, to obtain crystallite size and microstrain, followed a similar methodology to that of the instrumental effects described above. However, the main differences are the parameters that were allowed to be refined. The experimental setup parameters obtained, described in Section 4.4.2, were used. The zero refinement and sample displacement parameters were left refining in case of any sample preparation misalignment. To ensure that the instrumental effects were incorporated, in the ‘Peak Type - PVII’ menu, the six parameters calculated from the LaB₆ refinement were input and fixed. These parameters were included for both the α -Zr and ZrH₂ phases.

With regards to the cold worked zirconium samples, two phases were added: α -Zr and ZrH₂. As phase proportion and analysis were not necessary, as used previously, the Le Bail refinement was implemented. As the crystallite size and microstrain were of interest, a Lorentzian profile for crystallite size and Gaussian profile for microstrain, in both phases, were allowed to refine. To maintain consistency, a Lorentzian profile and Gaussian profile for crystallite size and microstrain respectively, were applied to all samples. These profiles were used to align with the NIST standard documentation refinements for LaB₆ and Si. The sample parameters that were refined during the Le Bail fitting of the samples are shown in Table 4.8.

Table 4.8: *A table of the sample parameters that were either refined or fixed during the sample Le Bail analysis.*

Parameter	Fix/Refine
LP	Fix
<i>a</i> Lattice Parameter	Refine
<i>c</i> Lattice Parameter	Refine
Crystallite Size (L)	Refine
Strain (G)	Refine
Scale	Refine

Chapter 5

Accuracy and Sensitivity of CMWP

5.1 Introduction

In recent years in the UK, the operating lives of nuclear reactors have been extended, resulting in nuclear fuel having an increase in burn-up and time within the reactor. Life extension is the increase of time within the reactor which could be due to improvement in material safety margins whereas increased burn-up is the increase in the enrichment of the fuel which means a longer sustained chain reactor and a longer time in the reactor. This has the potential of impacting the end of life properties of the cladding during post-discharge and storage. Consequently, the investigation of the physical and mechanical property changes is paramount. To investigate physical changes within a material Convolutional Multiple Whole Profile (CMWP), which uses line broadening analysis, is used to determine physical parameters such as crystallite size and dislocation density.

Convolutional Multiple Whole Profile (CMWP) has been used on multiple materials, including Aluminium-Magnesium Alloys and 22SiMn2TiB steel (Fe-0.22C-0.87Si-1.64Mn-0.024Ti-0.0015B-0.0025N wt%), however, the main focus of utilising the technique has been on the Zircaloy-4 (Zr-4) and Zircaloy-2 (Zr-2) systems. The research using CMWP on these materials has focused largely on two types of XRD geometries: synchrotron XRD and a Cu source lab XRD. Data produced from synchrotron XRD (SXRD) have a high intensity and resolution. As a consequence, line broadening caused by dislocations is very distinct. However, the reliability of the assessment of the lab data, on a range of lab XRD machines, using CMWP is yet to be determined.

To validate CMWP on lab XRD, a simple zirconium system of varying deformation was analysed: as-received, heat treated, 30% cold worked, 48% cold worked and 60% cold worked. The technique's ability to 1) calculate the trend in dislocation density with increasing deformation will be investigated and 2) the accuracy of the values calculated will be evaluated. The crystallite size values from CMWP will also be compared to values produced from existing, well established methods. To further assess the capabilities of CMWP, these deformed samples will be tested, using different radiation sourced lab XRD machines: copper (Cu), cobalt (Co) and silver (Ag).

5.2 Methodology

In this section, a quick overview of the methodology will be presented. A detailed explanation of the methodology can be found in Chapter 4.

The foil of zirconium, received from Goodfellows, was sectioned into five strips. One of the strips was left as it was, therefore was labelled as zirconium as-received (Zr-AR). The remaining four strips underwent a heat treatment to a) to ensure the material was all α -zirconium and b) to remove as much deformation damage as possible. One of these strips was then used as a neutral sample and labelled zirconium heat treated (Zr-HT).

The final three strips of the zirconium foil underwent cold rolling, at the University of Manchester, to various degrees of deformation, to be used as analogues for radiation damage. The samples were, as mentioned in Table 4.1 in Chapter 4, cold rolled to 30%, 48% and 60%, which were labelled as Zr-30, Zr-48 and Zr-60 respectively. The samples used for further analysis were taken from the centre of the material, avoiding any cracks, in order to provide a sample representative of the damage produced.

The samples were sectioned into 10 mm x 10 mm blocks, using a Secotom, and prepared, using an automatic grind and polisher, to achieve a surface level finish appropriate for XRD. Following this, the five samples underwent XRD scans, using different X-ray radiation sources (Cu, Co and Ag). A batch programme was created, with scan parameters stated in Table 5.1, to allow for a similar scanning environment for each sample.

Table 5.1: *The scanning parameters of the XRD machines used.*

Parameter	Cu Source (Sheffield)	Cu Source (Manchester)	Co Source (MRF)	Ag Source (Sheffield)
Angle Range/ °	30 - 105	28 - 115	35 - 112	10 - 42
Anti-scatter Slit/ inch	Parallel Plate Collimator	Double-Bounce Monochromator	Double-Bounce Monochromator	0.50
Divergence Slit/ inch				0.25
Beta Filter	None			Rhodium
Soller Slit/ Rads	0.04	None	None	0.04
Primary Mask/ mm	None	5	5	10
Step Size/ °	0.013	0.01	0.01	0.0072
Time per Step/ secs	3.0	11.0	3.0	200.4

To ensure the same range of peaks was analysed for all three radiation sourced XRD machines, PD4+ was used to acquire the Powder Diffraction Files (PDF) of Zr. These were used to obtain the corresponding 2θ ranges for Cu, Co and Ag wavelengths. The equivalent 2θ range for: Ag source XRD was found to be 5 - 35° and Co source XRD was found to be 35 - 111°.

The same pre-scan was done for the Emyrean Ag source experiments to ensure the correct sample orientation, due to cold rolling induced preferential grain orientation. Same as with the X'Pert, all five zirconium sample scans were automated. The scan parameters for the Emyrean are shown in Table 5.1. There was no monochromator for this specific machine therefore a rhodium beta-filter was used, however, there did not seem to be an absorption edge present amongst the diffraction patterns.

The setup for Manchester Cu source XRD and the MRF Co source XRD used an XYZ stage, which meant that due to different sample heights, each sample had to be aligned before being scanned. An alignment procedure used was called the direct beam half cut method. The intensity of the beam was monitored and the height of the sample was adjusted. The height of the sample was continually adjusted until the intensity was halved as this denotes the beam being halved (i.e. the surface of the sample was at the centre of the beam).

There was also a tilt alignment, only for the MRF Co source XRD machine, which had the capability of tilting the sample ensuring that the beam was parallel to the sample surface when

$\theta = 0$. The sample tilt was adjusted until a maximum intensity was found, indicating the beam was parallel to the sample surface. The height and tilt alignments were done iteratively to ensure correct alignment.

Once the data was collected, the data was processed for CMWP and TOPAS. The instrumental profile data was processed so that the data was converted into reciprocal d spacing (k), and the diffraction pattern was split so that each peak was its individual file. The $K\alpha_1$ was centred on zero and the background intensity was removed. So that the CMWP could read the instrumental data files, the files were saved as 'dat' files with the $K\alpha_1$ peak being the file name and there being no file extension in the name (e.g. 30.407). If the instrumental data was noisy, it was fitted using Split PseudoVoigt/Pearson7 or PseudoVoigt/Pearson7 profiles and the calculated pattern would be used as the instrumental profile data. The PseudoVoigt/Pearson7 fitting was only done on the instrumental diffraction data.

The peak index file details the peaks, its plane and the associated phase. A peak index file was created for each sample from each radiation source, using ICSD to help identify peak positions, where the α -zirconium peaks were labelled as phase zero, the delta zirconium hydride peaks were labelled as phase one, the overlapping peaks of the two main phases were labelled phase two and any unknown phases were labelled phase three. The initial fitting parameters were set up within CMWP, which included the wavelength of the incident radiation, the data sampling and limitations parameters, ideal lattice parameters, the background spline and the initial six physical parameters that mainly contribute to the CMWP fitting. The average contrast factor (C_{hkl}) and burgers vector (B) were based on a thesis and a paper that experimentally calculated these values for a cold worked zirconium system, 0.25 and 0.515 respectively, with the premise being that in a cold worked system there will be mainly a dislocation loops [211, 213].

When the initial CMWP fittings were run, the contrast factor physical parameters a_1 and a_2 were producing values that were unrealistic. According to the Dragomir *et al.* contrast factor paper, it suggests that a_2 should not be negative, especially for deformed samples. Therefore, in order to obtain more reasonable values, a_1 and a_2 were fixed to values based on values found in the Dragomir *et al.* paper (2 and 0.5 respectively) so that the other physical parameters are calculated to a more reasonable value range [212]. This was done on the basis of the theory of least square refinement, where if the initial values are not within an appropriate range then an accurate fitting would not occur, therefore, a suitable starting value must be used. The a_1 and a_2 parameters were then freed and the CMWP analysis was run again, allowing for a more valid fitting. Once a reasonable fit had been obtained, the background spline was adjusted using the 'MK Spline 2' function, in order to provide a better fitting. The 'MK Spline 2' function allows a user to adjust the background spline and see how that affects the previous fitting, however, too much manipulation of the background spline would either over influence the fitting and provide misrepresented results or cause further fitting issues (i.e. inaccurate fittings).

The analysis was iteratively run until there were minimal changes in the physical parameter values. If the errors were large ($\geq 20\%$), then initial parameters and background spline were adjusted in an attempt to reduce them. It was also possible that if the dislocation density (ρ or d) was very large (larger than expected) or was reaching its upper limit whilst the dislocation arrangement parameter (M^* or e) was very small or reaching its lower limit, then the outer cutoff radius (R_e) needed to be adjusted. This is because R_e can get too small and needs to be increased by introducing a larger limiting factor, R_c . Jones concluded that a very large ' d ' and very small ' e ' affects the quality of fit due to R_e approaching atomic distances or smaller causing the strain profile function to breakdown and become inaccurate [211]. Once a final run

was completed, the dislocation density, dislocation arrangement, crystallite size and crystallite size distribution parameters were extracted from the output file and compared between samples and radiation sources.

For comparison with more standard diffraction analysis - a TOPAS refinement was carried out. To determine suitable instrument parameters, refinement of NIST standard material was carried out for the instrumental setup. This allows the separation of the instrumental and sample broadening terms, yielding a more accurate value for micro-strain and crystallite size in the sample. Using the NIST standard documentation (Certification of Standard Reference Material 660c) the lattice parameters, crystallite size and microstrain were inputted for the LaB_6 and fixed. Therefore, when fitting the LaB_6 diffraction pattern, the only refining parameters were the peak shape and broadening effect associated with the peak type (PVII) constants. The refining process was continued until the difference between the measured and calculated pattern was minimal, which was determined graphically and via a goodness of fit (GOF) value.

Once the instrumental parameters were defined, diffraction data from the zirconium samples underwent TOPAS analysis using the peak type constants as non-refining parameters (i.e. instrumental parameters). The lattice parameters, the crystallite size and the microstrain were all refined. With TOPAS, the crystallite size and the microstrain can not use the same type of refining profile (Gaussian or Lorentzian) otherwise a calculated pattern cannot be produced as the two profiles refine against each other. The correct assignment of a Gaussian and Lorentzian profile for the crystallite size and microstrain was determined through trial and error, where, for the copper radiation source data, all samples were analysed using both variations of profiles for each peak broadening parameter. It was found that using Lorentzian for crystallite size and Gaussian for microstrain produced practically the same values for both parameters for Zr-30, Zr-48 and Zr-60. Hence, for all proceeding TOPAS analysis, a Gaussian profile was used for crystallite size and a Lorentzian profile was used for the microstrain. The number of iterations of analysis was determined by using convergence criteria - where the change in the measured and calculated pattern was minimised. This was corroborated by the NIST standard documentation which used a Lorentzian profile for microstrain and a Gaussian profile for crystallite size as well.

A direct comparison between CMWP and TOPAS was only possible between the crystallite size parameters. TOPAS uses a simplified model where it only determines the crystallite size (i.e. using the Scherrer equation) whereas CMWP uses crystallite size and crystallite size distribution as the contributing factors to the size profile. As stated previously, CMWP uses a log-normal distribution to calculate the mean crystallite size and distribution. Concerning the strain profile calculated by CMWP, there is no direct comparison to TOPAS, as the software determines the physical parameters which are the components of the strain profile whereas TOPAS only ascertains microstrain values.

Line dislocation density calculations, via TEM image analysis, were attempted on a Zr-HT sample to provide a comparison for CMWP dislocation density results. A Smith-Guttman line intercept method was used, as described in Section 2.4.1, where a grid was placed on top of the three TEM bright-field images and the number of intercepts was counted. The grid placed on the TEM images is shown in Figure 5.1. As it was not possible to obtain a sample thickness via EELS, an average sample thickness was obtained from the literature [142, 214]. It has been assumed that the sample thickness will be a close approximation and therefore the dislocation density values will not be far off their real values. The total line length was determined by using the scale bar to calculate the length with respect to the micrographs (i.e. 3 cm measured length = 500 nm distance within the micrograph). The values for the Smith-Guttman line intercept

method are shown in Table 5.2. As the three images show significant differences in deformation, as can be seen in Figure 5.1, the line dislocation line density was calculated for each and then averaged.

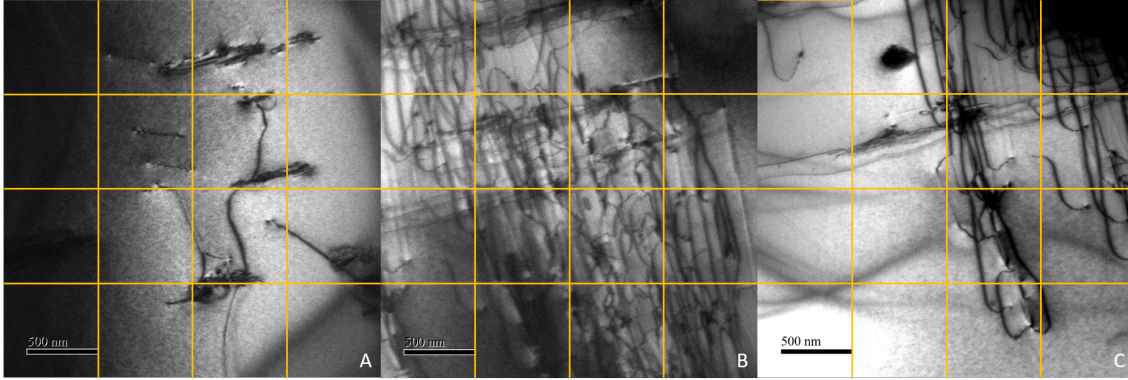


Figure 5.1: The grid placed on TEM images of Zr-HT (from three different locations) to obtain the number of interception points to calculate line dislocation density. The images were taken on a JOEL JEM F200 with a 200 keV electron beam.

Table 5.2: A table showing the Smith-Guttman line intercept values obtained from analysing the TEM micrographs of Zr-HT and literature.

Image	Number of Intercepts (N)	Total Line Length (l)	Sample Thickness (t)
A	36		
B	120	$143100 \times 10^{-9} \text{ m}$	$135 \times 10^{-9} \text{ m}$
C	55		

The sample preparation for BSE/EDX was the same as for XRD - detailed in Section 4. The BSE/EDX images were obtained from the Inspect F50 in Sheffield, using a spot size of 2.5 and energy of 20 keV and 10 keV (for BSE and EDX respectively). The EBSD imagery was taken on a Tescan in Manchester and the analysis was carried out using the Aztec software. The TEM images were taken on a JOEL JEM F200 at the University of Sheffield and the analysis was done manually.

5.3 Results and Discussion

5.3.1 Sample Confirmation/Verification

The Zr samples were expected to be single phase, however, from the diffraction pattern there can be seen two distinct phases. Figure 5.2, showing the Zr-AR-Cu (Manchester) diffraction data with, what is believed to be, the peak positions for the two phases within the material: α -Zr and the unknown phase. From this, there can be seen some asymmetry with the peak at approximately 32° . This is believed to be due to the overlapping of two peaks, the (100) from Zr and the secondary phase, which is indicated by the first green and yellow markers. There are also overlapping peaks at approximately 37° , 65° and 68° .

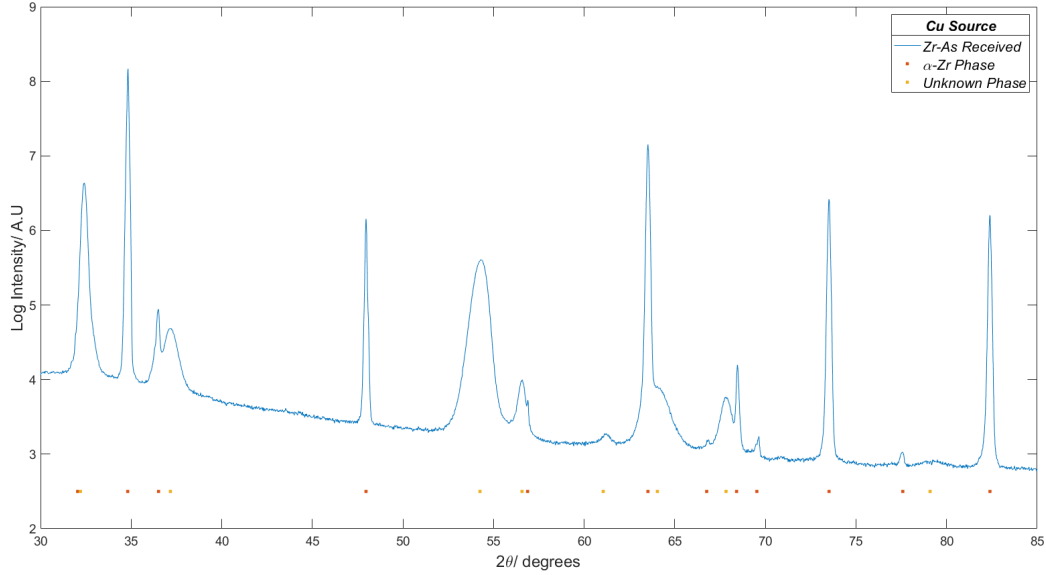


Figure 5.2: *The identification of the peak positions of α -zirconium phase and unknown phases.*

To try and identify the secondary phase in the material, back-scattered electron (BSE) and energy-dispersive X-ray (EDX) analysis were initially conducted on the sample, shown in Figure 5.3. From the BSE image on the left, there can be seen some contrast differences in various features such as the light grey strip at the top left, dark grey regions surrounded by a lighter grey boundary (non-uniform region), the black cavity features and the dark grey matrix. The light grey strip (showing a significant contrast difference to the bulk), shows no concentration of other elements making it compositionally not significant but could be due to sample surface imperfections. Usually, with BSE images, a contrast signifies a difference in elements, as explained in Section 3.2, however, it can also indicate grain orientation, which may be the case in this scenario. Looking at the EDX maps on the right of Figure 5.3, all perceived present elements, are evenly distributed throughout the scanned area. The elements are evenly distributed and not concentrated on any of the microstructural features that are shown on the BSE image, therefore, was believed to be statistically insignificant. The determination of light elements before sodium (Na) is not very reliable via EDX analysis, therefore, the quantification of boron, carbon and oxygen is likely to be inaccurate [215]. There was some concentration of iron and oxygen at the non-uniform region and cavity, however, that was not replicated across similar microstructural features and, therefore, deemed to be insignificant.

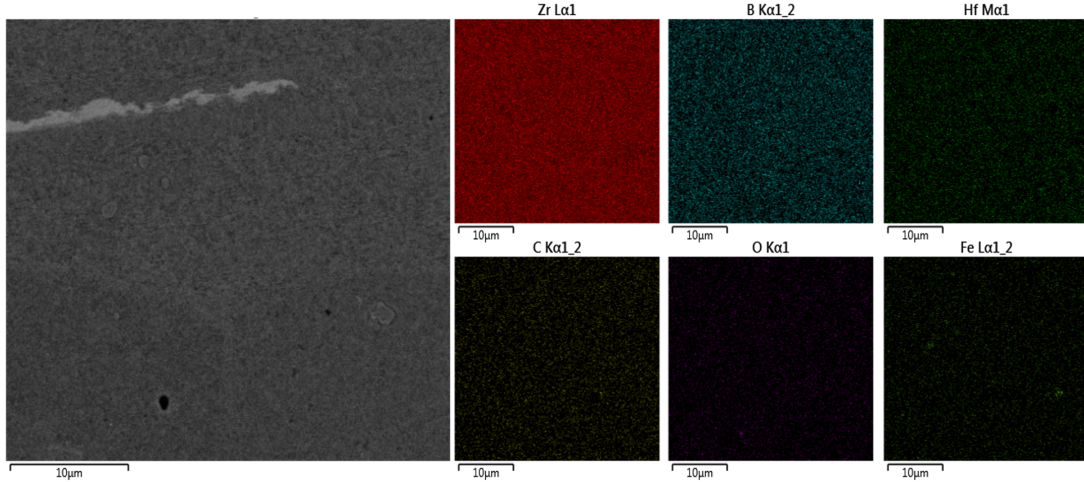


Figure 5.3: A BSE image and the resultant EDX results for Zr-HT show the even distribution of all elements that were determined by the instrumentation.

Initial XRF results from Goodfellows, presented in Table 5.3, show that the material appears to be pure zirconium, with the common impurities of hafnium (Hf), nitrogen (N), oxygen (O) and hydrogen (H) being relatively low. The iron-chromium (FeCr) and carbon (C) were assumed to be from the sample holder and not from the sample itself. The zirconium foil was determined to be pure according to ASTM 551/551M - 12 [216].

Table 5.3: XRF results from Goodfellows.

Element	Weight Percent / wt. %		
	Top	Middle	Bottom
Zr + Hf	≥ 99.2	≥ 99.2	≥ 99.2
Hf	1.0	1.0	1.0
FeCr	0.1	0.1	0.1
C	0.01	0.02	0.02
N	0.005	0.005	0.004
O	0.14	0.13	0.13
H	0.0004	< 0.0003	< 0.0003

However, the XRD results did not corroborate the Goodfellows' results, which showed a prominent secondary phase, therefore a secondary XRF analysis was conducted at The University of Manchester. The University of Manchester XRF results, in Table 5.4, indicated a less pure zirconium than initially thought with a possible calcium (Ca) impurity with a weight percentage of ~2%.

Table 5.4: XRF results from University of Manchester.

Element	Weight Percent / wt. %
Zr	96.66
Hf	1.045
Ca	2.031
Cr	0.040
Fe	0.225

Both the XRF results were taken on a bench-top machine and calibrated based on the dimensions

and density of the sample and not against standards, therefore, there was room for inaccuracies with the output data. From previous XRD data, no Ca has been observed, contradicting the results shown in Table 5.4. As stated in Section 3.4, there is a possibility of overlapping characteristic fluorescence energy levels from different elements, therefore, could lead to misleading results if not calibrated with the element standards. Hence a tertiary elemental analysis was also carried out via Inductively Coupled Plasma Optical Emission spectroscopy (ICP-OES) for base metal elements and Thermoconductivity & IR Absorption for nitrogen, oxygen and hydrogen. The Sheffield Assay Office conducted both ICP-OES and Thermoconductivity & IR Absorption following the standards ATM150 and ATM149 respectively [217].

Table 5.5: *ICP-OES and HVE composition results via the Sheffield Assay Office.*

Element	Weight Percent/ wt.%
Zr	98.7
Hf	0.88
H	0.0016
O	0.302
Fe	0.082
Ti	< 0.005
Zn	< 0.005
Ni	< 0.005
Cu	< 0.005

The chemical elemental analysis, from the Sheffield Assay Office, is presented in Table 5.5. The results semi-corroborate the XRF analysis from Goodfellows, indicating a relatively high purity of zirconium (98 wt.%). The main differences are the impurities found, which included titanium (Ti), zinc (Zn), nickel (Ni) and copper (Cu), however, these impurities add up to less than 0.02 wt.%. Also, it suggests that there is, compared to Goodfellows, approximately four times larger H content, at 0.0016 wt.%. The errors in each XRF measurements were not known

The Sheffield Assay Office determined the H content of the sample to be 0.0016 wt.% which is equal to 16 ppm. Initially, with this very low hydrogen content in these samples, the phase was not believed to be δ -zirconium hydride as the relative intensities of the secondary phase compared to the Zr peaks suggest a very large quantity of this phase. However, comparing the XRD patterns of these samples to other Zr/Zircaloy samples that have been hydrogen charged, such as Zr-4 samples in the following results chapter (Section 7) which have H content of 30+ ppm, the peak positions line up.

The secondary phase identification was conducted using the Powder Diffraction File software (PDF-4+/PDF-5+); Fachinformationszentrum Karlsruhe (ICSD), National Institute of Standards and Technology (NIST) as well as other material phase databases were used. The compounds/elements, determined from the elemental analysis, were used for the basis of the phase identification.

Initially, with the low level of impurities and H content, it was thought that the secondary phase could possibly come from hafnium as that had the highest weight percent. However, as can be seen from the diffraction pattern overlay in Figure 5.4, neither the pure HCP hafnium phase nor the tetragonal hafnium oxide phase fits the measured diffraction pattern.

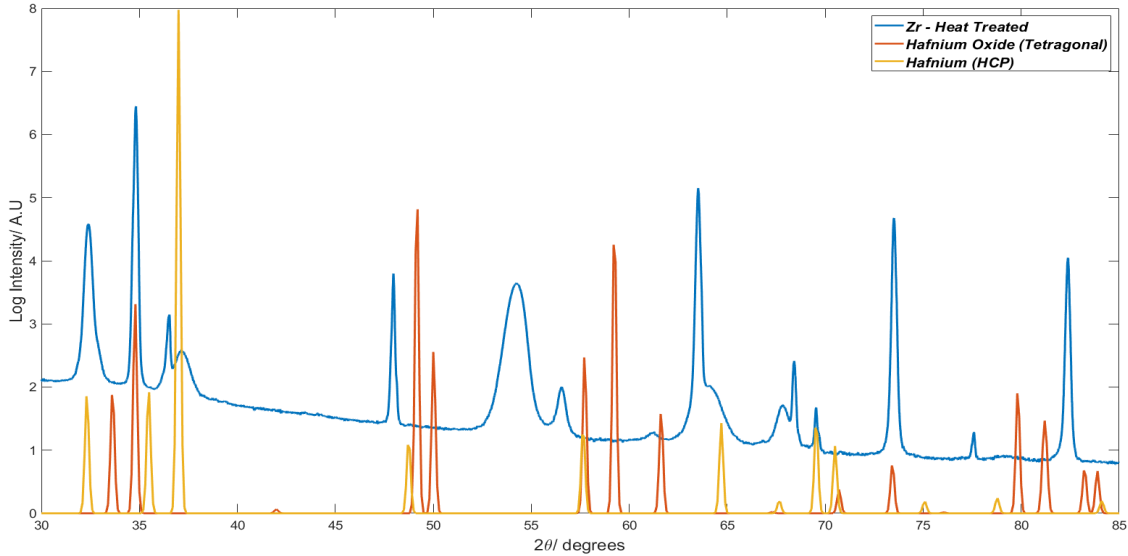


Figure 5.4: An overlay of Zr-HT-M and diffraction patterns of possible secondary phases.

Following this, the next suspects were: calcium oxide, delta zirconium hydride and beta zirconium. The Fe and Cr impurities, though minimal, could reduce the phase transformation temperature from alpha to beta zirconium, making it possible for the beta zirconium to form under the heat treatment conditions [35]. However, as can be seen in Figure 5.5, beta zirconium does not fit any of the secondary phase peaks. It was also believed that the Fe and Cr detected in the Manchester XRF results were from the crucible as the Fe detected from the ICP-OES analysis was significantly lower. Fe fractions this low would not be expected to significantly affect the transformation temperature.

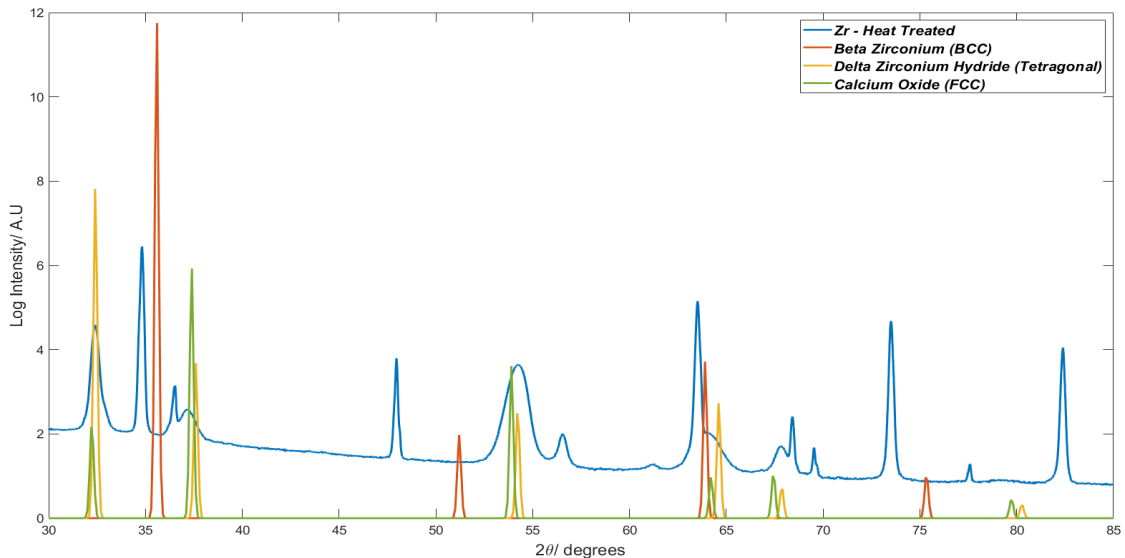


Figure 5.5: An overlay of Zr-HT-M and diffraction patterns of possible secondary phases.

As calcium was found in the UoM XRF results, calcium and/or its compounds were tested through the PDF-4/5+ system and calcium oxide was the closest to the peak positions. Initially, the Ca was thought to be a surface impurity from the material preparation and/or storage stage,

which may explain why calcium was not found in other elemental analyses. Though close, the majority of the peaks did not line up which led to the conclusion that the secondary phase had very similar lattice parameters and was an FCC structure ($Fm\bar{3}m$). From the BSE images and the elemental analysis, the remaining option was an FCC zirconium phase. Currently, there are some theories, from Qing Jiang *et al.* and Boran Tao *et al.*, of a fatigue-induced FCC zirconium phase or said FCC phase forming during the cooling and ageing of the zirconium/zircaloy respectively [218, 219]. These practically observed FCC zirconium phases, via TEM, are in the early stages of research, therefore with the little data to corroborate it, these phases are unlikely to be present.

However, even with the low weight percent of hydrogen in the sample, δ -zirconium hydride was the more likely candidate for the secondary phase. There are two peaks at approximately 36° and 64° (110 and 211 peaks respectively) that don't quite match the measured diffraction pattern, however, the majority of the peaks line up with the peak positions as seen in Figure 5.5 as well as aligning well with delta zirconium hydride diffraction found in the literature (Figure 2.5 [26]). This was then corroborated using the SE images from the electropolished Zr-HT samples, an example shown in Figure 5.6, which shows the absence of needle-like structures. It is believed that the multiple electropolishing stage removed the delta hydrides from the surface. These needle-like structures, as shown in the literature, resemble delta hydride morphology formed in zirconium and zirconium alloys [220]. These needle-like structures were not observed during SE/BSE analysis of samples that were prepared as stated in Table 4.2 on page 47.

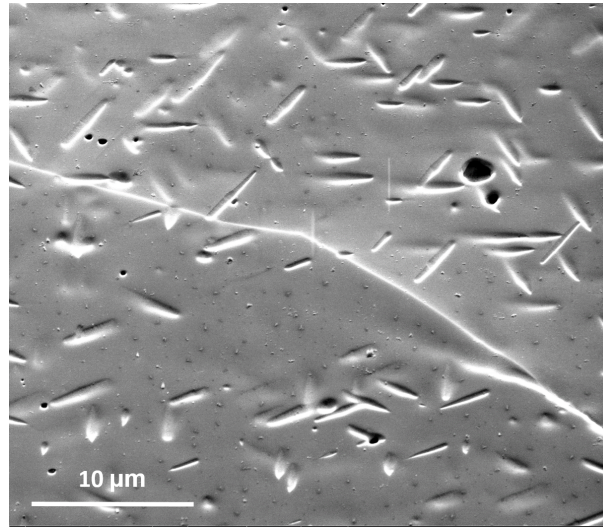


Figure 5.6: An SE image of a Zr-HT sample, after electropolishing, which revealed needle-like structures.

Furthermore, the diffraction pattern of Zr-AR-M was compared to a diffraction pattern from a Zr-4 hydrogen charged sample with a known hydrogen content of 34.7 wt.ppm (sample discussed in detail in Section 7). The two datasets were taken on different diffraction optics, therefore, to allow for comparison, the background was stripped and the data was normalised. A close-up of the diffraction pattern comparison is shown in Figure 5.7. The hydride peaks are indicated with '*hkl*s' above them. The comparison shows that the hydride peaks in Zr-AR-M are significantly larger than in the Zr80CW-RT sample with 34.7 wt.ppm hydrogen content. This could suggest that, as there is known to be less than 34.7 wt.ppm (hydrogen content = 16 wt.ppm), there is a significant texture or size difference in the hydrides present. The SE image in Figure 5.6 indicates a relative random orientation of the needle-like structure, therefore, the texture of the material

could be the significant factor, especially where Zr-AR-M is recrystallised and the Zr-4 sample has been cold rolled to 80%, which would affect relative intensities of the peak. As texture is believed to be the main contributor, future work would be required to determine whether these hydrides are surface contaminations that are introduced from sample preparation. The effect on the hydride peaks when conducting a lab XRD scan of an uncut sample or a bulk scan via Synchrotron XRD (sXRD), would ascertain whether they are surface level contaminations.

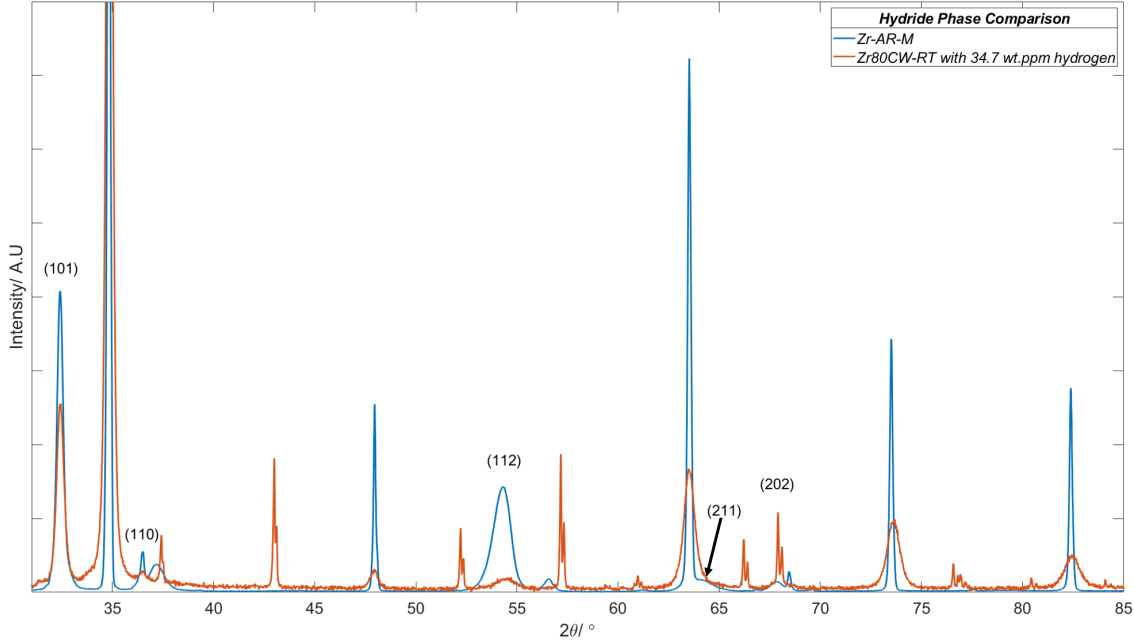


Figure 5.7: A comparison of diffraction patterns between Zr-AR-M and Zr80CW-RT, a sample with known hydrogen content, to gauge the significance of the hydrogen content within Zr-AR-M.

As stated previously, the secondary phase is assumed to be an FCC structure, however, delta hydride has two forms: $ZrH_{1.6}$, the delta hydride formed under equilibrium, which is a cubic structure (space group = $Fm\bar{3}m$) and ZrH_2 , the delta hydride formed under non-equilibrium conditions, which is a tetragonal crystal structure (space group = $I4/mmm$) [221]. The difference between the cubic and tetragonal crystal structure is a lattice distortion, which causes the relationship between lattice parameters to be $a = b \neq c$. In an ideal system, the correlation between the cubic and tetragonal lattice parameters is shown in Equation 5.1 and in an ideal scenario, where there is no lattice distortion, X_{LD} in Equation 5.2 would be 1.

$$\frac{\sqrt{2}}{2} a_{\text{cubic}} = a_{\text{tetragonal}} \quad (5.1)$$

$$a_{\text{cubic}} = c_{\text{cubic}} = X_{LD} c_{\text{tetragonal}}$$

$$\frac{\left(\frac{a_{\text{tetragonal}}}{\sqrt{2}/2}\right)}{c_{\text{tetragonal}}} = X_{LD} \quad (5.2)$$

The data was fit using TOPAS to determine the level of lattice distortion in the delta hydride phase. Using a Le Bail fit with the α -Zr and ZrH_2 phases, and the ‘goodness’ of fit is shown in Figure 5.8. The lattice parameters calculated from this fit are: $a_{\text{tetragonal}} = 3.40$ nm and

$c_{tetragonal} = 4.73$ nm. Using Equation 5.2, X_{LD} was calculated to be 1.02. This shows that there is a small amount of lattice distortion, as there is a 0.02 deviation from 1, thus explaining why the secondary phase fitting was close to an FCC structure but worked with the ZrH_2 tetragonal phase. Comparatively, in an ideal system (i.e. using the CIF files), where $a_{tetragonal} = 3.509$ nm and $c_{tetragonal} = 4.448$ nm, X_{LD} was calculated to be 1.12. Thus, showing a much larger distortion. An additional observation is that the delta hydride peaks are very broad and do not change with the increase in deformation (Zr-HT to Zr-60), which suggests that either the delta hydrides are very small and evenly distributed or that they are highly deformed.

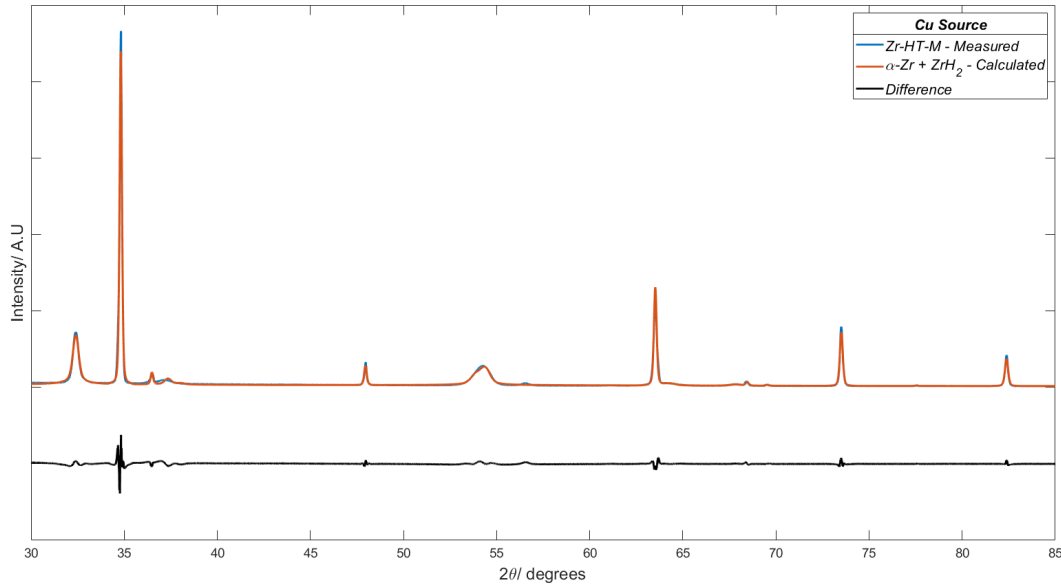


Figure 5.8: A Le Bail TOPAS fit of Zr-HT-Cu (Manchester), using α -Zr and ZrH_2 , showing qualitatively the goodness of fit.

A set of EBSD images was taken to 1) prove the increased deformation due to cold rolling, 2) attempt an investigation into the secondary phase, and 3) provide a comparative measure of crystallite size analysis as grains were difficult to distinguish in BSE SEM images. An initial set of high magnification EBSD images were taken for Zr-HT, Zr-30 and Zr-48, to primarily to investigate the secondary phase. However, the deformation and higher strain within the Zr-30 and Zr-48 meant that a proper EBSD map was not possible. Figure 5.9 shows a high magnification map of Zr-48. Though the misorientation, caused by the cold rolling deformation, can be seen within the grains indicated by the colour gradient, a large proportion of the image is filled with blank space, which represents the non-indexed areas. The large number of dislocations from deformation distorts the crystal structure, making it difficult to distinguish, giving rise to non-indexed regions.

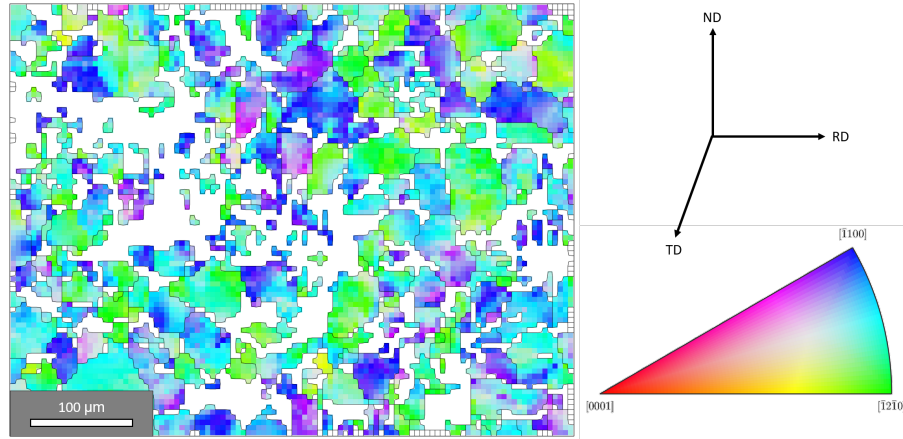


Figure 5.9: A high magnification EBSD map of Zr-48 showing the difficulties with indexing due to the high deformation and strain within the material. EBSD map taken in the ND-TD direction. The upper and lower misorientation angle thresholds were set to 10° and 3° respectively.

To overcome this issue and increase the chance of indexing on the deformed samples, a much longer scan time was run on a low magnification. Due to the high deformation within Zr-48 and Zr-60, the indexing of the samples was extremely poor and with the increased map size and scan time, only Zr-HT and Zr-30 were imaged - these EBSD maps are shown in Figure 5.10 and Figure 5.11 respectively. In Figure 5.10, there can be seen a relatively uniform equiaxed grain structure which is indicative of a recrystallised α -zirconium microstructure, corroborated by Long *et al.* (Figure 2.6) as shown in Section 2.2. This is also shown via the solid colours of each grain which indicates little to no strain within each grain. This is corroborated by the Kernel Average Misorientation (KAM) map, a quantifiable measure of local grain misorientation, which showed the lack of misorientation lines (red lines). This is shown in Figure 5.12a.

There were some discrepancies in the indexing between each of the stitched frames, however, they are believed to negligibly affect further analysis. Referencing the IPF key at the bottom of the figure, the colour gradient suggests there is very little number of grains with the basal (0001) orientation but a more even spread of grains in the remaining prismatic and pyramidal planes. The further qualitative analysis of the EBSD map of Zr-HT shows that there is no visual indication of the secondary phase, however, this could be due to two reasons: first being that they are on the nano-scale which would not be detected on the scale of map that was produced or that as EBSD is a surface level technique, the final bulk electropolishing step could have removed the ZrH_2 from the surface.

Figure 5.11, which represents the EBSD map of Zr-30, shows an elongation of the grains (left to right of image) indicating the mechanical deformation of the grains. This is confirmed by the colour gradients within the grain, showing the micro-strain and grain misorientation caused by the cold rolling. This is corroborated by the vast amount of misorientation lines shown in the KAM map presented in Figure 5.12b. There still can be seen some white regions within the map but with the longer scan time the number of non-indexed regions was significantly reduced. As with the Zr-HT EBSD map, there were some discrepancies in the indexing between each of the stitched frames, however, they are believed to negligibly affect further analysis. On visual investigation of the Zr-30 EBSD map, some small regions within the grains could suggest the secondary phase. However, on closer inspection, those small inner-grain areas were determined to be non-indexed regions. As with the Zr-HT EBSD map, there was no clear indication of a

secondary phase.

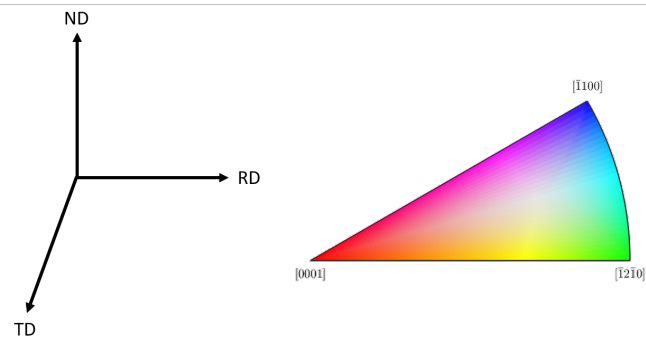
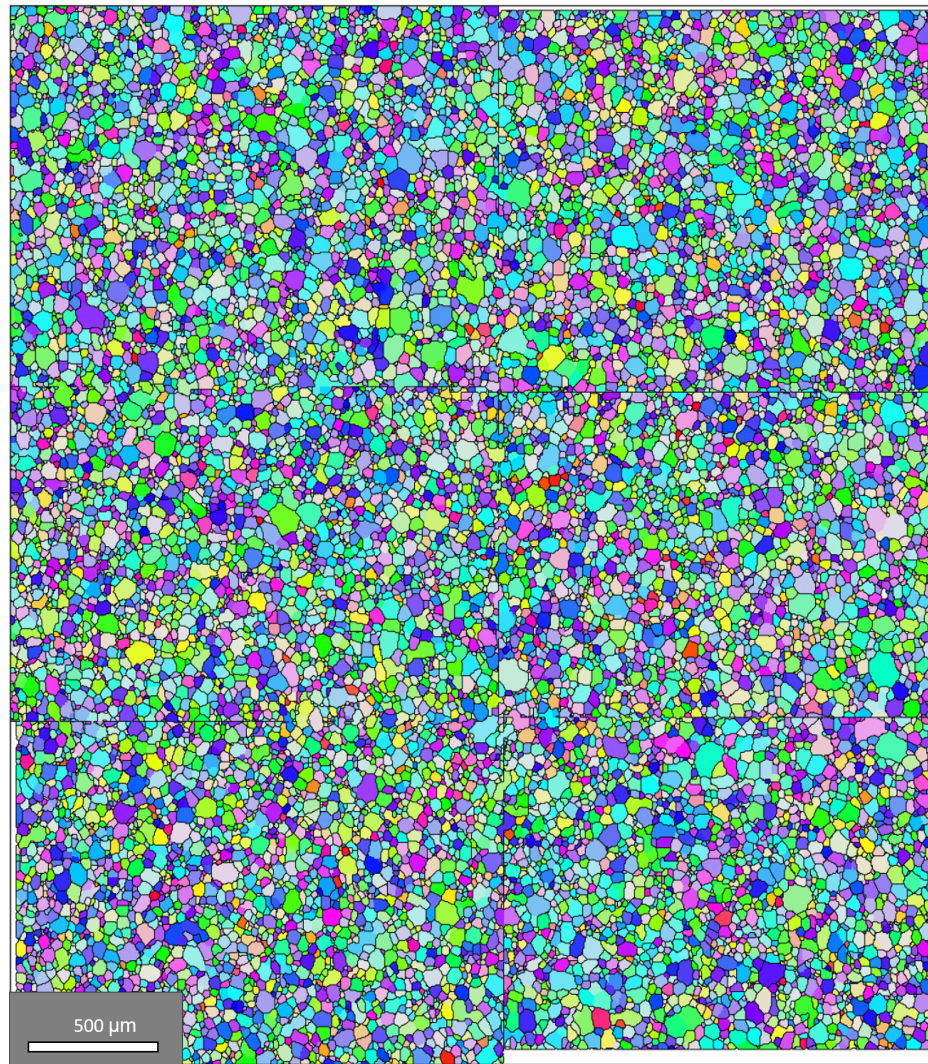


Figure 5.10: EBSD Map of Zr-HT to show alpha zirconium and grain orientation. EBSD map taken in the ND-TD direction. The upper and lower misorientation angle thresholds were set to 10° and 3° respectively.

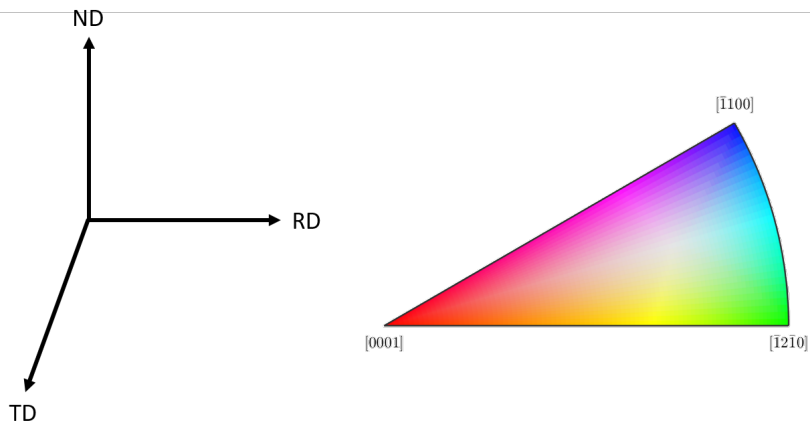
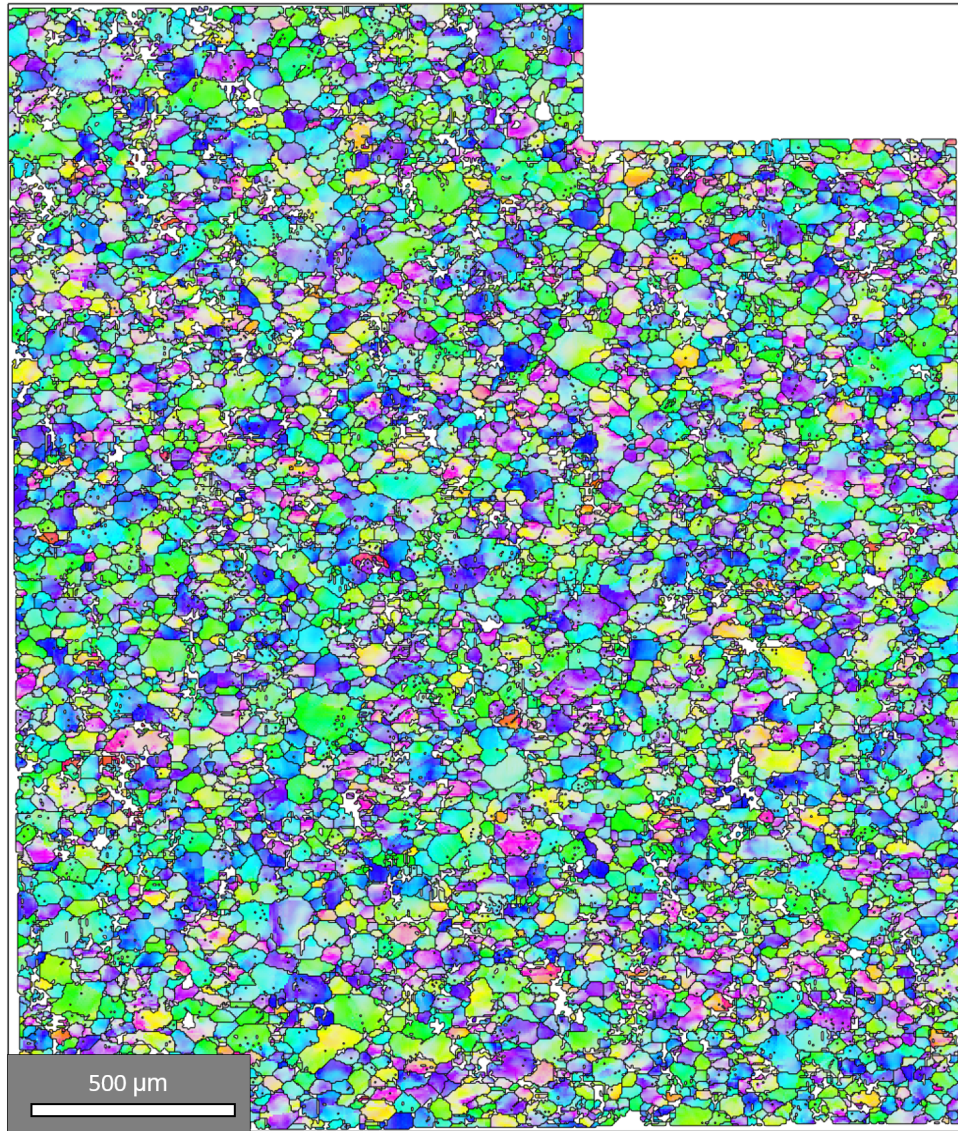


Figure 5.11: EBSD Map of Zr-30 to show grain misorientation and preferential grain orientation. EBSD map taken in the ND-TD direction. The upper and lower misorientation angle thresholds were set to 10° and 3° respectively.

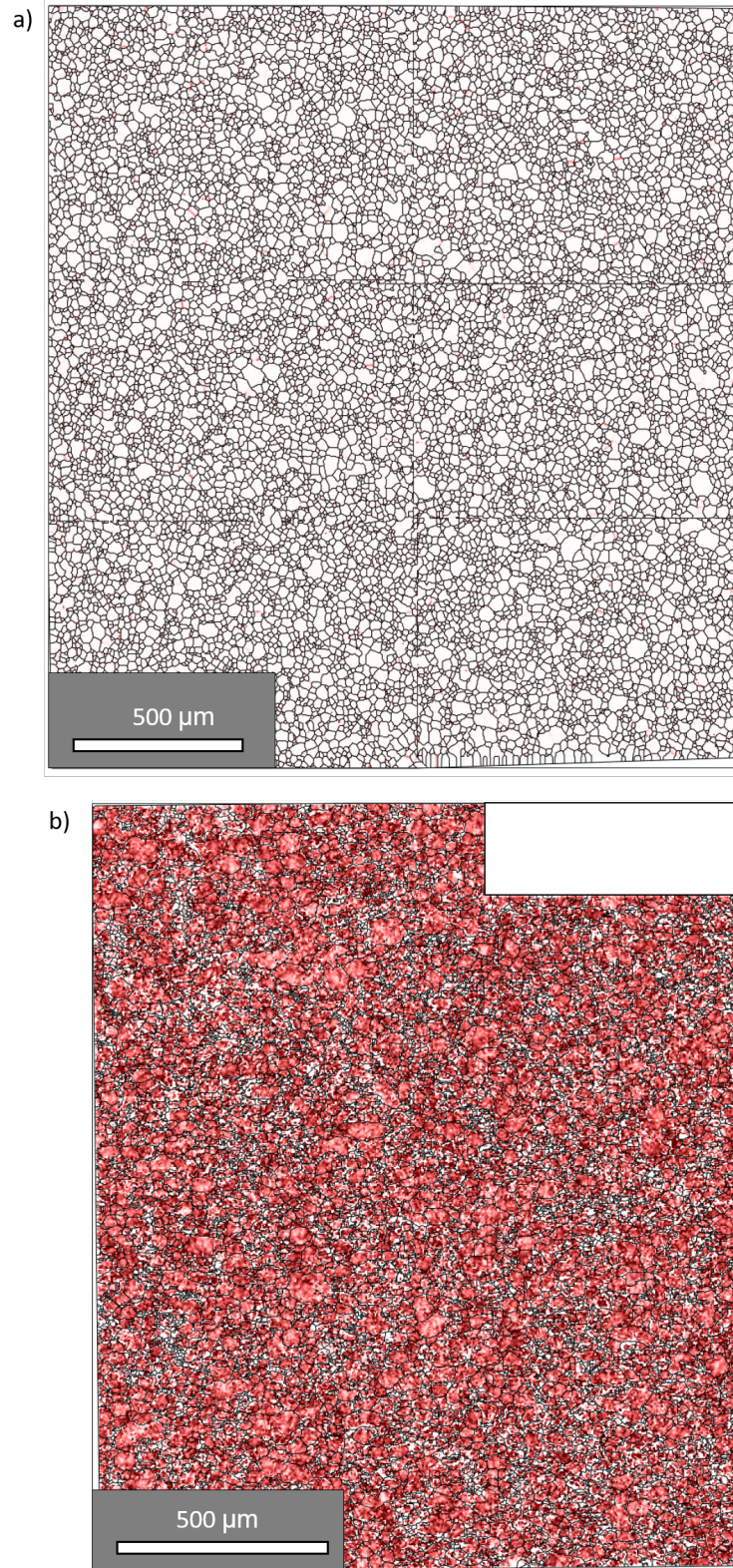


Figure 5.12: The misorientation in the material represented by KAM maps for: a) Zr-HT and b) Zr-30. The misorientation angle threshold was set to 2.5° .

5.3.2 Qualitative Comparison of Different XRD Radiation Sources

As determined from Section 5.3.1, it is assumed that the secondary phase is the tetragonal ZrH_2 phase, which was used throughout the following XRD analysis. Using the peak index of α -Zr and ZrH_2 , as shown in Table 5.6, the peaks in the Zr-AR sample from the Manchester Cu source XRD were identified. This is shown in Figure 5.13. The first peak at approximately 32° , due to the large overlap of the primary peaks of both α -Zr and ZrH_2 , was input as a tertiary phase when undergoing CMWP analysis and, therefore, fitted separately.

As indicated by the two crosses, two peaks do not match with the peak index of α -Zr and ZrH_2 ; both peaks at approximately 56° and 61° were input as a quaternary phase when undergoing CMWP analysis and fitted separately.

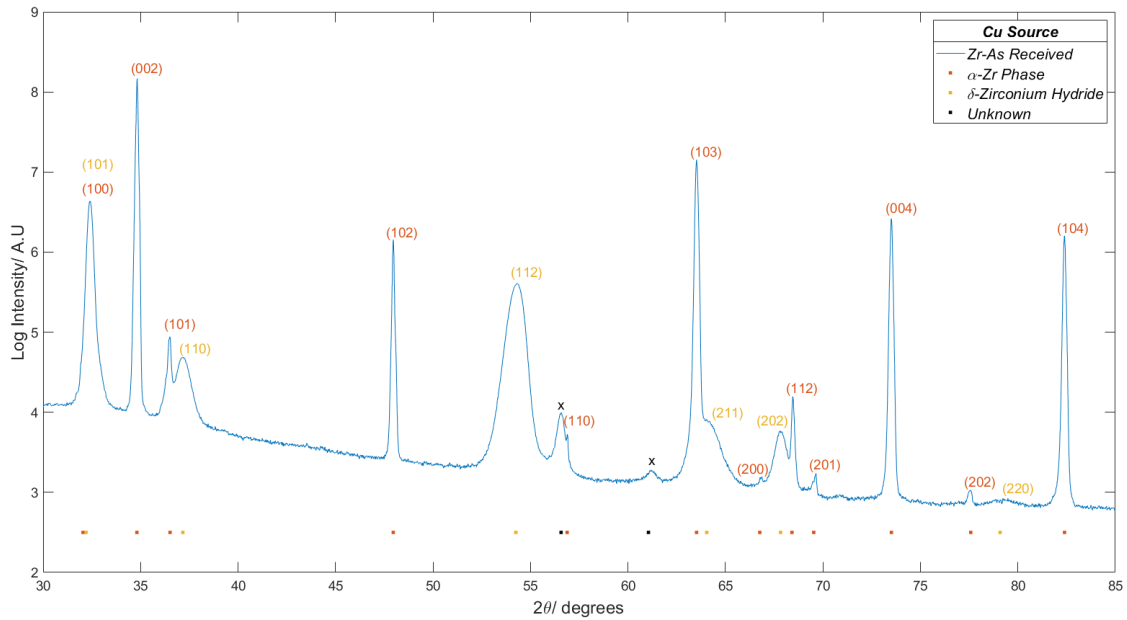


Figure 5.13: A diffraction pattern of Zr-AR taken from the Manchester Cu source XRD machine, with its peak indexing of α -zirconium phase and delta zirconium hydride.

Table 5.6: The peak index for both alpha zirconium and delta zirconium hydride for a Cu radiation source.

α -Zirconium				δ - ZrH_2			
<i>hkl</i>	2θ	<i>hkl</i>	2θ	<i>hkl</i>	2θ	<i>hkl</i>	2θ
1 0 0	31.85	2 0 0	66.56	1 0 1	32.40	2 0 2	67.84
0 0 2	35.60	1 1 2	68.24	1 1 0	36.06	1 0 3	68.62
1 0 1	36.39	2 0 1	69.30	0 0 2	40.51	2 2 0	76.50
1 0 2	47.70	0 0 4	73.18	2 0 0	51.91	3 0 1	85.52
1 1 0	56.74	2 0 2	77.28	1 1 2	55.34		
1 0 3	63.27	1 0 4	82.02	2 1 1	62.53		

5.3.2.1 Cu Source

The diffraction patterns from the double bounce monochromated Cu source diffractometer in Manchester is presented in Figure 5.14, showing the comparison between the varying mechanically

damaged Zr samples. Qualitatively, there seems to be no significant difference between the as-received and the heated treated diffraction patterns, which may indicate that the material was recrystallised by the supplier, once manufactured and processed. Additionally, as the mechanical damage increased, there is an indication of peak broadening, with the 60% cold worked zirconium sample exhibiting the most broad peaks.

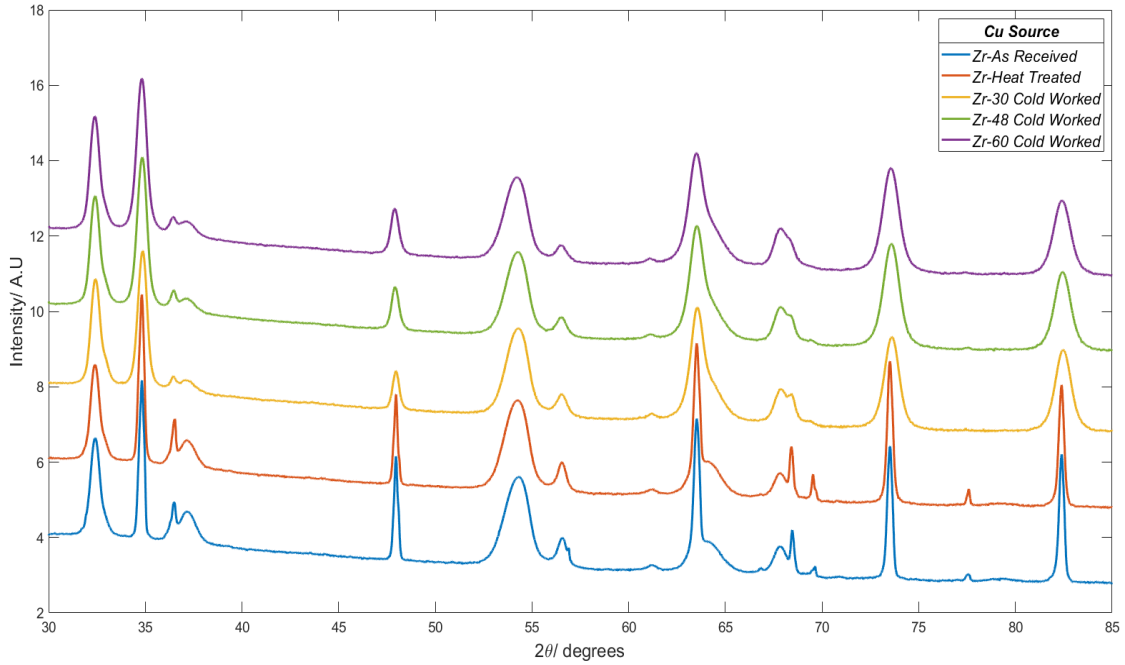


Figure 5.14: A comparison of monochromated Cu source (Manchester) XRD results for Zr samples.

This is observed clearly, in Figure 5.15, in the zirconium peak at 45° and the cluster of zirconium and ZrH_2 peaks between $60 - 70^\circ$. The peak broadening can be observed more clearly in Figure 5.15, where the (102) and (103) are magnified. From the close-up of the (102) peak, it can be seen that the Zr-HT sample is slightly narrower, with a lower intensity than the Zr-AR sample, however, when looking at the magnified (103) peak, it can be seen they are fairly similar. The peak broadening of the zirconium (103) peak is severe, even with the 30% CW sample, such that there is overlapping of the α -zirconium and δ zirconium hydride peaks. The overlapping becomes more significant as the cold working increases.

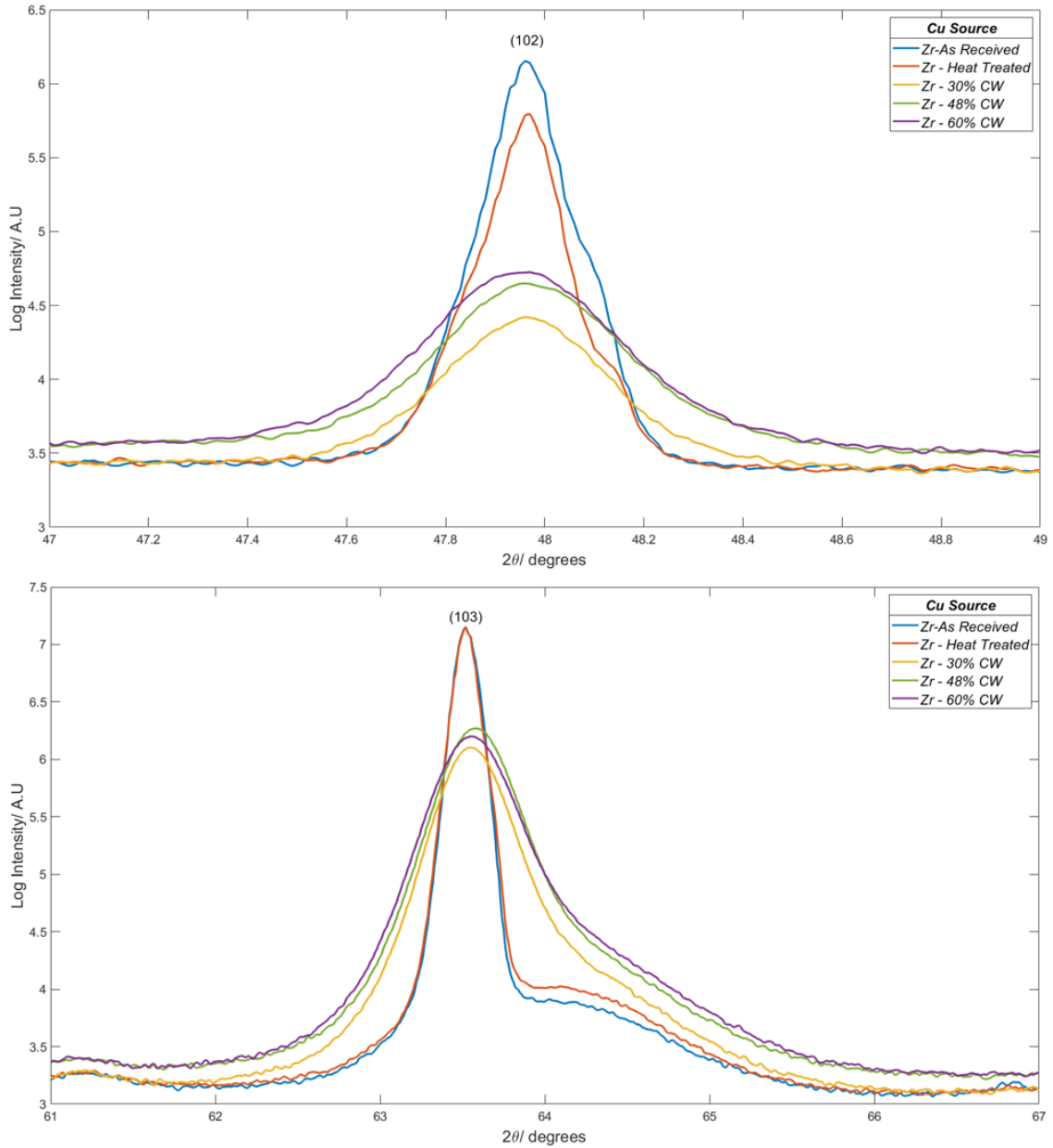


Figure 5.15: A magnification of peaks at approximately 45° and 64° to show the peak broadening effect caused by the increase in mechanical deformation from heat treated to 60% cold worked samples.

5.3.2.2 Co Source

The stacked diffraction patterns for the cobalt radiation source diffractometer are shown in Figure 5.16. As stated previously, the general trend in the diffraction patterns is that as the mechanical damage increases the peak broaden increases due to strain broadening. Also, same as with the copper source XRD where the radiation is double bounce monochromated, which means that both $K\alpha_1$ and $K\beta$ are removed via a physical barrier instead of a filter, there are no absorption edges to be concerned about. Furthermore, there is no major difference between as-received and heat treated samples, which is the same as the Cu and Ag source data, thus

indicating that there is no qualitative difference in the trend between samples diffraction patterns between different radiation sourced diffractometers. This does not imply that there is no quantitative difference between the radiation sources.

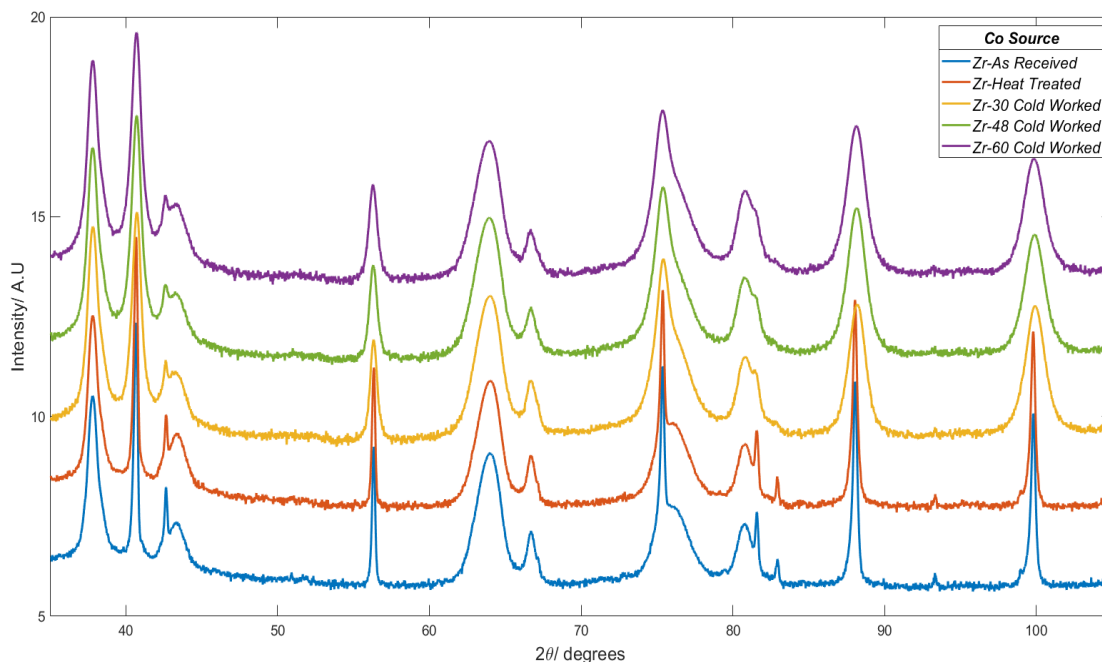


Figure 5.16: A comparison of monochromated Co source XRD results for Zr samples.

5.3.2.3 Ag Source

Figure 5.17 shows the comparison of the same samples above but from the Ag source diffractometer in Sheffield. As observed in the Cu source data, there is relatively little change between the as-received and heat treated samples, and there does seem to be an increase in peak broadening as the severity of the cold work increased. There can also be seen a big step change between 15° - 16° , which is present only in the Ag source data; the data was run on two separate occasions and the step change was still present at the same angle. At first, it was thought to be the sample but the step change was still present at the same angle. Therefore, currently, the origin of this step size is unknown.

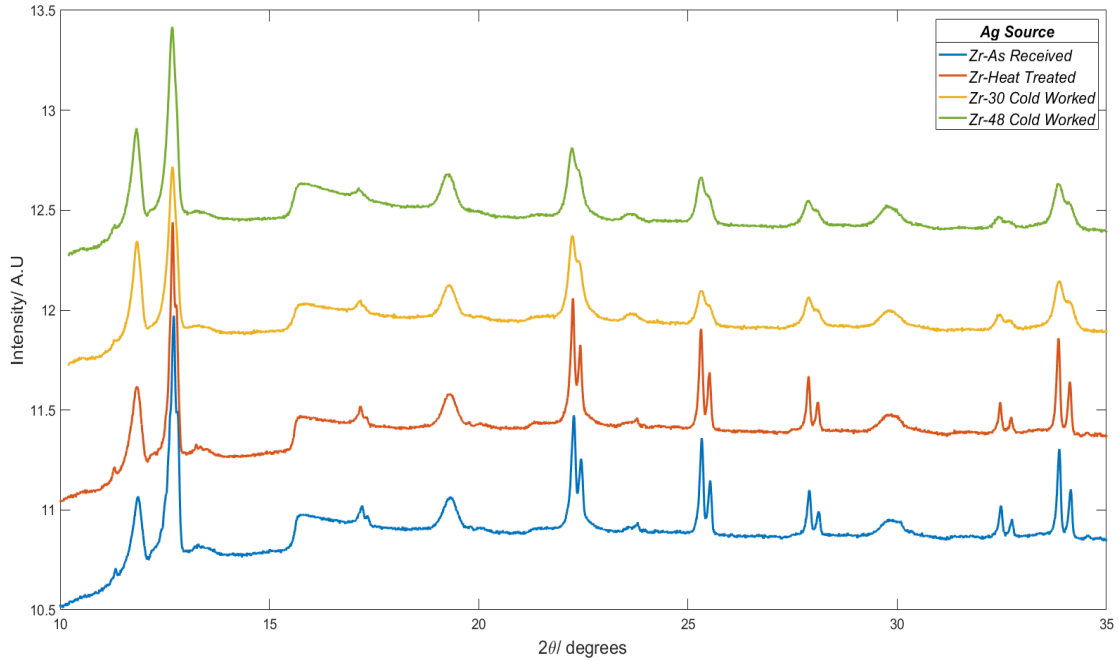


Figure 5.17: A comparison of Ag source XRD results for Zr samples.

TOPAS and CMWP analysis was attempted on Ag source data, however, due to the step change and the high background-to-peak ratio, both analyses failed to run. Following this, as a consequence of the step change, a modified version of the data was attempted, where all the data before the step change was adjusted so that it was in line with the beginning of the step change, as shown in Figure 5.18. With the modified data a CMWP analysis was able to run, however, the modified regions were causing an issue with the fitting where the analysis wouldn't finish or the run would finish but the fitting would be poor and the errors were incredibly large.

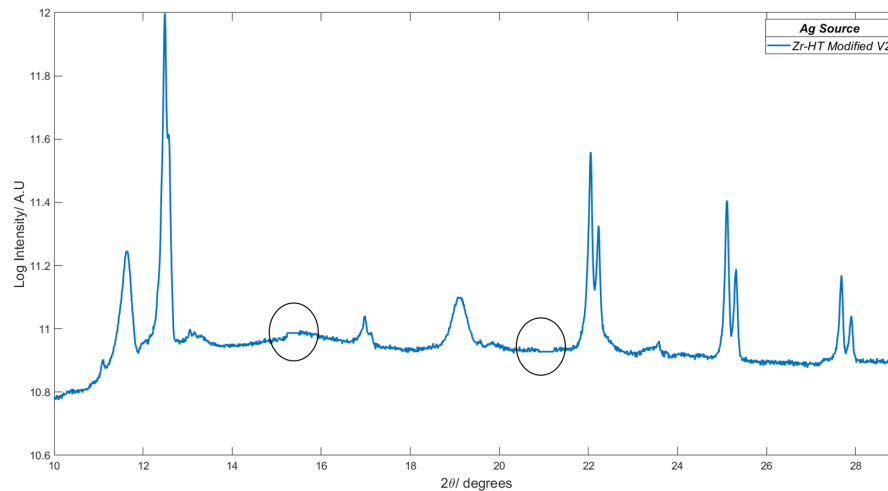


Figure 5.18: The initial modified Zr-HT Ag source diffraction pattern used to overcome the step change present around 15 - 16° and around 21 - 22°.

As the data modification in Figure 5.18 was not adequate, a further modification was attempted by removing all the data points before the step change, this is shown in Figure 5.19. As the

primary peaks for both phases were removed, it was assumed that the results from the analysis would not be entirely comparable to the different radiation sources and TOPAS, however, the trend between the varying deformed samples within the Ag source analysis would still be important to investigate. Furthermore, there can be seen a smoothed region between 21 - 22°. This region is due to the removal of an absorption edge (caused by the beta filter) produced with the peak at approximately 22°, which can be seen in the original data in Figure 5.17. There can also be seen an absorption edge from the peak at approximately 28°, however, due to the nature of the absorption edge, removing it would likely affect the tail end of the corresponding peak, hence affecting further analysis. Despite the further modifications, the CMWP analysis on the modified Zr-HT-Ag sample produced large errors on all physical parameters ($> 30\%$), with a GOF of approximately 3. Though the GOF seemed reasonably low, the dislocation density value was above $300 \times 10^{14} \text{m}^{-2}$, which is not a realistic value, as well as the dislocation arrangement parameter reaching its lower limit of 0.05, giving another indication of a poor fit. If there was a good fit, the amount of data manipulation would be a concern. Thus concluding that Ag source diffraction data may not be suitable for CMWP analysis. A further study could be conducted on a simpler system, such as Si (NIST 640e standard), on an Ag source to determine whether CMWP can produce a reasonable fit. Additionally, another Ag source diffractometer should be considered to determine whether the issue arose from the instrument or the Ag source.

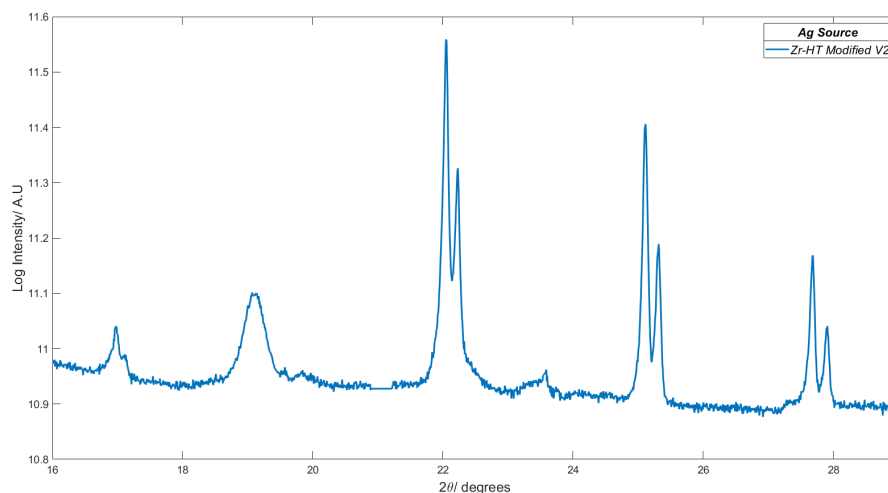


Figure 5.19: *The final modified Zr-HT Ag source diffraction pattern used to overcome the step change present around 15 - 16°.*

5.3.3 Crystallite Size and Dislocation Density Analysis

Moving forward the CMWP quantitative analysis of each data set, from the different radiation source XRD, will be discussed with a comparison to TOPAS and EBSD results for crystallite size.

5.3.3.1 Crystallite Size

The crystallite sizes were determined via a CMWP refinement, a Le Bail TOPAS analysis and post-processing of the EBSD map data. Qualitative analysis of TEM images was attempted, however, no insight into crystallite size could be determined. From the EBSD it is possible to obtain a measurement of the size distribution and average crystallite size, which can be compared

to the TOPAS and CMWP results. After some post-processing of the Zr-HT and Zr-30, the crystallite size range of each sample is shown in Figure 5.20a and Figure 5.20b respectively. The maximum diameter was determined from the post-processing to best account for non-spherical grains. With further analysis of both histograms, the average crystallite size was determined to be $43.6 \mu\text{m}$ and $27.6 \mu\text{m}$ for Zr-HT and Zr-30 respectively. Due to the heavy deformation in Zr-48 and Zr-60, EBSD analysis was not possible.

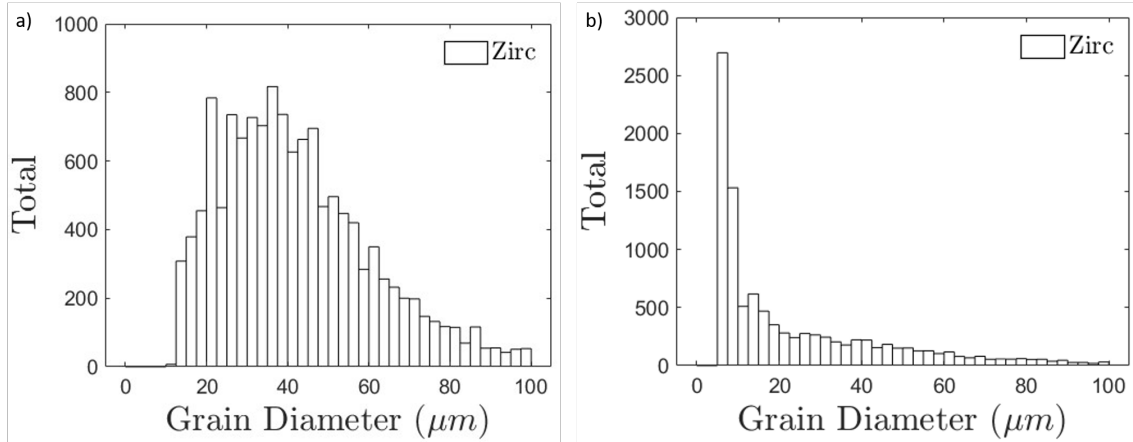


Figure 5.20: The crystallite size distributions calculated from EBSD maps from a) Zr-HT and b) Zr-30.

The comparison of crystallite size for the CMWP - Cu, TOPAS - Cu, CMWP - Co, TOPAS - Co and EBSD analytical techniques are shown in Table 5.7. It can be observed that within all techniques and radiation sources the general trend is that as deformation increases, the crystallite size decreases due to the strain-inducing misorientation within the grain from the formation or movement of dislocations which break the crystals into smaller diffracting volumes. The inverse relation between deformation and crystallite is corroborated by Conrad *et al.* [222].

The CMWP analysis has determined the same trend as the TOPAS analysis, which is a model XRD analysis technique, therefore, validating CMWP. However, there are some quantitative discrepancies between the techniques.

Table 5.7: Crystallite size results from different radiation sources using multiple analysis techniques.

Samples	Crystallite Size/ nm						
	CMWP - Cu		CMWP - Co		TOPAS - Cu	TOPAS - Co	EBSD
Zr-AR	501.7	+ 21.2 - 41.9	356.9	+13.7 - 22.8	168 ± 6.8	331.1 ± 7.0	-
Zr-HT	372.5	+ 35.9 - 96.5	144.0	+ 13.2 - 17.6	317.5 ± 6.2	329.2 ± 5.3	43.6×10^3
Zr-30	80.5	+ 7.7 - 7.9	94.1	+ 5.3 - 4.4	70.0 ± 1.5	87.7 ± 2.0	27.6×10^3
Zr-48	70.1	+ 4.6 - 7.4	88.3	+ 25.2 - 51.9	46.9 ± 0.5	44.7 ± 0.8	-
Zr-60	56.1	+ 4.4 - 2.8	66.6	+ 3.6 - 5.7	36.6 ± 0.6	41.6 ± 0.6	-

There are some inconsistencies with the CMWP Zr-HT-Co, TOPAS Zr-AR-Cu and CMWP Zr-

AR-Cu crystallite sizes. These have been calculated to have been approximately 0.5, 0.5 and 1.5 respectively of the crystallite sizes of CMWP Zr-HT-Cu & Zr-AR-Co and TOPAS Zr-HT-Cu, Zr-HT-Co & Zr-AR-Co. When looking at the other physical parameters that contribute to peak broadening, there are no outliers that seem to be heavily skewed or different from each other that would suggest they were contributing to the discrepancies - these are shown in Appendix B. Therefore, these anomalies are thought to be due to the quality of fit. When looking at Zr-HT, an undeformed and recrystallised sample, the XRD crystallite sizes are orders of magnitude smaller than what is found in the literature (i.e. average crystallite size of between 1 and 20 μm) [70]. However, the literature aligns more with the EBSD analysis and this is likely due to the characterisation technique and the limit of resolution; the literature analysis uses optical and EBSD which has a resolution limit of 1 μm , and the EBSD step size in this body of work is 5 μm , hence the crystallites size are more similar in comparison to the XRD analysis.

One of the main differences between CMWP and TOPAS analysis is the crystallite sizes for the deformed samples, where TOPAS has an underestimation for all deformed samples, except TOPAS Zr-30-Co, compared to the CMWP results. One explanation for this is the complexity of the CMWP fit, theoretically providing a more detailed understanding of the material with the increased number of parameters used to refine the size profile. Therefore, the crystallite size and crystallite size distribution parameters from CMWP are more representative values than the simplified TOPAS analysis. The crystallite size distribution parameter increases with increasing deformation, from approximately 0.3 to 0.5 and 0.2 to 0.4, for Cu and Co diffraction data respectively. This would suggest a larger range of crystallite sizes and, therefore less destructive interference, thus contributing to a broadening of the diffraction peak as deformation increases.

There were orders of magnitude discrepancies between the XRD analysis and EBSD (nanometers and microns respectively). There are two possible explanations for the difference between the two techniques: an EBSD resolution limitation or an XRD pseudo-grain misinterpretation. As the EBSD images were on a large scale, the step size was relatively large, therefore not having a small enough resolution to pick up smaller grains (or possible nano-grains). This is because in order to obtain grain size, the rule of thumb is that the smallest grain size that is detectable is 3 times the step size. This means that there needs to be at least 3 measurements of crystallites in the same orientation for EBSD to determine a cluster of crystallites to be a grain. If there are crystallites in different orientations but there are less than 3 within that step size, they are grouped together with the closest cluster of crystallites with the most similar orientation [223]. The minimum cluster of step sizes to obtain a grain was manually set to 3 in the post-processing of the EBSD map. The step size (i.e. pixel size in the Aztec software) used to process the EBSD data, was set to be 5 μm and 4.5 μm for Zr-HT and Zr-30 respectively, therefore, the lower limit of grain size determination is approximately 15 μm and 13.5 μm . Hence, inferring that the EBSD average grain size calculation was an overestimation of the true average grain size. Additionally, the average crystallite sizes obtained from the EBSD mapping were found to be near the approximate lower limit of EBSD grain size determinate, at 43.6 μm and 27.6 μm for Zr-HT and Zr-30 respectively.

The second possible explanation is the pseudo-grain misinterpretation from XRD. During XRD analysis, the determination of crystallite size is obtained from the continuum of cells in the same orientation, where the continuum is broken at a grain boundary due to crystallite misorientation [224]. It is theorised that the needle-like structures (shown in Figure 5.6), that are believed to be evenly distributed throughout the material, are acting as breaks in the continuum of crystallites in the same orientation (i.e. pseudo α -Zr grain boundaries), possibly causing an underestimation of the average crystallite size. Though there is a possible slight underestimation of the crystallite

size from the XRD analysis, the step size in EBSD is the limiting factor, it is therefore believed that the crystallite sizes determined by XRD, especially CMWP, are more representative of the true crystallite size.

The comparison of the CMWP crystallite size between the Cu and Co reveals that, disregarding the anomalies mentioned previously, they follow the same trend, where with increasing deformation there is a decrease in crystallite size. This is shown graphically in Figure 5.21. However, there are some distinct differences in the values of crystallite size for the cold worked materials. A graphical representation of the trend in TOPAS determined crystallite size is shown in Figure B9 Appendix B.

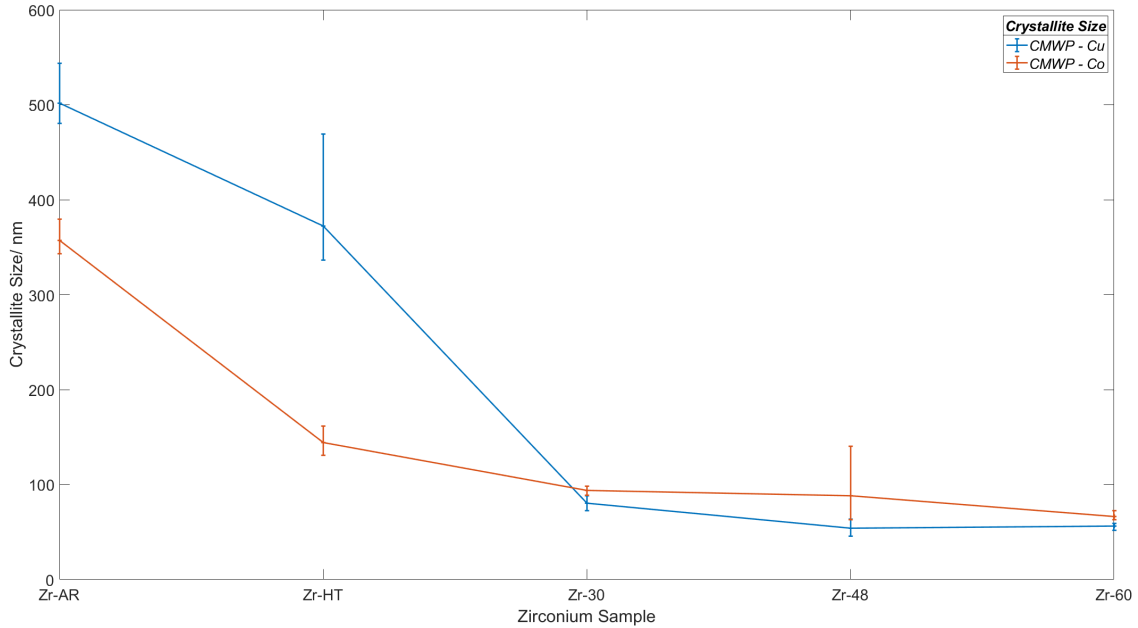


Figure 5.21: A graph showing the comparison of crystallite size trend, determined by CMWP, for the Cu and Co X-ray source experiments.

As can be seen in Table 5.7, CMWP-Cu predicts a smaller crystallite size than CMWP-Co. There were no particular differences in the experimental setup as both used a 2D detector and both used a double-bounce monochromator to remove $K\alpha_2$ and $K\beta$. In both experiments, the direct beam half-cut method was used to align the sample, however, the alignment would affect peak positions and this would be accounted for in the peak-index file. Therefore, though a difference in alignment is possible, is not believed to be a factor in the difference in the quality of fit.

A key distinction between the two data sets was the peak-to-noise ratio (i.e. noise). With the normalised diffraction patterns shown in Section 5.3.2, it can be seen that the Co diffraction data was more noisy than the Cu data. As stated previously, the experimental setup for both radiation sources was similar, however as shown in Table 5.1 on page 62, the time per step for the Co experiment was a third of the Cu, contributing to the noisier data. Though the CMWP instrumental profile takes into account the instrumental broadening effects, the data is fitted using the Pearson7/PseudoVoigt functions which innately smoothed the data, possibly incorporating the background noise less within the refinement. Therefore, the inherently noisier Co diffraction was more difficult to fit, providing a poorer quality of fit. This is corroborated in a thesis by Xu, which determines peak-to-noise ratio being a contributing factor to discrepancies

in CMWP results. A quantitative example of the quality of fit for both CMWP Zr-HT-Cu and Zr-HT-Co are shown in Figure 5.22 and Figure 5.23 respectively. The remaining CMWP fittings are shown in Appendix B.

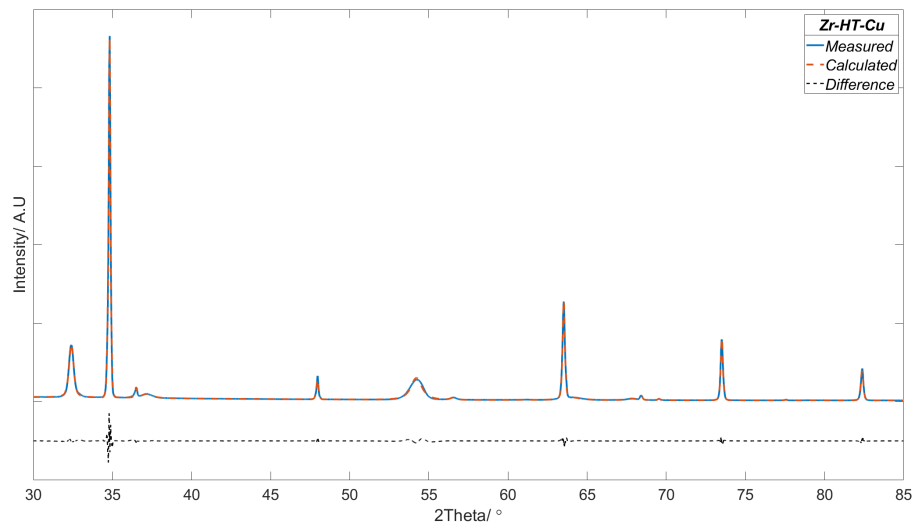


Figure 5.22: An example of the quality of fit for CMWP Zr-HT-Cu. The measured pattern was taken on a Cu source XRD machine with an approximate 24 hour scan time. The blue line is the measured pattern, the red line is the calculated pattern and the black dotted line is the difference.

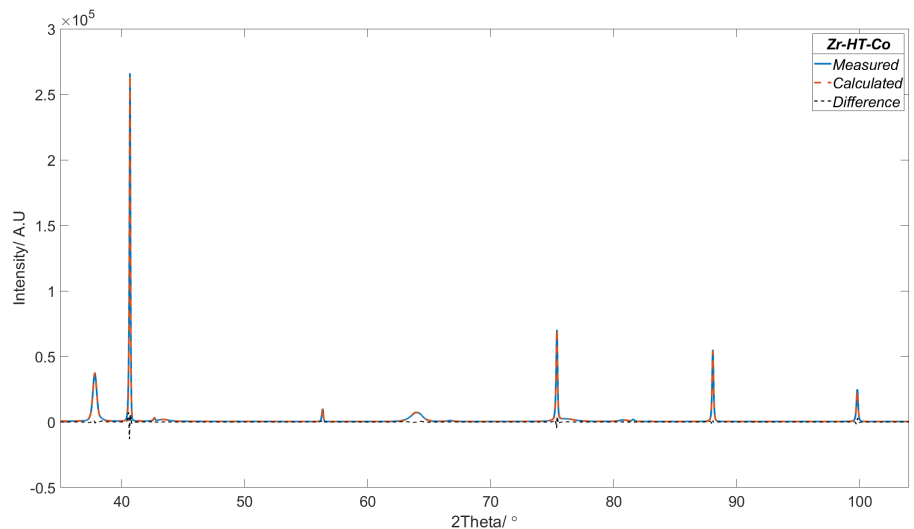


Figure 5.23: An example of the quality of fit for CMWP Zr-HT-Co. The measured pattern was taken on a Co source XRD machine with an approximate 6.5 hour scan time. The blue line is the measured pattern, the red line is the calculated pattern and the black dotted line is the difference.

This was attempted to be corroborated by comparing the weighted sum of square residuals (WSSRs), the difference between the measured and calculated diffraction pattern, between samples and radiation sources. The WSSRs are weighted based on the magnitude of intensities, and as the Co experiments had substantially higher intensities (approximately two orders of magnitude larger), the WSSRs between the Cu and Co CMWP analysis were initially not comparable

(this is shown in Appendix B in Table B1. The WSSRs were normalised (Table 5.8) to allow for comparison, where closer to zero correlates to a smaller WSSR and a better fit.

For both the Co and Cu normalised WSSRs, Zr-HT and Zr-AR were at least double the values of the deformed samples, which suggests that the fittings were slightly worse. Whereas the normalised WSSRs for all the deformed samples were fairly similar, determined to be around 0.3, suggesting that not only are they a better fit than the as-received and heat treated samples but the trends found in the physical parameters are valid (i.e. the decrease in crystallite size with the increase in deformation). The WSSRs did not show any significant insight in the differences between the Cu and Co CMWP results.

Table 5.8: *The normalised weighted sum of square residual (WSSR) between the measure and CMWP fitted patterns for Cu and Co source XRD data.*

Samples	Normalised WSSR	
	CMWP - Cu	CMWP - Co
Zr-AR	0.59	1.00
Zr-HT	1.00	0.84
Zr-30	0.31	0.35
Zr-48	0.32	0.35
Zr-60	0.28	0.37

5.3.3.2 Dislocation Density

The dislocation density obtained from CMWP was to be compared to the dislocation density calculated from TEM, as this is a current and standard method used. A set of three TEM images, in bright-field mode, were taken of Zr-HT and analysed. The line dislocation density was calculated (method described in methodology - using Equation 2.9) and as the three images showed varying degrees of deformation, the average dislocation density was determined to be more representative of the sample. The results are shown in Table 5.9.

Table 5.9: *A table showing the line dislocation densities, and the average, calculated by employing the Smith-Guttman line interception method on TEM micrographs. Images A, B and C refer to three different sites on one sample of Zr-HT.*

Image	Dislocation Density/ $\times 10^{12} \text{ m}^{-2}$
A	3.73
B	12.42
C	5.69
Average	7.28

Although the line intercept method was implemented on Zr-HT TEM micrographs, the counting of interception points, between line and dislocation, was difficult - especially in highly dislocated images (such as Figure 5.1b). In the more highly strained samples, the dislocation lines and networks would be more vast, making it even more difficult to obtain the dislocation density. This provided an additional reason to calculate an average of the dislocation density over the three images.

When comparing the TEM dislocation density values to undeformed Zr alloys from the literature, there can be seen a difference of a factor of approximately 20 ($\sim 1 - 2 \times 10^{14} \text{ m}^{-2}$ v. 7.28×10^{12}). However, there is a distinction to be made between these values and that is the dislocation density obtained from the literature is determined via XRD analysis, which may contribute to

the notable difference. This disagreement in values between TEM and literature XRD can be corroborated by Ungar *et al.*, which compared TEM and CMWP (of sXRD diffraction data) dislocation density analysis in proton irradiated Zr-2, and found that XRD analysis can produce line dislocation density analysis of factor 20 bigger than TEM at higher proton fluences ($> 11 \times 10^{25} \text{ n.m}^{-2}$). The main difference between these two studies is that one is comparing dislocation density from irradiated material and the current study is investigating cold worked material.

The dislocation densities (ρ or d) from CMWP are presented below in Table 5.10, showing the correlation between deformation, dislocation density and radiation sources. Both Zr-AR and Zr-HT are recrystallised samples and, therefore are expected to have dislocation densities below $1 \times 10^{14} \text{ .m}^{-2}$, which was found to be the case with the CMWP Cu and Co analysis. As the deformation increases, from Zr-30% cold worked to Zr-60% cold worked, the dislocation was expected to increase which was found to be the case for both CMWP Cu and CMWP Co. However, there are two things that need to be discussed: 1) the statistical insignificance of the difference between Zr-48-Cu and Zr-60-Cu and 2) the difference between Cu and Co dislocation density.

There can be seen an overlap of the dislocation densities of Zr-48-Cu and Zr-60-Cu, which denotes the statistical insignificance of the difference between the two calculated dislocation densities. At first, it was thought to be an overall quality of fit issue, however, the WSSRs for both samples are fairly similar and of good quality, therefore a more detailed investigation was undertaken. The four physical parameters under consideration for the differences are shown in Table 5.11. It can be noted that there are no outlying errors within the average crystallite size and crystallite size distribution parameters, concluding they are not contributing to the discrepancies. On a closer inspection of both the dislocation parameters, it can be seen that for Zr-48-Cu the dislocation arrangement parameter also had large errors that are causing overlap with Zr-60-Cu, suggesting the strain profile fitting within CMWP Zr-48-Cu could be of poor quality.

The second point of interest is the difference between Cu and Co, where CMWP Co predicts higher dislocation densities than CMWP Cu. As stated previously, there are no experimental setup differences apart from the radiation source and the time per step. The radiation source and time per step would affect the resolution of the data as well as the peak-to-noise ratio, affecting the fit quality, such as the ability to subtract background effects. This was discussed by Xu, when comparing sXRD and lab XRD data, indicating that the peak-to-noise was a contributing factor to the difference in dislocation density (a difference of a factor of 2) [174]. This implies that the radiation source and the subsequent effect on peak-to-noise ratio and resolution will have an impact on dislocation density, which is seen here.

The two radiation sources also have different penetration depths and scattering effects, which are dependent on the wavelength. Co, which has a longer wavelength (approximately 1.70 \AA) than Cu (approximately 1.54 \AA), expands the diffraction pattern to the higher 2θ range. Short wavelengths such as Ag source X-rays, scatter weakly and contract to the lower 2θ range, consequently losing the d -spacing accuracy and resolution. This resulted in the inability to accurately analyse the Ag source data. Furthermore, cobalt source X-rays, with longer wavelengths than Cu source X-rays, have lower energy, which will affect its penetration depth (i.e. shallower penetration). It was determined that the maximum penetration depth for Cu and Co diffraction experiments was $35.5 \text{ }\mu\text{m}$ and $23.6 \text{ }\mu\text{m}$. Though the damage in the deformed samples is believed to be uniform throughout the depth of the material, there is an increase in deformation at and near the surface due to sample preparation. With a shallower penetration depth, it is plausible that the dislocation density would be determined to be higher as the deformation at and near the surface is of a higher proportion of the area investigated than it would be for Cu XRD.

Table 5.10: CMWP dislocations density results from different radiation sources.

Samples	Dislocation Density/ $\times 10^{14} \text{ m}^{-2}$				
	CMWP - Cu		CMWP - Co		CMWP - Ag
Zr-AR	0.53	+ 0.04 - 0.04	0.17	+ 0.02 - 0.02	
Zr-HT	0.69	+ 0.05 - 0.05	0.73	+ 0.07 - 0.07	361.1 + 119.2 - 83.0
Zr-30	2.93	+ 0.22 - 0.19	5.68	+ 0.12 - 0.18	
Zr-48	5.48	+ 0.58 - 0.22	8.36	+ 1.40 - 1.22	
Zr-60	5.66	+ 0.27 - 0.14	13.2	+ 0.91 - 0.48	

Table 5.11: The comparison of the main physical parameters, for Zr-30-Cu, Zr-48-Cu and Zr-60-Cu, that are believed to be the main contributors to the outlier data of Zr-48-Cu.

Samples	Crystallite Size/ nm	Crystallite Distribution/ nm	Dislocation Density/ $\times 10^{14} \text{ m}^{-2}$	Dislocation Arrangement
Zr-30-Cu	80.5 + 7.7 - 7.9	0.328 + 0.031 - 0.041	2.93 + 0.22 - 0.19	0.516 + 0.040 - 0.057
Zr-48-Cu	70.1 + 4.6 - 7.4	0.424 + 0.060 - 0.035	5.48 + 0.58 - 0.22	0.99 + 0.076 - 0.107
Zr-60-Cu	56.1 + 4.4 - 2.8	0.466 + 0.023 - 0.029	5.66 + 0.27 - 0.14	1.01 + 0.086 - 0.052

When comparing the CMWP results to literature (Section 2.2.4), which discusses undeformed and 30% cold worked zirconium alloys, CMWP Cu is closer to Holt *et al.* whereas CMWP Co is closer to Moran *et al.*. The dislocation density, determined by Holt *et al.* and Moran *et al.*, were found to be $3 - 4 \times 10^{14} \text{ m}^{-2}$ and $20 \times 10^{14} \text{ m}^{-2}$ respectively. The materials were cold rolled to a similar level of deformation (approximately 30%), which allows for a near-direct comparison. The main difference that needs to be considered is that the literature discusses zirconium alloys, whereas this study focuses on non-alloyed zirconium, which could be a contributing factor to any discrepancies. The data was collected using high energy XRD (HE-XRD), neutron diffraction (Moran) and standard lab XRD (Holt), therefore, a variety of experimental setups and areas of investigations were compared [75, 79]. Indicating that the CMWP may have a sensitivity to the experimental setup used as this would capture a slightly different area of investigation as well as have varying peak-to-noise ratios. However, due to the closeness between the CMWP Cu result and the literature, it could suggest that CMWP Cu had a more accurate analysis.

To be able to obtain dislocation density from the TOPAS analysis, many assumptions need to be taken to deconvolute the strain profile. Also, to be able to obtain the strain profile from CMWP, an assumption on the L parameter (Fourier transform parameter - the distance between dislocations) was necessary. Therefore unlike with the crystallite size analysis, there could not be any comparative analysis between the strain profile/dislocation density of TOPAS and CMWP. However, it was observed that the microstrain did increase with the increase in deformation, where the strain increased from approximately 0.15 to 0.75 for both Cu and Co data, which can be seen in Figure 5.24.

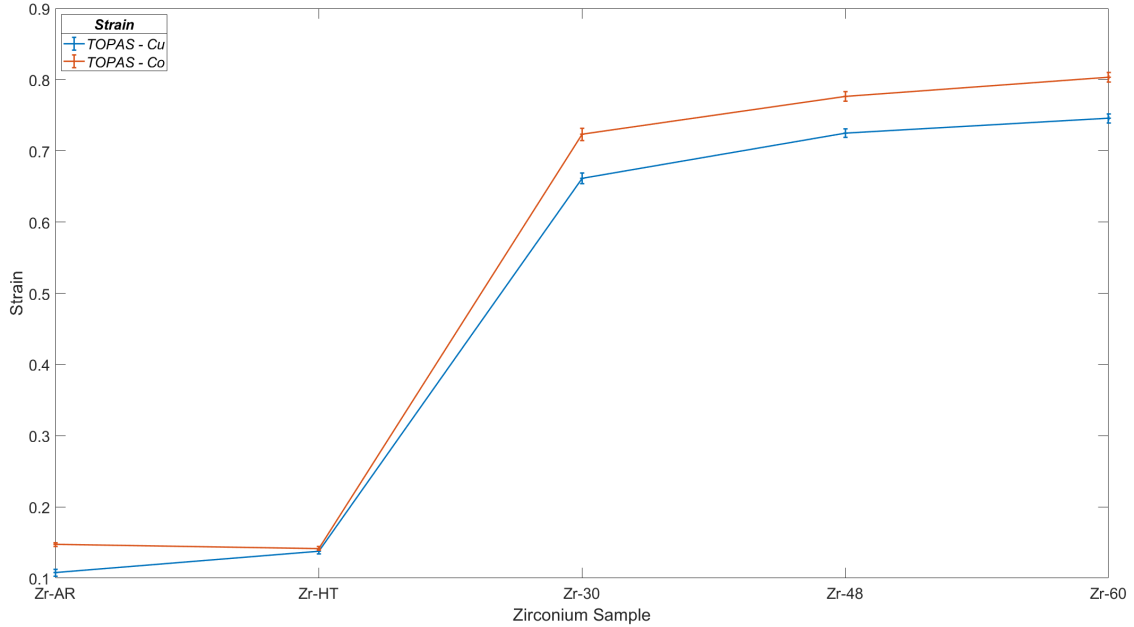


Figure 5.24: A graph showing the increase in strain, calculated from TOPAS using a Gaussian function, with an increase in deformation (Zr-AR to Zr-60) for both Cu and Co diffraction data. The blue line represents Cu data obtained from UoM and the red line represents Co data from MRF.

Furthermore, FWHM analysis was conducted on four distinct Zr peaks (i.e. not overlapping with zirconium hydride peaks), on all three radiation source diffraction data, to determine whether the increase in strain and dislocation density is accurate. This is shown in Figure 5.25, where \circ , ∇ , \triangle and \square indicate 002, 102, 004 and 104 hkl peaks respectively. The blue, red and yellow lines represent the Cu, Co and Ag source diffraction data respectively. It can be ascertained from Figure 5.25 that there is an increase in FWHM (i.e. peak broadening), with all four hkl s, as there is an increase in deformation. This indicates a decrease in crystallite size, an increase in strain (and therefore dislocations) or both. Hence confirming the trends found in both crystallite size and strain/dislocation density from CMWP and TOPAS analysis. It can also be seen that there is a larger amount of peak broadening in the Co diffraction data, for all hkl s, which aligns with the CMWP-Co results, which also show a larger increase in the dislocation density, from Zr-AR to Zr-60, in comparison to CMWP-Cu results. Furthermore, this data shows that with the Ag source diffraction data, the FWHM follows the same trend as Cu and Co diffraction data. This suggests that even though it could not be analysed by TOPAS or CMWP, a simplified strain model could still determine the increase in strain with the increase in deformation.

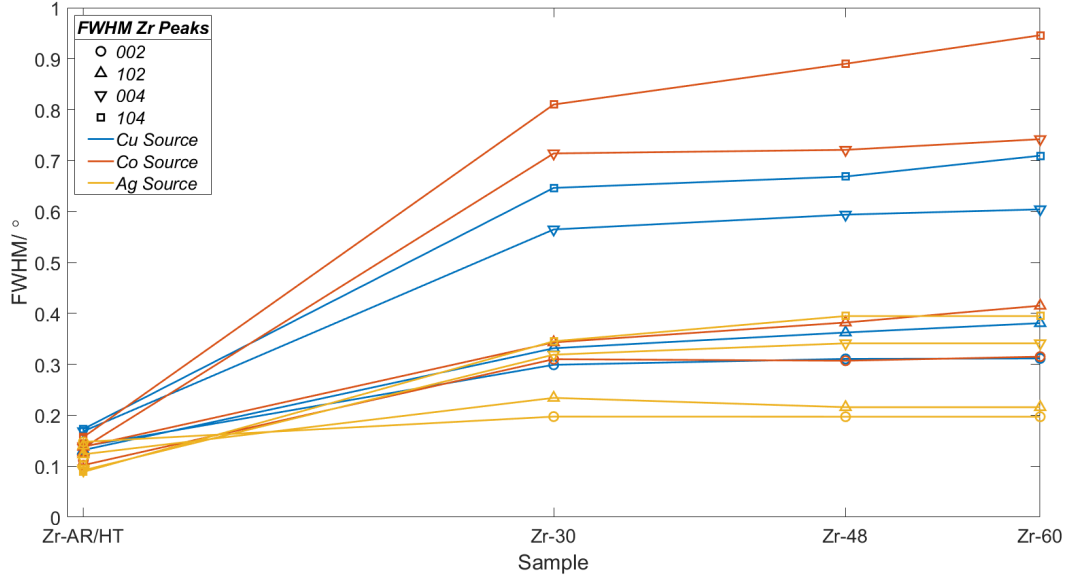


Figure 5.25: A graph showing the correlation between FWHM and deformation from four distinct Zr peaks: 002, 102, 004 and 104. The blue, red and yellow lines represent the FWHM from Cu, Co and Ag diffraction data respectively.

5.4 Conclusion

The objective of this chapter was to carry out a technique development study on Convolutional Multiple Whole Profile (CMWP), determining the accuracy of the technique by comparing the results from Cu, Co and Ag source XRD on zirconium samples that have a range of deformation (as-received, heat treated, 30% cold worked, 48% cold worked and 60% cold worked).

With all XRD experimental setups, the Zr-HT and Zr-Ar samples were qualitatively fairly similar, suggesting that the Zr-Ar may have been recrystallised. There was found to be a trend of increase in peak broadening with an increase in deformation; Zr-HT with the narrowest peaks and Zr-60 with the broadest, which aligns with past investigations and crystallite size/strain profile theory. The samples were supposed to be nominally hydrogen free, however, it was found, via all radiation sources' diffraction patterns, that there was a secondary phase. This was determined to be δ -zirconium hydride via phase fitting analysis on PDF5+ and comparison to hydride Zr-4 diffraction data.

It was found that Ag source XRD was not a viable option for CMWP as the peak-to-noise ratio (i.e. noise) was high and the peaks were broad (the recrystallised sample being similarly broad to the instrumental profile), meaning the analysis could not be initiated. There was also a step change in the diffraction data, hindering the refinement process, suggesting that there could be some experimental setup corrections that could improve the diffraction data, leading to a possible completion of the CMWP analysis. A continuation of the study by using a simpler crystal system, such as Si, could help validate whether Ag source can be used for CMWP analysis.

With regards to the crystallite size analysis, there were found to be discrepancies between both XRD analyses and the EBSD calculation. This was determined to be mainly due to EBSD step size (approximately 5 μm for both scans) being the limiting factor, leading to an overestimation. There were also possible discrepancies in the crystallite size from the XRD, where the secondary

phase may be interfering with the continuum of crystallite size in the same orientation, however, it was still believed to be the more accurate representation of the true crystallite size.

When comparing the crystallite size between the XRD analysis techniques, there were found to be slight differences between the two. This was believed to be due to the more in depth analysis provided by CMWP, where it takes into account crystallite size distribution as well as average crystallite size. Therefore, though both show the same trend of decreasing crystallite size with increasing deformation, TOPAS analysis was believed to be an underestimation of the true crystallite value.

The comparison of CMWP determined that the crystallite size and dislocation density between the two radiation sources showed the same trend in the case of both physical parameters. In the case of dislocation density, the Zr-HT sample was found to be close to $1 \times 10^{14} \text{ m}^{-2}$, similar to the literature. Also, as the deformation increased there was an increase in dislocation density. There was a small disagreement between the values of CMWP Cu and CMWP Co and that was determined to be due to noise, resolution and time per step of the experimental setup, causing difficulty subtracting background contributions, and leading to an overestimation in the CMWP Co results.

It was determined that cobalt radiation source CMWP analysis can accurately predict the trend in crystallite size and dislocation density with varying deformation. Although, there may need to be a refinement of the experimental setup to increase the accuracy of the actual values. Concluding that the optimal lab based setup for CMWP is a copper source XRD machine, ideally with a double-bounce monochromator and a 2D detector, as this provides the highest resolution data with minimal noise.

Chapter 6

Grazing Incident X-Ray Diffraction for CMWP

This chapter will conduct an optimisation study on the application of CMWP and whether it is a valid technique to analyse grazing incident diffraction data from lab XRD experiments.

6.1 Introduction

When investigating irradiation damage within nuclear materials, proton or heavy ion beam implantation is commonly used as an analogue since it does not activate the material to the same extent as neutron irradiation. Proton or heavy ion beam implantation can replicate the displacements per atom (dpa), produced by neutron irradiation, by fine-tuning the fluence (number of atoms, in a given time, per unit area) and energy of the incident beam [225]. However, due to the charge of the ions, there will be considerably more interaction with the target material, hence a larger stopping mechanism. This produces a damage depth profile that is fairly shallow in comparison to neutron irradiated materials, therefore the area of investigation is much closer to the material surface [5, 226]. To investigate near-surface deformation using a laboratory XRD, a grazing incidence XRD (GIXRD) geometry is ideally used.

In this chapter, the focus of the investigation will be on the viability of using lab GIXRD in determining the crystallite size and dislocation density of a known system using CMWP. A Si NIST standard, with a known crystallite size and microstrain (as well as dislocation density), was used as the basis of the study, to ensure the accuracy of the line profile analysis conducted by CMWP and TOPAS. As the analysis was conducted on a powder sample where the strain and crystallite size are uniformly distributed throughout the material, the GIXRD analysis will be compared to a standard laboratory XRD geometry: Gonio XRD.

There has been previous work on using sXRD in a grazing incident capacity such as Hattie Xu who did beamline experiments at the Diamond facility to investigate damage with zirconium systems but none on lab GIXRD [174]. Depending on whether lab GIXRD analysis can accurately determine the crystallite size and dislocation density of the Si sample, future work will then delve into more complex systems such as zirconium and Zircaloy cladding materials. This would unlock the potential to use CMWP to probe the shallower damage depth profiles of ion implanted materials.

6.2 Methodology

The Panalytical X'Pert diffractometer (with a Cu source), in grazing incident geometry, has a minimum omega incident (ω) angle capability of 0.10° . When changing the ω angle, the depth of the sample the beam interacts with changes, hence the angle for GI has to be carefully selected. Trials runs were performed on a range of ω angles in order to determine the minimum angle required for CMWP analysis. The range of ω angles were 0.11° , 0.32° , 1.00° , 1.30° , 1.50° , 1.75° and 2.00° . The quality of the diffraction data was compared and 1.30° was chosen as the lowest viable ω angle. At this given angle there was still noise that affected the CMWP analysis, therefore, a smoothing function (i.e. point moving average) was applied to the diffraction data via a post-processing MATLAB script. To ensure that the smoothing function did not alter the results (i.e. the peak shapes), a range of point moving averages was trialled. The detailed analysis and discussion of this are presented in Section 6.3.2. The chosen ω angle was 1.30° with a 5 moving point average.

Diffraction patterns were taken for a silicon (Si) NIST standard (the sample) and a LaB₆ NIST standard (instrumental parameter sample) - the diffracted 2θ angle range was $26 - 98^\circ$ and $20 - 105^\circ$ respectively. The scanning parameters are shown in Table 6.1. The parallel beam monochromator replaces the need for a beta-nickel filter (i.e. absorption filter), as it preferentially diffracts the $K\alpha$ wavelengths (both $K\alpha_1$ and $K\alpha_2$), thus preventing the possibility of the issue of an absorption edge. The parallel plate collimator minimises the need for incident optics to help focus the beam; the parallel plate collimator optic uses mirrors to reduce divergence and make the beam as parallel as possible. However, due to the parallel plate collimator and the parallel beam monochromator, the intensities were drastically reduced, therefore, the GI scans were run for a much longer time: 20 hours for Si and 24 hours for LaB₆.

Table 6.1: Scanning parameters for the Panalytical X'Pert Powder in grazing incident geometry.

Parameter	Value
Omega (ω) / $^\circ$	1.30
Angle Range / $^\circ$	26 - 98 / 20 - 105
Incident Optics	Parallel Plate Collimator
Filter	None
Soller Slit / Rads	0.4
Primary Mask / mm	None
Step Size / $^\circ$	0.013
Time per step / secs	13

For CMWP, the instrumental data was processed the same as in Section 5, where the diffraction pattern was split into its separate peaks, converted into reciprocal space (k) and centred on the $K\alpha_1$ peak. The background was removed and the peaks were fitted if there was any additional noise. A Split Pearson7/PseudoVoight function was used for asymmetrical peaks and two separate Pearson7/PseudoVoight functions for when there are $K\alpha_1$ and $K\alpha_2$ peaks. They were saved in the same format as stated in Section 5. For the TOPAS refinement, for both the LaB₆ and the Si, the region of diffuse scattering was removed using a background removal function in the Fityk software in order to improve the accuracy of line profile analysis.

To determine whether heavy ion implantation was viable with lab grazing incident XRD analysis, an initial investigation of self interstitial ion implantation in zirconium was conducted. The

energy for the Zr ion penetration depth simulations was determined by combining both the conservation of momentum (Equation 6.1) and the conservation of kinetic energy (Equation 6.2), to produce an energy transfer model (Equation 6.3). Where the ‘p’ and ‘t’ notation refer to the projectile atom (i.e. neutron) and target atom (i.e. Zr ion) respectively. The subscript numbers denote the state of the atom before and after collision, where ‘1’ is before and ‘2’ is after. As the Zr ion before the collision is at rest, the momentum and kinetic energy values can be equated to zero (i.e. $m_{t1}v_{t1}$ and $E_{k,t1}$).

$$m_p v_{p1} + m_t v_{t1} = m_p v_{p2} + m_t v_{t2} \quad (6.1)$$

$$E_{k,p1} + E_{k,t1} = E_{k,p2} + E_{k,t2} \quad (6.2)$$

$$E_{k,t2} = \frac{4m_p m_t}{(m_p + m_t)^2} E_{k,p1} \quad (6.3)$$

The values for mass and energy of the projectile (i.e. neutron) and target (i.e. Zr ion) are shown in Table 6.2 [227]. These values were then inputted into Equation 6.3, where the final energy of a Zr ion after a ballistic/elastic collision with a 2 MeV neutron was determined to be approximately 0.0865 MeV or 86.5 keV. This value can then be used in SRIM calculations in order to calculate the penetration from the self-interstitial zirconium ion.

Table 6.2: *The mass, initial energy and final energy of a projectile (i.e. neutron) and target (i.e. Zr ion) in ballistic/elastic collision for the calculation of the transfer energy to a Zr ion if momentum and kinetic energy are conserved.*

Species	Mass/ amu	Initial Energy/ MeV	Final Energy/ MeV
Neutron	1.008 (m_p)	2 ($E_{k,p1}$)	0 ($E_{k,p2}$)
Zr ⁺	91.224 (m_t)	0 ($E_{k,t1}$)	86.5 ($E_{k,t2}$)

Now that an approximation of the self-interstitial zirconium ion energy was determined, the penetration depth needed to be predicted. This was done using the software called Stopping and Range of Ion in Matter (SRIM), which allows the user to design a theoretical ion implantation experiment and predict the damage profile within the target layers - the interface for the software is shown in Figure 6.1.

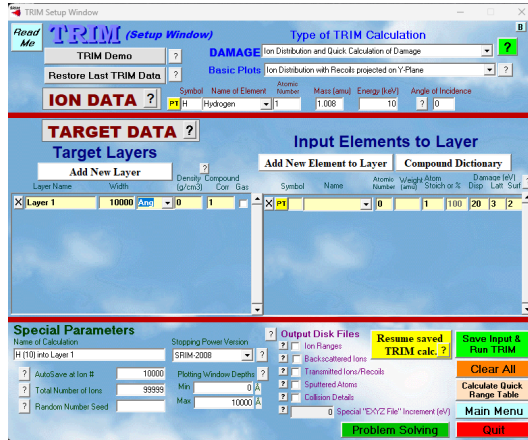


Figure 6.1: The interface of the SRIM software that was used to predict the damage depth profile of a self-interstitial zirconium ion, with an energy of 86.5 keV, within the target zirconium layer.

The target layer was comprised of elements, that were determined via the ICP-OES results in Chapter 5, an average density was used and the layer width was set to 1000 Å. As stated above, the incident ion parameters were set as a zirconium ion with an energy of 86.5 keV and an incidence angle of zero, meaning that the attacking species is perpendicular to the target layer and the penetration depth was maximised. The software predicts the damage depth profile by simulating the damage cascade that is produced from the previously explained interaction (Figure 6.2).

The energy determined from the equations above was used to simulate a damage cascade, which in turn was used to create an ion frequency vs. penetration depth histogram. The damage cascade in Figure 6.2a) and histogram in Figure 6.2b) were both used to estimate a penetration damage depth value using two different methods: the penetration depth from the centre of the damage cascade (peak dpa region) and the maximum penetration depth respectively.

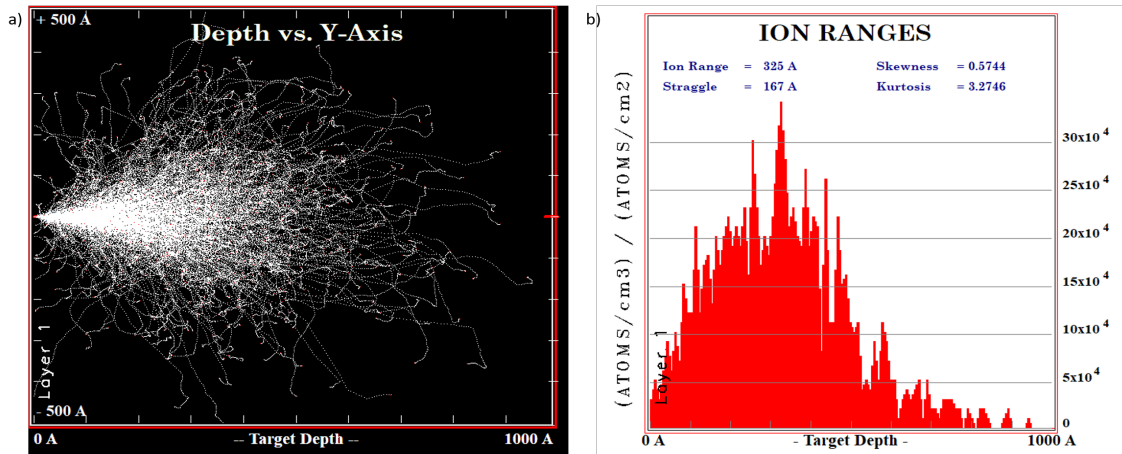


Figure 6.2: Two visual representations of the damage depth profile of an 86.5 keV Zr ion implanted into a target Zr interface at a perpendicular angle. a) The damage cascade produced and b) The frequency of ions at various target depths.

The grazing incident angle was calculated to investigate the stated damage depth profile, this was done using Equation 6.4. In Equation 6.4, ' ω ' denotes the grazing incident angle, ' x ' is the

desired penetration depth and ‘ μ ’ is the attenuation coefficient for the target material. As the target material was predominantly zirconium, the attenuation coefficient was taken solely for zirconium as the other constituting elements had little effect on the coefficient value. The value was calculated and procured from [228], resulting in an attenuation coefficient of $11.7887 \mu\text{m}$ for a Cu source XRD setup.

$$\omega = \sin^{-1} \left(\frac{x}{3\mu} \right) \quad (6.4)$$

6.3 Results and Discussion

6.3.1 Minimum Grazing Incident Angle

As mentioned in Section 6.2, the ω angle had to be carefully selected. For this reason, trial runs were performed at grazing incident angles of 0.11° , 0.32° , 1.00° , 1.30° , 1.50° , 1.75° and 2.00° . The diffraction data for the majority of these grazing incident angles are shown in Figure 6.3. The comparison of ω angle 0.11° and 1.30° is shown separately, in Appendix C Figure C1, as the 0.11° data skewed the graph.

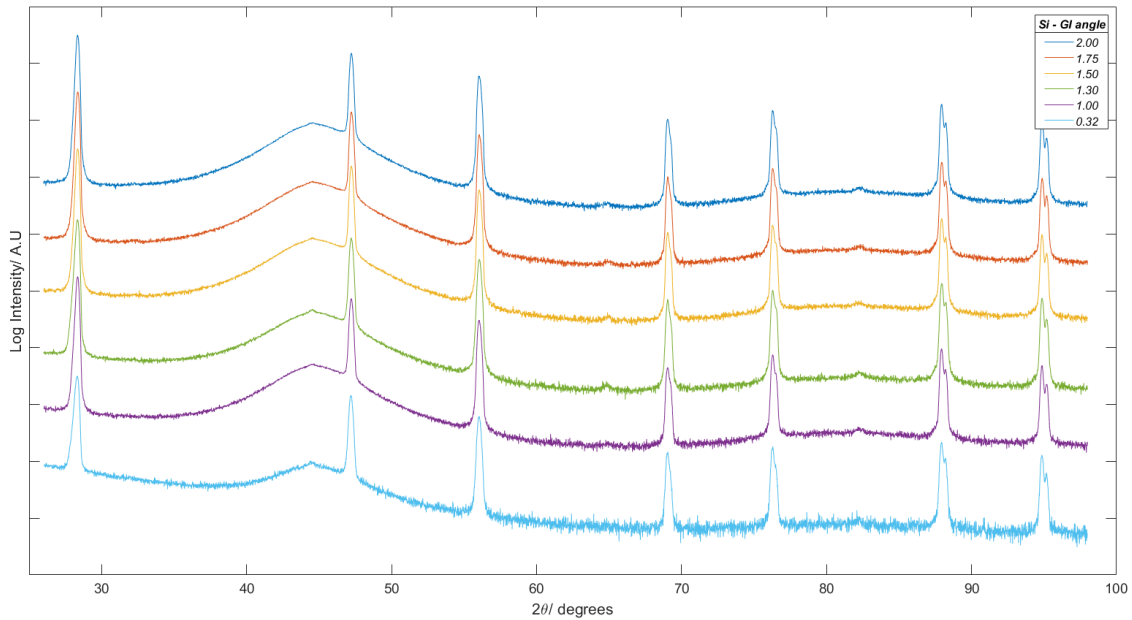


Figure 6.3: A comparison of diffraction patterns for the different grazing incident angle (ω angle) used on Si to determine viability of CMWP on lab XRD. The ω angles tested are: 0.32° , 1.00° , 1.30° , 1.50° , 1.75° and 2.00° .

The lower ω angle limitation of the lab diffractometer was 0.10° , however, it was decided to use an angle just above the limit: 0.11° . As can be seen by Figure 6.3, with the increase in the ω angle, there can be seen a decrease in noise. This is because an increase in ω angle means that more material is interacted with, with a smaller beam footprint, resulting in less scattering and less noise. An attempt was made at the 0.11° ω angle, however, it was found that the data was extremely noisy. Post-processing was tried to smooth the data sufficiently for line profile analysis however it also highly affected the peak height and shape. As the post-processing of the

data would affect peak broadening, any further analysis via CMWP or TOPAS would provide unrepresentative results.

From 1.30° onwards, there can be seen no significant change in the diffraction data or noise reduction. Therefore, it is believed that 1.30° is the lower limit of ω angle that can be used in grazing incident geometry for line profile analysis. The penetration depth from 1.30° (i.e. the maximum depth in which the X-rays interact), using Equation 6.5, was determined to be 800 nm (8000 Å equivalent).

$$x = 3\mu \sin \omega \quad (6.5)$$

The diffraction data from 1.30° , though providing the best results at the lowest feasible ω angle, still had to be processed to reduce the noise for accurate examination from CMWP and TOPAS analysis. Significantly higher angles may be used to reduce noise, though the interaction layer from said higher ω angles will be substantially deeper and would inappropriate for shallow depth analysis.

6.3.2 Post-Processing of Data

6.3.2.1 Smoothing Function

It was determined that with the Si, at 1.30° , the collected data was still too noisy for an accurate CMWP and TOPAS analysis, therefore, it was decided to smooth the data using a point moving average function. Xu *et al.* found that the noise-to-peak ratio was a contributor to the accuracy in determining physical parameters, where a large noise-to-peak ratio increases the difficulty and error of the analysis. By producing a smooth data set, a better peak-to-noise ratio was created, reducing the errors in the calculations and hence providing a better fit. A range of point moving averages were trialled, where the minimal post-processing would not sufficiently smooth the diffraction and the higher smoothing functions would affect the peak heights and shapes.

In Figure 6.4 the comparison of the 5, 10 and 15 point moving average function on the Si, with a 1.30° ω angle, is shown; the 5 point moving average least affects the shapes of the peaks whilst reducing the noise significantly enough that the CMWP analysis was minimally affected. The 10 point moving average, even though the smoothing function reduced the noise significantly, more than the 5 point moving average, the effects on the peak shape were substantial where it was believed that any further analysis would not be accurate or representative. Furthermore, the 15 point moving average had no significant increase in smoothing in comparison to the 10 point moving average but had considerable effects on the peak shape, making it unsuitable for further analysis. This is depicted clearly in Figure 6.5, which is a magnified peak at approximately 88° , showing the effects of all three smoothing functions compared to the original data. Therefore a 5 point moving average was used going forward in data analysis. The fittings and the physical parameters for the unsmoothed, 10 and 15 moving point averages are shown in Appendix C.

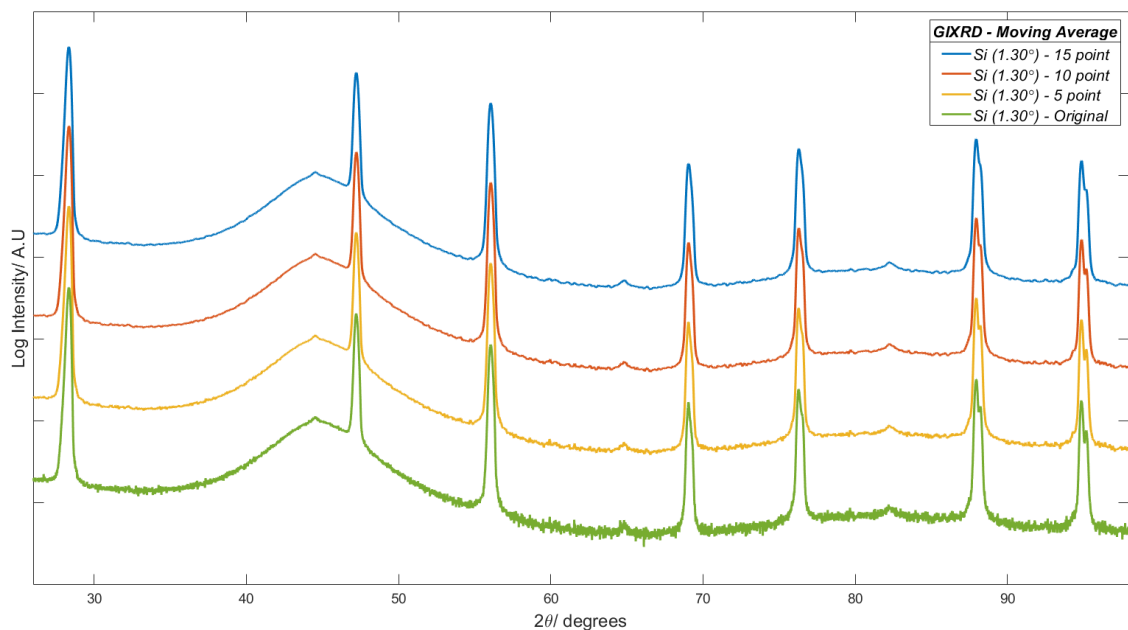


Figure 6.4: A comparison of a 5, 10 and 15 point moving average processing on the instrumental data, S_i , to demonstrate the optimal number for the smoothing function.

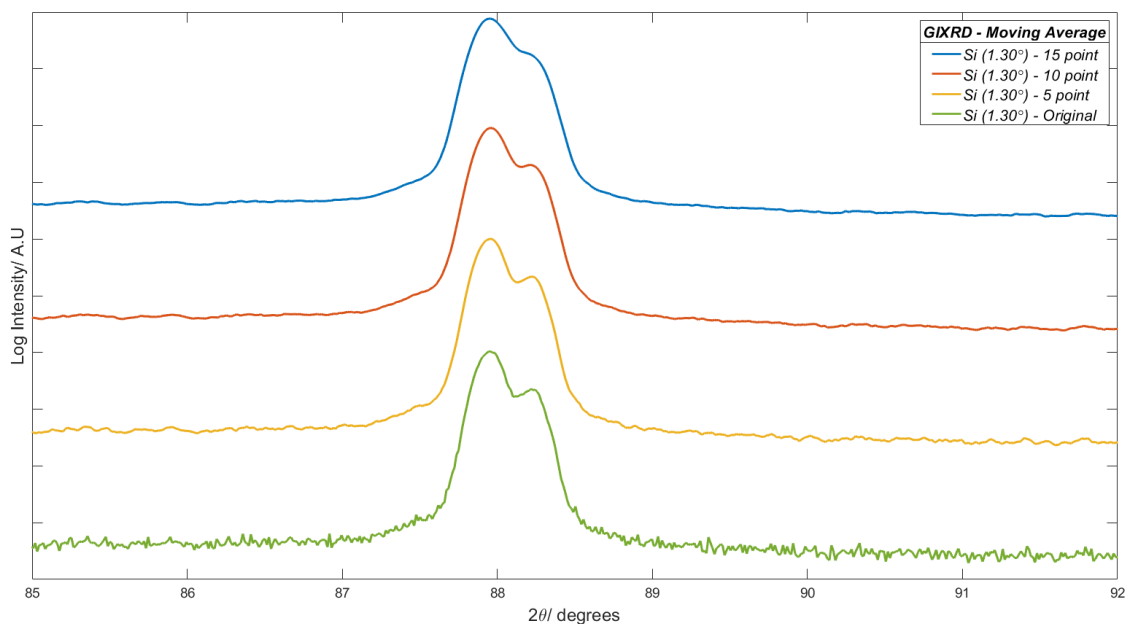


Figure 6.5: A magnified image of a peak at approximately 88° , showing the comparison of the range of point moving averages.

6.3.2.2 Region of Diffuse Scattering

Having established suitable grazing incidence angle and data smoothing, it was now possible to attempt to fit the data collected on the LaB₆ and Si samples. When attempting to fit the LaB₆ data in TOPAS to obtain the instrumental parameters of the X'Pert diffractometer, the region of diffuse scattering was not able to be fitted, therefore, hindering the overall fitting. This is

shown in Figure 6.6, where the region of diffuse scattering is circled in green. Various background parameters were used to fit the region of diffuse scattering but were unsuccessful. The poor fitting of the LaB_6 led to the imprecise prediction of the instrumental effects, therefore, producing an inaccurate refinement of the Si sample. To overcome this issue, a background removal function was implemented, using the Fityk software. The function was focused mainly around the region of diffuse scattering, thus drastically improving the Le Bail TOPAS refinement, as shown in Figure 6.7.

The region of diffuse scattering appeared in both the LaB_6 and Si diffraction data, therefore to keep consistent, the region of diffuse scattering was removed from the Si data set as well, to ensure that there were no other factors influencing the background and instrumental parameters during refinement. The removal of the region of diffuse scattering in the Si sample can be seen in Figure 6.8.

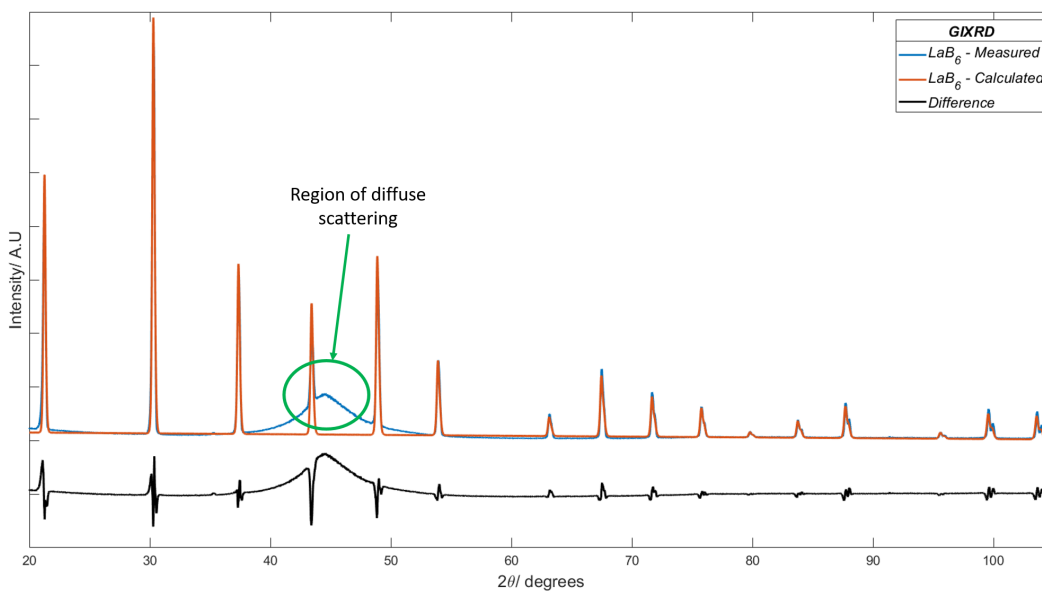


Figure 6.6: *The Le Bail TOPAS refinement of the original GIXRD LaB_6 , showing the effects of the region of diffuse scattering on the fitting.*

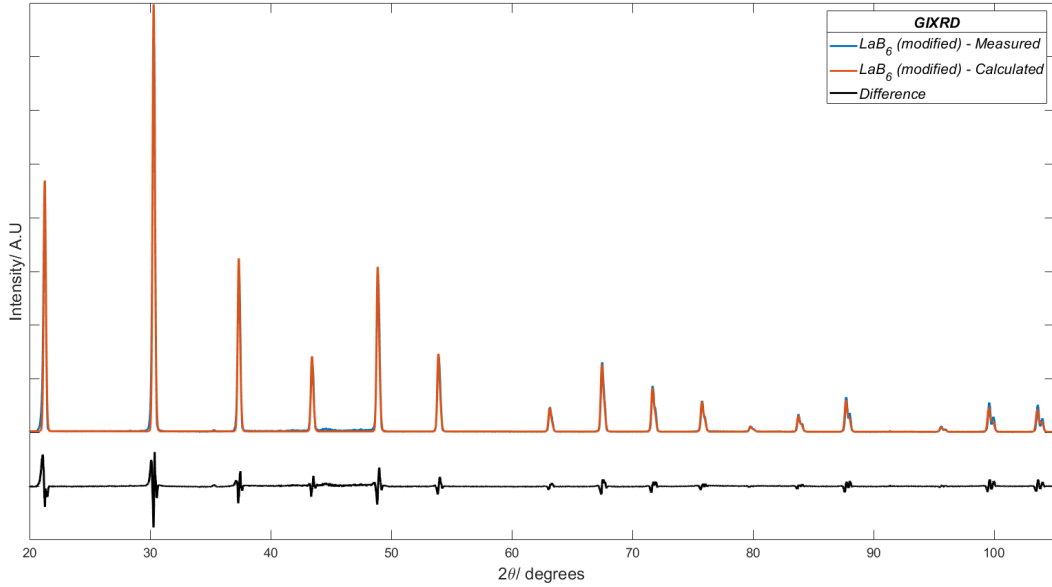


Figure 6.7: The Le Bail TOPAS refinement of the modified GIXRD LaB_6 , showing the improvement of the fitting.

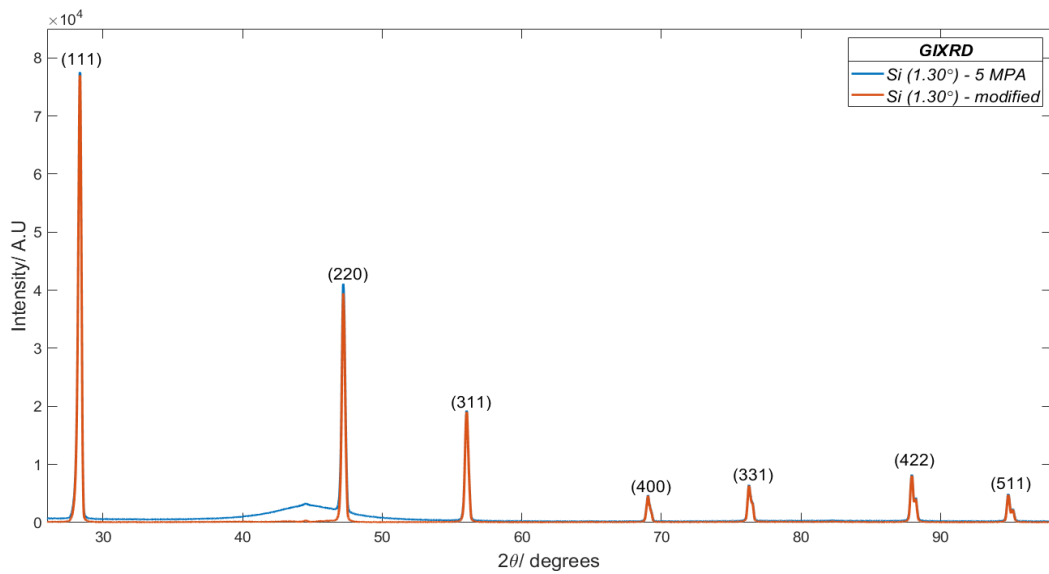


Figure 6.8: The removal of the diffuse scattering for TOPAS analysis. The blue line is the original diffraction data and the orange line is the modified diffraction data.

Regarding the CMWP analysis, the region of diffuse scattering was not removed from either LaB_6 or Si diffraction data. The region of diffuse scattering did not affect the peak shape but the total peak intensity, so it was incorporated as an extra background function. When creating the LaB_6 instrumental profile, the relative peak intensities are used (i.e. minus the background), therefore the region of diffuse scattering had no effect. With the Si diffraction data, in CMWP, a background spline was generated that incorporated the region of diffuse scattering, as shown in Figure 6.9. The blue line is the measured diffraction pattern, and the orange line is the background spline. This counteracted the effects of the region of diffuse scattering on the fitting.

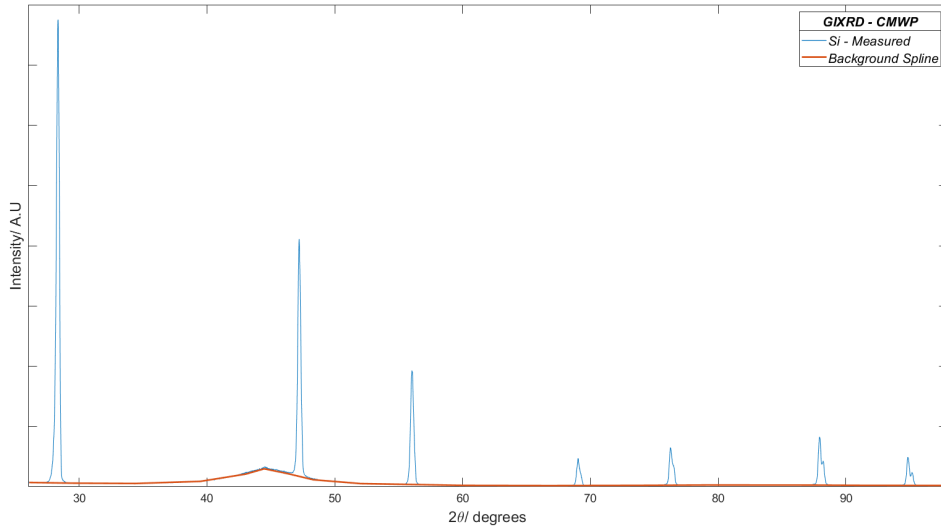


Figure 6.9: *The background spline in CMWP that minimises the effects of the region of diffuse scattering.*

6.3.2.3 Absorption Edges

The phenomenon of absorption edges was present in the Gonio Si diffraction data, which occurs (as explained in section 3) when the $K\beta$ filter cuts off the $K\beta$ wavelength leaving a stepped edge (also referred to as shoulder) on the left of a peak. These become more prominent close to peaks with high intensities and, therefore, are more likely to affect future analysis.

As these absorption edges affect line profile analysis, especially in the case of CMWP, the diffraction data was slightly modified so that they could be removed. Starting from the absorption edge at the higher 2θ angle, all the data before that phenomenon was increased manually, using a translation function, so that it was flush with subsequent data. This was repeated for all absorption edges and can be seen in Figure 6.10. The blue line is the original diffraction data and the orange line is the modified diffraction data.

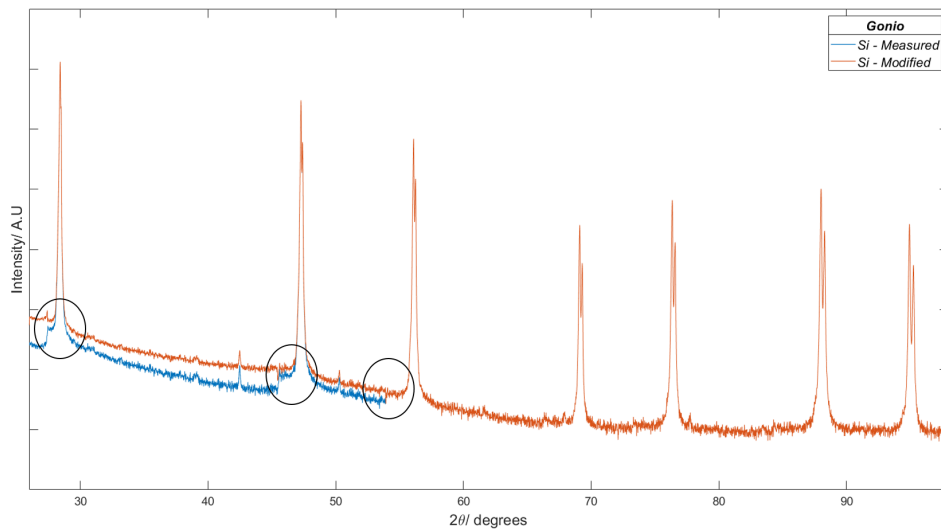


Figure 6.10: *The removal of the absorption edge on the Gonio Si diffraction data. The blue line is the original diffraction data and the orange line is the modified diffraction data.*

6.3.3 Crystallite Size Analysis

The crystallite size for Si was calculated using two diffraction analysis techniques: TOPAS and CMWP for both experimental setups. For the TOPAS analysis, a simplified whole line profile fitting technique was performed: Le Bail analysis. The LaB₆ was analysed initially to obtain the instrumental effects. This was obtained by fixing the lattice parameters, crystallite size and microstrain to the values found in the NIST standard documentation, and only refining the ‘Peak Type’, which was chosen to be PVII, similar to the one used in the NIST standard documentation. These parameters were then fixed when refining the Si data. The crystallite sizes from the NIST standard documentation, TOPAS and CMWP from both geometries can be found in Table 6.3. The table shows that the crystallite size determined by GI CMWP, TOPAS and Gonio TOPAS are fairly similar, whereas the Gonio CMWP is twice as large. All four analyses do not agree with the NIST 640f standard which states a crystallite size of 400 nm [229].

Table 6.3: *The comparison of crystallite size from NIST standard documentation, GIXRD CMWP analysis, Gonio CMWP analysis and TOPAS for Si.*

Sample	Crystallite Size/ nm					
	NIST Standard	Grazing Incident		Gonio		
		CMWP	TOPAS	CMWP	TOPAS	
Si	400 [229]	235.7 + 72.8 - 42.2	225.5 ± 3.6	684.3 + 241.6 - 263.5	255.5 ± 4.5	

As stated previously, when performing the TOPAS analysis on the Si, the 5 moving point average data with the removed region of diffuse scattering was used. The fitting for both the GI and Gonio TOPAS fittings are shown in Figure 6.11 and Figure 6.12 respectively. The crystallite size was found to be 225.5 ± 3.6 nm and 255.5 ± 4.5 nm for GI and Gonio respectively. Quantitatively, the quality of fit was fairly similar, with Goodness of Fits (GOFs) values of ~ 6.9 and ~ 7.9 for GI and Gonio respectively, therefore, though there are slight differences between the crystallite sizes, the values are fairly comparable. The difference in the crystallite sizes is likely due to modification of both the LaB₆ and Si for the GI diffraction data - the removal of the diffuse scattering region from both samples and the smoothing function on the Si diffraction data. The smoothing of the GI diffraction data would lead to a slight broadening in the peaks, therefore, yielding a smaller crystallite size than unmodified data which would have narrow peaks. This is shown in the decreasing crystallite sizes from the 10 moving point average to the 15 moving point average - the table presented in Appendix C.

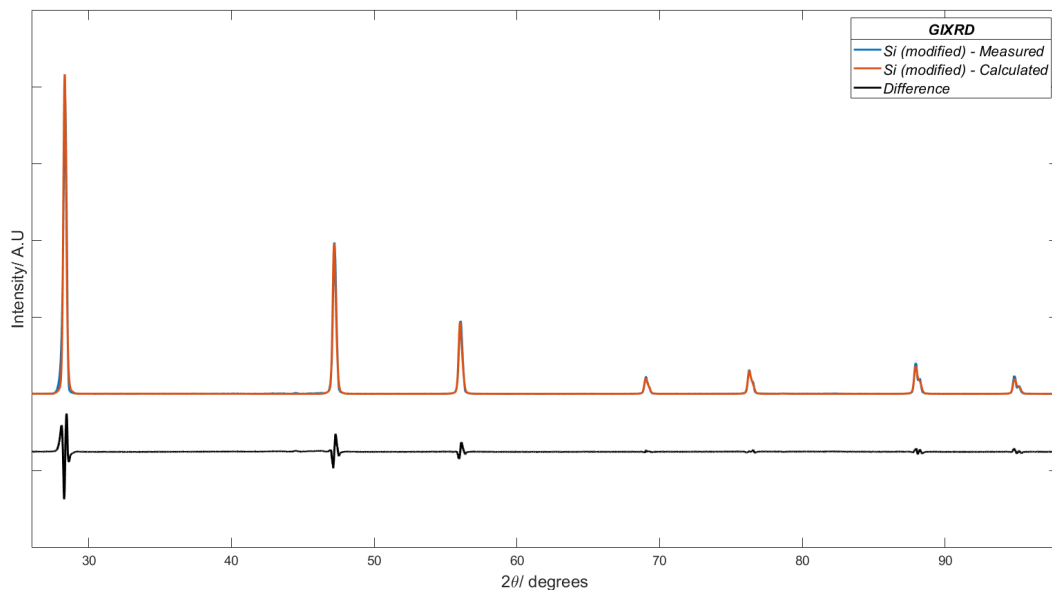


Figure 6.11: *The Le Bail TOPAS refinement of the modified GIXRD Si.*

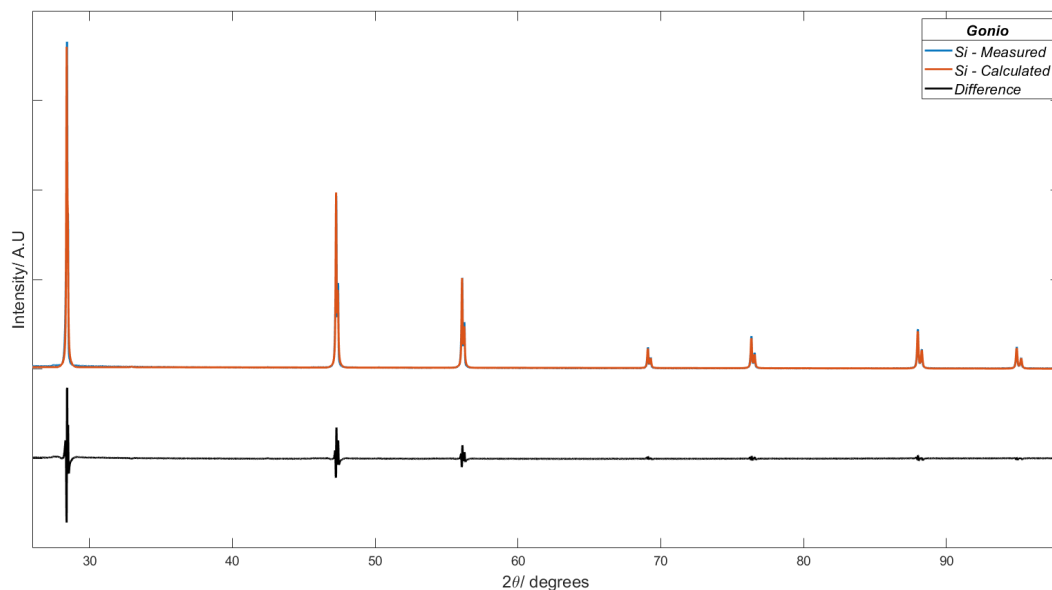


Figure 6.12: *The Le Bail TOPAS refinement of the Gonio Si.*

The difference between the NIST standard documentation (400 nm) and the TOPAS analysis is believed to be mainly from the instrumental effects. From the documentation, the parameters that were refined were the lattice parameter, crystallite size and microstrain, where the microstrain was refined to approximately zero and the lattice parameter was determined to be 0.5431 nm [229]. In both experimental setups, the microstrain was refined to approximately zero and the lattice parameters were found to be 0.5428 nm and 0.5430 nm for (GI and Gonio respectively). Normally, the lattice parameter for a standard such as Si would not be refined, however, as the standard is being used as a test, they were allowed to be refined. There were very small changes in the lattice parameters, however, these will contribute to a peak shift and not to peak broadening. The main cause for the difference in crystallite size between the NIST

standard documentation and experimental TOPAS analysis may be due to the instrumental effects. Multiple iterations of the instrumental refinement and parameters were trialled as well as different peak types (e.g. different starting values, fixed some parameters and ran the analysis, started from scratch multiple times), despite that, the crystallite size was still calculated to be lower than the NIST standard.

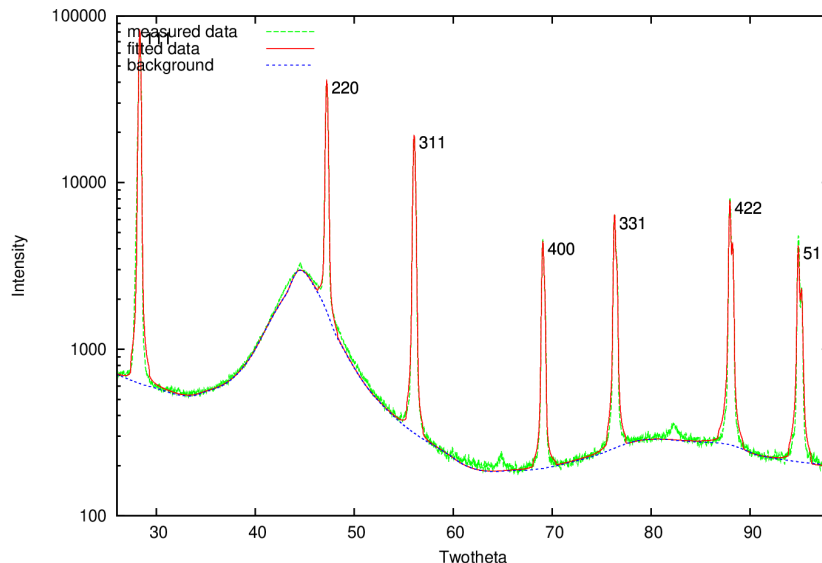


Figure 6.13: *The CMWP fitting of the GIXRD Si diffraction data.*

For the GI CMWP analysis, the fitting is shown in Figure 6.13, and qualitatively, as can be seen by the difference line, the calculated pattern is fairly similar to the measured diffraction pattern. The crystallite size was determined to be 235.7 nm, with the dislocation density and dislocation arrangement physical parameters refining to approximately zero, meaning minimal ordered dislocations. The difference between the NIST standard documentation and that from the GI CMWP analysis is believed to be due to the more in depth analysis that occurs with CMWP. Where TOPAS bases the analysis of the crystallite size and strain profile, CMWP breaks both profiles down into their physical parameters. With the focus on crystallite size, CMWP calculates the average crystallite size as well as the crystallite size distribution (calculated to be 0.05), which may be a contributor to the difference in crystallite size compared to the TOPAS analysis. The instrumental effects were also calculated differently, where they are determined for each peak and, therefore, could also be a contributor to a lower crystallite size.

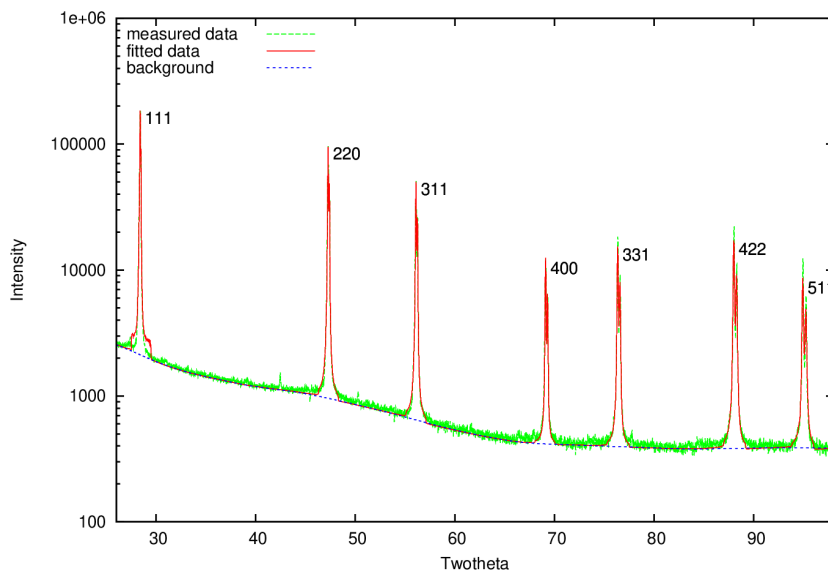


Figure 6.14: *The CMWP fitting of the Gonio Si diffraction data.*

The Gonio CMWP analysis on the Si standard determined that the crystallite size was 684.3 nm, with the dislocation density parameter refined to nearly zero. However, the dislocation arrangement parameter was found to be maxed at the upper limits provided, suggesting that any dislocations present are highly disordered, hence contributing to the broadening effect and therefore, affecting the refinement of the crystallite size parameter. Multiple attempts were made, with numerous starting parameters (e.g. setting M to zero and then refining), but the refinement did not improve. Qualitatively, the Gonio CMWP fitting was found to be much worse than the GI CMWP fitting, this can be observed in Figure 6.14. Primarily on the (111) peak but also present on the (220) and (311), there can be seen sharp shoulders on the calculated pattern. This is believed to be due to a cut-off parameter for a Gaussian function, where once it is believed to be sufficiently small enough, the fitting for the peak will sharply cut-off and join with the background spline. This phenomenon was also observed in the GI CMWP analysis of Si, however, the cut-off parameter on the quality of fit seemed to be less significant, therefore affecting the overall output less. It was also found that in the Gonio CMWP analysis, the errors for each of the physical parameters were high (i.e. all above 30%), which suggests a poor quality of fit.

Another reason for the poor quality of fit from the Gonio CMWP analysis is believed to be due to the slight modification of the diffraction data to remove the absorption edges, which was implemented as CMWP would produce larger cut-off edges that would hinder the fitting and results. Despite best efforts, the Gonio CMWP fitting did not work. It can be seen that the crystallite sizes from the GI geometry and the Gonio TOPAS geometry are similar, though different from the NIST standard documentation, where possible reasons have been explained above. It is believed that using GI geometry for CMWP could be a viable option. Further refinement of the Gonio XRD scan program needs to occur to ensure the reduction of absorption edges present in order to minimise further line profile analysis.

6.3.4 Viability of Heavy Ion Implantation Study

The study above determined the minimal ω angle required in order to investigate materials, with line profile analysis (i.e. CMWP and TOPAS), using a grazing incident geometry in a lab XRD.

The next step was to determine whether this method could be used for the assessment of damage effects in heavy ion irradiated materials.

The initial investigation used a self-interstitial ion in bulk zirconium, with an equivalent energy of a 2 MeV neutron, as this would simulate a primary knock-on atom (PKA) and the subsequent damage cascade. The energy of the Zr^+ ion was calculated using an energy and momentum transfer model and was determined to be 86.5 keV. This was then inputted in SRIM to calculate the peak damage depth and peak ion implantation depth (straggling ion depth). The calculations for these are discussed in the methodology and were found to be 500 Å and 950 Å respectively.

From the peak damage depth of 500 Å, using Equation 6.4, an ω angle of 0.081° was calculated. This penetration depth was used as it incorporates the majority of the damage produced. Comparing this ω angle to the lowest viable ω angle of 1.30° and the machine's lowest operational ω angle of 0.10° , it was deemed unfeasible to investigate as it was inaccessible. Likewise, calculating the ω angle for the maximum penetration depth of the damage cascade of 950 Å yielded a value of 0.154° . The caveat with this damage depth is that it incorporates the straggling displaced atoms (not within the main damage cascade region), hence encompassing a lot of the low deformed region, which could skew the strain profile/dislocation density results. Despite the increase in penetration, similar to the peak damage depth angle, the incident angle was lower than the lowest viable ω angle.

However, looking at past literature, discussed in Section 2.2.8, much higher ion implantation energies are used. The energies and fluences that were used, to investigate the effects of increased dpa on the evolution of defects such as bubbles and dislocation, were fine tuned to ensure that the implanted species remained within the sample. The ω angle for these respective energies and penetration depths were calculated and shown in Table 6.4. The table shows that most common ion implanted studies can be investigated via grazing lab XRD as the ω angles are close or above the lowest useable ω angle of 1.30° . Therefore, if using a self ion implanted beam in zirconium, the energy must be at least 1.2 MeV, or if using another ion species, the damage depth must be a minimum of 800 nm. This will allow a grazing incident angle of 1.30° to incorporate all the damage produced from the ion implantation and, therefore, have sufficient quality data to be analysed by TOPAS/CMWP with minimal post-processing. This suggests that ion implantation is viable for grazing incident lab XRD and that the energies must be tuned to ensure the penetration depth is significant enough.

Table 6.4: A table showing the grazing incident angles (omega angles) required to investigate ion irradiated zircaloys found in the literature.

Species	Energy/ MeV	Damage Depth/ nm	Omega (ω) Angle/ $^\circ$
C^+ [108]	1.4	1000	1.62
Si^+ [108]	1.8	1000	1.62
Cu^+ [108]	2.225	1000	1.62
Kr^+ [109]	0.1	45	0.07
Kr^{2+} [110]	1	800	1.29
Zr^+ [111]	0.6	400	0.64
Zr^{4+} [112]	40	5500	8.95

6.4 Conclusion

The objective of this chapter was to investigate the viability of using a grazing incidence geometry for CMWP analysis for the determination of crystallite size and dislocation density. This was done by measuring silicon (Si) XRD NIST standard specimen with a known crystallite size and microstrain/dislocation density. The NIST standard documentation was compared to the TOPAS and CMWP analysis of both grazing incident and Gonio geometries.

The initial investigation was to determine the lowest viable incident (ω) angle. This was conducted by testing a range of ω angles: 0.11° , 0.32° , 1.00° , 1.30° , 1.50° , 1.75° and 2.00° . It was observed that the ω angle 1.00° and below were too noisy for line profile analysis and any smoothing function effective enough to reduce the noise sufficiently would also severely affect the peak shapes. It was also ascertained that there was no significant reduction in noise from 1.30° to 2.00° . Therefore, it was determined that 1.30° was the lowest viable ω angle (corresponding to a penetration depth of 800 nm) for grazing incident line profile analysis.

When considering the Gonio diffraction and the subsequent analysis, it was found that the crystallite sizes were determined to be approximately two thirds of the NIST documentation, at 255.5 nm for the TOPAS analysis. However, the microstrain was calculated to be approximately zero, which matched the NIST standard documentation. The differences between the two sets were believed to be due to the instrumentation used and therefore, the noise-to-peak ratio and instrumental effects on the diffraction pattern. Though instrumental effects were taken into consideration, the method of fitting for the instrumental effects may have differed, between the method used and the NIST standard method, causing the difference. Furthermore, the Gonio CMWP analysis produced a vast overestimation of the crystallite size, with the dislocation density refined to zero and dislocation arrangement parameters refined to their upper limit. This was believed to be because of the absorption edges and its effects on the quality of fit. The absorption edges had very little effect when performing the TOPAS analysis, but when conducting the CMWP analysis, the phenomenon hindered the analysis as the software thought they were peaks, therefore affecting the goodness of fit. Even after the removal of the absorption edges, the fitting of the modified data still produced cut-off edges which hindered the fitting.

In the GI geometry, in both analytical techniques, the microstrain/dislocation density and dislocation arrangement parameters were also refined to approximately zero, congruent with the NIST standard documentation. With regards to the crystallite sizes, they were determined to be 225.5 nm and 235.7 nm for TOPAS and CMWP respectively. Though the two analytical techniques were in agreement with each other, they were similar to the Gonio TOPAS analysis, being approximately two thirds of the NIST standard documentation. The smoothing of the data and the instrumental effects were believed to be the main contributors to the difference in crystallite size.

From this, it can be concluded that grazing incident XRD may be viable for CMWP analysis. However, further refinement of the experimental setup, to reduce the post-data processing which was believed to be the main limiting factor in the quality of fit, is required. One suggestion could be the implementation of a piece of equipment called a 'knife edge', which focuses the X-ray beam on the sample (i.e. narrow it), and therefore, would help reduce the noise as well as possibly removing/minimising the diffused feature. Another consideration is the angle of incidence used. If GIXRD was used to look at a cold-rolled sample (e.g. with bulk damage in Zr samples from the previous experimental chapter), you can use a higher GI angle as the deformation within the material would be uniform throughout the depth of the sample. The current system had a

known crystallite size and microstrain/dislocation density of zero in order to focus on crystallite size, therefore, the next step to optimise GIXRD with CMWP would be to focus on dislocation density. Hence, using an undeformed and deformed sample, with a known crystallite size, would be the subsequent stage to better understand the evaluation of dislocation density using GIXRD with CMWP.

Considering this in the context of the viability of the method as a probe for damage in ion implanted materials, the damage will be shallower and the damage depth profile will not be uniform. The penetration depth from an 86.5 keV Zr ion (2 MeV neutron equivalent) was calculated to be 500 Å and 950 Å. These penetration depths corresponded to ω angles of 0.081° and 0.154°, which were not only lower than the lowest viable incident angle of 1.30° but also lower than the machine's lowest operational angle capability - 0.10°. However, looking at past ion implantation studies and the energies used, the penetration depths produced and the corresponding ω angles were mainly equal to or above 1.30°. Suggesting that ion implantation is viable to be analysed via grazing incident lab XRD but the ion implantation depths must be a minimum of 800 nm. This is to ensure that all the damage is encompassed within the XRD interaction volume and has minimal post-processing (i.e. smoothing) to then be analysed by TOPAS/CMWP. However, further consideration of grazing incident lab XRD setup and equipment (i.e. knife edge) may reduce this minimal damage depth to allow analysis of thinner samples.

Chapter 7

The Application of Lab HT-XRD on Hydrogen Charged Zr-4

7.1 Introduction

A common problem, that is life-limiting for the fuel rods within fission reactors, is the effect of hydrogen on the cladding material. More specifically, the hydrogen embrittlement caused in the zirconium alloy cladding within water-cooled nuclear reactors, which can lead to earlier failure of the component. During reactor operation, at the surface of the cladding, the water coolant and zirconium alloy react, forming a zirconium oxide passive layer and hydrogen [97, 230]. The hydrogen migrates into the cladding material, due to high mobility at nuclear operational temperatures (300 - 650 °C for BWR to AGRs), and remains in solution (tetrahedral interstitial sites) or within microstructural features (i.e. hydrogen trapping) [231]. This is believed to cause dilation in both axes but more prominently in the *c*-axis due to the anisotropic nature of hexagonal closed-packed (HCP) zirconium. Additionally, during post-discharge and storage, the cladding material will cool causing the hydrogen to precipitate and form hydrides. This is known to induce dislocations upon their formation and will remain after hydride dissolution [232].

Previous work, by Swan *et al.*, investigated the measurement of hydrogen trapping in cold worked zirconium alloys using high temperature synchrotron XRD (HT-sXRD) and the effects of the dissolution of hydrides on the lattice parameters (i.e lattice parameter expansion due to hydrogen dissolution) [233]. A Zircaloy-4 alloy (Zr-4) was 80% cold worked and then split, where one section was hydrogen charged to *nominally* 100 wt.ppm and the other section was left at *nominally* 10 wt.ppm. HT-sXRD was conducted from room temperature to 800 °C, where the data were analysed using Total Pattern Analysis Solutions (TOPAS) to determine the lattice parameter at each temperature point, to identify the lattice parameter expansion due to hydrogen in solution and at microstructural traps. Also, the data were analysed using Convolutional Multiple Whole Profile (CMWP) to determine the dislocation density [233]. This study was to determine the change of hydrogen in solution due to hydrogen escaping from traps, thereby determining the trap capacity and binding energy for hydrogen. Which in turn determines the extent of hydride formation to help create accurate predictive models of hydrogen embrittlement and delayed hydride cracking.

This chapter is a validation study on the use of a high temperature laboratory XRD machine (HT-XRD) to evaluate lattice parameters and dislocation density. Techniques such as HT-XRD have the potential to be used as an analogue for analysis of irradiated samples in an active nuclear facility, replicating using a hot cell for irradiated samples. A hot cell defined as bringing

‘cold’ materials back to active/‘performance’ temperatures. The HT-XRD experimentation is relatively quick and easy to setup whereas using a HT-sXRD requires a lot of preparation and high operational costs. The validation of HT-XRD for this type of study will open up the opportunity to look at active samples more routinely. The main focus of this study is to compare the use of HT-XRD and HT-sXRD (by Swan *et al.*) to evaluate the lattice parameter expansion due to the hydride dissolution. Furthermore, the study will include the comparison of CMWP results, building on the technique development study presented in Chapter 5 and Chapter 6.

7.2 Overview of Previous Work

The premise of the study by Swan *et al.* was to investigate hydrogen trapping within cold worked Zr-4 material using high temperature sXRD [233]. The study was to obtain diffraction data from two sets of samples: a sample of base hydrogen content (low hydrogen content) with additional traps induced via cold working and a sample with the same deformation and charged to known hydrogen content. The diffraction data was obtained from a cyclic temperature range: room temperature up to 800 °C and back to room temperature.

The base material, which was a recrystallised-annealed Zr-4 plate, was cathodically hydrogen-charged using a 0.1 M KOH in a H₂O solution for 24 hours. To evenly distribute the hydrogen, the sample was placed in a furnace (under argon gas) for 16 days at 500 °C. To induce the deformation within the base material and the hydrogen-charged material, they both underwent cold rolling to an 80% thickness reduction via a cross-rolling procedure (90° rotation after each pass until the desired thickness was reached). The sXRD samples were produced from both materials, via standard cutting equipment (Buehler), to the dimension of 4 x 4 x 1 mm. Following this, they were ground until they were approximately 1 mm thick. The total hydrogen contents were determined via hot vacuum extraction (HVE) at an external facility - Canadian Nuclear Laboratories (CNL). The hydrogen content was found to be 67 ± 3 wt.ppm and 9.2 ± 0.7 wt.ppm for the hydrogen charged material (Zr80CWH) and base cold worked material (Zr80CW) respectively, and these values were used for any further analysis. The sXRD diffraction scanning parameters are shown in Table 7.1. The scan time and temperature rate meant that a scan was taken over a temperature range of 0.83 K, however, to reduce noise, groups of 6 scans were averaged meaning the data was taken over a temperature range of 5 K. The sample was also never held at any given temperature.

Table 7.1: The sXRD scanning and temperature parameters used in the diffraction experiments.

Experimental Parameter	Value
Energy/ keV	80
Wavelength/ Å	0.155
Sample-detector distance/ m	1.7
$2\theta/ ^\circ$	7
Scan time/ s	10
Temperature rate/ Kmin ⁻¹	5
Temperature range/ K	293 - 1073

The data was analysed using a Le Bail model, via TOPAS, to determine microstructural information such as lattice parameters. However, due to the large data set (approximately 156 diffraction patterns), the analysis was automated using a MATLAB script, which used the output

of the previous temperature as the initial parameters for the next (e.g. the determined lattice parameter for 400 K was used as the input for 405 K).

The initial post-processing step was to calculate the total lattice expansion, which is discussed in section 7.3, and plot that against the temperature, to observe the effects of thermal expansion and hydrogen in solution on the lattice parameters. It was found that there was a relatively linear relationship, between total lattice expansion and temperature, up to 570 °C for a and c lattice parameter. After 650 °C, the paper suggests that the correlation between lattice parameter and temperature becomes less linear due to the start of recrystallisation and the effect that has on the diffraction pattern (becomes spotty - shown in Figure 4 of Swan *et al.* paper). This was supported by Nguyen *et al.*, however, at a different starting temperature but this is believed to be due to the different temperature rate (100 K/min compared to 5 K/min) [234].

The data also shows that the linear increase in the total expansion in a lattice was the same for both Zr80CW and Zr80CWH up to 200 °C, where the contribution of the hydride dissolution takes effect, and the additional expansion due to hydrogen in solution causes a non-linear deviation - evident in Figure 7 of the Swan *et al.* paper. Similar to a lattice parameter, the total expansion of c lattice parameter was the same for both Zr80CW and Zr80CWH but up to a lower temperature point of approximately 150 °C. Beyond this temperature, the deviation between the samples becomes quickly apparent due to the effects of hydride dissolution and the additional expansion. Dissimilar to the a lattice parameter, the steepest correlation between the total c lattice parameter expansion and temperature was at the higher temperatures. The data for c was not used in any further studies as the result could not be corroborated by any other investigation, mainly due to no studies on terminal solid solubility of dissolution (TSSD) of hydrogen having values as low as the ones found in this research (33.5 wt.ppm). Furthermore, the final total lattice expansions were determined to be approximately 3.6 - 4.0 % and 1.1 - 1.3 % for a and c lattice parameters respectively. This increase in lattice parameters is believed to be significant enough to be within the limits of precision of a lab XRD, hence further studies using a lab XRD to investigate the lattice parameter expansion due to hydrogen dissolution was deemed viable and necessary.

Line dislocation density studies were also carried out on Zr80CW and Zr80CWH, using CMWP, from room temperature to 800 °C using 50 °C intervals. As expected, the line dislocation density was found to decrease for both samples as temperature increased, from $16.6 \times 10^{14} \text{ m}^{-2}$ to $6.4 \times 10^{14} \text{ m}^{-2}$ at 478 °C. After this point, the CMWP analysis started to produce large dislocation density values, therefore it was assumed that the dislocation density had reached approximately zero and the continual peak broadening due to thermal expansion was affecting the CMWP fitting. Hence, the dislocation density was assumed to be zero after 473 °C. It was also discovered that there were minimal differences in the dislocation density values between Zr80CW and Zr80CWH, which contradicts the literature, which states that hydrogen in traps may stabilise dislocations.

7.3 Methodology

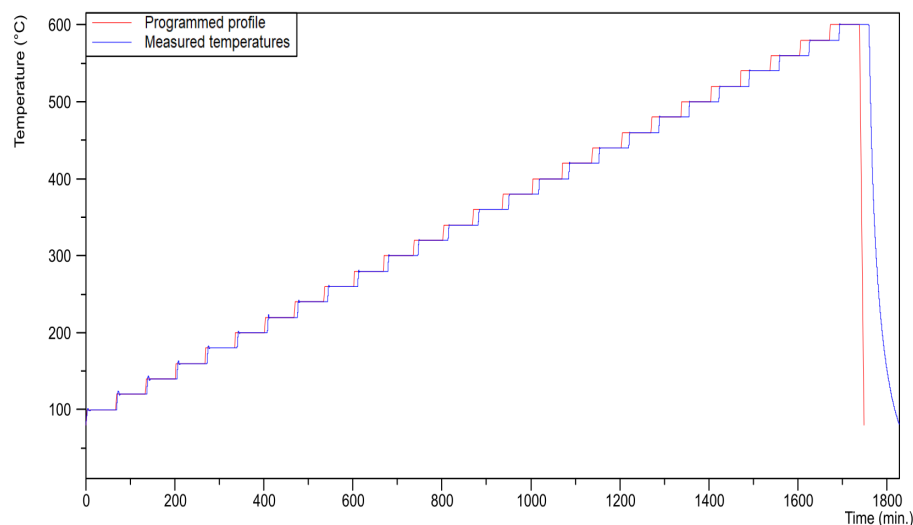
Three different samples were prepared for HT-XRD: Zr-4 + 80% cold worked (Zr80CWA), Zr-4 + 80% cold worked + hydrogen charged (Zr80CWH) and Zr-4 + 80% cold worked from a different region of the original bulk material (Zr80CWB). The Zr80CWA and Zr80CWB samples were *nominally* 10 wt.ppm hydrogen content but, with an HVE measurement in the parental material, were found to contain approximately 30 wt.ppm hydrogen content. The Zr80CWH

sample was *nominally* charged to 100 wt.ppm of hydrogen, however, after an HVE test at CNL, was found to be 67 wt.ppm.

The three samples provided by NNL were sectioned, using a Struers Secotom-50, so that they had a 10 x 10 mm surface and the sample depth was approximately 1 mm. Each sample was cold mounted using an Epoxy Resin. This was used instead of hot mounting to ensure no deformation annealing and to prevent the uptake/release of hydrogen which would change the hydrogen content. The Epoxy Resin was made with a mass ratio of 7:3 epoxy to hardener, which was then left to set in a vacuum to remove any bubbles in the resin. The resin had set after approximately 24 hours. Once the resin was set, the samples had the top layer of resin and oxide removed, with a course grinding paper (P240), on a Buehler Automet before it was prepared and removed from resin for XRD, using the method stated in section 4.2 on page 47.

The samples, along with a standard Lanthanum Hexaboride (LaB_6), were scanned in a high temperature XRD geometry using an XYZ stage. The alignment of the samples was carried out to ensure that the surface of the sample was in the centre of the beam. In this circumstance, the direct beam half-cut method was used for all samples, where the XYZ stage was moved in the Z direction until the counts per second were half of its maximum value.

The samples were scanned using a Cu source Panalytical X'Pert, the instrument parameters are presented in Section 4.4.3. The temperature range at which the samples were scanned was room temperature to 600 °C (high active nuclear reactor temperature - 600°C for AGRs) [25]. The first scan was at room temperature, the second scan was at 100 °C and then all subsequent scans were every 20 °C until 600 °C, totalling 27 scans. An example of the heating profile is shown in Figure 7.1. The samples were held at each temperature for 5 minutes before the scan was taken. This differed from HT-sXRD as the samples were much larger in HT-XRD, therefore it was to ensure the temperature had stabilised and equilibrium was reached at each temperature. The scans were longer than HT-sXRD, with it being an hour long, to compensate for the lower signal-to-noise ratio in HT-XRD. The scanning parameters are found in section 4.4 on page 54.



lab XRD instrument was used to produce a master INP file. The INP files included both the zirconium and zirconium hydride phases, which were allowed to be refined throughout the whole temperature range, including after the hydride peaks disappeared. The initial lab XRD INP file was created by refining the standard to obtain the instrumental parameters and then running an initial refinement on one of the samples. One of the main differences between the initial and the master input file was the ability to use the master INP file via a MATLAB code which automates the fitting and refining process for all the samples sequentially. The XY files of the data had to be labelled with a five digit suffix (e.g. Zr80CWA_00001.xy', where '00001' was the room temperature sample and '00027' was the 600 °C sample). The MATLAB script then ran the master INP file, starting at '00001' to determine the a and c lattice parameters, whilst also refining the crystallite size profile using the Lorentzian function and the strain profile using the Gaussian function. The MATLAB code was provided for us by NNL.

The script used the previous sample's refining parameters and the resulting master INP file as starting parameters for the following samples. This was to have starting parameters in a closer remit to achieve an appropriate fit. The data were also run in reverse order, 600 °C to room temperature, to check the accuracy of the fittings via MATLAB and to confirm whether the parameters calculated were independent of the fitting method. This was done by reversing the numbers on the files and then using the master INP file from the first run as the initial master INP file. The fittings were checked manually at approximately every 100°C, to ensure the MATLAB script was running correctly.

The output file from the batch MATLAB fitting was then processed in order to get the required data, which was a and c lattice parameters with their corresponding temperature. The a and c lattice parameters, separately, for each sample were plotted against each other to determine the difference between the samples. The lattice parameters were then, using Equation 7.1 and Equation 7.2, converted to total lattice parameter expansion. This was done to be able to compare results against the sXRD data presented in Swan *et al.* [233].

$$\varepsilon_a = \frac{a - a_0}{a} \quad (7.1)$$

$$\varepsilon_c = \frac{c - c_0}{c} \quad (7.2)$$

For the CMWP analysis, a LaB₆ sample was run in the HT-XRD geometry but only at room temperature. This was used to determine the instrumental effects and assumed the same for the samples at all temperatures. The processing of the LaB₆ was the same as described in Chapter 4. Due to the data being fairly noisy, the individual peaks were fitted using a Pearson7 function in Fityk (peak fitting software) in order to produce smoother peaks that would be usable for CMWP. Time constraints and duration of CMWP analysis for each sample meant that only every 100°C was a sample analysed, including room temperature. The peak index file was created, in order to locate the peaks for each phase, for all three samples, including all three phases: alpha zirconium, delta zirconium hydride and the alumina crucible (Al₂O₃). This third phase was included because some unexpected peaks appeared in the diffraction pattern (as described in the following section). The third phase was identified using the ICSD database and comparing plausible phases that were likely to occur and using measured diffraction patterns of Al₂O₃.

7.4 Results

7.4.1 Qualitative Diffraction Pattern Analysis

When inspecting the diffraction pattern of Zr80CWA, it was determined that there were three distinct separate phases: α -zirconium, δ -zirconium hydride and an unknown tertiary phase, as shown in Figure 7.2.

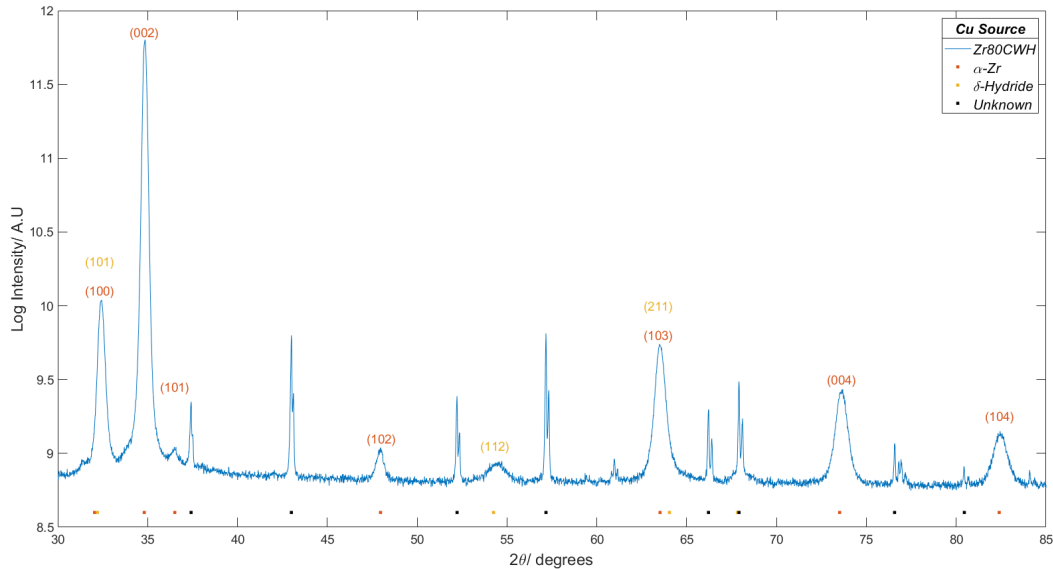


Figure 7.2: An example of a peak indexed sample, with the unknown tertiary phase.

Initially, it was thought that there could have been some surface contamination, however, the peaks were significant, which would be unlikely for any contamination, hence this was ruled out. Another possibility was that the beam footprint could have been larger than the sample, and the beam could have interacted with the crucible, hence producing a signal for Al_2O_3 . This was confirmed when overlaying the alumina crucible diffraction pattern on the HTXRD diffraction patterns for all three samples (Figure 7.3). Two Al_2O_3 diffraction patterns were used: one with the crucible's surface aligned with the centre of the beam and one where the surface was offset by the height of a sample. The offset Al_2O_3 sample provided diffraction peaks that were shifted from their original positions and these peaks aligned with the lower 2θ angles (up to approximately 65°), whereas the aligned Al_2O_3 sample provided diffraction peaks that aligned with the higher 2θ angles (above 65°).

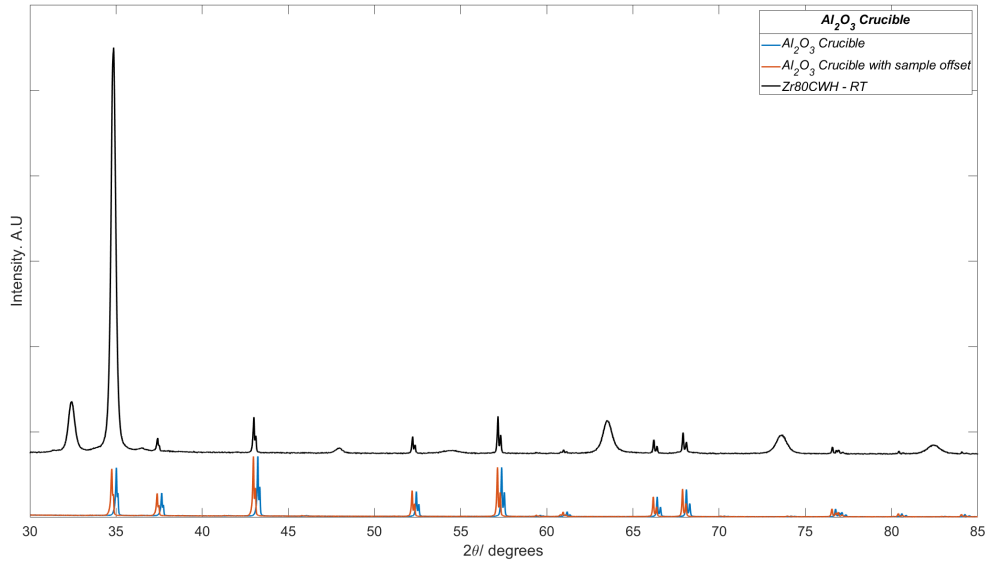


Figure 7.3: Phase identification of the tertiary phase in the HTXRD experiments, resulting in the identification of Al_2O_3 .

The diffraction patterns for Zr80CWA at room temperature to 600 °C are shown stacked in Figure 7.4, where the room temperature scan is at the top and the 600 °C sample is at the bottom. As the temperature increases, there is a decrease in the peak broadening of the zirconium peaks (indicated by crosses), which was due to the annealing of dislocations, decreasing the strain within the system. This can be seen clearly in the peaks at approximately 49°, 63°, 73° and 83° in Figure 7.4. The material where the Zr80CWA sample originated underwent HVE and was found to have a hydrogen content of approximately 10 wt.ppm, which is considered low enough that the presence will be minimal on the diffraction patterns in the form of small hydride peaks. However, in the case of Zr80CWA, when measured characterised by XRD, very prominent hydride peaks were observed, suggesting that the sample contained a higher concentration of hydrogen than initially expected [233, 235]. This was determined to be approximately 30 wt.ppm, via HVE, when looking at another sample from the parent material. At approximately 32° (2θ), the delta hydride peak, with an increasing temperature can be seen to reduce in intensity and then disappear at 200 °C. This is believed to be due to the dissolution of hydrides, where all hydrogen goes back into solution or microstructural traps.

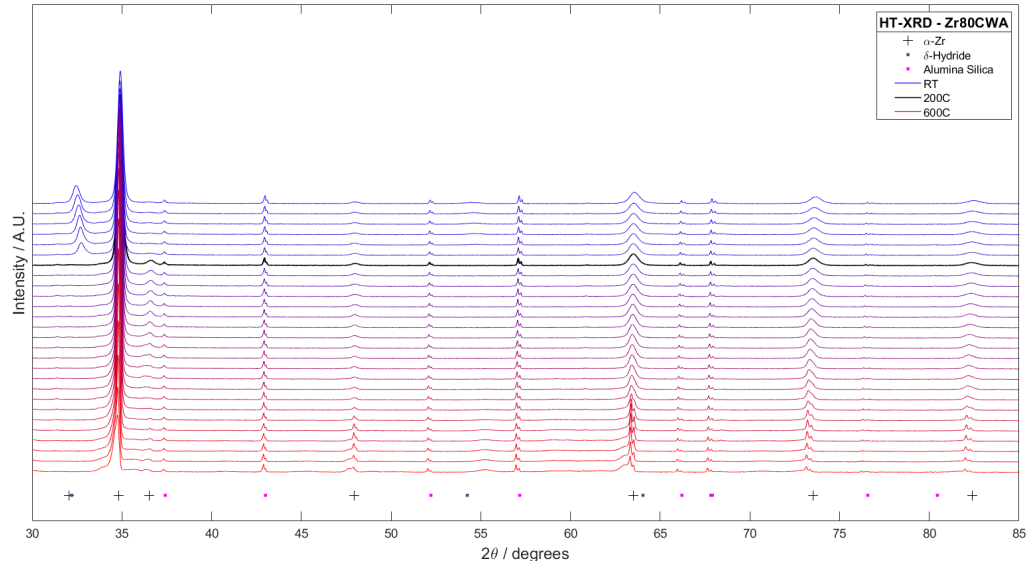


Figure 7.4: A comparison of the diffraction patterns, from room temperature to 600 °C (blue to red colour gradient), for Zr80CWA. The temperature at which the hydride peaks disappear is indicated by the black line - which is at 200 °C.

At the higher temperatures (above 460 °C), to the left of the (002) peak (indicated by a green circle in Figure 7.5), there appears to be a shoulder. Initially, it was thought to be due to satellite peaks or a phase change but that was deemed not plausible. However, another thought was that there could be leaching of Al from the alumina crucible into the Zr material, from the bottom of the sample and reaching within the area on x-ray interaction, causing lattice distortion at the very bottom of the sample [236]. The lattice distortion produced by the Al in the matrix could cause a change in d -spacing for the (002) plane, therefore, causing a peak shift. However, as there would be only a small amount of lattice distortion and the gradient at which that would occur would depend on the leaching gradient of the Al, a small and very broad peak would be created, presenting itself as a shoulder of the (002) peak. This shoulder is also present at (102) and (103) peaks, indicated by the blue and yellow circle respectively, as shown in Figure 7.5. The cause of the shoulder was not ascertained.

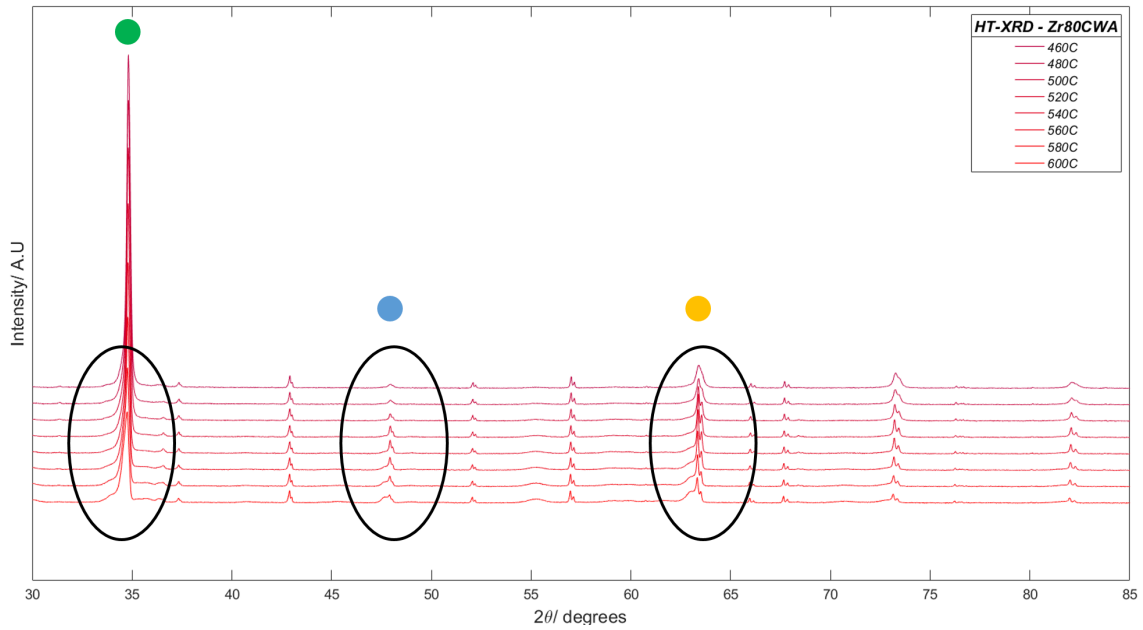


Figure 7.5: The formation of a shoulder at the left of (002), (102) and (103) peaks, above 460 °C. These hkl peaks are indicated by green, blue and yellow circles respectively.

Zr80CWH was hydrogen charged to a nominal concentration of 100 wt.ppm but was found to be approximately 67 wt.ppm via HVE. The Zr80CWH diffraction data can be found in Figure 7.6, showing the comparison of the data from room temperature to 600 °C, where the room temperature data is at the top and the 600 °C is at the bottom. As with Zr80CWA, as the temperature increased, there was a decrease in peak broadening in the zirconium peaks, which is seen at 49°, 63°, 73° and 83°, indicating anneal of the dislocations. The delta hydride peak disappears at 260 °C, a higher temperature than Zr80CWA, suggesting that there was more hydrogen within Zr80CWH, which was expected.

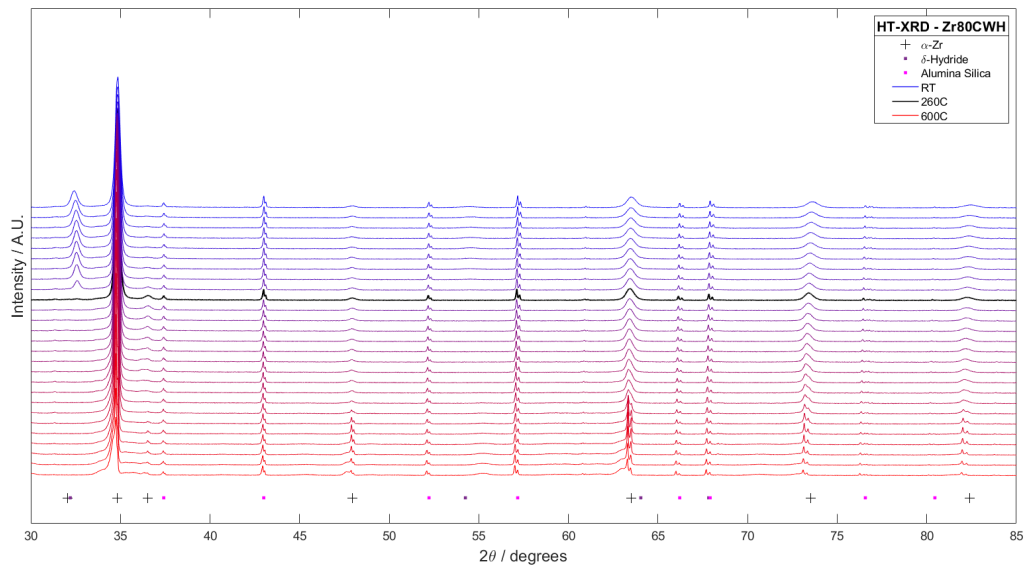


Figure 7.6: A comparison of the diffraction patterns, from room temperature to 600 °C (blue to red colour gradient), for Zr80CWH. The temperature at which the hydride peaks disappear is indicated by the black line - which is at 260 °C.

A similar trend to Zr80CWA and Zr80CWH was found with Zr80CWB, with regards to zirconium peaks reducing in broadness and hydride peaks reducing and eventually disappearing as temperature increases. The Zr80CWB sample was meant to be a material from the same parent material as Zr80CWA, with a hydrogen content of either *nominally* 10 wt.ppm or 30 wt.ppm (calculated via HVE by NNL). However, as it can be seen in Figure 7.7, the (111) peak of the delta hydride phase disappears at 280°C, which was not only higher than the original Zr80CWA sample but higher than the Zr80CWH (a sample that was intentionally hydrogen charged).

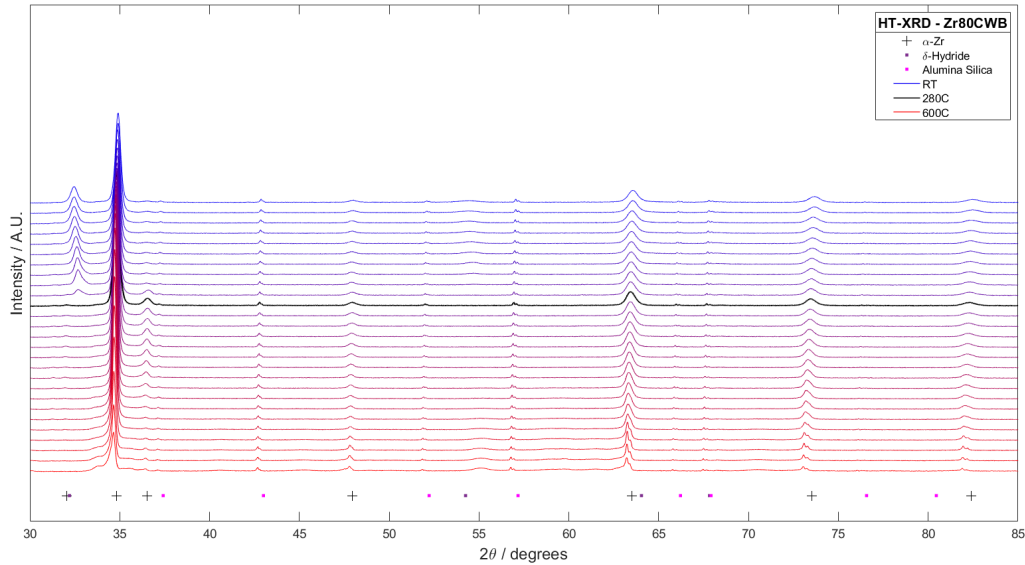


Figure 7.7: A comparison of the diffraction patterns, from room temperature to 600 °C (blue to red colour gradient), for Zr80CWB. The temperature at which the hydride peaks disappear is indicated by the black line - which is at 280 °C.

7.4.2 Hydrogen Content

To quantify the hydrogen content of the three samples, literature was used to obtain terminal solid solubility for dissolution (TSSD) curves of hydrogen in zirconium systems - which can be found in Section 2.2.7 (Figures 2.13 - 2.14). As the temperature at which all hydrogen had dissolved back into the matrix and microstructure traps is known for each sample, elucidated by the temperature at which all hydride peaks disappear from the diffraction data, the hydrogen content can be interpolated from the TSSD curves - these hydrogen content values were categorised as ‘actual’ hydrogen content values. The literature demonstrated multiple methods in which the TSSD and hydrogen content was measured, therefore, the H content was calculated by averaging the values determined from all three TSSD curves. The average hydrogen content for Zr80CWA, Zr80CWH and Zr80CWB was 11 wt.ppm, 34.7 ± 1.8 wt.ppm and 52 ± 2.1 wt.ppm respectively. The ‘actual’ hydrogen content values were then compared against the measured hydrogen content values which is displayed in Figure 7.8. The diagonal black line representing the ideal hydrogen content, where the actual and expected hydrogen content values were equal.

From Figure 7.8, it can be seen that the actual and expected H content are drastically different, bar Zr80CWA. The reason for this could be: 1) the Zr80CWA parent material was inhomogeneous in its composition, 2) due to the unknown conditions they were stored in or for how long, which could have affected the hydrogen content 3) a different sample could have been accidentally provided.

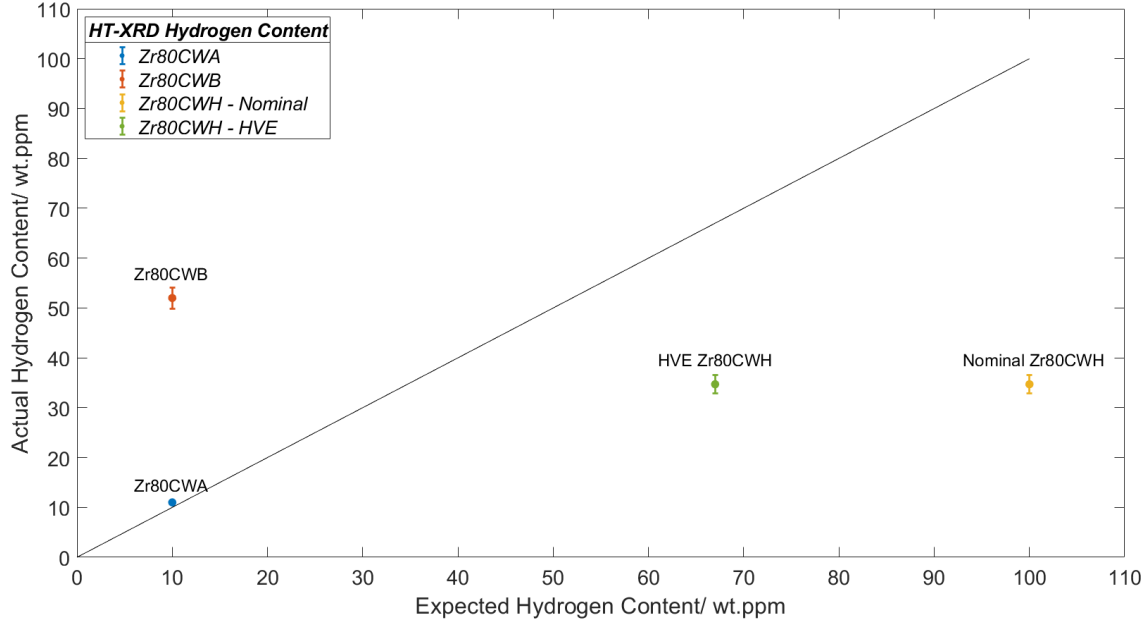


Figure 7.8: A graph showing the comparison of ‘expected’ hydrogen content values, determined through HVE measurements or nominal state, and the ‘actual’ hydrogen content values, determined through interpolations of TSSD curves found in literature.

7.4.3 Lattice Parameter Expansion

The analysis of the diffraction patterns for each sample to obtain lattice parameters, for the whole temperature range, was done using a Le Bail fit in TOPAS. The focus of the analysis was to determine the lattice parameters expansion from hydrogen entrapment and swelling, by removing the thermal expansion profile which would have been determined from a non-hydrogen charged sample. The lattice parameter expansion from hydrogen would be obtained by determining the total lattice parameter expansion from a sample containing hydrogen and removing the total lattice parameter expansion from a sample containing minimal hydrogen. As none of the samples that were tested had minimal hydrogen content, the thermal expansion of the lattice parameters could not be obtained as the effects of hydrogen and temperature could not be separated. However, the overall trend of the lattice parameter expansion was still investigated.

An example of the lattice parameter expansion, for both a (blue line) and c (red line) lattice parameter, from room temperature to 600 °C is shown in Figure 7.9. There can be seen a relatively linear increase in c lattice parameter as expected up to the hydrogen saturation solubility limit within Zr. After the hydrogen saturation point, the expansion is believed to slow down once there is no more hydrogen available to enter the solution from traps or hydrides. However, the lattice parameter is currently dominated by thermal expansion, therefore, the plateau would not be seen unless the thermal expansion could be subtracted from the total lattice expansion or the hydrogen saturation point had not been met [97, 101].

For a lattice parameter, it can be observed that there is a slow decrease until 540 °C (with some fluctuations) and then a drastic increase until 600 °C. When looking at the data as a whole, the trend that occurs does not seem realistic as the a lattice parameter should not decrease with the increase in hydrogen in solution. Furthermore, the release of intergranular strains (Type II strain) was a potential cause in the change in a lattice parameter, however, Type II strain parameters were not required for the fitting and therefore was believed not to be the cause.

As the lattice parameter expansion is dominated by thermal expansion, a lattice parameter should still increase steadily. The inaccuracy in lattice parameter is believed to be due to the geometry of the lab XRD and the orientation of the crystallite in a cold rolled material; the correlation between XRD geometry and crystallite orientation is explained later in this section. Another theory for the inaccuracy of the a lattice parameter was the change in sample surface height due to thermal expansion, however, the TOPAS fitting accounted for that by refining the ‘sample displacement’ parameter which incorporates height displacement for thermal expansion. Therefore, this was ruled out as a contributing factor for any inaccuracies during the whole diffraction pattern analysis.

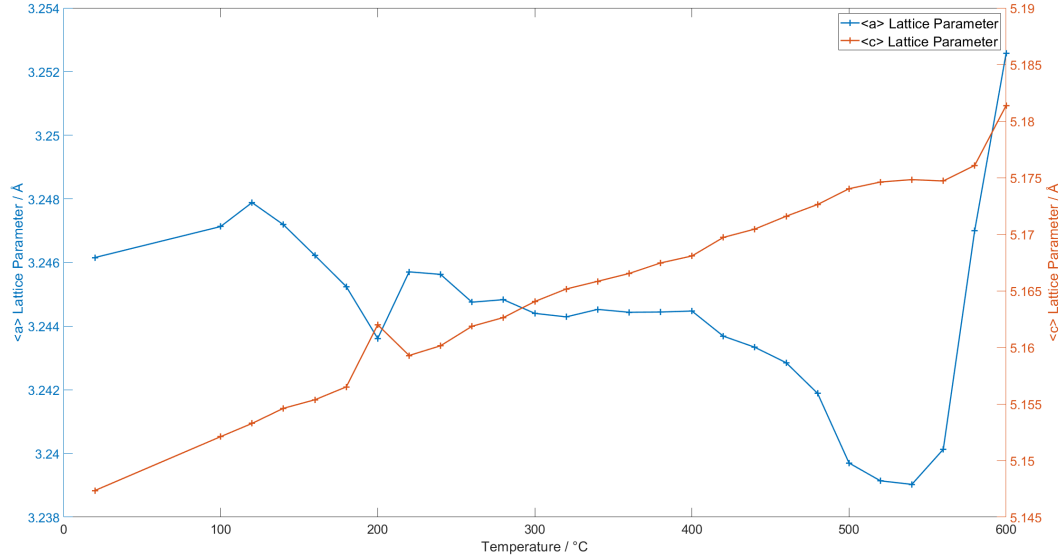


Figure 7.9: An example of the trend of both a and c lattice parameter expansion, from HT-XRD, for Zr80CWA from room temperature to 600 °C.

An anomalous result is present at 200 °C for sample Zr80CWA for both a and c lattice parameter, in which there is a decrease and increase in the lattice parameter respectively. Looking at the diffraction patterns for 200 °C and the surrounding temperatures, no significant visual difference between the zirconium peaks can be seen, however, between 180 - 200 °C the hydride peak disappears, therefore, this could be a possible reason for the change in lattice parameter. Having said that, this does not explain why the lattice parameter drops back to the original trend or the fact that neither the Zr80CWH nor the Zr80CWB data have the same change in lattice parameter, making this a less plausible explanation. Another possible explanation is the quality of the fit at 200 °C for Zr80CWA; Figure 7.10 shows the comparison of the GOF values (defined as r_p/r_{exp}) for Zr80CWA, Zr80CWB and Zr80CWH. Though there seems to be a decrease in a goodness of fit (GOF) at 200 °C, there is a similar trend with the Zr80CWB and Zr80CWH at their respective temperature where the delta hydride peak disappears. This, however, does not correlate to any spike in the lattice parameter data.

From Figure 7.10, it can be seen that the goodness of fit is relatively good (closer to one) up to the transition temperature at which the hydrides go back into solution/microstructural traps. Once the hydrogen is fully back in solution/traps, the GOF starts to increase and fluctuate. At the temperature at which the artefacts appear (approximately 460 °C), GOF increased even more. As the TOPAS analysis was a fairly straightforward refinement process with the lattice parameter, crystallite size and microstrain being the only parameters being refined, there were

no parameters that could highly affect the fitting and cause a spike in lattice parameters. A plausible explanation for this is the appearance of artefacts at higher temperatures that seem to overlap with the zirconium peaks. The aforementioned reason will cause difficulties in fitting the diffraction patterns, though being representative of the lattice parameter expansion trend, there may be some slight inaccuracy with specific values.

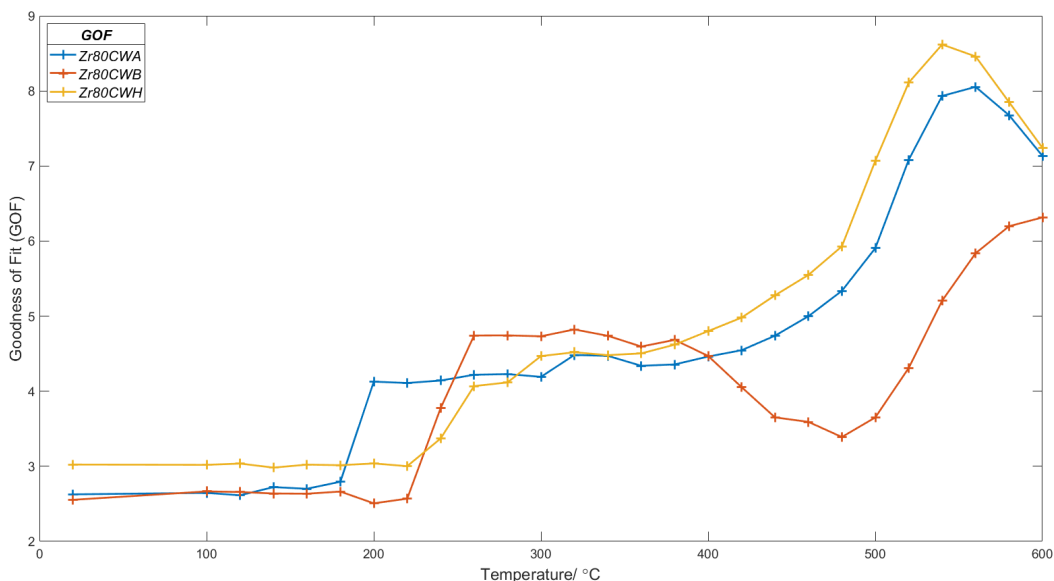


Figure 7.10: A comparison of the goodness of fit (GOF) values, from the TOPAS analysis, for Zr80CWA, Zr80CWB and Zr80CWH.

As stated in the Methodology, the TOPAS analysis included both the zirconium and zirconium hydride phase in the analysis throughout the temperature range, including after the hydride peaks disappeared. As the hydride phase was included during analysis when there was no hydride peaks present, it was believed that it could possibly contribute to the background and therefore affect the overall fitting. However, this was deemed not the case as can be seen by an example fitting of Zr80CWA at 340 °C, where no hydride peaks are present. This is shown in Figure 7.11. The straight black line represents the hydride phase contribution, the red line represents the zirconium contribution and the blue line is the measure diffraction pattern.

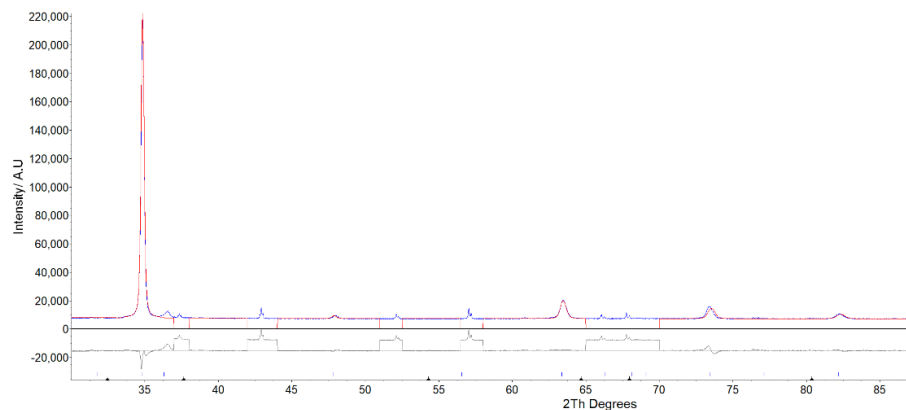


Figure 7.11: An example of a Le Bail TOPAS fitting of Zr80CWA, at 340 °C, to show the contribution of the hydride phase once the hydride peaks have disappeared.

With a material (i.e. zirconium) that has been cold rolled, especially heavily deformed material, there will be crystallite alignment. In these deformed samples, there is usually a high proportion of the basal planes that are near-parallel to the surface and the axial planes will be perpendicular to the surface as demonstrated in Figure 7.12. Therefore in the lab XRD setup shown in Figure 7.12a, where the X-rays are diffracted back out of the sample, the majority of the microstructural information will be determined from the latitudinal axis/basal plane spacing (i.e. c lattice parameter). This is because to achieve a diffraction pattern, constructive interference needs to occur, which in this circumstance, occurs from the basal plane due to its position relative to the scattering vector and the detector. It can be surmised, that due to the texture leading to minimal axial planes aligning with Bragg conditions, minimal data on the a lattice parameter will be collected meaning that the data would have larger errors or less representative of the Zirc-4 sample.

Whereas for the c lattice parameter, as the constructive interference will, theoretically, mainly be coming from between basal planes, the microstructural information will correlate more to the c lattice parameter, suggesting that it will be more representative of what is occurring in the Zirc-4 sample.

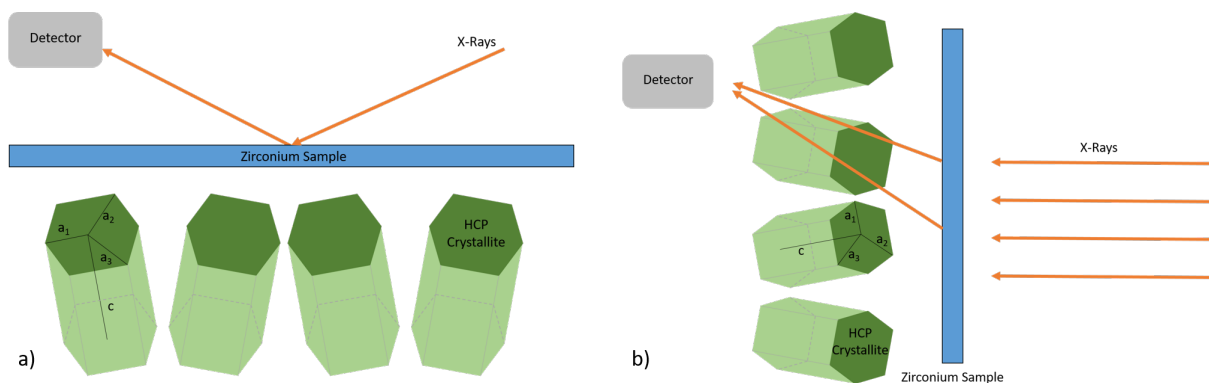


Figure 7.12: A schematic diagram of a) lab and b) synchrotron XRD with the alignment of grains, due to cold rolling, to demonstrate the effects on the diffraction pattern.

For a sXRD setup, where the diffraction principle is via transmission and not reflection (Figure 7.12b), the alignment of the grains is believed to have the opposite effect. In transmission XRD, with grain alignment, the majority of the microstructural information will come from the longitudinal axis (a lattice parameter). This is because the basal planes, will likely not diffract the X-rays to the detector due to the relation between the basal plane, scattering vector and the detector. Whereas the axial planes, which relate to the a lattice parameter, are more likely to diffract towards the detector. Therefore, it is believed that lattice parameter results relating to c are less reliable and not representative of the crystal structure. The effects of the grain alignment can be seen in the sXRD diffraction pattern of Zr80CWA, Figure 7.13, where the (0002) plane signal is very weak.

In Figure 7.9, there can be seen an increase in a and c lattice parameters after approximately 520 °C, which could be the result of the loss of texture at high temperature. At the higher temperatures, the orientational effects may be annealed out, therefore, it is possible to get better a and c correlation at those higher temperatures. However, looking at the literature, it suggests that the texture in zirconium is very unlikely to change unless undergoing a long heat treatment process at high temperatures. Therefore, this theory was deemed not viable for the HT-XRD data and the reason behind the sudden spike after 520 °C is still unknown.

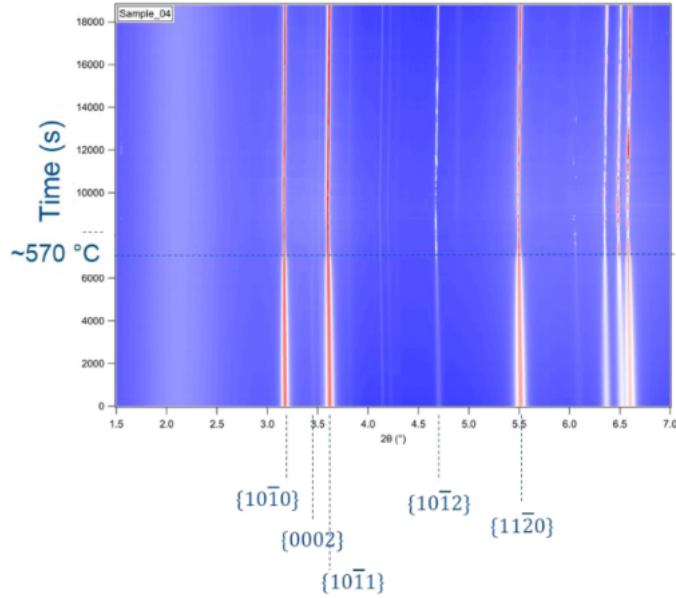


Figure 7.13: A diffraction pattern of Zr80CWA via sXRD, showing the faint signal from the basal plane (0002) [233].

The synchrotron paper by Swan *et al.* presents the lattice parameter expansion as a percentage of the expansion (i.e. total lattice parameter expansion), as shown in Figure 7.14 and Figure 7.17. In order to compare the lab XRD and synchrotron data, the lattice parameter expansion for the XRD was converted into total expansion, as described in Section 7.3. The primary basal peak in the sXRD diffraction pattern (Figure 7.13, (0002), was showing a very faint signal, validating the grain alignment explanation above, where the evaluated c lattice parameter results are likely to be less representative of the actual c lattice parameter.

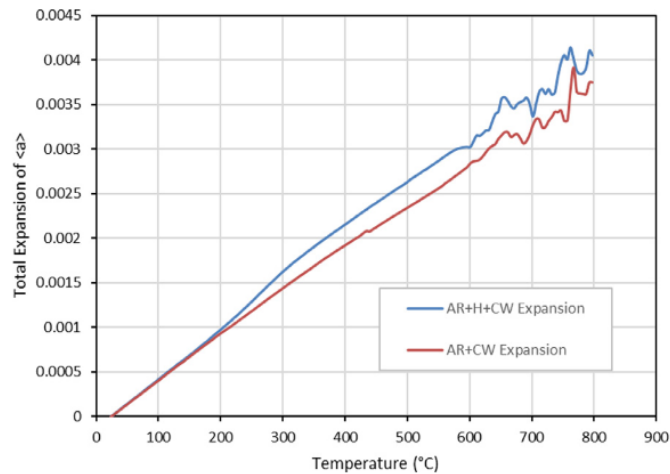


Figure 7.14: A comparison of the a lattice parameters, from HT-sXRD, for Zr80CWA and Zr80CWH from room temperature to 800 °C [233]

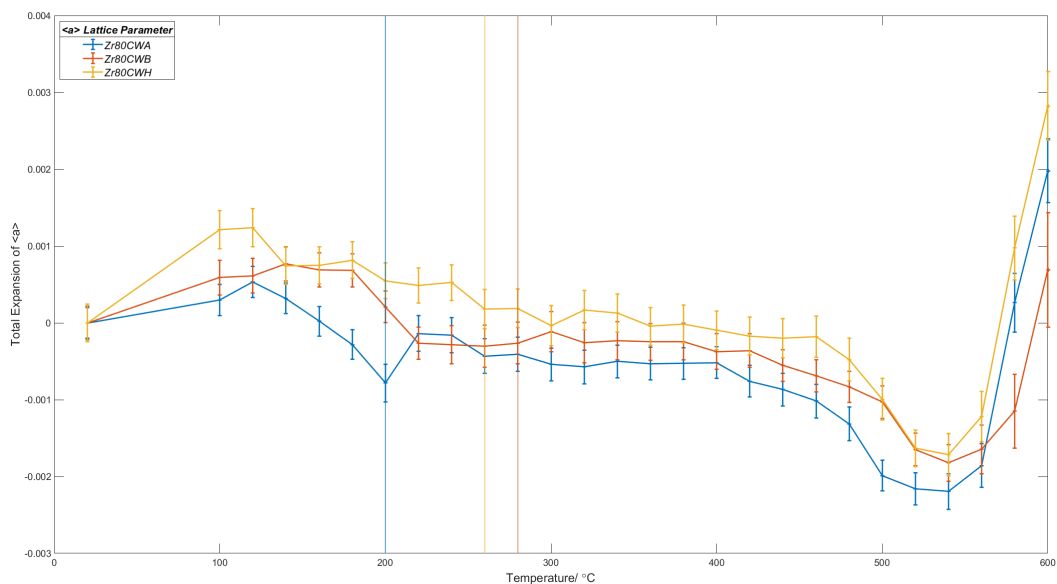


Figure 7.15: A comparison of the a lattice parameters, from HT-XRD Le Bail TOPAS analysis, for Zr80CWA, Zr80CWB and Zr80CWH from room temperature to 600 °C. The vertical lines indicate the temperature at which the hydride peaks disappear for their respective samples.

Comparing Figure 7.14 and Figure 7.15, there can be seen a drastic difference between the HT-XRD and HT-sXRD total expansion for a . There is, with HT-sXRD, a linear increase of the a lattice parameter up to 600 °C, thereafter there is still an increase but with some fluctuation. Suggesting the data past 600 °C could be going through a recrystallisation process, leading to less texture being observed; the difference in signal between a high and low temperature scan can be seen in Figure 7.16. The spottiness of the 670 °C diffraction indicates a change in texture and the possible recrystallisation of the material [233, 234].

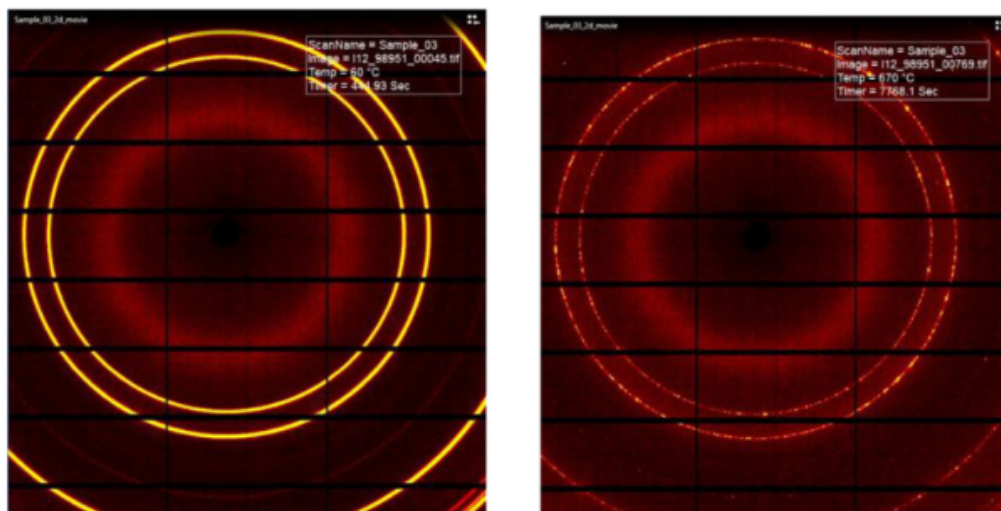


Figure 7.16: A comparison of the two diffraction patterns of Zr80CWH, from HT-sXRD, at 60 °C (left) and 670 °C (right), to show the difference in intensities [233].

In spite of the differences in the general trend for total a lattice parameter expansion between

the two equipment setups, the final total expansion for both, at 600 °C for Zr80CWH, were very close (~ 0.003 and ~ 0.0028 for HT-sXRD and HT-XRD respectively). Whereas for Zr80CWA, the difference between the two was more significant (~ 0.0027 and ~ 0.002 for HT-sXRD and HT-XRD respectively). The difference between the two samples most likely comes from the more accurate representation of the a lattice parameter expansion from HT-sXRD.

The total c lattice parameter expansion for both HT-sXRD and HT-XRD are shown in Figure 7.17 and Figure 7.18 respectively. When comparing the two, for all samples, there is observed a linear increase in the total lattice expansion up to 600 °C. However for the HT-sXRD, similarly to the a lattice parameter, after the 600 °C there is still an increase but there are fluctuations with the data. The total c expansion for Zr80CWA, at 600 °C, was approximately 0.0081 and 0.0065 for HT-sXRD and HT-XRD respectively, which shows a significant difference between the two. With the Zr80CWH sample, the total expansion at 600 °C was roughly 0.01 and 0.0075 for HT-sXRD and HT-XRD respectively. The total expansion for the HT-sXRD was determined to be bigger for both samples but this is believed to be due to the faint (0002) plane. Where peaks are broader at higher 2θ , and TOPAS is weighted based on the primary peak, there could be some inaccuracies in the HT-sXRD analysis. The HT-sXRD data is missing its primary peak, therefore it is plausible that due to the fitting bias, there is an overestimation of the lattice parameters, consequently producing a higher overall total lattice expansion [237].

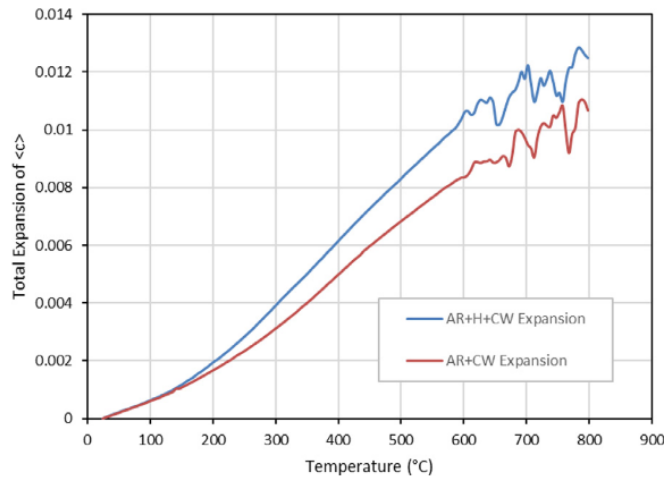


Figure 7.17: A comparison of the c lattice parameters, from HT-sXRD, for Zr80CWA and Zr80CWH from room temperature to 800 °C [233].

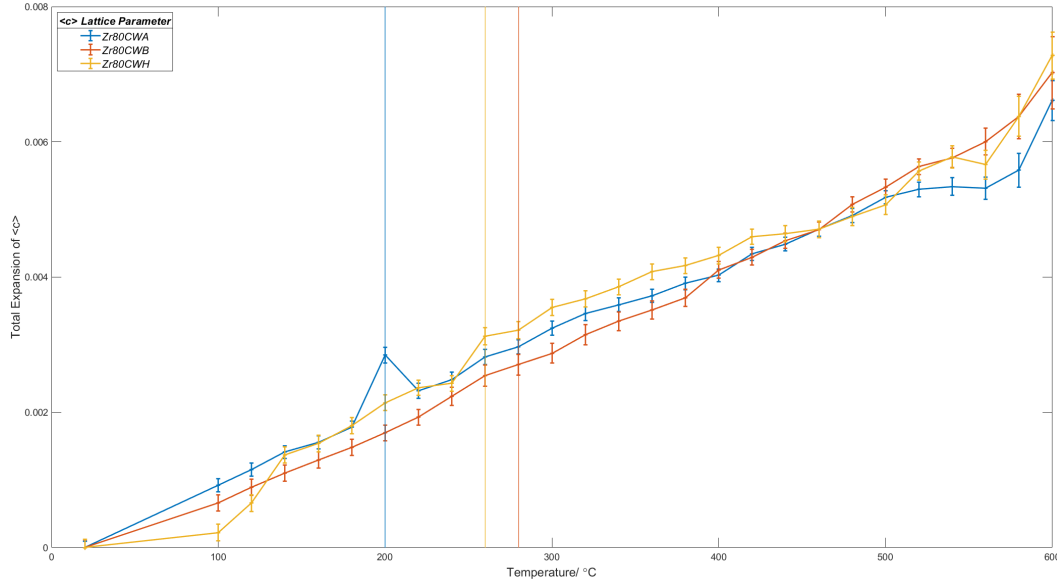


Figure 7.18: A comparison of the c lattice parameters, from HT-XRD Le Bail TOPAS analysis, for Zr80CWA, Zr80CWB and Zr80CWH from room temperature to 600 °C. The vertical lines indicate the temperature at which the hydride peaks disappear for their respective samples.

To further examine the data and to check the validity of the trend found in whole diffraction pattern analysis, single peak TOPAS analysis was conducted using a similar method to previously used. When conducting the single peak analysis, the ‘Sample Displacement’ and ‘Zero Error’ parameters were fixed once the value for room temperature was found. This was to limit the number of unknowns in the analysis and was believed to provide more accurate values for the desired parameters. Initially, the 104 Zr peak was chosen due to it not being severely affected by the artefacts at the higher temperatures as well as having no overlapping peaks with the hydride phase. When analysed it was found to have a similar trend in the c lattice parameters, where there could be seen a steady increase in c lattice parameter. However, with a lattice parameter, not only was there no general trend but there seemed to be a binning issue (i.e. various plateau regions). The cause of this was believed to be due to the analysis of a plane where both a and c lattice parameter was required to be refined during a single peak analysis (i.e. too many unknowns refining for a single peak analysis).

To overcome this, the 004 peak was analysed to determine the c lattice parameter expansion. This was achieved by fixing the a lattice parameter at the value determined from a whole diffraction pattern analysis at room temperature (an initial room temperature scan before HT-XRD scans). The 104 peak was then re-analysed, fixing the c lattice parameter at the value determined for each temperature from the previous analysis. The total lattice parameter expansion from both analyses is shown in Figure 7.19. There can be seen a relative linear relation for both a and c lattice parameters. Fluctuations can be seen in both lattice parameters and are likely to be contributed to the fixing of ‘Sample Displacement’, ‘Zero Error’ and either a or c lattice parameter. Also, though the artefacts were very small, it is likely they contributed to the fluctuation in data past 460 °C. Looking at the final total lattice parameter expansion values, in the case of both a and c lattice parameters, they are double the final total lattice parameter expansion values determined via the global fitting. This is believed to be due to the incorporation of the fixed ‘Sample Displacement’ and ‘Zero Error’ parameters, and therefore considered to be

inaccurate. Hence, it is believed that the single peak analysis did validate the trend found within the global fitting but could not be used as a comparison due to the inaccuracies in the total lattice parameter expansion values from the assumption made to conduct the analysis.

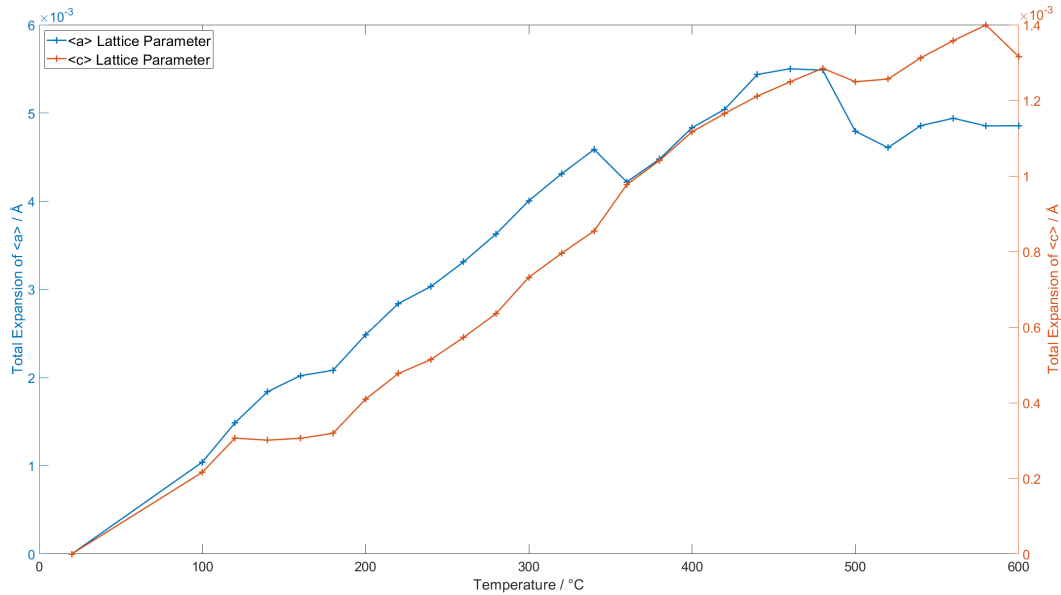


Figure 7.19: The trend determined for the total lattice parameter expansion of both *a* and *c* lattice parameter from HT-XRD data. The analysis was conducted on Zr80CWA, from room temperature to 600 °C, specifically on two separate peaks - 004 peak for *c* lattice parameter and 104 Zr peak for *a* lattice parameter.

There was no baseline sample, with no hydride effects, to remove the effects of thermal expansion and determine the correlation between lattice parameter expansion and primarily hydrogen dissolution. Therefore, it was attempted to determine the effects of hydrogen dissolution on lattice parameter expansion between the samples of calculated hydrogen content. The total lattice parameter expansion from Zr80CWA (11 wt.ppm) was removed from Zr80CWH and Zr80CWB (34.7 and 52 wt.ppm), which is shown in Figure 7.20. However, in both cases of *a* and *c* lattice parameters, no distinct correlation can be seen. Therefore, future work is still required to determine the effects of hydrogen on lattice parameters within zirconium using lab XRD.

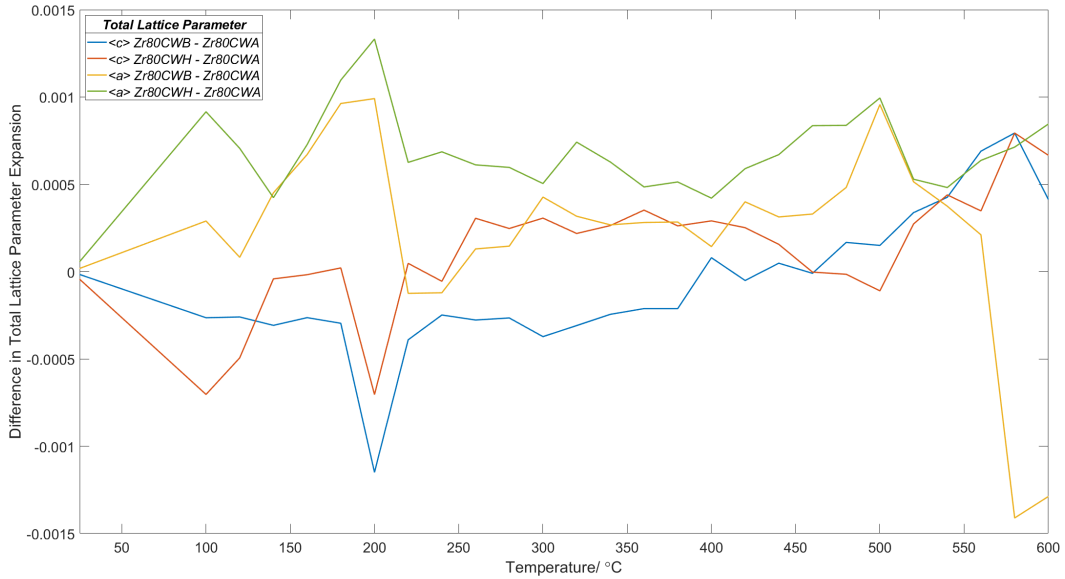


Figure 7.20: A graphical representation of the difference in total lattice parameter expansion to determine the effects of hydrogen dissolution on said expansion. The difference between Zr80CWA-Zr80CWH (Δ 23.7 wt.ppm) and Zr80CWA-Zr80CWH (Δ 41 wt.ppm) for both a and c total lattice parameter expansion is shown in red/green and blue/yellow respectively.

7.4.4 CMWP - Line Dislocation Density

CMWP analysis was conducted on both the HT-sXRD and HT-XRD for Zr80CWA and Zr80CWH data as shown in Figure 7.21 and Figure 7.22 respectively. In Figure 7.21, the dislocation density for both samples starts approximately at $18 \times 10^{14} \text{m}^{-2}$ and then with increasing temperature, starts to decrease as the dislocations begin to anneal out. The final value for Zr80CWA was at approximately $7 \times 10^{14} \text{m}^{-2}$ at 500 °C, whereas Zr80CWH final dislocation density measurement was at 600 °C with a value of approximately $3 \times 10^{14} \text{m}^{-2}$. The graph from Figure 7.21 is taken directly from Swan *et al.*'s paper [233].

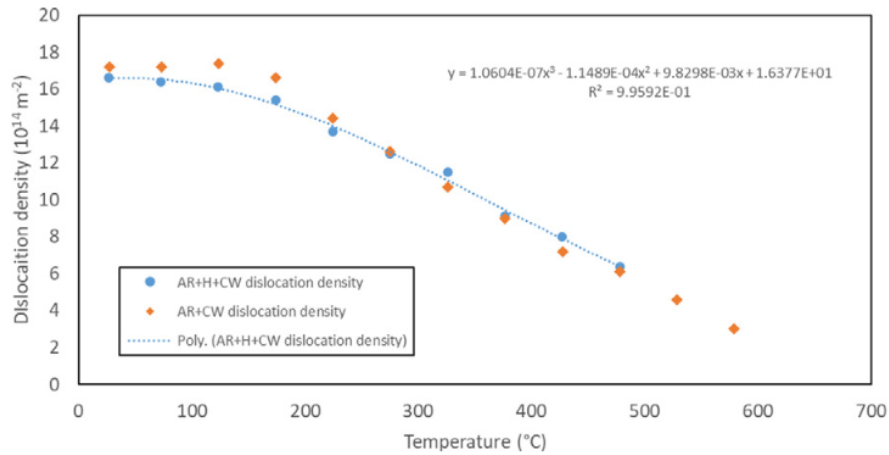


Figure 7.21: A graph showing the dislocation density, determined from CMWP, on the HT-sXRD data. Graph taken from Swan *et al.* paper [233].

The HT-XRD Zr80CWH dislocation density, shown in Figure 7.22, starts off at $\sim 30 \times 10^{14} \text{m}^{-2}$ and then with increasing temperature the dislocation decreases reaching approximately $2.5 \times 10^{14} \text{m}^{-2}$ at $400 \text{ }^\circ\text{C}$. At room temperature, Zr80CWA had a dislocation density of $30 \times 10^{14} \text{m}^{-2}$ then it began to decrease with increasing temperature, following the trend of the Zr80CWH sample, ending with a value of $\sim 1 \times 10^{14} \text{m}^{-2}$ at $400 \text{ }^\circ\text{C}$. There can be seen some difference at $200 \text{ }^\circ\text{C}$ and $300 \text{ }^\circ\text{C}$, however, as can be seen from the overlapping error bars, the differences are not statistically significant. The large difference at $200 \text{ }^\circ\text{C}$ can also be seen in the lattice parameter expansion and GOF within the TOPAS analysis of Zr80CWA. As there is no distinctive anomaly in the diffraction pattern that may be responsible, the cause of this large step is currently unknown.

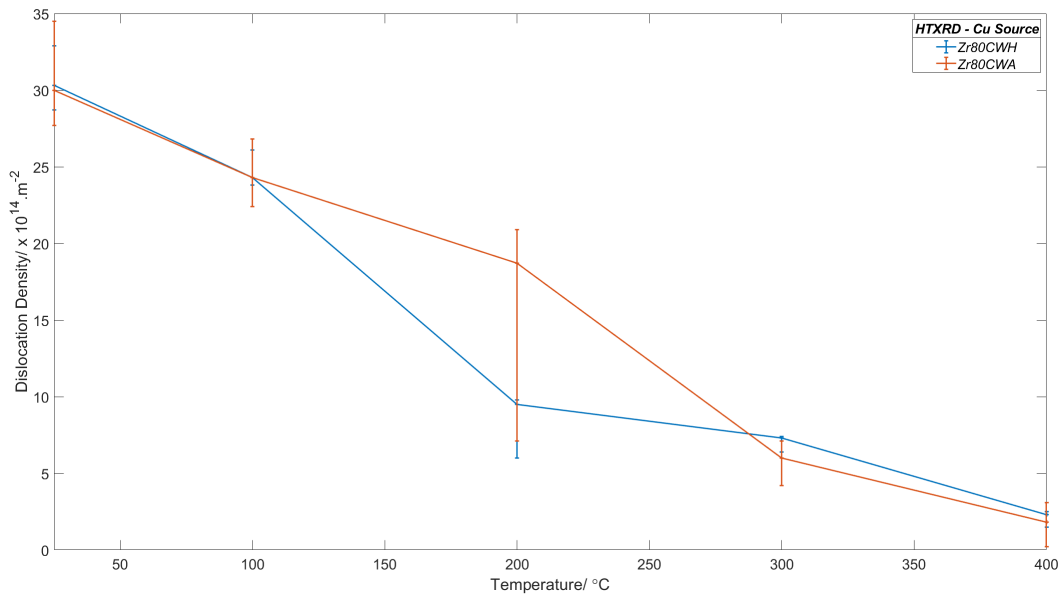


Figure 7.22: A graph showing the dislocation density, determined from CMWP, on the HT-XRD data.

When comparing the dislocation densities between the two experimental setups (Figure 7.21 and Figure 7.22), it can be seen that the values decrease considerably more quickly in the HT-XRD data than in the HT-sXRD. Additionally, the maximum value (initial room temperature dislocation density value) on the copper source is higher than the synchrotron value. One theory is the effects of texture with each geometry experimental setup (i.e. transmission and Gonio geometry). As explained previously (page 123), when discussing the effects of texture and experimental geometry on lattice parameter expansion, the cold rolled texture plays a significant role in data produced and therefore subsequent analysis. Cold rolled material predominantly produces *a* type dislocation (discussed in Section 2.2.5, therefore, when analysing Gonio data from HT-XRD, which has a bias towards *c* lattice parameter and basal planes, the dislocation density analysis could be hindered. This could lead to a discrepancy in dislocation density values, especially compared to the HT-sXRD analysis which has a bias towards *a* lattice parameter and non-basal plane information.

Another theory is the hold times at which the scans were taken. During the HT-sXRD experiments, the samples were scanned for 10 seconds over a range of temperatures (approximately 0.83 K) whereas with the HT-XRD, as explained in Section 4, the samples were held for an hour at the given temperature. The difference in hold times suggests that, during the HT-XRD

experiments, the longer hold times would allow for more annealing of dislocations and, therefore, would have lower dislocation density values at each given temperature. The exception to this is at room temperature, where the starting dislocation density for HT-XRD is approximately double that for HT-sXRD with regards to both Zr80CWA and Zr80CWH, which could contribute to the texture explanation stated above.

From Figure 7.21, the last CMWP result shown was at 500 °C for Zr80CWA and 600 °C for Zr80CWH; Swan *et al.* suggest that after 500 °C/600 °C, the dislocation density was zero. This was also found in this study but at a lower temperature for the HT-XRD data - approximately 400 °C. This was because, after 400 °C, CMWP seemed to have been fitting the high temperature diffraction patterns by refining the dislocation density to values above the initial room temperature value (approximately $100 \times 10^{14} \text{m}^{-2}$ where the initial room temperature value was $30 \times 10^{14} \text{m}^{-2}$), therefore providing unrealistic physical parameters. One possible theory was that as temperature increased and the strain was reduced, there can be seen a clearer separation of $K\alpha_1$ and $K\alpha_2$ peaks, which could affect the fitting. Though the instrumental profile incorporates both $K\alpha_1$ and $K\alpha_2$, it can be seen by the fitting on the doublet of the Al_2O_3 peaks, that they are not fitted very well. A close-up of the doublet fitting of an Al_2O_3 peak is shown in Figure 7.23 and full fitting is shown in Appendix D. However, upon further examination of CMWP fittings, from room temperature to 400 °C, the quality of the doublet fitting on Al_2O_3 was fairly consistent and therefore was not believed to be a significant contributing factor to the error of fittings.

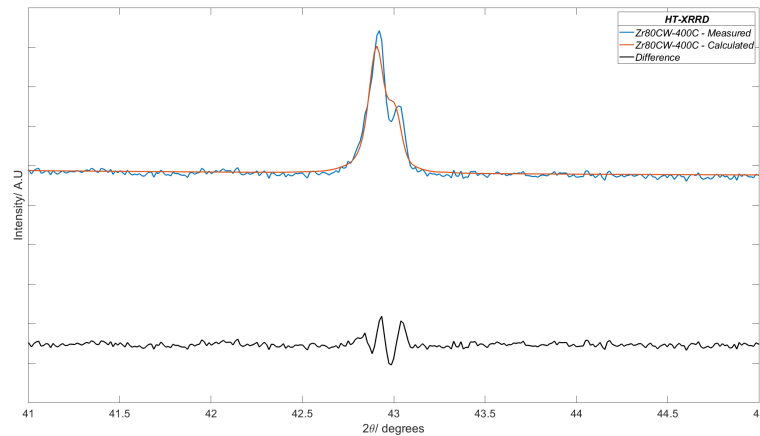


Figure 7.23: A close-up of the CMWP fitting, of Zr80CW-400C, on a Al_2O_3 double peak found around 43° .

Another possibility in the inaccuracy of the CMWP dislocation density after 400 °C, is the appearance of artefacts on tails of peaks from 460 °C onwards (shown in Figure 7.5). The artefact causes peak broadening, as well as affecting the overall CMWP fitting, which may be contributing to the sudden increase of dislocation density to unreasonable values. This was also a limiting factor discussed by Xu, in her thesis work, suggesting that global fittings (i.e. whole diffraction pattern fitting) including satellite peaks/artefacts are very difficult and individual peak analysis may be more feasible [174]. The increase in GOF (shown in Figure 7.10) corroborates the effects of the artefacts as it indicates the increased difficulty and accuracy of the fit from 460 °C onwards. Both the theory of the doublet and the artefacts suggest that the difficulty of the data was the main issue in analysing the data after 400 °C but also suggest a limitation of CMWP analysis. This is further corroborated in the Gaussian strain and Lorentzian crystallite size profiles, calculated via Le Bail analysis in TOPAS, shown in Figure 7.24 and Figure 7.25

respectively. The black vertical line in the figures represents the temperature at which the artefact started to appear and approximately when the doublet peaks began forming. It can be seen, from Figure 7.24 and Figure 7.25, that after the formation of the artefacts, the trend in crystallite size and strain drastically changed and the errors in the determined values increased significantly.

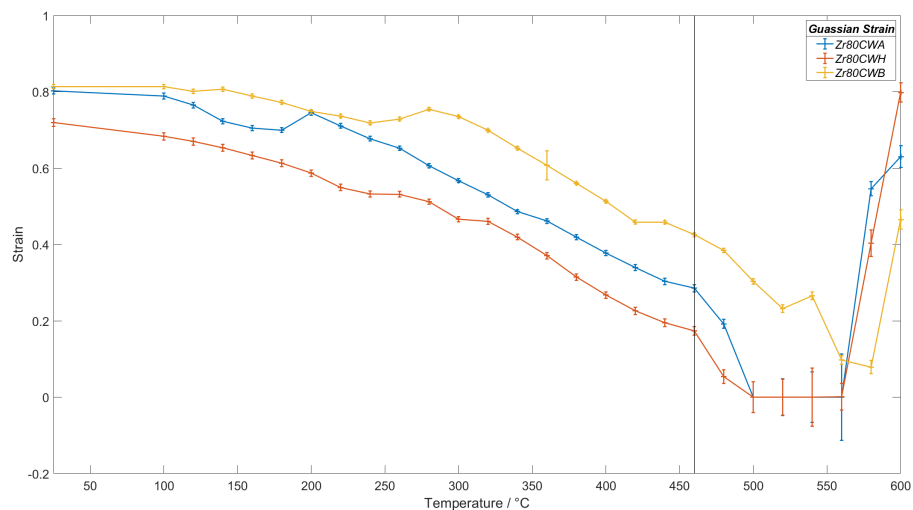


Figure 7.24: A graph showing the TOPAS calculated Gaussian strain, using Le Bail analysis, on Zr80CWA, Zr80CWH and Zr80CWB. The black line represents the temperature at which the artefacts began appearing on the peak.

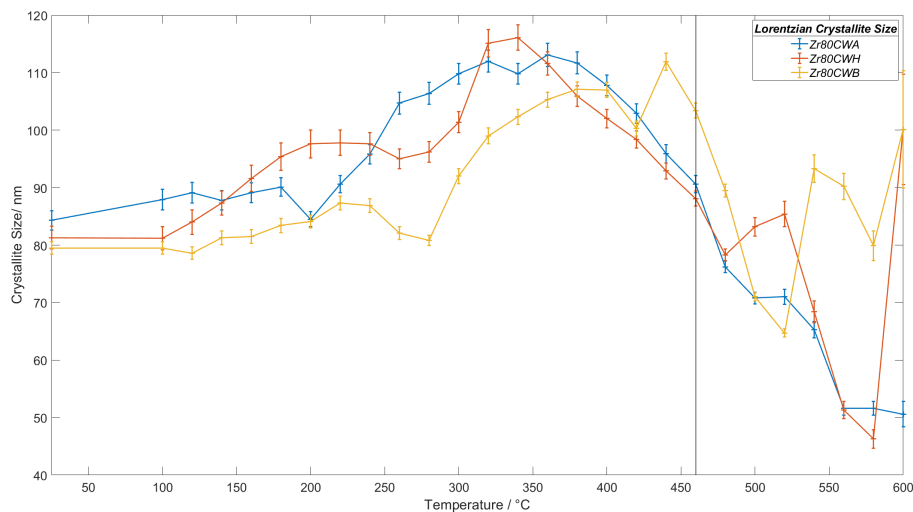


Figure 7.25: A graph showing the TOPAS calculated Lorentzian crystallite size, using Le Bail analysis, on Zr80CWA, Zr80CWH and Zr80CWB. The black line represents the temperature at which the artefacts began appearing on the peak.

7.5 Conclusion

The main focus of this results chapter was to determine whether a high temperature laboratory XRD machine could be used to determine the lattice parameter expansion of Zr-4, from the dis-

solution of hydrides into solution and microstructural traps, instead of using a high temperature synchrotron XRD.

When comparing the diffraction patterns from HT-XRD and HT-sXRD it was discovered that due to the nature of the diffraction setup, where HT-XRD was in reflection and HT-sXRD was in transmission, the key difference was the peaks that were measured, especially with cold rolled material and the associated grain alignment. Due to the grain alignment, where the basal planes are relatively parallel with the surface, with the HT-XRD the (1000) peak was weak, whereas with HT-sXRD the (0002) peak was weak. Hence, when considering the two diffraction setups, in transmission diffraction the c is poorly represented whereas in reflection diffraction the a was not well determined. However, in spite of this, both methods successfully presented lattice parameter expansion with the alternate lattice parameter: reflection diffraction with c (~ 0.0065 fractional increase) and transmission diffraction with a (~ 0.008 fractional increase).

With regards to the dislocation density, it was found that there was a comparable trend between the two techniques, where the dislocation density reached $\sim 3 - 5 \times 10^{14} \text{m}^{-2}$ at the final accurate CMWP analysis. However, it was found to have different starting dislocation densities and slight discrepancies between the two techniques could be attributed to the noise-to-peak ratio in the HT-XRD, which would affect the quality of fit. It was also found that the temperature at which CMWP analysis became inaccurate differed between the two techniques and this was believed to be contributed to the hold times at each temperature in each setup (approximately 10 secs over 0.83 K for HT-sXRD and an hour for each given temperature for HT-XRD). Another factor contributing to the discrepancy in dislocation density between the two techniques is the texture of the cold rolled material and the geometry of the XRD analysis (i.e. transmission for HT-sXRD and Gonio for HT-XRD). Due to the bias towards c lattice parameter and basal plane information, the HT-XRD analysis may determine a different dislocation density when compared to HT-sXRD analysis, which has a bias towards a lattice parameter and non-basal plane information. This is more prevalent with cold worked material as the dislocations are predominantly a types which reside on the basal plane.

The total expansion and the critical temperature of total hydride dissolution also help predict the relative hydrogen content of the samples. Zr80CWA, for c lattice parameter in HT-XRD, had the lowest total expansion and the lowest total hydride dissolution temperature, indicating it had the lowest hydrogen content of 11 wt.ppm which was close to the predicted hydrogen content of 10 wt.ppm. Zr80CWH had the highest total c lattice parameter expansion suggesting that it had the highest hydrogen content, which was not the case. There are overlapping error bars between Zr80CWH and Zr80CWB, suggesting that the conclusion from total lattice parameter expansion was statically insignificant, which follows as Zr80CWB had a higher dissolution temperature, suggesting a hydrogen content higher than Zr80CWB. Using TSSD curves from the literature it was determined that Zr80CWH and Zr80CWB had hydrogen contents of 34.7 ± 1.8 wt.ppm and 52 ± 2.1 wt.ppm, which was far from the expected values of 67 wt.ppm (determined by HVE) and 10 wt.ppm (believed to be nominally hydrogen content of non-hydrided Zr) respectively.

The continually increasing c lattice parameter from the HT-XRD results indicates that HT-XRD could be a viable replacement technique for HT-sXRD with it successfully acting as an analogue for a hot cell and producing accurate and representative diffraction patterns. Where a hot cell is defined as bringing an irradiated sample (heavy ion, proton or neutron irradiation) to active nuclear reactor temperatures.

The next stage of this investigation is to determine the effects of hydride dissolution on lattice parameter expansion. The differences between hydrogen charged and non-hydrogen charged

samples have to be fully separated and therefore further work is needed. This can be achieved by conducting HT-XRD on a Zr-4 with an as-received hydrogen content (with no hydride peak present), therefore the lattice parameter expansion will be assumed to be primarily from thermal expansion. The effects of the thermal expansion would be subtracted from the total lattice parameter expansion of Zr80CWH, to obtain the expansion due to H entering solution, as was done in the HT-sXRD experiments [233].

Chapter 8

Conclusions

In the nuclear industry, a major concern is the failure of material, especially cladding material, during post-discharge storage, due to radiation induced deformation and hydrogen induced cracking (HIC). Furthermore, current primary investigation techniques into these failure mechanisms are complex, time consuming and have high operational costs, such as TEM and synchrotron XRD. This work aimed to delve into a technique development of a novel X-ray diffraction (XRD) analytical technique called Convolutional Multiple Whole Profile (CMWP) and its validity in lab based XRD applications. This is aimed to be done by using multiple radiation sources and laboratory XRD geometries/set-ups (i.e. Gonio, grazing incident and high temperature) and determining the accuracy of the values. This research also seeks a deeper understanding of the effects of hydrogen on zirconium crystal structures under harsh environments using laboratory high temperature XRD (HT-XRD) diffractometers.

It was determined that the trend from Zr-HT, ZR-AR to Zr-60 (Zr - heat treated, Zr - as-received to Zr - 60% cold worked) was similar for all three radiation source XRD diffractometers, where Zr-HT had the narrowest, most defined peaks and as the strain increased, the peaks broadened with Zr-60 being the broadest. This indicates that Zr-HT has the largest crystallite size and lowest dislocation density and visa versa for Zr-60, which was corroborated by the CMWP results. It was discovered that the diffraction pattern, produced from Ag source XRD, could not be accurately analysed by CMWP or TOPAS, due to the step changes present, the noise and the peak broadness in relation to the instrumental profile sample, Lanthanum Hexaboride (LaB_6). Additionally, it was determined that though there was a similar trend between Cu and Co CMWP/TOPAS analysis, there was a disparity between the numerical values, where Co analysis was predicting higher values than Cu for both crystallite size and dislocation density. This was attributed to different resolutions, peak-to-noise ratios and penetration depths from each radiation source. The Cu diffraction data was determined to be the most accurate and representative of the materials' true microstructural information, however, with further refinement of the Co experimental setup, it is believed to be a suitable radiation source for CMWP characterisation.

Tests were undertaken to explore the validity of using CMWP for GI measurements. Numerous grazing incident (GI) angles were tested, in accordance with varying damage penetration depth calculations and the lowest viable angle was determined to be 1.30° due to minimal noise and post-processing. The subsequent CMWP and TOPAS analysis determined the crystallite size to be approximately two thirds (~ 225 nm and ~ 235 nm respectively) of the Si NIST 640f standard documentation (400 nm) - this work was trialled on an XRD standard material as it has a known crystallite size and microstrain. The Gonio CMWP and TOPAS results were found to be ~ 680 nm and ~ 255 nm respectively. In all four analyses, the microstrain/dislocation

density was refined to close to zero, agreeing with the NIST standard documentation. From this, it is believed that GIXRD could be a viable technique for CMWP analysis, with a minimal ω angle of 1.30° advised. Further improvements on the experimental setup are required (e.g. knife edge to reduce noise) to reduce post-processing. The differences between GI/Gonio and the NIST documentation are believed to be due to the post-processing of the data in order for it to be analysed (e.g. smoothing function for GI data, removal of absorption edges for Gonio data and instrumental effect analysis). Furthermore, the viability of investigating heavy ion implanted damaged materials was deemed feasible for lab XRD setup. After looking at preliminary calculations and the literature, the energy of the heavy ion must be tuned so that the species reaches a minimum penetration depth of 800 nm to ensure all damage, especially the region of peak dpa, is encompassed within the X-ray interaction volume.

Experiments were conducted to ascertain the viability of using lab HT-XRD in order to determine lattice parameter expansion from the dissolution of hydrides in Zr-4 alloy. On inspection of the HT-XRD diffraction patterns for Zr80CWA, Zr80CWB and Zr80CWH, all showed a similar trend of a decrease in peak broadening as the temperature increased. However, in each sample, there was a difference in the critical temperature in which the hydride peak disappeared (i.e. when all hydrogen goes into solution or microstructural traps). Zr80CWA total dissolution of hydrides occurred at approximately 200°C , whereas for Zr80CWB and Zr80CWH it happened at 280°C and 260°C respectively, suggesting that Zr80CWA had the lowest hydrogen content and Zr80CWB had the highest. This was corroborated when using TSSD curves from literature to obtain hydrogen of each sample - the average hydrogen content for Zr80CWA, Zr80CWH and Zr80CWB was 11 wt.ppm, 34.7 ± 1.8 wt.ppm and 52 ± 2.1 wt.ppm respectively. When comparing the total lattice parameter expansions between HT-XRD and HT-SXRD, it was discovered both techniques predicted the total lattice parameter expansion (i.e. thermal expansion plus hydride dissolution) to be similar. However, due to the texture of the sample and the scattering vector, in the laboratory diffraction experiments (reflection diffraction), c lattice parameter was more accurately represented whereas for synchrotron diffraction experiments (transmission diffraction), a lattice parameter was more accurately represented. Therefore, it is believed that HT-XRD is a good replacement for HT-SXRD and can be used as an analogue for a hot cell to investigate irradiated materials. Due to issues with acquiring a nominally low hydrogen containing sample, it was not possible to compare the differences between a hydrogen charged and non-hydrogen charged sample, with HT-XRD, thus further work is required. CMWP was able to determine dislocation density from HT-XRD, though they differed to the HT-SXRD results. This was believed to be due to the longer hold times and slower heating rate in HT-XRD to allow for the sample to reach equilibrium at each temperature, leading to greater annealing of dislocations, and lower dislocation density at each given temperature. The texture in the cold rolled sample, where the dislocations are primarily a type (i.e. reside on the basal plane), are also believed to play a role in the difference in dislocation density.

Overall, the aim of this research was to find increasing uses or limitations of the Convolutional Multiple Whole profile methodology, in order to improve efficiency, operational costs and the scope of characterising deformation in materials, especially nuclear materials. Multiple radiation sources and XRD geometries are applicable to be used with CMWP, making it a more viable option to characterise material at laboratory facilities. The main limitations and considerations of the technique are the quality of data (i.e. noise and artefacts, and experimental setup related to that), majorly overlapping peaks within the phase of concern and depth of damage (when considering grazing incident geometry). It is hoped that these studies will help further expand the use of CMWP using data obtained from lab diffractometers.

Chapter 9

Future Work

The initial direction for further investigation into Convolutional Multiple Whole Profile (CMWP) and its capabilities would be to develop the current work that has taken place in this PhD. In multiple cases, the refinement of the experimental procedure would help validate some of the conclusions stated. As well as including mechanical testing, such as hardness testing, to verify the increase in deformation and compare to the dislocation densities calculated.

Firstly, to ensure that the results between radiation sources were directly comparable, especially with a focus on cold worked deformation, the area of investigation should be the same. Therefore, calculating a fixed incident angle using the attenuation length determined for each experimental setup would help ensure the same penetration depth.

Another common radiation source in most XRD laboratories is Molybdenum (Mo), which though has a shorter wavelength than Cu (0.71 \AA) and therefore contracts the diffraction pattern and is more penetrative. It provides high resolution data and can usually be used in two geometries: reflection and transmission. The transmission geometry would be a useful comparison to Synchrotron XRD (sXRD), providing a simpler and financially more viable option to sXRD. Thus, determining whether Mo source XRD can be used in conjunction with CMWP would increase the range of facilities and capabilities of CMWP.

Equipment and experimental setup improvements should be considered with regards to the grazing incident XRD (GIXRD) experimental chapter. The first being the reduction of the noise to minimise post-processing, this can be achieved by using a variable knife edge. The knife edge will not only reduced background intensity but also reduce scattering at the smaller angles, which would remove the area of diffuse scattering present in the current GIXRD diffraction data. This would improve the quality of diffraction data but also possibly help reduce the incident grazing angle, achieving a more appropriate penetration depth - providing less noisy data that require less post-processing (shallower penetration depths in line with ion implanted or irradiated samples). The next step in furthering the validation of using GIXRD in conjunction with CMWP would be using the improved experimental setup on an undeformed and deformed zirconium system, to determine whether it can predict an increase in dislocation density from the increased strain within the material. Additionally, studying different damage sources, of deeper damage depth profile (e.g. cold working or ion implantation from lighter elements - He or Al) would help deepen the understanding of CMWP capabilities with GIXRD. Finally, exploring multiple XRD standards to help improve the validation of the technique.

The use of TEM two beam analysis is the main current convention in determining dislocation density. A direct comparison between multiple radiation XRD CMWP results and TEM would

help validate the technique, especially as current comparisons have been mainly between proton implanted data on Cu source and sXRD only. Exploring the potential similarities and differences between the different radiation sources XRD and sXRD, would further the understanding of the limitations of each technique and the potential optimum scenarios to use them, as well as whether they should be used in conjunction.

In this work, we limited our study to Zr materials, however in the nuclear industry, other than cladding material, many other components undergo harsh conditions that lead to failure and the possible disruption of active operations. An exploration into using CMWP on different materials such as structural steel components (i.e. most common stainless steel (SS) alloys used are 304SS and 316SS), could lead to a greater understanding of other failure mechanisms and the prevention of such cases. Thus increasing the catalogue of materials proven to work with CMWP.

The necessity to characterise materials, especially the insight provided by CMWP, is not limited to only the nuclear industry. There are many facets of engineering that require the investigation of materials which are under constant harsh conditions or subjected to extreme environments, one example being in the aerospace industry. Nickel superalloys, used in engines (bulk phase being FCC) and titanium alloys, used in structural components (bulk phase being HCP) are constantly under fatigue and extreme temperature conditions. Validating a more accurate characterisation technique of the deformation within these materials will deepen the understanding of the failure mechanism present, providing more information to either prolong the lifespan of current materials or to produce new alloys that are able to withstand these conditions longer.

Hopefully, this future work will help unlock the further potential of CMWP and make it more accessible to use.

Bibliography

- [1] Tanweer Alam et al. “A review on the clad failure studies”. In: *Nuclear Engineering and Design* 241.9 (Sept. 2011), pp. 3658–3677. ISSN: 00295493. DOI: 10.1016/j.nucengdes.2011.08.009. URL: <https://linkinghub.elsevier.com/retrieve/pii/S0029549311006340> (visited on 04/23/2024).
- [2] C. Lemaignan. “Zirconium Alloys: Properties and Characteristics”. In: *Comprehensive Nuclear Materials*. Elsevier, 2012, pp. 217–232. ISBN: 978-0-08-056033-5. DOI: 10.1016/B978-0-08-056033-5.00015-X. URL: <https://linkinghub.elsevier.com/retrieve/pii/B978008056033500015X> (visited on 04/23/2024).
- [3] G. Ribárik. “Modeling of Diffraction Patterns Based on Microstructural Properties”. Publication Title: PhD Thesis. PhD thesis. Eotvos Lorand University, 2008. 48–51.
- [4] G. Ribárik, J. Gubicza, and T. Ungár. “Correlation between strength and microstructure of ball-milled Al-Mg alloys determined by X-ray diffraction”. In: *Materials Science and Engineering A* 387-389 (2004). ISBN: 3613722801, pp. 343–347. ISSN: 09215093. DOI: 10.1016/j.msea.2004.01.089.
- [5] M. Topping et al. “The effect of irradiation temperature on damage structures in proton-irradiated zirconium alloys”. In: *Journal of Nuclear Materials* 514 (Feb. 2019), pp. 358–367. ISSN: 00223115. DOI: 10.1016/j.jnucmat.2018.12.006. URL: <https://linkinghub.elsevier.com/retrieve/pii/S0022311518314132> (visited on 04/02/2024).
- [6] Naresh Chejara et al. “Study of defect production in neutron irradiated Cu, Ni and Pb using positron annihilation spectroscopy (PAS)”. In: *Materials Today: Proceedings* 42 (2021). Publisher: Elsevier Ltd., pp. 1651–1656. ISSN: 22147853. DOI: 10.1016/j.matpr.2020.07.479. URL: <https://doi.org/10.1016/j.matpr.2020.07.479>.
- [7] J. Koutsky and J. Kocik. *Radiation Damage of Structural Materials*. Vol. 79. Publication Title: Materials Science Monographs. 1994. 355 pp. ISBN: 0-444-98708-8.
- [8] R. Golser. *Application of Particle and Laser Beams in Materials Technology*. Publication Title: Application of Particle and Laser Beams in Materials Technology. 1995. 53–76. ISBN: 978-90-481-4510-2. DOI: 10.1007/978-94-015-8459-3.
- [9] Maria Cristina Tanzi, Silvia Fare, and Gabriele Candiani. “Organization, Structure, and Properties of Materials”. In: *Foundations of Biomaterials Engineering*. Academic Press, Jan. 1, 2019, pp. 3–103. ISBN: 978-0-08-101034-1. DOI: 10.1016/B978-0-08-101034-1.00001-3. (Visited on 07/29/2021).
- [10] Jules L. Routbort. “Plasticity (Engineering)”. In: *Encyclopedia of Physical Science and Technology*. Vol. 26. Academic Press, Jan. 1, 2003, pp. 425–440. DOI: 10.1016/B0-12-227410-5/00585-8. (Visited on 07/28/2021).

- [11] G. Schoeck. “Dislocation Theory of Plasticity of Metals”. In: *Advances in Applied Mechanics*. Vol. 4. Elsevier, 1956, pp. 229–279. ISBN: 978-0-12-002004-1. DOI: 10.1016/S0065-2156(08)70374-0. URL: <https://linkinghub.elsevier.com/retrieve/pii/S0065215608703740> (visited on 08/23/2024).
- [12] R. A. Holt and R. W. Gilbert. “c-Component Dislocations in Neutron Irradiated Zircaloy-2”. In: *Journal of Nuclear Materials* 116 (1983), pp. 127–130.
- [13] Cong Dai et al. “Atomistic simulations of the formation of c-component dislocation loops in alpha-zirconium”. In: *Journal of Nuclear Materials* 478 (Sept. 2016), pp. 125–134. ISSN: 00223115. DOI: 10.1016/j.jnucmat.2016.06.002. URL: <https://linkinghub.elsevier.com/retrieve/pii/S0022311516302513> (visited on 03/13/2024).
- [14] M. Griffiths. “A review of microstructure evolution in zirconium alloys during irradiation”. In: *Journal of Nuclear Materials* 159 (Oct. 1988), pp. 190–218. ISSN: 00223115. DOI: 10.1016/0022-3115(88)90093-1. URL: <https://linkinghub.elsevier.com/retrieve/pii/S0022311588900931> (visited on 08/23/2024).
- [15] Thomas Soye et al. “Mobility of $\langle c + a \rangle$ dislocations in zirconium”. In: *Acta Materialia* 197 (Sept. 2020), pp. 97–107. ISSN: 13596454. DOI: 10.1016/j.actamat.2020.07.026. URL: <https://linkinghub.elsevier.com/retrieve/pii/S1359645420305322> (visited on 08/23/2024).
- [16] Ryan B. Sills et al. “Dislocation Networks and the Microstructural Origin of Strain Hardening”. In: *Physical Review Letters* 121.8 (Aug. 20, 2018). Publisher: American Physical Society, p. 085501. DOI: 10.1103/PhysRevLett.121.085501. URL: <https://journals.aps.org/prl/abstract/10.1103/PhysRevLett.121.085501> (visited on 07/28/2021).
- [17] H. M. Mikk-Oja and V. K. Lindroos. “The Formation of Dislocation Networks”. In: *Surface Science* 31 (C 1972), pp. 422–455. ISSN: 00396028. DOI: 10.1016/0039-6028(72)90270-1.
- [18] Princeton University. *Frank-Reed Source*. Princeton University. 2021. URL: https://www.princeton.edu/~maelabs/mae324/07/07mae_25.htm (visited on 07/28/2021).
- [19] M. Monavari. “Continuum Dislocation Kinematics”. Publication Title: Friedrich-Alexander University. PhD thesis. 2017.
- [20] Louissette Priester. *Grain Boundaries: From Theory to Engineering*. Vol. 172. Publication Title: Zeitschrift für Kristallographie - Crystalline Materials Issue: 3-4 ISSN: 2194-4946. 2013. ISBN: 978-94-007-4968-9. DOI: 10.1524/zkri.1990.190.3-4.315.
- [21] Shrabani Majumdar, D. Bhattacharjee, and K. K. Ray. “On the micromechanism of fatigue damage in an interstitial-free steel sheet”. In: *Metallurgical and Materials Transactions A: Physical Metallurgy and Materials Science* 39.7 (2008), pp. 1676–1690. ISSN: 10735623. DOI: 10.1007/s11661-008-9537-y.
- [22] H. Wiedersich. *Theory of Defect Clustering and Void Formation*. 1975.
- [23] K. Une and S. Ishimoto. “Dissolution and precipitation behavior of hydrides in Zircaloy-2 and high Fe Zircaloy”. In: *Journal of Nuclear Materials* 322.1 (Oct. 2003), pp. 66–72. ISSN: 00223115. DOI: 10.1016/S0022-3115(03)00320-9. URL: <https://linkinghub.elsevier.com/retrieve/pii/S0022311503003209> (visited on 03/14/2024).

- [24] T.R. Allen, R.J.M. Konings, and A.T. Motta. “Corrosion of Zirconium Alloys”. In: *Comprehensive Nuclear Materials*. Elsevier, 2012, pp. 49–68. ISBN: 978-0-08-056033-5. DOI: 10.1016/B978-0-08-056033-5.00063-X. URL: <https://linkinghub.elsevier.com/retrieve/pii/B978008056033500063X> (visited on 03/14/2024).
- [25] Jacob Bair, Mohsen Asle Zaeem, and Michael Tonks. “A review on hydride precipitation in zirconium alloys”. In: *Journal of Nuclear Materials*. TAGSI/FESI Symposium. Vol. 466. Structural Integrity of Nuclear Power Plant. 2013, pp. 12–20. DOI: 10.1016/j.jnucmat.2015.07.014. URL: <https://linkinghub.elsevier.com/retrieve/pii/S0022311515301008> (visited on 03/14/2024).
- [26] M. Nedim Cinbiz et al. “Nanoindentation study of bulk zirconium hydrides at elevated temperatures”. In: *Journal of Alloys and Compounds* 726 (Dec. 2017), pp. 41–48. ISSN: 09258388. DOI: 10.1016/j.jallcom.2017.07.319. URL: <https://linkinghub.elsevier.com/retrieve/pii/S0925838817327044> (visited on 11/28/2024).
- [27] G.R. Odette, M.J. Alinger, and B.D. Wirth. “Recent Developments in Irradiation-Resistant Steels”. In: *Annual Review of Materials Research* 38.1 (2008). ISBN: 9780824317386, pp. 471–503. ISSN: 1531-7331. DOI: 10.1146/annurev.matsci.38.060407.130315.
- [28] IAEA. *Corrosion of Zirconium Alloys in Nuclear Power Plants*. Austria: International Atomic Energy Agency, Jan. 1993.
- [29] Muhammad Ali et al. “Formation mechanism of composite secondary phase particles in a solution-treated Si-modified Zircaloy-4”. In: *Scripta Materialia* 239 (Jan. 2024), p. 115827. ISSN: 13596462. DOI: 10.1016/j.scriptamat.2023.115827. URL: <https://linkinghub.elsevier.com/retrieve/pii/S1359646223005481> (visited on 11/04/2024).
- [30] Fan Zhao et al. “The role of secondary phase precipitates in zircaloy corrosion: From point defects to local percolation”. In: *Corrosion Science* 229 (Apr. 2024), p. 111856. ISSN: 0010938X. DOI: 10.1016/j.corsci.2024.111856. URL: <https://linkinghub.elsevier.com/retrieve/pii/S0010938X24000404> (visited on 11/04/2024).
- [31] Pratik P. Joshi, Nilesh Kumar, and Korukonda L. Murty. “Materials for Nuclear Reactors”. In: *Encyclopedia of Materials: Metals and Alloys*. Elsevier, 2022, pp. 364–376. ISBN: 978-0-12-819733-2. DOI: 10.1016/B978-0-12-803581-8.12070-3. URL: <https://linkinghub.elsevier.com/retrieve/pii/B9780128035818120703> (visited on 11/04/2024).
- [32] J. Wei et al. “The effect of Sn on autoclave corrosion performance and corrosion mechanisms in Zr–Sn–Nb alloys”. In: *Acta Materialia* 61.11 (June 2013), pp. 4200–4214. ISSN: 13596454. DOI: 10.1016/j.actamat.2013.03.046. URL: <https://linkinghub.elsevier.com/retrieve/pii/S1359645413002565> (visited on 11/04/2024).
- [33] G. Sundell, M. Thuvander, and H.-O. Andrén. “Tin clustering and precipitation in the oxide during autoclave corrosion of Zircaloy-2”. In: *Journal of Nuclear Materials* 456 (Jan. 2015), pp. 409–414. ISSN: 00223115. DOI: 10.1016/j.jnucmat.2014.10.003. URL: <https://linkinghub.elsevier.com/retrieve/pii/S0022311514006862> (visited on 11/04/2024).
- [34] Takashi Sawabe and Takeshi Sonoda. “An atom probe study on the Fe distribution in Zr-based alloys with different Fe content under high fluence neutron irradiation”. In: *Journal of Nuclear Materials* 567 (Aug. 2022), p. 153809. ISSN: 00223115. DOI: 10.1016/j.jnucmat.2022.153809. URL: <https://linkinghub.elsevier.com/retrieve/pii/S0022311522002951> (visited on 11/04/2024).

- [35] Zaheen D Shah. “Characterizing and Modelling Precipitation in Zirconium Alloys”. PhD thesis. University of Manchester, 2019. URL: https://pure.manchester.ac.uk/ws/portalfiles/portal/162162388/FULL_TEXT.PDF.
- [36] Arthur T. Motta, Adrien Couet, and Robert J. Comstock. “Corrosion of Zirconium Alloys Used for Nuclear Fuel Cladding”. In: *Annual Review of Materials Research* 45.1 (July 1, 2015), pp. 311–343. ISSN: 1531-7331, 1545-4118. DOI: 10.1146/annurev-matsci-070214-020951. URL: <https://www.annualreviews.org/doi/10.1146/annurev-matsci-070214-020951> (visited on 11/04/2024).
- [37] Rong Yuan et al. “An origin of corrosion resistance changes of Zr alloys: effects of Sn and Nb on grain boundary strength of surface oxide”. In: *Acta Materialia* 209 (May 2021), p. 116804. ISSN: 13596454. DOI: 10.1016/j.actamat.2021.116804. URL: <https://linkinghub.elsevier.com/retrieve/pii/S1359645421001841> (visited on 11/05/2024).
- [38] David W. Shoesmith and Dmitrij Zagidulin. “The corrosion of zirconium under deep geologic repository conditions”. In: *Journal of Nuclear Materials* 418.1 (Nov. 2011), pp. 292–306. ISSN: 00223115. DOI: 10.1016/j.jnucmat.2011.07.028. URL: <https://linkinghub.elsevier.com/retrieve/pii/S0022311511007203> (visited on 11/05/2024).
- [39] Elizabeth Kautz et al. “Investigating zirconium alloy corrosion with advanced experimental techniques: A review”. In: *Journal of Nuclear Materials* 585 (Nov. 2023), p. 154586. ISSN: 00223115. DOI: 10.1016/j.jnucmat.2023.154586. URL: <https://linkinghub.elsevier.com/retrieve/pii/S0022311523003537> (visited on 11/05/2024).
- [40] Raghvendra Tewari et al. “Zirconium and its Alloys: Properties and Characteristics”. In: *Reference Module in Materials Science and Materials Engineering*. 2020, pp. 284–302. ISBN: 978-0-08-102865-0. DOI: 10.1016/B978-0-12-803581-8.11735-7.
- [41] Erich Tenckhoff. “Review of deformation mechanisms, texture, and mechanical anisotropy in Zirconium and Zirconium base alloys”. In: *ASTM Special Technical Publication* 2.1467 (2005). ISBN: 0803134932, pp. 25–50. ISSN: 00660558. DOI: 10.1520/stp37501s.
- [42] A. R. Massih and Lars O. Jernkvist. “Solid state phase transformation kinetics in Zr-base alloys”. In: *Scientific Reports* 11.1 (2021). Publisher: Nature Publishing Group UK ISBN: 0123456789, pp. 1–16. ISSN: 20452322. DOI: 10.1038/s41598-021-86308-w. URL: <https://doi.org/10.1038/s41598-021-86308-w>.
- [43] A. R. Massih and Lars O. Jernkvist. “Solid state phase transformation kinetics in Zr-base alloys”. In: *Scientific Reports* 11.1 (Mar. 29, 2021), p. 7022. ISSN: 2045-2322. DOI: 10.1038/s41598-021-86308-w. URL: <https://www.nature.com/articles/s41598-021-86308-w> (visited on 08/30/2024).
- [44] IAEA. *Characteristics of Advanced Reactors*. IAEA ARIS. 2013. URL: <https://aris.iaea.org/sites/operating.html> (visited on 03/15/2023).
- [45] Paul Breeze. “Nuclear power”. In: *Power Generation Technologies*. ISSN: 03020797. 2019, pp. 399–429. ISBN: 978-0-08-102631-1. DOI: 10.1016/B978-0-08-102631-1.00017-1.
- [46] Damien Fénon. *Nuclear Corrosion Science and Engineering*. Ed. by Damien Fénon. Publication Title: Woodhead Publishing Limited in Energy. Woodhead Publishing Limited, 2012. 939–987. ISBN: 978-1-84569-765-5. URL: <http://www.sciencedirect.com/science/article/pii/B978184569765500263>.

- [47] F. Long et al. “Microstructure characterization of a hydride blister in Zircaloy-4 by EBSD and TEM”. In: *Acta Materialia* 129 (May 2017), pp. 450–461. ISSN: 13596454. DOI: 10.1016/j.actamat.2017.03.016. URL: <https://linkinghub.elsevier.com/retrieve/pii/S1359645417302033> (visited on 05/14/2024).
- [48] F. M. Mazzolai, J. Ryll-Nardzewski, and C. J. Spears. “An investigation of the zirconium-hydrogen system by internal friction”. In: *Il Nuovo Cimento B Series 11* 33.1 (1976), pp. 251–263. ISSN: 03693554. DOI: 10.1007/BF02722491.
- [49] Thrinadh Jadam et al. “Performance of microwave-irradiated WC-Co insert during dry machining of Inconel 718 superalloys”. In: *Sustainable Manufacturing and Design*. Elsevier, 2021, pp. 103–132. ISBN: 978-0-12-822124-2. DOI: 10.1016/B978-0-12-822124-2.00006-8. URL: <https://linkinghub.elsevier.com/retrieve/pii/B9780128221242000068> (visited on 11/05/2024).
- [50] K.Y. Zhu et al. “Texture Evolution and Associated Nucleation and Growth Mechanisms during Annealing of a Zr Alloy”. In: *Metallurgical and Materials Transactions A* 40.10 (Oct. 2009), pp. 2423–2434. ISSN: 1073-5623, 1543-1940. DOI: 10.1007/s11661-009-9909-y. URL: <https://link.springer.com/10.1007/s11661-009-9909-y> (visited on 11/05/2024).
- [51] D. Bhattacharyya et al. “Origin of dislocations within tensile and compressive twins in pure textured Zr”. In: *Acta Materialia* 57.2 (Jan. 2009), pp. 305–315. ISSN: 13596454. DOI: 10.1016/j.actamat.2008.09.014. URL: <https://linkinghub.elsevier.com/retrieve/pii/S1359645408006563> (visited on 11/05/2024).
- [52] Heavy Technology. *Metallurgical Zirconium Nuclear Applications*. M Heavy Technology. July 6, 2024. URL: <https://www.mheavytechnology.com/news/zirconium/> (visited on 11/05/2024).
- [53] Yuan Liu et al. “Texture and Twinning Evolution of Cold-Rolled Industrial Pure Zirconium”. In: *Processes* 12.5 (May 7, 2024), p. 948. ISSN: 2227-9717. DOI: 10.3390/pr12050948. URL: <https://www.mdpi.com/2227-9717/12/5/948> (visited on 11/05/2024).
- [54] Y.N Wang and J.C Huang. “Texture analysis in hexagonal materials”. In: *Materials Chemistry and Physics* 81.1 (July 2003), pp. 11–26. ISSN: 02540584. DOI: 10.1016/S0254-0584(03)00168-8. URL: <https://linkinghub.elsevier.com/retrieve/pii/S0254058403001688> (visited on 11/06/2024).
- [55] M. Grange, J. Besson, and E. Andrieu. “Anisotropic behavior and rupture of hydrided ZIRCALOY-4 sheets”. In: *Metallurgical and Materials Transactions A* 31.3 (Mar. 2000), pp. 679–690. ISSN: 1073-5623, 1543-1940. DOI: 10.1007/s11661-000-0010-9. URL: <https://link.springer.com/10.1007/s11661-000-0010-9> (visited on 11/05/2024).
- [56] Wenbin Guo et al. “Texture development and mechanical behavior of Zircaloy-4 alloy plates fabricated by cold rolling and annealing”. In: *Materials Science and Engineering: A* 807 (Mar. 2021), p. 140846. ISSN: 09215093. DOI: 10.1016/j.msea.2021.140846. URL: <https://linkinghub.elsevier.com/retrieve/pii/S0921509321001155> (visited on 11/05/2024).
- [57] H. Qiao et al. “Modeling the micromechanical behaviors of Zircaloy-2 alloy under large deformation”. In: *Journal of Nuclear Materials* 569 (Oct. 2022), p. 153912. ISSN: 00223115. DOI: 10.1016/j.jnucmat.2022.153912. URL: <https://linkinghub.elsevier.com/retrieve/pii/S0022311522003981> (visited on 11/05/2024).

- [58] Ian Reid. “Texture produced in cold-rolled and recrystallized zircaloy-2 and Zr-2.5 wt% Nb alloys”. In: *Canadian Metallurgical Quarterly* 9.1 (Jan. 1970), pp. 345–352. ISSN: 0008-4433, 1879-1395. DOI: 10.1179/cmq.1970.9.1.345. URL: <http://www.tandfonline.com/doi/full/10.1179/cmq.1970.9.1.345> (visited on 11/05/2024).
- [59] Christopher S. Daniel et al. “A detailed study of texture changes during alpha–beta processing of a zirconium alloy”. In: *Journal of Alloys and Compounds* 804 (Oct. 2019), pp. 65–83. ISSN: 09258388. DOI: 10.1016/j.jallcom.2019.06.338. URL: <https://linkinghub.elsevier.com/retrieve/pii/S0925838819324351> (visited on 11/05/2024).
- [60] F.C. Campbell, ed. *Elements of Metallurgy and Engineering Alloys*. ASM International, June 1, 2008. ISBN: 978-1-62708-251-8. DOI: 10.31399/asm.tb.emea.9781627082518. URL: <https://dl.asminternational.org/handbooks/book/94/Elements-of-Metallurgy-and-Engineering-Alloys> (visited on 11/05/2024).
- [61] H.P. Stüwe, A.F. Padilha, and F. Siciliano. “Competition between recovery and recrystallization”. In: *Materials Science and Engineering: A* 333.1 (Aug. 2002), pp. 361–367. ISSN: 09215093. DOI: 10.1016/S0921-5093(01)01860-3. URL: <https://linkinghub.elsevier.com/retrieve/pii/S0921509301018603> (visited on 11/05/2024).
- [62] M. Bobby Kannan, P. Bala Srinivasan, and V.S. Raja. “Stress corrosion cracking (SCC) of aluminium alloys”. In: *Stress Corrosion Cracking*. Elsevier, 2011, pp. 307–340. ISBN: 978-1-84569-673-3. DOI: 10.1533/9780857093769.3.307. URL: <https://linkinghub.elsevier.com/retrieve/pii/B9781845696733500080> (visited on 11/05/2024).
- [63] Dierk Raabe. “Recovery and Recrystallization: Phenomena, Physics, Models, Simulation”. In: *Physical Metallurgy*. Elsevier, 2014, pp. 2291–2397. ISBN: 978-0-444-53770-6. DOI: 10.1016/B978-0-444-53770-6.00023-X. URL: <https://linkinghub.elsevier.com/retrieve/pii/B978044453770600023X> (visited on 11/05/2024).
- [64] D. Juul Jensen. “Annealing Textures”. In: *Encyclopedia of Materials: Science and Technology*. Elsevier, 2001, pp. 319–323. ISBN: 978-0-08-043152-9. DOI: 10.1016/B0-08-043152-6/00066-8. URL: <https://linkinghub.elsevier.com/retrieve/pii/B0080431526000668> (visited on 11/06/2024).
- [65] Hee Young Kim and Shuichi Miyazaki. “Thermomechanical Treatment and Microstructure Control”. In: *Ni-Free Ti-Based Shape Memory Alloys*. Elsevier, 2018, pp. 111–145. ISBN: 978-0-12-809401-3. DOI: 10.1016/B978-0-12-809401-3.00004-5. URL: <https://linkinghub.elsevier.com/retrieve/pii/B9780128094013000045> (visited on 11/06/2024).
- [66] F. Gerspach, N. Bozzolo, and F. Wagner. “About texture stability during primary recrystallization of cold-rolled low alloyed zirconium”. In: *Scripta Materialia* 60.4 (Feb. 2009), pp. 203–206. ISSN: 13596462. DOI: 10.1016/j.scriptamat.2008.09.031. URL: <https://linkinghub.elsevier.com/retrieve/pii/S1359646208007070> (visited on 11/06/2024).
- [67] Angelo José De Oliveira Zimmermann and Angelo Fernando Padilha. “Rolling and recrystallization behavior of pure zirconium and zircaloy-4”. In: *Matéria (Rio de Janeiro)* 24.3 (2019), e12451. ISSN: 1517-7076. DOI: 10.1590/s1517-707620190003.0767. URL: http://www.scielo.br/scielo.php?script=sci_arttext&pid=S1517-70762019000300363&tlng=en (visited on 11/06/2024).

- [68] Qinghui Zeng et al. “Recrystallization mechanism and texture evolution of pre-twinned Zr702 during annealing”. In: *Materials Characterization* 195 (Jan. 2023), p. 112541. ISSN: 10445803. DOI: 10.1016/j.matchar.2022.112541. URL: <https://linkinghub.elsevier.com/retrieve/pii/S1044580322008233> (visited on 11/06/2024).
- [69] IAEA. *Grain size determination in zirconium alloys*. Technical Report IAEA-TECDOC-794. International Atomic Energy Agency, Apr. 1995, p. 9. URL: https://inis.iaea.org/collection/NCLCollectionStore/_Public/26/069/26069284.pdf?r=1&r=1.
- [70] Mariusz Jedrychowski et al. “Monte Carlo modelling of recrystallization in alpha Zirconium”. In: *Computational Materials Science* 199 (2021). ISSN: 09270256. DOI: 10.1016/j.commatsci.2021.110742.
- [71] V. Kalavathi and Rajesh Kumar Bhuyan. “A detailed study on zirconium and its applications in manufacturing process with combinations of other metals, oxides and alloys – A review”. In: *Materials Today: Proceedings* 19 (2019), pp. 781–786. ISSN: 22147853. DOI: 10.1016/j.matpr.2019.08.130. URL: <https://linkinghub.elsevier.com/retrieve/pii/S2214785319331177> (visited on 08/30/2024).
- [72] Chunguang Yan et al. “Effects of ion irradiation on microstructure and properties of zirconium alloys-A review”. In: *Nuclear Engineering and Technology* 47.3 (2015). Publisher: Elsevier B.V, pp. 323–331. ISSN: 2234358X. DOI: 10.1016/j.net.2014.12.015. URL: <http://dx.doi.org/10.1016/j.net.2014.12.015>.
- [73] Sang Il Choi and Ji Hyun Kim. “Radiation-induced dislocation and growth behavior of zirconium and zirconium alloys-A review”. In: *Nuclear Engineering and Technology* 45.3 (2013). Publisher: Korean Nuclear Society, pp. 385–392. ISSN: 2234358X. DOI: 10.5516/NET.07.2013.035. URL: <http://dx.doi.org/10.5516/NET.07.2013.035>.
- [74] Ronald B. Adamson, Christopher E. Coleman, and Malcolm Griffiths. “Irradiation creep and growth of zirconium alloys: A critical review”. In: *Journal of Nuclear Materials* 521 (2019), pp. 167–244. ISSN: 00223115. DOI: 10.1016/j.jnucmat.2019.04.021.
- [75] R. A. Holt. “In-reactor deformation of cold-worked Zr-2.5Nb pressure tubes”. In: *Journal of Nuclear Materials* 372.2 (2008), pp. 182–214. ISSN: 00223115. DOI: 10.1016/j.jnucmat.2007.02.017.
- [76] F. Long, L. Balogh, and M. R. Daymond. “Evolution of dislocation density in a hot rolled Zr-2.5Nb alloy with plastic deformation studied by neutron diffraction and transmission electron microscopy”. In: *Philosophical Magazine* 97.31 (Nov. 2, 2017), pp. 2888–2914. ISSN: 1478-6435, 1478-6443. DOI: 10.1080/14786435.2017.1356940. URL: <https://www.tandfonline.com/doi/full/10.1080/14786435.2017.1356940> (visited on 03/14/2024).
- [77] Levente Balogh et al. “Dislocation structure evolution induced by irradiation and plastic deformation in the Zr-2.5Nb nuclear structural material determined by neutron diffraction line profile analysis”. In: *Acta Materialia* 60.15 (Sept. 2012), pp. 5567–5577. ISSN: 13596454. DOI: 10.1016/j.actamat.2012.06.062. URL: <https://linkinghub.elsevier.com/retrieve/pii/S1359645412004545> (visited on 03/20/2024).
- [78] P. Mukherjee et al. “Deformation characteristics of rolled zirconium alloys: a study by X-ray diffraction line profile analysis”. In: *Acta Materialia* 52.19 (Nov. 2004), pp. 5687–5696. ISSN: 13596454. DOI: 10.1016/j.actamat.2004.08.030. URL: <https://linkinghub.elsevier.com/retrieve/pii/S1359645404005117> (visited on 03/20/2024).

- [79] M. Morán et al. “Dislocation density evolution in cold-rolled Zr-2.5%Nb pressure tubes under thermal treatments by high energy XRD and neutron TOF diffraction peak profile analysis”. In: *Journal of Alloys and Compounds* 929 (Dec. 2022), p. 167196. ISSN: 09258388. DOI: 10.1016/j.jallcom.2022.167196. URL: <https://linkinghub.elsevier.com/retrieve/pii/S0925838822035873> (visited on 03/14/2024).
- [80] Lu Wu et al. “Study of Dislocation Loops Growth in Zr–Sn–Alloys Under Neutron Irradiation by Rate Theory Modelling”. In: *METALLOFIZIKA I NOVEISHIE TEKHNologii* 44.9 (Dec. 13, 2022), pp. 1077–1101. ISSN: 10241809, 10241809. DOI: 10.15407/mfint.44.09.1077. URL: <http://mfint.imp.kiev.ua/en/abstract/v44/i09/1077.html> (visited on 08/23/2024).
- [81] A. Harte et al. “The effect of matrix chemistry on dislocation evolution in an irradiated Zr alloy”. In: *Acta Materialia* 130 (May 2017), pp. 69–82. ISSN: 13596454. DOI: 10.1016/j.actamat.2017.03.024. URL: <https://linkinghub.elsevier.com/retrieve/pii/S135964541730215X> (visited on 08/23/2024).
- [82] Alexander Klumpp et al. “Influence of work-hardening on fatigue crack growth, effective threshold and crack opening behavior in the nickel-based superalloy Inconel 718”. In: *International Journal of Fatigue* 116 (Nov. 2018), pp. 257–267. ISSN: 01421123. DOI: 10.1016/j.ijfatigue.2018.06.033. URL: <https://linkinghub.elsevier.com/retrieve/pii/S0142112318302652> (visited on 11/21/2024).
- [83] R. C. McClUNG. “A literature survey on the stability and significance of residual stresses during fatigue”. In: *Fatigue & Fracture of Engineering Materials & Structures* 30.3 (Mar. 2007), pp. 173–205. ISSN: 8756-758X, 1460-2695. DOI: 10.1111/j.1460-2695.2007.01102.x. URL: <https://onlinelibrary.wiley.com/doi/10.1111/j.1460-2695.2007.01102.x> (visited on 11/21/2024).
- [84] Hichem Bounezour et al. “Effects of work hardening on mechanical metal properties—experimental analysis and simulation by experiments”. In: *The International Journal of Advanced Manufacturing Technology* 101.9 (Apr. 2019), pp. 2475–2485. ISSN: 0268-3768, 1433-3015. DOI: 10.1007/s00170-018-3071-x. URL: <http://link.springer.com/10.1007/s00170-018-3071-x> (visited on 11/21/2024).
- [85] Steven J. Zinkle. “Radiation-Induced Effects on Microstructure”. In: *Comprehensive Nuclear Materials*. Elsevier, 2020, pp. 91–129. ISBN: 978-0-08-102866-7. DOI: 10.1016/B978-0-12-803581-8.12075-2. URL: <https://linkinghub.elsevier.com/retrieve/pii/B9780128035818120752> (visited on 11/09/2024).
- [86] Huilong Yang. “Anisotropic effects of radiation-induced hardening in nuclear structural materials: A review”. In: *Journal of Nuclear Materials* 561 (Apr. 2022), p. 153571. ISSN: 00223115. DOI: 10.1016/j.jnucmat.2022.153571. URL: <https://linkinghub.elsevier.com/retrieve/pii/S0022311522000678> (visited on 11/09/2024).
- [87] Yaoxu Xiong et al. “Interactions between irradiation-induced defects and dislocations in concentrated solid solution alloys”. In: *Journal of Nuclear Materials* 597 (Aug. 2024), p. 155144. ISSN: 00223115. DOI: 10.1016/j.jnucmat.2024.155144. URL: <https://linkinghub.elsevier.com/retrieve/pii/S0022311524002460> (visited on 11/09/2024).
- [88] H.S. Sen and T. Polcar. “Helium migration in Zr-Nb multilayers under electric field”. In: *Journal of Nuclear Materials* 555 (Nov. 2021), p. 153133. ISSN: 00223115. DOI: 10.1016/j.jnucmat.2021.153133. URL: <https://linkinghub.elsevier.com/retrieve/pii/S0022311521003561> (visited on 11/09/2024).

- [89] Ronald Adamson, Malcolm Griffiths, and Charles Patterson. *Irradiation Growth of Zirconium Alloys A Review*. Review. Sweden: Advanced Nuclear Technology International, 2017.
- [90] Yukitaka Murakami. “21 - Hydrogen Embrittlement”. In: *Metal Fatigue*. Second. Academic Press, 2019, pp. 567–607. ISBN: 978-0-12-813876-2.
- [91] W. Qin, J. A. Szpunar, and J. Kozinski. “Hydride-induced degradation of zirconium alloys: a criterion for complete ductile-to-brittle transition and its dependence on microstructure”. In: *Proceedings of the Royal Society A: Mathematical, Physical and Engineering Sciences* 471.2182 (Oct. 2015), p. 20150192. ISSN: 1364-5021, 1471-2946. DOI: 10.1098/rspa.2015.0192. URL: <https://royalsocietypublishing.org/doi/10.1098/rspa.2015.0192> (visited on 03/22/2024).
- [92] K S Chan. “An assessment of delayed hydride cracking in zirconium alloy cladding tubes under stress transients”. In: *International Materials Reviews* 58.6 (Aug. 2013), pp. 349–373. ISSN: 0950-6608, 1743-2804. DOI: 10.1179/1743280412Y.0000000013. URL: <https://journals.sagepub.com/doi/full/10.1179/1743280412Y.0000000013> (visited on 09/03/2024).
- [93] Pierre-Clément A. Simon et al. “Quantifying the effect of hydride microstructure on zirconium alloys embrittlement using image analysis”. In: *Journal of Nuclear Materials* 547 (Apr. 2021), p. 152817. ISSN: 00223115. DOI: 10.1016/j.jnucmat.2021.152817. URL: <https://linkinghub.elsevier.com/retrieve/pii/S0022311521000404> (visited on 03/22/2024).
- [94] Kimberly B. Colas et al. “Effect of thermo-mechanical cycling on zirconium hydride reorientation studied in situ with synchrotron X-ray diffraction”. In: *Journal of Nuclear Materials* 440.1 (Sept. 2013), pp. 586–595. ISSN: 00223115. DOI: 10.1016/j.jnucmat.2013.04.047. URL: <https://linkinghub.elsevier.com/retrieve/pii/S0022311513006557> (visited on 03/21/2024).
- [95] W. Qin et al. “Threshold stress of hydride reorientation in zirconium alloy nuclear fuel cladding tubes: A theoretical determination”. In: *Journal of Nuclear Materials* 563 (May 2022), p. 153659. ISSN: 00223115. DOI: 10.1016/j.jnucmat.2022.153659. URL: <https://linkinghub.elsevier.com/retrieve/pii/S0022311522001556> (visited on 09/19/2024).
- [96] N.A.P. Kiran Kumar and J.A. Szpunar. “EBSD studies on microstructure and crystallographic orientation of -hydrides in Zircaloy-4, Zr-1% Nb and Zr-2.5% Nb”. In: *Materials Science and Engineering: A* 528.21 (Aug. 2011), pp. 6366–6374. ISSN: 09215093. DOI: 10.1016/j.msea.2011.05.022. URL: <https://linkinghub.elsevier.com/retrieve/pii/S0921509311005594> (visited on 09/19/2024).
- [97] Arthur T. Motta et al. “Hydrogen in zirconium alloys: A review”. In: *Journal of Nuclear Materials* 518 (May 2019), pp. 440–460. ISSN: 00223115. DOI: 10.1016/j.jnucmat.2019.02.042. URL: <https://linkinghub.elsevier.com/retrieve/pii/S0022311518316763> (visited on 02/28/2024).
- [98] B. J. Bai et al. “Hydride Embrittlement in Zircaloy-4 Plate: Part II. Interaction Between the Tensile Stress and the Hydride Morphology”. In: *Metallurgical and Materials Transactions A* 25.6 (June 1994), pp. 1199–1208. ISSN: 15431940. DOI: 10.1007/BF02652294.

- [99] Patrick A. Raynaud, Donald A. Koss, and Arthur T. Motta. “Crack growth in the through-thickness direction of hydrided thin-wall Zircaloy sheet”. In: *Journal of Nuclear Materials* 420.1 (Jan. 2012), pp. 69–82. ISSN: 00223115. DOI: 10.1016/j.jnucmat.2011.09.005. URL: <https://linkinghub.elsevier.com/retrieve/pii/S0022311511008385> (visited on 03/22/2024).
- [100] Alireza Tondro et al. “Modelling the interactions of zirconium hydrides”. In: *Materials Today Communications* 32 (Aug. 2022), p. 103933. ISSN: 23524928. DOI: 10.1016/j.mtcomm.2022.103933. URL: <https://linkinghub.elsevier.com/retrieve/pii/S2352492822007875> (visited on 04/08/2024).
- [101] J.J. Kearns. “Terminal solubility and partitioning of hydrogen in the alpha phase of zirconium, Zircaloy-2 and Zircaloy-4”. In: *Journal of Nuclear Materials* 22.3 (June 1967), pp. 292–303. ISSN: 00223115. DOI: 10.1016/0022-3115(67)90047-5. URL: <https://linkinghub.elsevier.com/retrieve/pii/0022311567900475> (visited on 03/01/2024).
- [102] Mahmut N. Cinbiz, Donald A. Koss, and Arthur T. Motta. “The influence of stress state on the reorientation of hydrides in a zirconium alloy”. In: *Journal of Nuclear Materials* 477 (Aug. 2016), pp. 157–164. ISSN: 00223115. DOI: 10.1016/j.jnucmat.2016.05.013. URL: <https://linkinghub.elsevier.com/retrieve/pii/S0022311516301957> (visited on 03/22/2024).
- [103] M.C. Billone, T.A. Burtseva, and R.E. Einziger. “Ductile-to-brittle transition temperature for high-burnup cladding alloys exposed to simulated drying-storage conditions”. In: *Journal of Nuclear Materials* 433.1 (Feb. 2013), pp. 431–448. ISSN: 00223115. DOI: 10.1016/j.jnucmat.2012.10.002. URL: <https://linkinghub.elsevier.com/retrieve/pii/S0022311512005181> (visited on 03/22/2024).
- [104] Ju-Seong Kim et al. “Terminal solid solubility of hydrogen of optimized-Zirlo and its effects on hydride reorientation mechanisms under dry storage conditions”. In: *Nuclear Engineering and Technology* 52.8 (Aug. 2020), pp. 1742–1748. ISSN: 17385733. DOI: 10.1016/j.net.2020.01.022. URL: <https://linkinghub.elsevier.com/retrieve/pii/S1738573319307004> (visited on 11/07/2024).
- [105] G.P. Marino. “Hydrogen supercharging in Zircaloy”. In: *Materials Science and Engineering* 7.6 (June 1971), pp. 335–341. ISSN: 00255416. DOI: 10.1016/0025-5416(71)90016-4. URL: <https://linkinghub.elsevier.com/retrieve/pii/0025541671900164> (visited on 01/17/2025).
- [106] Konrad P Mazurkiewicz. “Effect of ion irradiation on the rate dependence of plastic deformation of extruded Zr-2.5Nb”. PhD thesis. The University of Western Ontario, 2023. (Visited on 12/03/2024).
- [107] Chunguang Yan et al. “Effects of ion irradiation on microstructure and properties of zirconium alloys—A review”. In: *Nuclear Engineering and Technology* 47.3 (Apr. 2015), pp. 323–331. ISSN: 17385733. DOI: 10.1016/j.net.2014.12.015. URL: <https://linkinghub.elsevier.com/retrieve/pii/S1738573315000170> (visited on 12/09/2024).
- [108] N. Daghbouj et al. “Characterizing heavy ions-irradiated Zr/Nb: Structure and mechanical properties”. In: *Materials & Design* 219 (July 2022), p. 110732. ISSN: 02641275. DOI: 10.1016/j.matdes.2022.110732. URL: <https://linkinghub.elsevier.com/retrieve/pii/S0264127522003549> (visited on 12/04/2024).

- [109] Luciano Pagano, Arthur T. Motta, and Robert C. Birtcher. “Bubble Formation in Zr Alloys Under Heavy Ion Implantation”. In: *MRS Proceedings* 398 (1995), p. 201. ISSN: 0272-9172, 1946-4274. DOI: 10.1557/PROC-398-201. URL: <http://link.springer.com/10.1557/PROC-398-201> (visited on 12/09/2024).
- [110] Y. Idrees et al. “In situ study of defect accumulation in zirconium under heavy ion irradiation”. In: *Journal of Nuclear Materials* 433.1 (Feb. 2013), pp. 95–107. ISSN: 00223115. DOI: 10.1016/j.jnucmat.2012.09.014. URL: <https://linkinghub.elsevier.com/retrieve/pii/S0022311512004916> (visited on 12/10/2024).
- [111] L. Tournadre et al. “Experimental study of the nucleation and growth of c-component loops under charged particle irradiations of recrystallized Zircaloy-4”. In: *Journal of Nuclear Materials* 425.1 (June 2012), pp. 76–82. ISSN: 00223115. DOI: 10.1016/j.jnucmat.2011.11.061. URL: <https://linkinghub.elsevier.com/retrieve/pii/S0022311511010178> (visited on 12/10/2024).
- [112] R.M. Hengstler-Eger et al. “Heavy ion irradiation induced dislocation loops in AREVA’s M5® alloy”. In: *Journal of Nuclear Materials* 423.1 (Apr. 2012), pp. 170–182. ISSN: 00223115. DOI: 10.1016/j.jnucmat.2012.01.002. URL: <https://linkinghub.elsevier.com/retrieve/pii/S0022311512000062> (visited on 12/10/2024).
- [113] L. Pagano, A.T. Motta, and R.C. Birtcher. “The formation of bubbles in Zr alloys under Kr ion irradiation”. In: *Journal of Nuclear Materials* 244.3 (Apr. 1997), pp. 295–304. ISSN: 00223115. DOI: 10.1016/S0022-3115(96)00757-X. URL: <https://linkinghub.elsevier.com/retrieve/pii/S002231159600757X> (visited on 12/09/2024).
- [114] Davor Balzar. “X-Ray Diffraction Line Broadening: Modeling and Applications to High-Tc Superconductors”. In: *Journal of Research of the National Institute of Standards and Technology* 98.3 (1993), pp. 321–353. ISSN: 1044-677X. DOI: 10.6028/jres.098.026. URL: <https://www.ncbi.nlm.nih.gov/pmc/articles/PMC4914239/> (visited on 11/22/2023).
- [115] Minoru Shiraishi and Michio Inagaki. “Chapter 10: X-Ray Diffraction Methods to Study Crystallite Size and Lattice Constants of Carbon Materials”. In: *Carbon Alloys - Novel Concepts to Develop Carbon Science and Technology*. Elsevier, 2003, pp. 161–174.
- [116] Paul Barnes, Simon Jacques, and Vickers Martin. *Sources of Peak Broadening*. Advanced Certificate in Powder Diffraction on the Web. 2006. URL: <http://pd.chem.ucl.ac.uk/pdnn/peaks/broad.htm> (visited on 11/22/2023).
- [117] H Dittrich and A Bieniok. “MEASUREMENT METHODS | Structural Properties: X-Ray and Neutron Diffraction”. In: *Encyclopedia of Electrochemical Power Sources*. Ed. by Jürgen Garche. Encyclopedia of Electrochemical Power Sources Reference Module in Chemistry, Molecular Sciences and Chemical Engineering. Elsevier, 2009, pp. 718–737. ISBN: 978-0-444-52745-5.
- [118] J.P. Cline. “NIST XRD Standard Reference Materials: Their Characterisation and Uses”. In: *National Institute of Standards and Technology Special Publication*. Proceedings of the International Conference: Accuracy in Powder Diffraction II 846 (October May 1992).
- [119] T.G. Fawcett and C.E. Crowder. “Establishing an Instrumental Peak Profile Calibration Standard for Powder Diffraction Analyses: International Round Robin Conducted by the JCPDS-ICDD and the U.S. National Bureau of Standards”. In: *Cambridge University Press*. Powder Diffraction 3.4 (Dec. 1988), pp. 209–218. DOI: 10.1017/S0885715600013506.

- [120] Marcus H. Mendenhall et al. “Certification of Standard Reference Material 660c for powder diffraction”. In: *Powder Diffraction* 35.1 (Mar. 2020), pp. 17–22. ISSN: 0885-7156, 1945-7413. DOI: 10.1017/S0885715620000068. URL: https://www.cambridge.org/core/product/identifier/S0885715620000068/type/journal_article (visited on 09/12/2024).
- [121] T. Ungár. “Microstructural parameters from X-ray diffraction peak broadening”. In: *Scripta Materialia* 51.8 (2004). ISBN: 3613722801, pp. 777–781. ISSN: 13596462. DOI: 10.1016/j.scriptamat.2004.05.007.
- [122] A.R. Bushroa et al. “Approximation of crystallite size and microstrain via XRD line broadening analysis in TiSiN thin films”. In: *Vacuum* 86.8 (Feb. 2012), pp. 1107–1112. ISSN: 0042207X. DOI: 10.1016/j.vacuum.2011.10.011. URL: <https://linkinghub.elsevier.com/retrieve/pii/S0042207X11003745> (visited on 11/24/2023).
- [123] B. D. Cully. “Crystal Quality”. In: *Elements of X-Ray Diffraction*. Second. University of Notre Dame: Addison-Wesley Publishing Company Inc., 1978, pp. 285–292.
- [124] S. Suminta et al. “Pressure Dependence of Crystal Structure and Ionic Conductivity on Composite Glass (AgI)_{0.7}(AgPO₃)_{0.3}”. In: *Atom Indonesia* 31.2 (Dec. 16, 2011). ISSN: 2356-5322, 0126-1568. DOI: 10.17146/aij.2005.364. URL: <http://aij.batan.go.id/index.php/aij/article/view/364> (visited on 03/08/2024).
- [125] Gyula Zilahi, Tamás Ungár, and Géza Tichy. “A common theory of line broadening and rocking curves”. In: *Journal of Applied Crystallography* 48.2 (Apr. 1, 2015), pp. 418–430. ISSN: 1600-5767. DOI: 10.1107/S1600576715001466. URL: <https://scripts.iucr.org/cgi-bin/paper?S1600576715001466> (visited on 03/08/2024).
- [126] Paul Barnes, Simon Jacques, and Vickers Martin. *Crystallite Size and Strain*. Advanced Certificate in Powder Diffraction on the Web. 2006. URL: <http://pd.chem.ucl.ac.uk/pdnn/peaks/size.htm> (visited on 05/21/2024).
- [127] Scott A Speakman. “Estimating Crystallite Size Using XRD”. Course Material. Course Material. MIT Center for Materials Science and Engineering. MIT. URL: <https://www.eng.uc.edu/~beaucag/Classes/Properties%20of%20Materials/MITCrystalSizeAnalysis.pdf> (visited on 05/21/2024).
- [128] Mikrajuddin Abdullah. “Derivation of Scherrer Relation Using an Approach in Basic Physics Course”. In: *Journal of Nanoscience and Nanotechnology* 1.1 (Nov. 2, 2008). ISSN: 1979-0880.
- [129] J. G. M. Van Berkum et al. “Applicabilities of the Warren–Averbach analysis and an alternative analysis for separation of size and strain broadening”. In: *Journal of Applied Crystallography* 27.3 (June 1, 1994), pp. 345–357. ISSN: 0021-8898. DOI: 10.1107/S0021889893010568. URL: <https://scripts.iucr.org/cgi-bin/paper?S0021889893010568> (visited on 03/11/2024).
- [130] L. Chekli et al. “Analytical characterisation of nanoscale zero-valent iron: A methodological review”. In: *Analytica Chimica Acta* 903 (Jan. 2016), pp. 13–35. ISSN: 00032670. DOI: 10.1016/j.aca.2015.10.040. URL: <https://linkinghub.elsevier.com/retrieve/pii/S0003267015013197> (visited on 03/11/2024).
- [131] A. L. Patterson. “The Scherrer Formula for X-Ray Particle Size Determination”. In: *Physical Review* 56.10 (Nov. 15, 1939), pp. 978–982. ISSN: 0031-899X. DOI: 10.1103/PhysRev.56.978. URL: <https://link.aps.org/doi/10.1103/PhysRev.56.978> (visited on 03/12/2024).

- [132] Lalmi Khier et al. “X-ray diffraction analysis of kaolin M1 and M2 via the Williamson–Hall and Warren–Averbach methods”. In: *Journal of Chemical Research* 45.7 (July 2021), pp. 668–673. ISSN: 1747-5198, 2047-6507. DOI: 10.1177/1747519820984729. URL: <http://journals.sagepub.com/doi/10.1177/1747519820984729> (visited on 03/18/2024).
- [133] J. I. Langford, D. Louër, and P. Scardi. “Effect of a crystallite size distribution on X-ray diffraction line profiles and whole-powder-pattern fitting”. In: *Journal of Applied Crystallography* 33.3 (June 1, 2000), pp. 964–974. ISSN: 0021-8898. DOI: 10.1107/S002188980000460X. URL: <https://scripts.iucr.org/cgi-bin/paper?S002188980000460X> (visited on 03/11/2024).
- [134] Davor Balzar and Nicolae Popa. “Analysing Microstructure by Reitveld Refinement”. In: *The Rigaku Journal* 22.1 (2005), pp. 16–25.
- [135] M. Fátima Vaz and M.A. Fortes. “Grain size distribution: The lognormal and the gamma distribution functions”. In: *Scripta Metallurgica* 22.1 (Jan. 1988), pp. 35–40. ISSN: 00369748. DOI: 10.1016/S0036-9748(88)80302-8. URL: <https://linkinghub.elsevier.com/retrieve/pii/S0036974888803028> (visited on 03/15/2024).
- [136] Vijay P. Singh. *Entropy-Based Parameter Estimation in Hydrology*. Red. by V. P. Singh. Vol. 30. Water Science and Technology Library. Dordrecht: Springer Netherlands, 1998. ISBN: 978-90-481-5089-2 978-94-017-1431-0. DOI: 10.1007/978-94-017-1431-0. URL: <http://link.springer.com/10.1007/978-94-017-1431-0> (visited on 03/15/2024).
- [137] Kangsik Kim et al. “Quantitative Evaluation of Dislocation Density in Epitaxial GaAs Layer on Si Using Transmission Electron Microscopy”. In: *Applied Microscopy* 44.2 (June 30, 2014), pp. 74–78. ISSN: 2287-5123. DOI: 10.9729/AM.2014.44.2.74. URL: <http://koreascience.or.kr/journal/view.jsp?kj=JHMBC&py=2014&vnc=v44n2&sp=74> (visited on 03/18/2024).
- [138] Cyril Stanley Smith and Lester Guttman. “Measurement of Internal Boundaries in Three-Dimensional Structures By Random Sectioning”. In: *JOM* 5.1 (Jan. 1953), pp. 81–87. ISSN: 1047-4838, 1543-1851. DOI: 10.1007/BF03397456. URL: <http://link.springer.com/10.1007/BF03397456> (visited on 11/18/2024).
- [139] D.G Brandon and Y Komem. “Quantitative analysis of dislocation distributions”. In: *Metallography* 3.1 (Mar. 1970), pp. 111–126. ISSN: 00260800. DOI: 10.1016/0026-0800(70)90010-8. URL: <https://linkinghub.elsevier.com/retrieve/pii/0026080070900108> (visited on 03/18/2024).
- [140] J. Gallet et al. “Experimental measurement of dislocation density in metallic materials: A quantitative comparison between measurements techniques (XRD, R-ECCI, HR-EBSD, TEM)”. In: *Materials Characterization* 199 (May 2023), p. 112842. ISSN: 10445803. DOI: 10.1016/j.matchar.2023.112842. URL: <https://linkinghub.elsevier.com/retrieve/pii/S1044580323002000> (visited on 03/18/2024).
- [141] Junhyun Kwon, Yong-Bok Lee, and Jung-Ki Shin. “Determination of dislocation densities using transmission electronic microscopy and positron annihilation spectroscopy”. Transactions of the Korean Nuclear Society Autumn Meeting. 2009.
- [142] X.D. Ren et al. “Dislocation evolution and properties enhancement of GH2036 by laser shock processing: Dislocation dynamics simulation and experiment”. In: *Materials Science and Engineering: A* 654 (Jan. 2016), pp. 184–192. ISSN: 09215093. DOI: 10.1016/j.msea.2015.12.007. URL: <https://linkinghub.elsevier.com/retrieve/pii/S0921509315307024> (visited on 11/18/2024).

- [143] M. Gandais et al. “Dislocation contrast by transmission electron microscopy: A method for Burgers vector characterization if the invisibility criterion is not valid”. In: *Philosophical Magazine A* 45 (1982), pp. 387–400. DOI: 10.1080/01418618208236178.
- [144] D. J. Dingley. “Dislocation Invisibility in Dark-Field Electron Microscopy”. In: *Physica Status Solidi* 38 (1970), pp. 345–355.
- [145] Yang Meng, Xinhua Ju, and Xiaopeng Yang. “The measurement of the dislocation density using TEM”. In: *Materials Characterization* 175 (May 2021), p. 111065. ISSN: 10445803. DOI: 10.1016/j.matchar.2021.111065. URL: <https://linkinghub.elsevier.com/retrieve/pii/S1044580321001959> (visited on 03/18/2024).
- [146] P.J. Phillips, M.J. Mills, and M. De Graef. “Systematic row and zone axis STEM defect image simulations”. In: *Philosophical Magazine* 91.16 (June 2011), pp. 2081–2101. ISSN: 1478-6435, 1478-6443. DOI: 10.1080/14786435.2010.547526. URL: <http://www.tandfonline.com/doi/abs/10.1080/14786435.2010.547526> (visited on 03/18/2024).
- [147] Sergio Neves Monteiro et al. “Novel methods for dislocation density estimation in highly compacted tangles”. In: *Journal of Materials Research and Technology* 9.2 (Mar. 2020), pp. 2072–2078. ISSN: 22387854. DOI: 10.1016/j.jmrt.2019.12.040. URL: <https://linkinghub.elsevier.com/retrieve/pii/S2238785419304612> (visited on 03/18/2024).
- [148] Amos Muiruri, Maina Maringa, and Willie du Preez. “Evaluation of Dislocation Densities in Various Microstructures of Additively Manufactured Ti64Al4V (Eli) by the Method of X-Ray Diffraction”. In: *Materials* 13 (2020). DOI: 10.3390/ma13235355.
- [149] Marzieh Rabiei et al. “X-ray Diffraction Analysis and Williamson-Hall Method in USDM Model for Estimating More Accurate Values of Stress-Strain of Unit Cell and Super Cells ($2 \times 2 \times 2$) of Hydroxyapatite, Confirmed by Ultrasonic Pulse-Echo Test”. In: *Materials* 14.11 (May 30, 2021), p. 2949. ISSN: 1996-1944. DOI: 10.3390/ma14112949. URL: <https://www.mdpi.com/1996-1944/14/11/2949> (visited on 03/15/2024).
- [150] G.K Williamson and W.H Hall. “X-ray line broadening from filed aluminium and wolfram”. In: *Acta Metallurgica* 1.1 (Jan. 1953), pp. 22–31. ISSN: 00016160. DOI: 10.1016/0001-6160(53)90006-6. URL: <https://linkinghub.elsevier.com/retrieve/pii/0001616053900066> (visited on 03/15/2024).
- [151] VD Mote, Y Purushotham, and BN Dole. “Williamson-Hall Analysis in Estimation of Lattice Strain in Nanometer-Size ZnO Particles”. In: *Journal of Theoretical and Applied Physics* 6.6 (2012).
- [152] Bantikatta Himabindu, N.S.M.P. Latha Devi, and Bhogoju Rajini Kanth. “Microstructural parameters from X-ray peak profile analysis by Williamson-Hall models; A review”. In: *Materials Today: Proceedings* 47 (2021), pp. 4891–4896. ISSN: 22147853. DOI: 10.1016/j.matpr.2021.06.256. URL: <https://linkinghub.elsevier.com/retrieve/pii/S2214785321046411> (visited on 03/18/2024).
- [153] S. Das Bakshi, D. Sinha, and S. Ghosh Chowdhury. “Anisotropic broadening of XRD peaks of α -Fe: Williamson-Hall and Warren-Averbach analysis using full width at half maximum (FWHM) and integral breadth (IB)”. In: *Materials Characterization* 142 (Aug. 2018), pp. 144–153. ISSN: 10445803. DOI: 10.1016/j.matchar.2018.05.018. URL: <https://linkinghub.elsevier.com/retrieve/pii/S1044580318307010> (visited on 03/18/2024).

- [154] Setsuo Takaki, Takuro Masumura, and Toshihiro Tsuchiyama. “Proposal of Simplified Modified Williamson-Hall Equation”. In: *ISIJ International* 58.12 (Dec. 15, 2018), pp. 2354–2356. ISSN: 0915-1559, 1347-5460. DOI: 10.2355/isijinternational.ISIJINT-2018-517. URL: https://www.jstage.jst.go.jp/article/isijinternational/58/12/58_ISIJINT-2018-517/_article (visited on 03/18/2024).
- [155] Setsuo Takaki, Takuro Masumura, and Toshihiro Tsuchiyama. “Dislocation Characterization by the Direct-fitting/modified Williamson–Hall (DF/mWH) Method in Cold Worked Ferritic Steel”. In: *ISIJ International* 59.3 (Mar. 15, 2019), pp. 567–572. ISSN: 0915-1559, 1347-5460. DOI: 10.2355/isijinternational.ISIJINT-2018-623. URL: https://www.jstage.jst.go.jp/article/isijinternational/59/3/59_ISIJINT-2018-623/_article (visited on 03/19/2024).
- [156] Wanchuck Woo et al. “X-Ray and Neutron Diffraction Measurements of Dislocation Density and Subgrain Size in a Friction-Stir-Welded Aluminum Alloy”. In: *Metallurgical and Materials Transactions A* 41.5 (May 2010), pp. 1210–1216. ISSN: 1073-5623, 1543-1940. DOI: 10.1007/s11661-009-9963-5. URL: <https://link.springer.com/10.1007/s11661-009-9963-5> (visited on 03/19/2024).
- [157] András Borbély. “The modified Williamson-Hall plot and dislocation density evaluation from diffraction peaks”. In: *Scripta Materialia* 217 (Aug. 2022). ISSN: 13596462. DOI: 10.1016/j.scriptamat.2022.114768. URL: <https://linkinghub.elsevier.com/retrieve/pii/S1359646222002640> (visited on 03/19/2024).
- [158] B. Bourniquel et al. “Warren-Averbach Analysis of X-ray Line Profile (even truncated) Assuming a Voigt -like Profile”. In: *International Conference on Residual Stresses*. Ed. by G. Beck, S. Denis, and A. Simon. Dordrecht: Springer Netherlands, 1989, pp. 184–189. ISBN: 978-94-010-7007-2 978-94-009-1143-7. DOI: 10.1007/978-94-009-1143-7_29. URL: http://link.springer.com/10.1007/978-94-009-1143-7_29 (visited on 03/18/2024).
- [159] Matteo Leoni. “Whole Powder Pattern Modelling”. In: *International Tables for Crystallography*. 2019, pp. 289–290.
- [160] Takashi Shintani and Yoshinori Murata. “Evaluation of the dislocation density and dislocation character in cold rolled Type 304 steel determined by profile analysis of X-ray diffraction”. In: *Acta Materialia* 59.11 (June 2011), pp. 4314–4322. ISSN: 13596454. DOI: 10.1016/j.actamat.2011.03.055. URL: <https://linkinghub.elsevier.com/retrieve/pii/S1359645411002102> (visited on 03/18/2024).
- [161] Kartik Prasad et al. “Synchrotron diffraction characterization of dislocation density in additively manufactured IN 718 superalloy”. In: *Materials Characterization* 179 (Sept. 2021), p. 111379. ISSN: 10445803. DOI: 10.1016/j.matchar.2021.111379. URL: <https://linkinghub.elsevier.com/retrieve/pii/S1044580321005015> (visited on 03/18/2024).
- [162] Mikhail A. Krivoglaz. *X-Ray and Neutron Diffraction in Nonideal Crystals*. Ed. by V. G. Baryakhtar et al. First. Berlin, Heidelberg: Springer Berlin Heidelberg, 1996. ISBN: 978-3-642-74293-4 978-3-642-74291-0. DOI: 10.1007/978-3-642-74291-0. URL: <https://link.springer.com/10.1007/978-3-642-74291-0> (visited on 03/11/2024).
- [163] M. Wilkens. “The determination of density and distribution of dislocations in deformed single crystals from broadened X-ray diffraction profiles”. In: *Physica Status Solidi (a)* 2.2 (June 16, 1970), pp. 359–370. ISSN: 00318965, 1521396X. DOI: 10.1002/pssa.19700020224. URL: <https://onlinelibrary.wiley.com/doi/10.1002/pssa.19700020224> (visited on 03/11/2024).

- [164] Hiroyuki Dannoshita et al. “Effects of dislocation arrangement and character on the work hardening of lath martensitic steels”. In: *Scripta Materialia* 236 (Nov. 2023), p. 115648. ISSN: 13596462. DOI: 10.1016/j.scriptamat.2023.115648. URL: <https://linkinghub.elsevier.com/retrieve/pii/S1359646223003718> (visited on 03/11/2024).
- [165] T.H. Simm, P.J. Withers, and J. Quinta Da Fonseca. “An evaluation of diffraction peak profile analysis (DPPA) methods to study plastically deformed metals”. In: *Materials & Design* 111 (Dec. 2016), pp. 331–343. ISSN: 02641275. DOI: 10.1016/j.matdes.2016.08.091. URL: <https://linkinghub.elsevier.com/retrieve/pii/S0264127516311546> (visited on 10/30/2024).
- [166] J.D. Kamminga and L.J. Seijbel. “Diffraction line broadening analysis if broadening is caused by both dislocations and limited crystallite size”. In: *Journal of Research of the National Institute of Standards and Technology* 109.1 (Jan. 2004), p. 65. ISSN: 1044677X. DOI: 10.6028/jres.109.005. URL: <https://nvlpubs.nist.gov/nistpubs/jres/109/1/j91kam.pdf> (visited on 10/30/2024).
- [167] Gábor Ribárik, Bertalan Jóni, and Tamás Ungár. “The Convolutional Multiple Whole Profile (CMWP) Fitting Method, a Global Optimization Procedure for Microstructure Determination”. In: *Crystals* 10.7 (2020), p. 623. ISSN: 2073-4352. DOI: 10.3390/cryst10070623.
- [168] Gábor Ribárik, Bertalan Jóni, and Tamás Ungár. “Global optimum of microstructure parameters in the CMWP line-profile-analysis method by combining Marquardt-Levenberg and Monte-Carlo procedures”. In: *Journal of Materials Science and Technology* 35.7 (2019). Publisher: The editorial office of Journal of Materials Science & Technology, pp. 1508–1514. ISSN: 10050302. DOI: 10.1016/j.jmst.2019.01.014. URL: <https://doi.org/10.1016/j.jmst.2019.01.014>.
- [169] Tamás Ungár et al. “Size-distribution of irradiation-induced dislocation-loops in materials used in the nuclear industry”. In: *Journal of Nuclear Materials* 550 (2021). ISSN: 00223115. DOI: 10.1016/j.jnucmat.2021.152945.
- [170] Russell Herman. *9.6 : The Convolution Operation*. Introduction to Partial Differential Equations. 2023. URL: <https://math.libretexts.org/@go/page/90975>.
- [171] Tamas Ungar and G Ribarik. *Introduction to the program CMWP-fit*. Reyni. 2009. URL: http://csendes.elte.hu/cmwp/doc/cmwp_intro.html (visited on 07/29/2021).
- [172] Levante Balogh, Gábor Ribárik, and Tamás Ungár. “Stacking faults and twin boundaries in fcc crystals determined by x-ray diffraction profile analysis”. In: *Journal of Applied Physics* 100.2 (2006). ISSN: 00218979. DOI: 10.1063/1.2216195.
- [173] Gladys Domizzi et al. “Blister growth in zirconium alloys: Experimentation and modeling”. In: *Journal of Nuclear Materials* 229 (1996), pp. 36–47. ISSN: 00223115. DOI: 10.1016/0022-3115(95)00204-9.
- [174] Hattie Xiao Dan Xu. “Dislocation Loop Formation during Proton Irradiation of Zirconium”. Doctor of Philosophy. The University of Manchester, 2020. URL: https://pure.manchester.ac.uk/ws/portalfiles/portal/194688920/FULL_TEXT.PDF.
- [175] Barbara L Dutrow and Christine M. Clark. *X-Ray Powder Diffraction (XRD)*. Geochemical Instrumentation and Analysis. 2020. DOI: 10.1093/oxfordhb/9780199681532.013.19. URL: https://serc.carleton.edu/research_education/geochemsheets/techniques/XRD.html.
- [176] Vladislav V Gurzhiy and St Petersburg. “Single-Crystal X-Ray Diffraction”. In: *Materials Characterization* 10 (2020), pp. 414–426. DOI: 10.31399/asm.hb.v10.a0006631.

- [177] Birkbeck College. *Laboratory X-ray Sources*. Advanced Certificate in Powder Diffraction on the Web. 2006. URL: <http://pd.chem.ucl.ac.uk/pdnn/inst1/xtube.htm> (visited on 01/20/2025).
- [178] Matteo Leoni and Saudi Aramco. “Introduction to Diffraction Methods”. In: *Materials Characterization* 10 (2020), pp. 389–398. DOI: 10.31399/asm.hb.v10.a0006643.
- [179] Joseph I Goldstein et al. *Microscopy and X-Ray Microanalysis*. 2018. 554 pp. ISBN: 978-1-4939-6674-5.
- [180] A.J. Garratt-Reed and D.C. Bell. *Energy Dispersive X-Ray Analysis in the Electron Microscope*. Publication Title: Royal Microscopical Society. 2003. ISBN: 0-203-53754-8.
- [181] J. Epp. *Materials Characterization Using Nondestructive Evaluation (NDE) Methods*. Ed. by Gerhard Hubschen et al. Woodhead Publishing, 2016. 81–124. ISBN: 978-0-85709-235-9.
- [182] Navinchandra Gopal Shimpi. *Biodegradable and Biocompatible Polymer Composites*. Woodhead Publishing, 2018. 75–76. ISBN: 978-0-08-100783-9.
- [183] George F. Harrington and José Santiso. “Back-to-Basics tutorial: X-ray diffraction of thin films”. In: *Journal of Electroceramics* 47.4 (Dec. 2021), pp. 141–163. ISSN: 1385-3449, 1573-8663. DOI: 10.1007/s10832-021-00263-6. URL: <https://link.springer.com/10.1007/s10832-021-00263-6> (visited on 05/22/2024).
- [184] Yale University. *XRD Principle*. West Campus Materials Characterization Core. 2024. URL: <https://ywcmatsci.yale.edu/principle-0> (visited on 05/22/2024).
- [185] Rachel E Lim. “Grain-resolved temperature-dependent anisotropy in hexagonal Ti-7Al revealed by synchrotron X-ray diffraction”. In: *Materials Characterization* (2021).
- [186] Malvern Panalytical. *Why stick to reflection geometry in powder diffraction?* Malvern Panalytical. May 1, 2019. URL: <https://www.malvernpanalytical.com/en/learn/knowledge-center/insights/why-stick-to-reflection-geometry-in-powder-diffraction>.
- [187] Eric Berthier and Henry Pelliére. “Benefits of Transmission Mode in XRD”. In: *Acta Crystallographica A* 75 (E765 2019). URL: <https://journals.iucr.org/a/issues/2019/a2/00/a59015/a59015.pdf>.
- [188] Aakriti Sharma and Dean Hesterberg. “9 - Synchrotron radiation-based spatial methods in environmental biogeochemistry”. In: *Multidimensional Analytical Techniques in Environmental Research*. Elsevier, 2020, pp. 231–265. ISBN: 978-0-12-818896-5. URL: <https://www.sciencedirect.com/science/article/abs/pii/B9780128188965000090>.
- [189] Bob Baoping He. “Introduction to two-dimensional X-ray diffraction”. In: *Powder Diffraction* 18.2 (2003), pp. 71–85. ISSN: 0885-7156. DOI: 10.1154/1.1577355.
- [190] Yukiko Namatame et al. “Use of multi-dimensional measurement in powder X-ray diffraction”. In: *Rigaku Journal* 34.1 (2018), pp. 9–13.
- [191] Lachlan Cranswick et al. “Powder Diffraction”. In: *Advanced Certificate in Powder Diffraction on the Web*. Ed. by University of London. London: UCL, 2016. URL: <http://pd.chem.ucl.ac.uk/pdnn/diff2/kinemat2.htm> (visited on 10/19/2023).
- [192] Seong H. Kim, Christopher M. Lee, and Kabindra Kafle. “Characterization of crystalline cellulose in biomass: Basic principles, applications, and limitations of XRD, NMR, IR, Raman, and SFG”. In: *Korean Journal of Chemical Engineering* 30.12 (2013), pp. 2127–2141. ISSN: 02561115. DOI: 10.1007/s11814-013-0162-0.

- [193] Weilie Zhou and Zhong Lin Wang. *Scanning microscopy for nanotechnology: Techniques and applications*. Publication Title: Scanning Microscopy for Nanotechnology: Techniques and Applications. 2007. 1–522. ISBN: 0-387-33325-8. DOI: 10.1007/978-0-387-39620-0.
- [194] M. Ezzahmouly et al. “Micro-computed tomographic and SEM study of porous bio-ceramics using an adaptive method based on the mathematical morphological operations”. In: *Heliyon* 5 (2019). Publisher: Elsevier Ltd, pp. 1–8. ISSN: 24058440. DOI: 10.1016/j.heliyon.2019.e02557. URL: <https://doi.org/10.1016/j.heliyon.2019.e02557>.
- [195] M. A. Sutton et al. “Scanning electron microscopy for quantitative small and large deformation measurements Part I: SEM imaging at magnifications from 200 to 10,000”. In: *Experimental Mechanics* 47.6 (2007). ISBN: 1134000790, pp. 775–787. ISSN: 00144851. DOI: 10.1007/s11340-007-9042-z.
- [196] Ivo Konvalina and Ilona Müllerová. “Efficiency of Collection of the Secondary Electrons in SEM”. In: *Microscopy and Microanalysis* 9 (S03 2003). Publisher: Cambridge University Press, pp. 108–109. ISSN: 1431-9276. DOI: 10.1017/S1431927603014041. URL: <https://www.cambridge.org/core/journals/microscopy-and-microanalysis/article/efficiency-of-collection-of-the-secondary-electrons-in-sem/6584404EAB134271FB3311BE76D571B0> (visited on 07/22/2021).
- [197] John Kuo. *Electron Microscopy Methods and Protocols*. 2007. ISBN: 978-1-58829-573-6.
- [198] K. D. Vernon-Parry. “Scanning Electron Microscopy: An Introduction”. In: *III-Vs Review* 13.4 (July 1, 2000). Publisher: Elsevier Advanced Technology, pp. 40–44. ISSN: 0961-1290. DOI: 10.1016/S0961-1290(00)80006-X. (Visited on 07/22/2021).
- [199] V. V. Nemoshkalenko and V. G. Aleshin. *Physical Principles of Electron Spectroscopy*. Publication Title: Electron Spectroscopy of Crystals. 2016. 55–88. ISBN: 978-3-319-39876-1. DOI: 10.1007/978-1-4613-2901-5_2.
- [200] Brent Fultz and James Howe. *Transmission Electron Microscopy and Diffractometry of Materials*. 2008. ISBN: 978-3-540-73885-5.
- [201] P. E. Champness. *Electron Diffraction in the Transmission Electron Microscope*. Publication Title: Royal Microscopical Society. Taylor and Francis, 2001.
- [202] Quang Duc Truong et al. “Direct Observation of Antisite Defects in LiCoPO₄ Cathode Materials by Annular Dark and Bright Field Electron Microscopy Direct Observation of Antisite Defects in LiCoPO₄ Cathode Materials by Annular Dark and Bright Field Electron Microscopy”. In: *ACS Applied Materials and Interfaces* (2013). DOI: 10.1021/am403018n. URL: <http://pubs.acs.org> (visited on 07/26/2021).
- [203] Guilin Wu and Stefan Zaeferrer. “Advances in TEM Orientation Microscopy by Combination of Dark-field Conical Scanning and Improved Image Matching”. In: *Ultramicroscopy* 109 (June 5, 2009), pp. 1317–1325. URL: <https://reader.elsevier.com/reader/sd/pii/S0304399109001363?token=C9C7E7E35D559E433F489952702B59016D67310919C7C7A31ABE3A8CC0&originRegion=eu-west-1&originCreation=20210726124141> (visited on 07/26/2021).
- [204] S Bals et al. “Annular dark field imaging in a TEM”. In: *Solid State Communications* 130 (Mar. 13, 2004), pp. 675–680. DOI: 10.1016/j.ssc.2004.03.035. URL: www.elsevier.com/locate/ssc (visited on 07/26/2021).

- [205] Alexandre Mussi, Ahmed Addad, and Fabien Onimus. “Dislocation electron tomography: A technique to characterize the dislocation microstructure evolution in zirconium alloys under irradiation”. In: *Acta Materialia* 213 (July 2021), p. 116964. ISSN: 13596454. DOI: 10.1016/j.actamat.2021.116964. URL: <https://linkinghub.elsevier.com/retrieve/pii/S135964542100344X> (visited on 09/12/2024).
- [206] Mohammad Jafari Eskandari and Masoud Araghchi. “Preparing metallic bulk samples for transmission electron microscopy analysis via laser ablation in an acidic liquid”. In: *Micron* 174 (Nov. 2023), p. 103535. ISSN: 09684328. DOI: 10.1016/j.micron.2023.103535. URL: <https://linkinghub.elsevier.com/retrieve/pii/S0968432823001336> (visited on 05/15/2024).
- [207] Shatendra K Sharma, Rafa Sitko, and Beata Zawisz. “Quantification in X-Ray Fluorescence Spectrometry”. In: *X-Ray Spectroscopy*. 2012.
- [208] Eva Margui and Rene Van Grieken. *X-Ray Fluorescence Spectrometry and Related Techniques: An Introduction*. Momentum Press.
- [209] Bruker. “How XRF works | Bruker”. In: <https://www.bruker.com/en/products-and-solutions/elemental-analyzers/handheld-xrf-spectrometers/how-xrf-works.html> 2023-10-13 (2023). URL: <https://www.bruker.com/en/products-and-solutions/elemental-analyzers/handheld-xrf-spectrometers/how-xrf-works.html> (visited on 10/13/2023).
- [210] Bruker. “Periodic Table of Elements and X-ray Energies Innovation with Integrity Handheld XRF”. In: *Bruker* 2023-10-13 (2015). ISBN: 44.48250.385. URL: www.bruker.com/hhxrf (visited on 10/13/2023).
- [211] Rebecca Jones. “The Effect of Niobium on the Microstructural Evolution of Zirconium Alloys during Proton Irradiation”. PhD thesis. The University of Manchester, 2019. 317 pp. URL: https://pure.manchester.ac.uk/ws/portalfiles/portal/173358596/FULL_TEXT.PDF (visited on 02/05/2024).
- [212] I. C. Dragomir and T. Ungár. “Contrast factors of dislocations in the hexagonal crystal system”. In: *Journal of Applied Crystallography* 35.5 (2002), pp. 556–564. ISSN: 00218898. DOI: 10.1107/S0021889802009536.
- [213] Levente Balogh, Fei Long, and Mark R. Daymond. “Contrast factors of irradiation-induced dislocation loops in hexagonal materials”. In: *Journal of Applied Crystallography* 49.6 (Dec. 1, 2016), pp. 2184–2200. ISSN: 1600-5767. DOI: 10.1107/S1600576716018136. URL: <https://scripts.iucr.org/cgi-bin/paper?S1600576716018136> (visited on 03/08/2024).
- [214] Yoon-Uk Heo. “Comparative study on the specimen thickness measurement using EELS and CBED methods”. In: *Applied Microscopy* 50.1 (Dec. 2020), p. 8. ISSN: 2287-4445. DOI: 10.1186/s42649-020-00029-4. URL: <https://appmicro.springeropen.com/articles/10.1186/s42649-020-00029-4> (visited on 11/18/2024).
- [215] J. S. Heslop-Harrison. “Energy Dispersive X-Ray Analysis”. In: *Modern Methods of Plant Analysis*. Vol. 11. Berlin, Heidelberg: Springer Berlin Heidelberg, 1990, pp. 244–277. ISBN: 978-3-642-83611-4. URL: https://doi.org/10.1007/978-3-642-83611-4_9.
- [216] B10 Committee. *Specification for Zirconium and Zirconium Alloy Strip, Sheet, and Plate*. Version 12. 2021. DOI: 10.1520/B0551_B0551M-12R21. URL: <http://www.astm.org/cgi-bin/resolver.cgi?B551B551M-12R21> (visited on 03/05/2024).
- [217] M Hawker. *Schedule of Accrediation*. Details of Accrediation 056. Sheffield: The Sheffield Assay Office, June 14, 2022, p. 2.

- [218] Qing Jiang et al. “Fatigue-Induced HCP-to-FCC Phase Transformation Resulting in Two FCC-Zr Variants in Pure Zirconium”. In: *Materials* 16.18 (Sept. 14, 2023), p. 6215. ISSN: 1996-1944. DOI: 10.3390/ma16186215. URL: <https://www.mdpi.com/1996-1944/16/18/6215> (visited on 01/08/2024).
- [219] Boran Tao et al. “FCC phase transformation of Zr alloy during air cooling and aging”. In: *Journal of Nuclear Materials* 551 (Aug. 1, 2021), p. 152989. ISSN: 0022-3115. DOI: 10.1016/j.jnucmat.2021.152989. URL: <https://www.sciencedirect.com/science/article/pii/S0022311521002129> (visited on 01/08/2024).
- [220] B Nath, G W Lorimer, and N Ridley. “The Relationship between Gamma and Delta Hydrides in Zirconium-Hydrogen Alloys of Low Hydrogen Concentration”. In: *Journal of Nuclear Materials* 49.3 (1973), pp. 262–280.
- [221] Philippe F. Weck et al. “Mechanical properties of zirconium alloys and zirconium hydrides predicted from density functional perturbation theory”. In: *Dalton Transactions* 44.43 (2015), pp. 18769–18779. ISSN: 1477-9226, 1477-9234. DOI: 10.1039/C5DT03403E. URL: <https://xlink.rsc.org/?DOI=C5DT03403E> (visited on 10/29/2024).
- [222] H. Conrad, M. Swintowski, and S. L. Mannan. “Effect of cold work on recrystallization behavior and grain size distribution in titanium”. In: *Metallurgical Transactions A* 16.5 (May 1985), pp. 703–708. ISSN: 0360-2133, 2379-0180. DOI: 10.1007/BF02814821. URL: <https://link.springer.com/10.1007/BF02814821> (visited on 04/10/2024).
- [223] Ametex. *Step Size Selection for EBSD Mapping*. 3. Gatan Ametek, 2024, p. 1. URL: https://www.edax.com/-/media/ametkedax/files/resources/tips_tricks/stepsizeselectionforebsdmapping.pdf?la=en&revision=77bb7ac1-0a59-491d-a503-722d6adcc007.
- [224] Frank Girgsdies. *Peak Profile Analysis in X-ray Powder Diffraction*. Fritz-Haber-Institut Max-Planck-Gesellschaft. 2009. URL: https://www.fhi.mpg.de/1075438/frank_girgsdies__peak_profile_fitting_in_xrd__151106.pdf.
- [225] Peng Wang et al. “Emulation of neutron damage with proton irradiation and its effects on microstructure and microchemistry of Zircaloy-4”. In: *Journal of Nuclear Materials* 557 (Dec. 2021), p. 153281. ISSN: 00223115. DOI: 10.1016/j.jnucmat.2021.153281. URL: <https://linkinghub.elsevier.com/retrieve/pii/S0022311521005043> (visited on 04/02/2024).
- [226] Rhys Thomas. “Characterisation of Irradiation Damage Using X-Ray Diffraction Line Profile Analysis”. PowerPoint presentation. PowerPoint presentation. Royce Training: Ion Beam Irradiation and Characterisation - Best Practice. Manchester, Mar. 2023.
- [227] Madeline Feltus. “Fission Reaction Physics”. In: *Encyclopedia of Physical Science and Technology (Third Edition)*. Third. New York: Academic Press, 2003, pp. 893–906. ISBN: 978-0-12-227410-7.
- [228] Eric Gullikson. *X-Ray Attenuation Length*. The Center for X-Ray Optics. 2024. URL: https://henke.lbl.gov/optical_constants/atten2.html (visited on 02/08/2024).
- [229] David Black et al. “Certification of SRM 640f Line Position and Line Shape Standard for Powder Diffraction”. In: *Powder Diffraction* 35.3 (May 31, 2020), pp. 156–159. DOI: 10.1017/S0885715620000366.
- [230] IAEA. *Waterside corrosion of zirconium alloys in nuclear power plants*. Austria: International Atomic Energy Agency, Jan. 1998.

- [231] Zi-Qi Wang et al. “Investigating behavior of hydrogen in zirconium by first-principles: From dissolution, diffusion to the interaction with vacancy”. In: *Nuclear Instruments and Methods in Physics Research Section B: Beam Interactions with Materials and Atoms* 458 (Nov. 2019), pp. 1–6. ISSN: 0168583X. DOI: 10.1016/j.nimb.2019.07.036. URL: <https://linkinghub.elsevier.com/retrieve/pii/S0168583X19305348> (visited on 11/28/2024).
- [232] M.A. Vicente Alvarez et al. “Quantification of dislocations densities in zirconium hydride by X-ray line profile analysis”. In: *Acta Materialia* 117 (Sept. 2016), pp. 1–12. ISSN: 13596454. DOI: 10.1016/j.actamat.2016.06.058. URL: <https://linkinghub.elsevier.com/retrieve/pii/S135964541630489X> (visited on 11/28/2024).
- [233] Helen Swan et al. “Measurement of hydrogen trapping in cold-work dislocations using synchrotron X-ray diffraction”. In: *Journal of Nuclear Materials* 571 (2022). Publisher: Elsevier B.V., p. 154012. ISSN: 00223115. DOI: 10.1016/j.jnucmat.2022.154012. URL: <https://doi.org/10.1016/j.jnucmat.2022.154012>.
- [234] Chi-Toan Nguyen et al. “Texture Evolution Under Fast Heating and Cooling Rates of Zirconium Alloys Studied In-Situ by Synchrotron X-Ray Diffraction”. In: *SSRN Electronic Journal* (2020). ISSN: 1556-5068. DOI: 10.2139/ssrn.3680386. URL: <https://www.ssrn.com/abstract=3680386> (visited on 11/07/2024).
- [235] R.S Daum, Y.S Chu, and A.T Motta. “Identification and quantification of hydride phases in Zircaloy-4 cladding using synchrotron X-ray diffraction”. In: *Journal of Nuclear Materials* 392 (July 4, 2009), pp. 453–463.
- [236] Kyle R. Overdeep et al. “Mechanisms of oxide growth during the combustion of Al:Zr nanolaminate foils”. In: *Combustion and Flame* 191 (May 2018), pp. 442–452. ISSN: 00102180. DOI: 10.1016/j.combustflame.2017.11.023. URL: <https://linkinghub.elsevier.com/retrieve/pii/S0010218017304625> (visited on 03/06/2024).
- [237] Bruker. “Introduction to TOPAS: TOtal Pattern Analysis Solutions”. Structure Course. Structure Course. May 11, 2020. (Visited on 03/05/2024).

Appendices

Appendix A

Experimental Procedure

Name	Size
24.861	1.1 kB
35.444	2.0 kB
43.780	1.7 kB
50.998	1.1 kB
57.540	1.5 kB
63.638	1.2 kB
75.003	1.5 kB
80.439	2.2 kB
85.786	1.7 kB
91.100	1.3 kB
96.421	1.1 kB
101.799	1.4 kB
107.285	1.7 kB
118.842	874 bytes

Figure A1: An example of file formatting for instrumental peak profile.

All range dependent							Use	Value	Code	Error	Min	Max
Background												
Chebyshev	<input checked="" type="checkbox"/>											
Order		1										
1/X Bkg	<input type="checkbox"/>	1000	Refine	0								
Goniometer radii												
Primary radius (mm)		300										
Secondary radius (mm)		300										
Equatorial Convolutions												
Point detector	<input checked="" type="checkbox"/>											
Receiving Slit Width (mm)	<input type="checkbox"/>	0.1	Fix	0								
FDS Shape, angle(°)	<input type="checkbox"/>	1	Fix	0								
VDS irradiated length (mm)	<input type="checkbox"/>	12	Fix	0								
VDS Scale Intensity	<input type="checkbox"/>											
Capillary	<input type="checkbox"/>											
Linear PSD	<input type="checkbox"/>											
Tube Tails	<input type="checkbox"/>											
Axial Convolutions												
Full Axial Model	<input type="checkbox"/>											

	Area	WL (Å)	Lortz. HW (σGauss HW (σ	
1	0.653817	1.540596	0.501844	0
2	0.346183	1.544493	0.626579	0

Figure A2: The TOPAS interface in which the relevant instrumental parameters can be fixed or refined.

Phase Details		Peak Type	hkl's	Additional Convolutions	Rpt/Text
	Value	Code	Error	Min	Max
Peak Type	PVII				
Ha	0.06679105	Refine	0.02080387		
Hb / Cos(Th)	0.00013997	Refine	0.02332314		
Hc Tan(Th)	0.00036048	Refine	0.01167142		
ma + 0.6	0.00048430	Refine	0.4331212		
mb / Cos(Th)	0.00011471	Refine	0.2637854		
mc / Tan(Th)	0.6211731	Refine	0.07095572		

Figure A3: An image demonstrating the refinement of the Peak Type - PVII parameter.

- Global
- 30pct_ColdWork.xy
- 48pct_ColdWork.xy
- 60pct_ColdWork.xy
- AsReceived.xy
- HeatTreated.xy
- Emission Profile
- Background
- Instrument
- Corrections
- Miscellaneous
- Structures/ hkl Phases
 - 110
200 Alpha Zr
 - 110
200 ZrH2
 - LaB6.xy

Phase Details		Peak Type	hkl's Is	Additional Convolutions	Rpt/Text	
	Use	Value	Code	Error	Min	Max
Use Phase	<input checked="" type="checkbox"/>					
Le Bail	<input checked="" type="checkbox"/>					
Delete hkl's on Refinement	<input checked="" type="checkbox"/>					
LP Search	<input checked="" type="checkbox"/>	0.4				
Spacegroup		P63/mmc				
a (Å)		3.2338326 @		0.0000000		
c (Å)		5.1481081 @		0.0000000		
Scale	<input checked="" type="checkbox"/>	1e-005 @		0		
Cry Size						
Cry size L (nm)	<input checked="" type="checkbox"/>	339.2 @		0.0		
Cry size G (nm)	<input type="checkbox"/>	200.0	Refine	0.0		
LVol-IB (nm)	<input type="checkbox"/>	0.000		0.000	k:	1
LVol-FWHM (nm)	<input type="checkbox"/>	0.000		0.000	k:	0.89
Strain						
Strain L	<input type="checkbox"/>	0.1	Refine	0		
Strain G	<input checked="" type="checkbox"/>	0.1374758 @		0		
e0	<input type="checkbox"/>	0.00000		0.00000		

Save Phase

Create str phase

Delete hkl Phase

Paste INP to Node/Selections

Figure A4: An example of the sample parameters that refined/fixed when performing Le Bail analysis.

Appendix B

Accuracy and Sensitivity of CMWP

CMWP Cu Source - Manchester

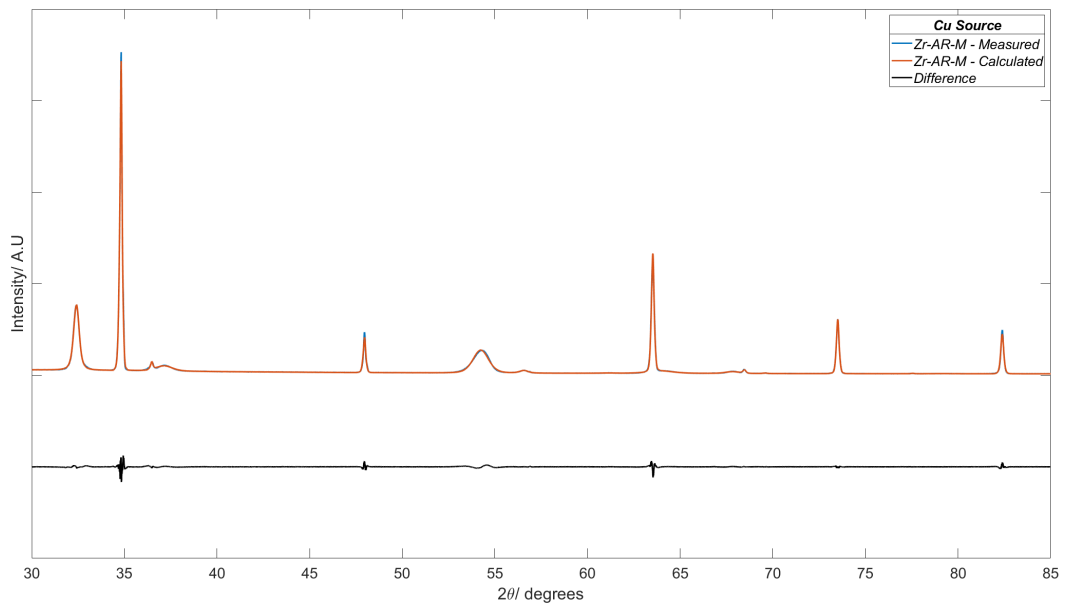


Figure B1: *The qualitative fit for the CMWP analysis of Zr-AR-M.*

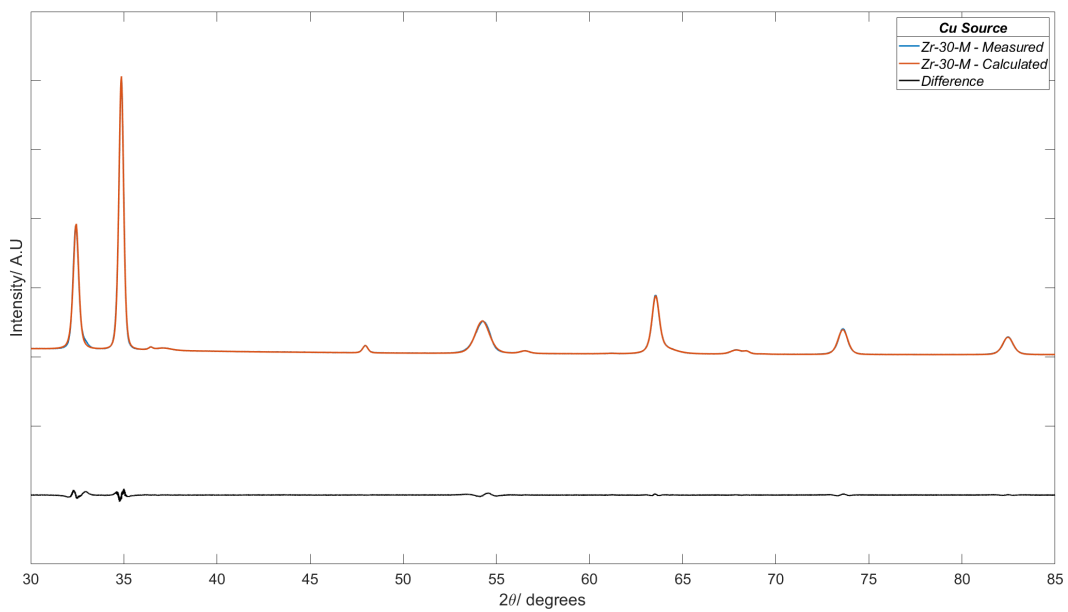


Figure B2: *The qualitative fit for the CMWP analysis of Zr-30-M.*

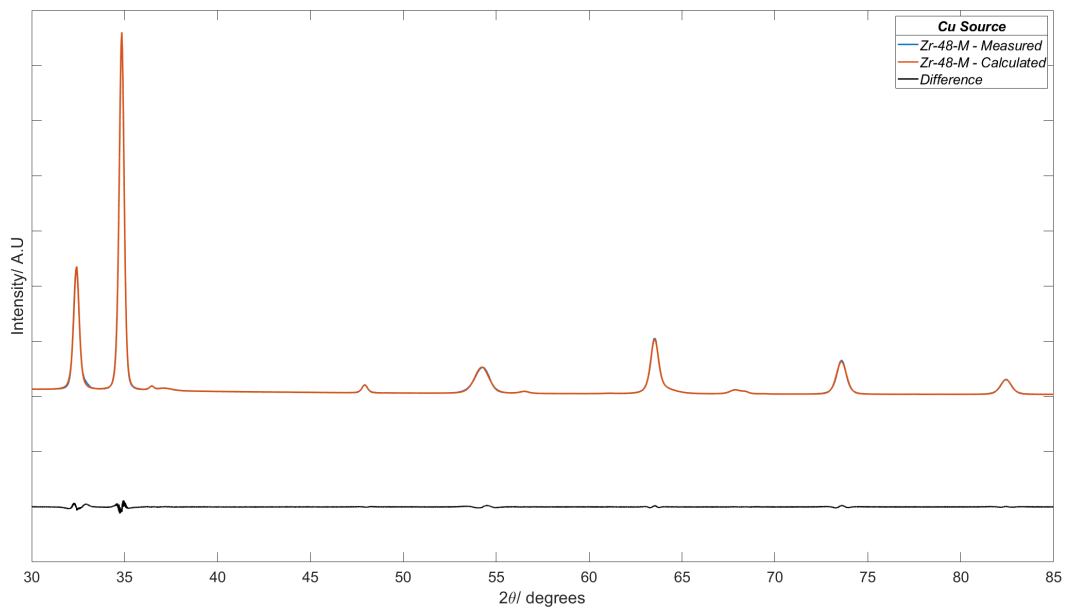


Figure B3: *The qualitative fit for the CMWP analysis of Zr-48-M.*

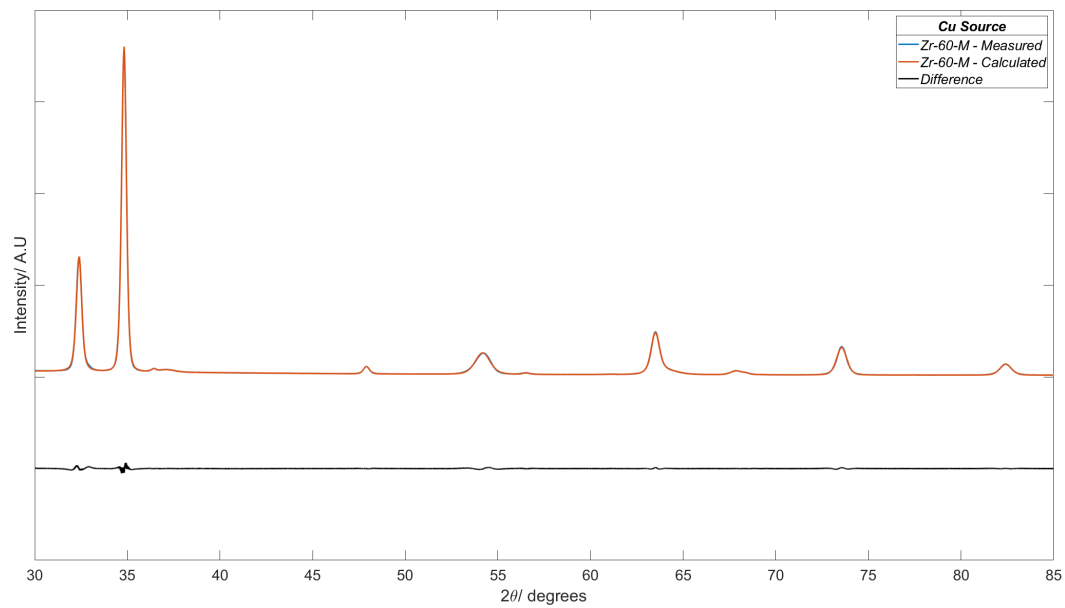


Figure B4: *The qualitative fit for the CMWP analysis of Zr-60-M.*

CMWP Co Source - MRF

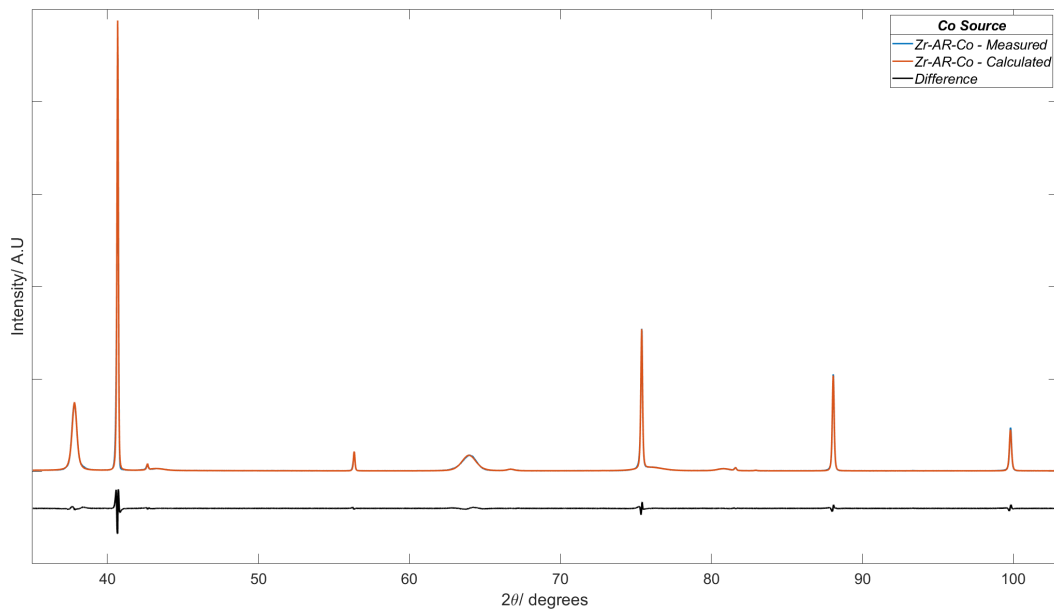


Figure B5: *The qualitative fit for the CMWP analysis of Zr-AR-Co.*

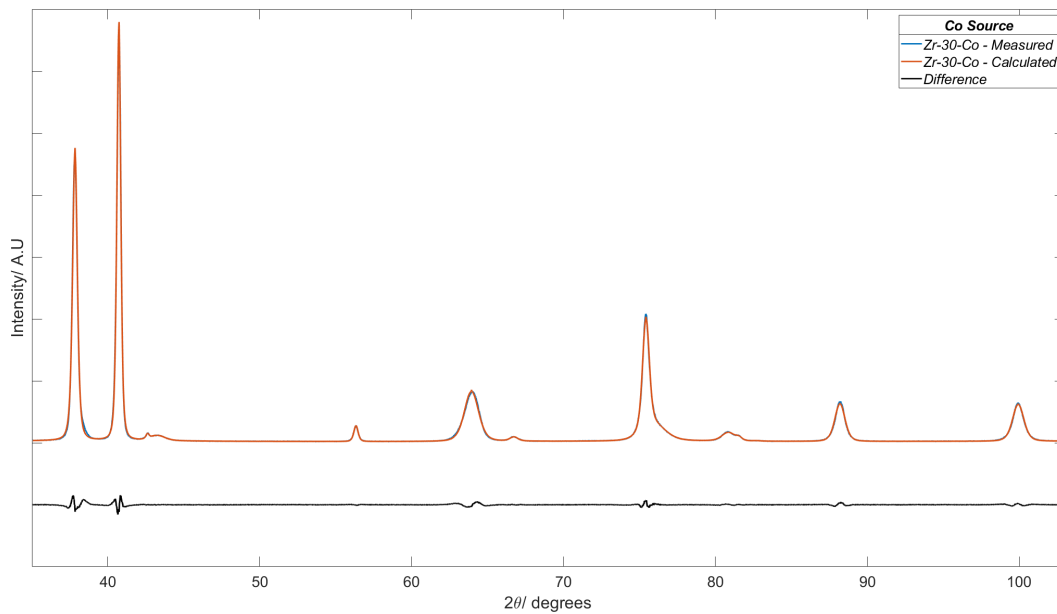


Figure B6: *The qualitative fit for the CMWP analysis of Zr-30-Co*

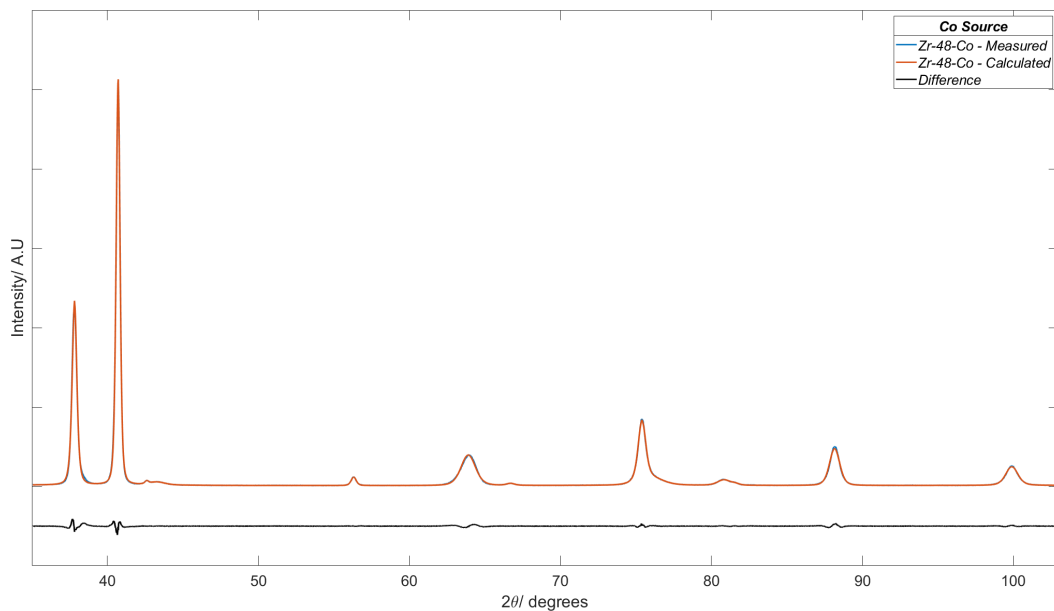


Figure B7: *The qualitative fit for the CMWP analysis of Zr-48-Co*

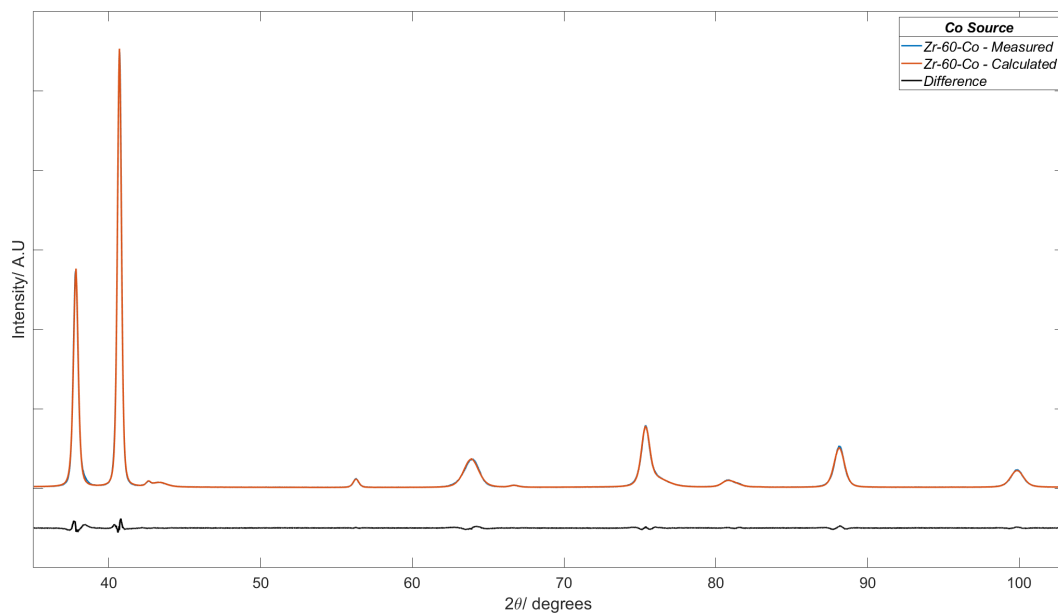


Figure B8: *The qualitative fit for the CMWP analysis of Zr-60-Co*

CMWP Physical Parameters

Table B1: *The weighted sum of square residual (WSSR) between the measure and CMWP fitted patterns for Cu and Co source XRD data.*

Samples	WSSR	
	CMWP - Cu	CMWP - Co
Zr-AR	818.2	46038.5
Zr-HT	1375.8	38528.7
Zr-30	421.5	16282.8
Zr-48	445.7	15958.2
Zr-60	388.5	17090.7

Table B2: *The crystallite size distribution parameter from CMWP fitted patterns for Cu, Co and Ag source XRD data.*

Samples	Crystallite Size Distribution					
	CMWP - Cu		CMWP - Co		CMWP - Ag	
Zr-AR	0.77	+ 0.08 - 0.11	0.05	+ 0.0043 - 0.000014		
Zr-HT	2.15	+ 0.35 - 0.65	0.61	+ 0.04 - 0.04	0.87	+ 0.45 - 0.28
Zr-30	0.33	+ 0.03 - 0.04	0.17	+ 0.04 - 0.09		
Zr-48	0.42	+ 0.06 - 0.03	0.32	+ 0.33 - 0.26		
Zr-60	0.47	+ 0.02 - 0.03	0.39	+ 0.05 - 0.03		

Table B3: *The Goodness of Fit (GoF) between the measure and CMWP fitted patterns for Cu, Co and Ag source XRD data.*

Samples	GoF		
	CMWP - Cu	CMWP - Co	CMWP - Ag
Zr-AR	0.388	3.70	2.99
Zr-HT	0.499	3.37	
Zr-30	0.278	2.17	
Zr-48	0.286	2.15	
Zr-60	0.267	2.23	

Table B4: The dislocation arrangement parameter from CMWP fitted patterns for Cu, Co and Ag source XRD data.

Samples	Dislocation Arrangement					
	CMWP - Cu		CMWP - Co		CMWP - Ag	
Zr-AR	0.26	+ 0.03 - 0.01	0.10	+ 0.01 - 0.01		
Zr-HT	0.09	+ 0.01 - 0.01	0.15	+ 0.01 - 0.01	0.05	+ 0.02 - 0.0003
Zr-30	0.52	+ 0.04 - 0.06	0.75	+ 0.07 - 0.03		
Zr-48	1.00	+ 0.08 - 0.11	1.10	+ 0.39 - 0.22		
Zr-60	1.01	+ 0.09 - 0.05	1.74	+ 0.15 - 0.16		

TOPAS Crystallite Size

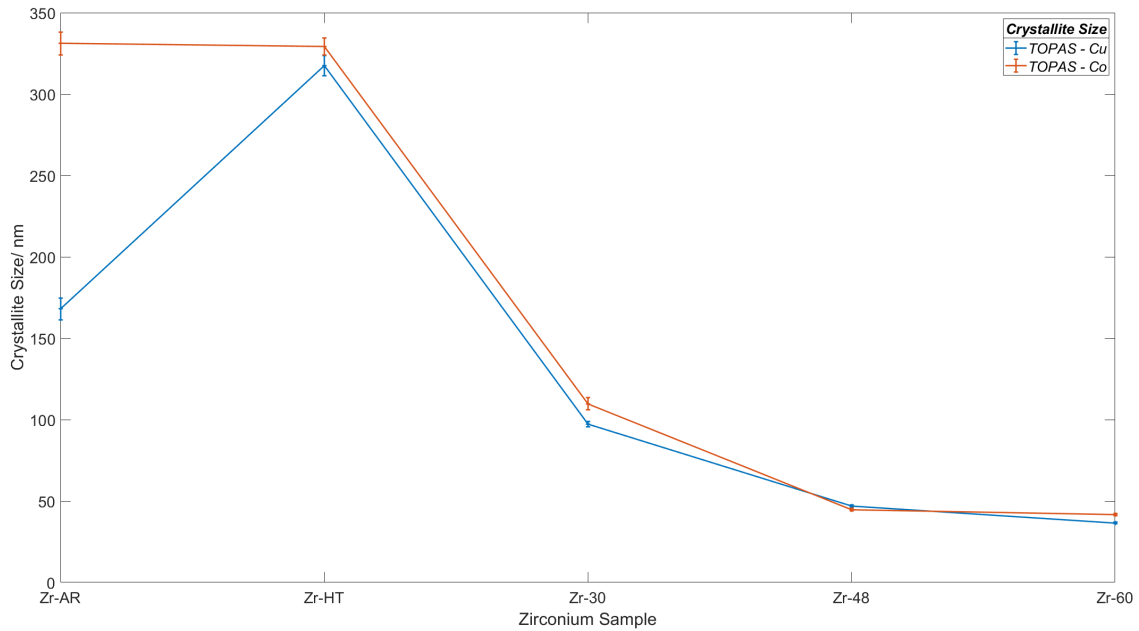


Figure B9: A graph showing the decrease in crystallite size, calculated from TOPAS using a Lorentzian function, with an increase in deformation (Zr-AR to Zr-60) for both Cu and Co diffraction data. The blue line represents Cu data obtained from UoM and the red line represents Co data from MRF.

Appendix C

Grazing Incident X-Ray Diffraction for CMWP

Minimum Grazing Incident Angle

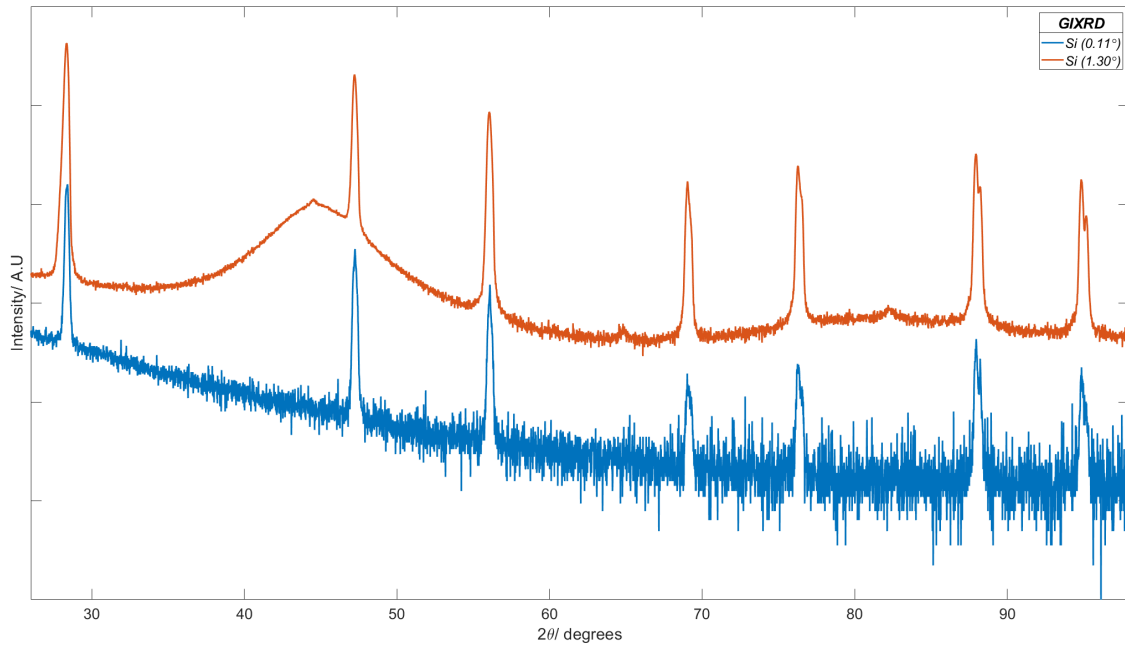


Figure C1: A comparison of the diffraction patterns for the ω angles 0.11° and 1.30° .

Smoothing Function Fitting

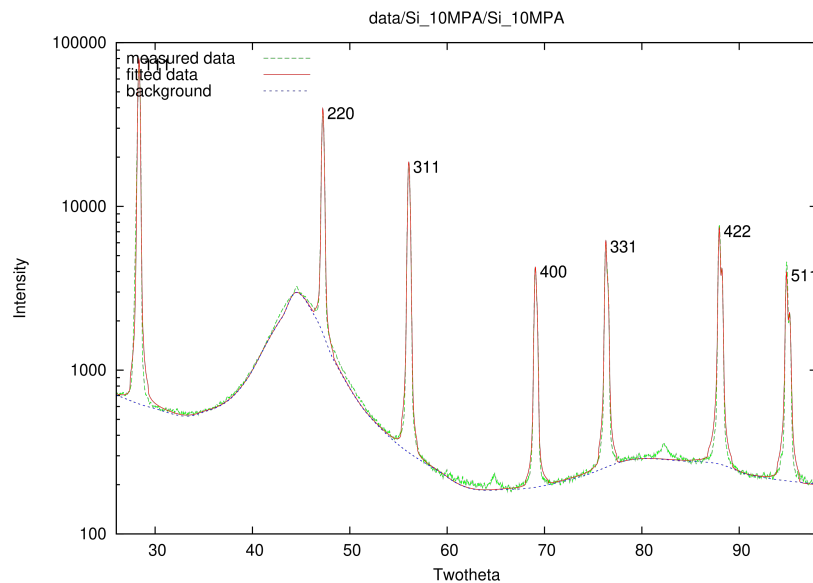


Figure C2: The goodness of fit of the CMWP fitting of Si when ω 1.30° and a smoothing function of 10 MPA.

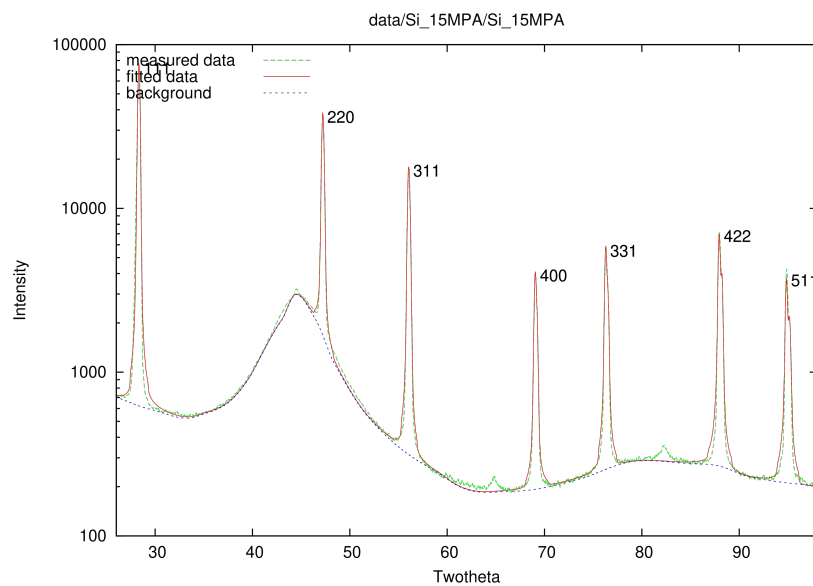


Figure C3: The goodness of fit of the CMWP fitting of Si when ω 1.30° and a smoothing function of 15 MPA.

Table C1: *Physical parameters for the fitting of Si at 1.30° with a smoothing function of 0 (unsmoothed), 10 MPA and 15 MPA.*

Sample	Crystallite Size/ nm		Crystallite Size Distribution/ nm		Dislocation Density/ x 10¹⁴.m⁻²		Dislocation Arrangement	
Unsmoothed	275.7	+ 106.9 - 59.9	0.05	+ 0.04 - 5.45e-5	0.013	+ 9.69e-3 - 2.90e-5	0.17	+ 0.24 - 0.09
10MPA	167.7	+ 35.4 - 24.0	0.05	+ 0.02 - 2.84e-8	0.010	+ 8.34e-3 - 7.09e-4	0.12	+ 0.43 - 0.04
15MPA	116.6	+18.2 - 12.9	0.05	+ 0.02 - 2.46e-6	0.017	+ 0.019 - 7.28e-3	0.06	+ 0.07 - 0.01

Appendix D

The Application of Lab HT-XRD on Hydrogen Charged Zr-4

CMWP - Line Dislocation Density

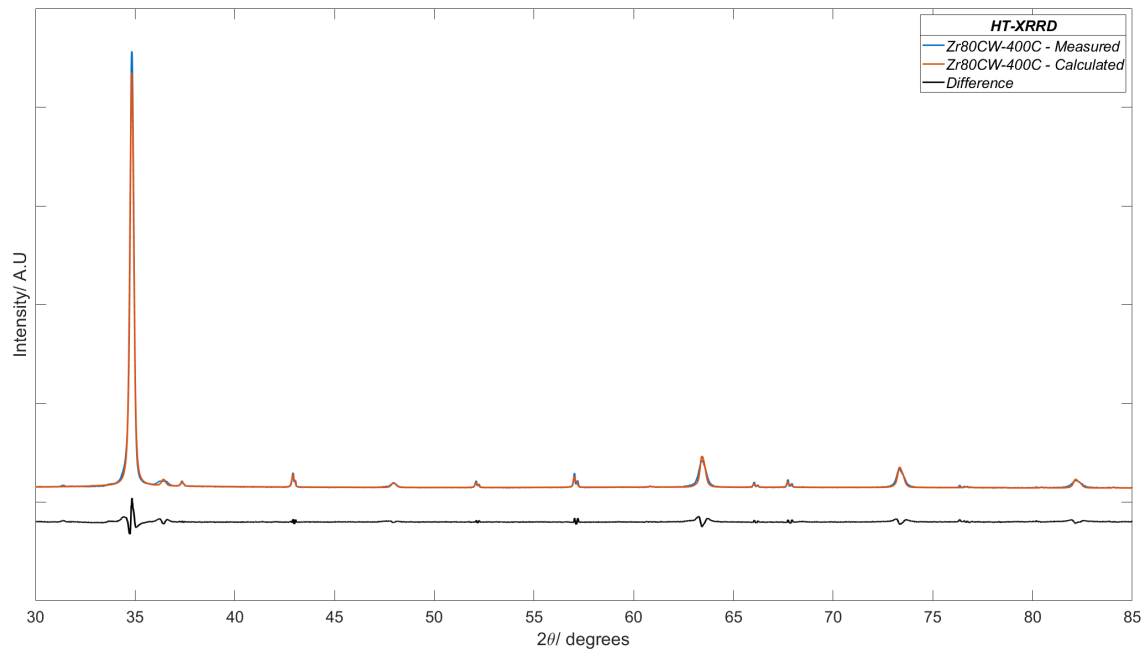


Figure C1: An example CMWP fitting on Zr80CW at 400 °C.